PREPARATION AND PROPERTIES OF NOVEL HETEROCYCLIC AROMATIC CONDUCTIVE POLYMERS BY STRAIGHTFORWARD CHEMICAL POLYMERIZATION AND THEIR APPLICATIONS FOR FUNCTIONAL FILMS

(   )

Kun Wang

Energy and Environment Science

Nagaoka University of Technology, Nagaoka, Japan

June 2014

Acknowledgements

Kun Wang

June 2014

Contents

Abbreviations used in this thesis are as follows

ECPs	Electrical conducting polymers
PPy	Polypyrrole
PANI	Polyaniline
PFu	Polyfuran
PA	Polyacetylene
PTP	Polythiophene
PPV	Poly (phenylene vinylene)
PEDOT	Poly(3,4-ethylenedioxythiophene)
S	Sulfur
N	Nitrogen
O	Oxygen
CB	Conduction band
VB	Valence band
HOMO	Highest Occupied Molecular Orbital
LOMO	Lowest Unoccupied Molecular Orbital
EL	Electroluminescence
PL	Photoluminescence
EMI	Electro-magnetic interference
OLED	Organic light emitting diode
PAA	Polyaminoanthracene
P(Py-*co*-FPy)	Poly(pyrrole-co-formylpyrrole)
P(Py-*co*-FFr)	Poly(pyrrole-co-furfural)
PSS	Polystyrene sulfonate
PS	Polystyrene
PVA	Polyvinyl alcohol
PMMA	Poly (methyl methacrylate)
CNTs	Carbon nanotube
MWCNTs	Multi-walled carbon nanotubes
SWCNTs	Single-walled carbon nanotubes
GO	Graphene oxide
1AA	1-Aminoanthracene
9AA	9-Aminoanthracene
[Ar]	Concentration of aromatic Polyaminoanthracene

GPC	Gel permeation chromatograms
Mw	Weight molecular weight
K$_{sv}$	The Stern–Volmer constant
[Q]	Concentration of quencher
A	Absorption
I	Fluorescence intensity
AA	Acetic acid
TFA	Trifluoroacetic acid
DFA	Difluoroacetic acid
TCA	Trichloroacetic acid
FA	Formic acid
TBAP	Tetrabutylammonium perchlorate
LiPF$_6$	Lithium hexafluorophosphate
TMS	*N*–2–aminoethyl–3–aminopropyltrimethylvinylsilane
DBSA	Dodecylbenzene sulfonic acid
DMF	*N,N*-dimethylformamide
DMSO	Dimethylsulfoxide
d$_6$–DMSO	Deuterated dimethylsulfoxide
NMP	N-methyl-2-pyrrolidone
THF	Tetrahydrofuran
CHCl$_3$	Chloroform chloroform
CDCl$_3$	Deuterated
I$_2$	Iodine
CH$_3$CN	Acetonitrile
ITO	Indium tin oxide
LBL	Layer-by-layer
R*rms*	Roughness parameter values
FT-IR	Fourier transform infrared
DSC	Differential scanning calorimetry
SEM	Scanning electron microscopy
AFM	Atomic force microscopy
CV	Cyclic voltammetry
C	Capacitance
Z'	Real component of impedance
Z''	Imaginary component of impedance
Wt	Weight percent

UV-vis	Ultraviolet visible
EIS	Electrochemical impedance spectroscopy
NMR	Nuclear magnetic resonance
C	Specific Capacitance
E_1, E_2	The cutoff potentials in CV curve.
m	Mass
v	Potential scan rate

Chapter 1

General Introduction

1.1 Heterocyclic Conductive Polymers

1.1.1 History of conductive polymers

Before middle 1970s, polymers were known as insulators. This situation was rapidly changed as a new kind of polymers appeared as intrinsically electrical conductive polymers (ECPs) or electroactive polymers in research and in industrial products over the past few decades. Actually, polyaniline was firstly conductive polymer and was synthesized in the 19th century. In 1862, Letheby reported anodic oxidation of aniline in diluted sulphuric acid solution and observed the blue-black shiny powder without mentioned about the electrical conductive [1]. The first highly-conductive organic compounds were charge transfer complexes reported on 1950s as polycyclic aromatic compounds showing semi-conductive charge-transfer in the present of complex salts with halogens ion [2]. Then, polyacetylene was synthesized by Natta et $al.$ as black powder in 1958 and was found as semi-conductor with electrical conductivity between 7×10^{-11} to 7×10^{-3} Ω/cm [3]. However, the ability of charge transfer and the doping mechanism was not well understood at that time. In 1963, researchers reported derivatives of polypyrrole with resistivities as low as 1 Ω/cm [4]. Subsequently,

DeSurville *et al*. reported high conductivity for polyaniline [5]. On 1977, shirakawa *et al*. reported similar high conductivity in oxidized iodine-doped polyacetylene. This was praised as the discovery and development of conductive polymers [6]. After this discovery, studying on conductive polymers with conjugated double bonds has been drawn to the attention of scientists and encouraged the rapid growth of this field. Nowadays, polyacetylene (PA), polypyrrole (PPy), polyaniline (PANI), polythiophene (PTP) and their derivatives or copolymers are contributed to the main class of conductive polymers and studied sufficiently.

1.1.2 Classification of typical conductive polymers

   Generally, according to the chemical structure and composition of conductive polymers, it was roughly classified that the frame work has aliphatic, aromatic, heterocyclic and hetero-atom containing type as shown in Figure 1.1. It should be pointed out that the classification is not so strict in PPy and PTP, but both of them could be divided into the aromatic or heterocyclic conductive polymers. The significant difference between PPy and PANI was presence of the hetero atom inside in the aromatic ring and in the main chain of their polymers. Meanwhile, there are quite a number of other conductive polymers such as poly (phenylenevinylene) (PPV) and its
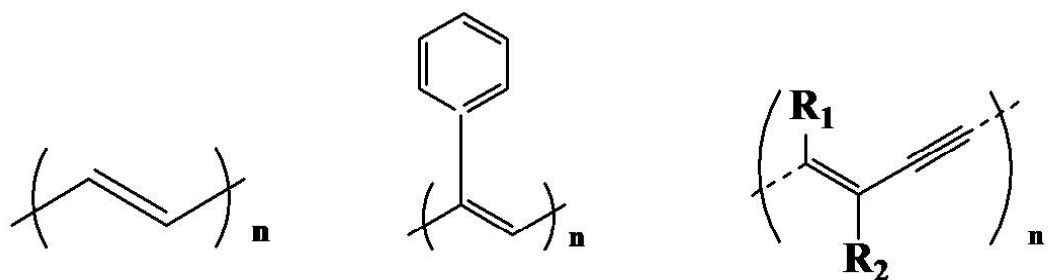
Polyacetylene [3,6]   Polyphenyl acetylene [7]   Polydiacetylene [8]

Aliphatic conducting polymers
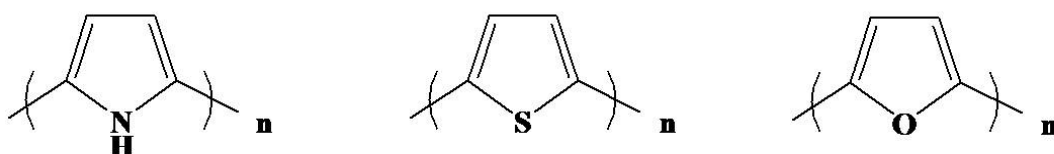
Polypyrrole [4]   Polythiophene [9]   Polyfuran [10]

Heterocyclic conducting polymers
(Inside the ring)
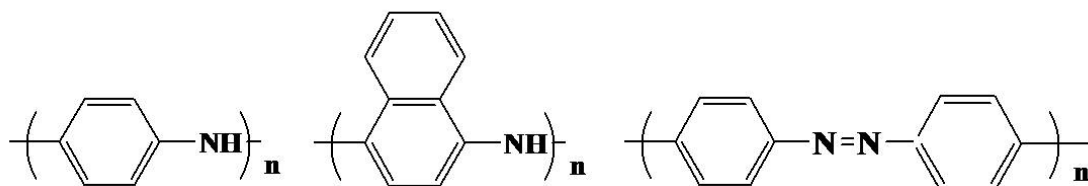
Polyaniline [5]   Polyaminonaphthalene [11]   Polyazobenzene [12]

Hetero atom containing conducting polymers
(In main chain)
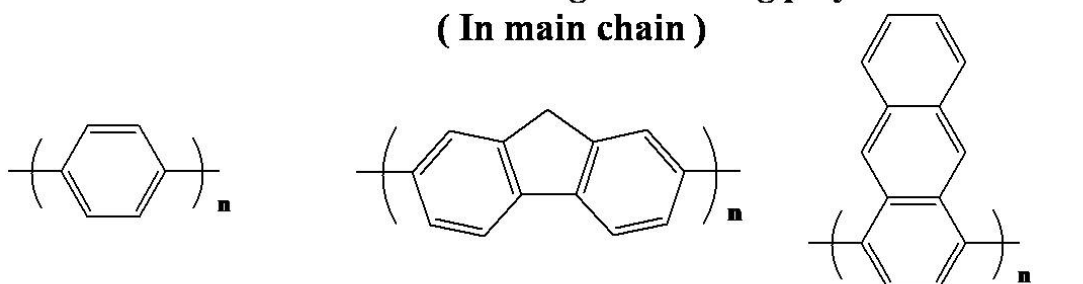
Polyphenyl [13]   Polyfluorene [14]   Polyanthracene [15]

Aromatic conducting polymers

Figure 1.1 Classification of typical conductive polymers.

derivatives which was classified into the mix-type conductive polymers [16]. All of these polymers had π-electrons in double bonds originated from the conjugated backbone having freely movement of the π-electrons through the polymers. Hence, such conductive polymer shows specific properties relative to typical insulating polymer having only single bonds.

1.2 Primary Property of Heterocyclic/Aromatic Conductive Polymers

1.2.1 Electrical property of conductive polymers

Compared with polyacetylene, conjugated polymers consisting of heterocyclic atom in the conjugated backbones are one of the most frequently classes of electrical conductive polymers, due to their highly conjugated π-bond systems, chemical stability, and excellent electronic properties. PPy, PTP and PANI are quietly differed from polyacetylene by their nondegenerate ground state. This is because of the energetic nonequivalence of their two limiting mesomeric forms, aromatic and quinoid, their high environmental stability, and their structural versatility, which allows modulation of their electronic and electrochemical properties by controlling the monomer structure [17]. On the other hand, exists of heterocyclic elements (including N, O, S) on the conjugated backbone could give extra-feature to these heterocyclic conductive polymers. It was

Polypyrrole

Polythiophene
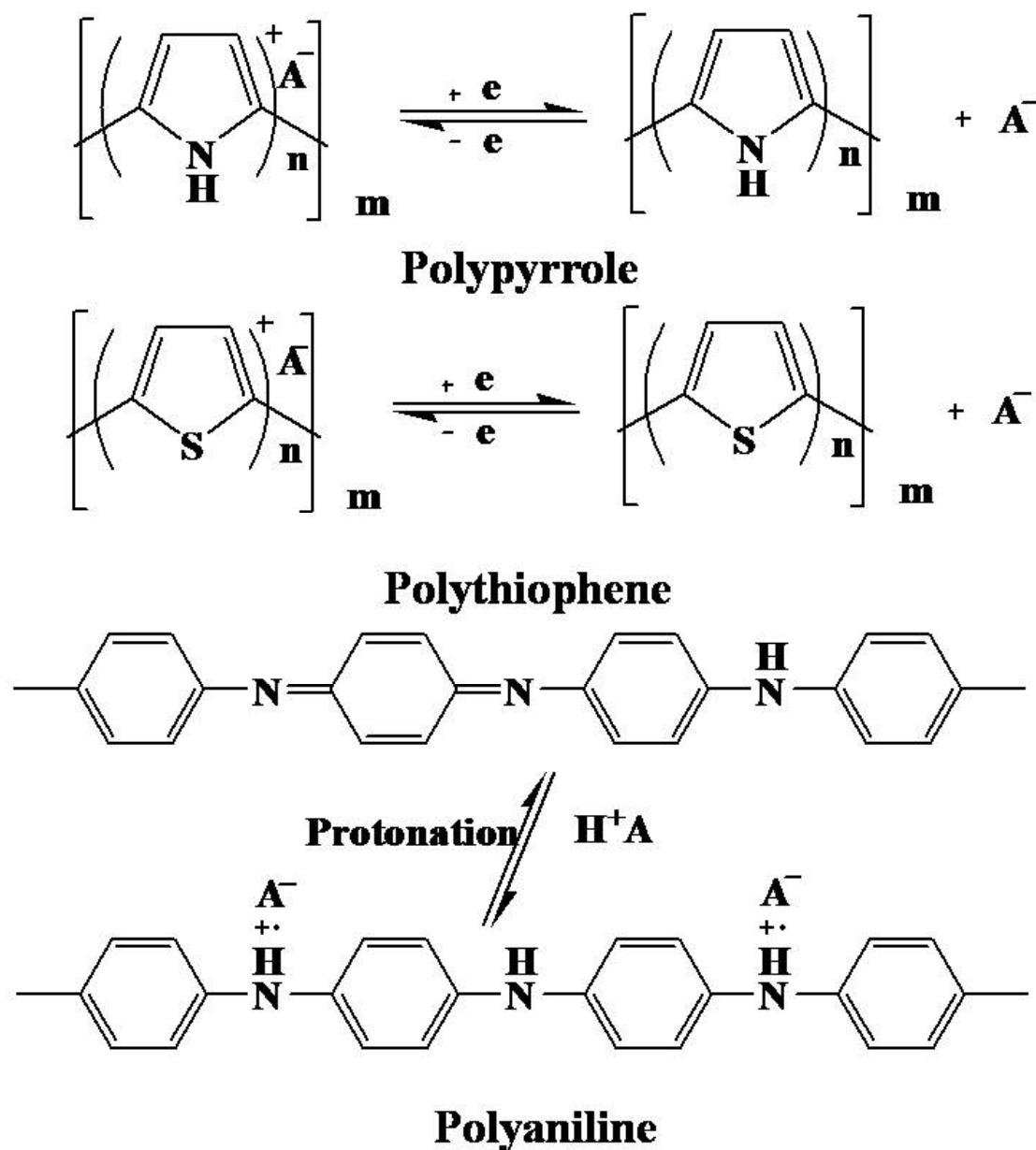
Polyaniline

Figure 1.2 Diagram of redoxreaction of polypyrrole, polythiophene and pretonation of

polyanilne between different redox forms.

reported that heterocyclic groups and hetero atomic ones in backbone of ECPs made it easily derivative for monomers or polymers, when novel polymers were prepared with excellent electrical, chemical and physical properties [18]. The best well known property of these ECPs is the ability to conduct electric current in their oxidized or reduced form as shown in Figure 1.2 [19]. Here, electron conduction is achieved by inducing a deficiency or excess of electrons in the polyconjugated chain. This process is called as doping by analogy with the insertion of electrons or holes in 3D inorganic semiconductors [20]. The conductive mechanism of the ECPs is extremely complex problem, since it could be crossing more than 15 orders of magnitude and the polymer shows different conductive mechanism under different conditions. Especially the preparation parameters would give significantly influence the conductivity of the ECPs [21], such as the type of solvent, oxidant, the countra-ion of dopants, or the electrochemical conditions for electrochemical polymerization.

CB	Polaron Level	Bipolaron Level	Bipolaron Band

| VB | | | |

(a)   **(b)**   **(c)**   **(d)**
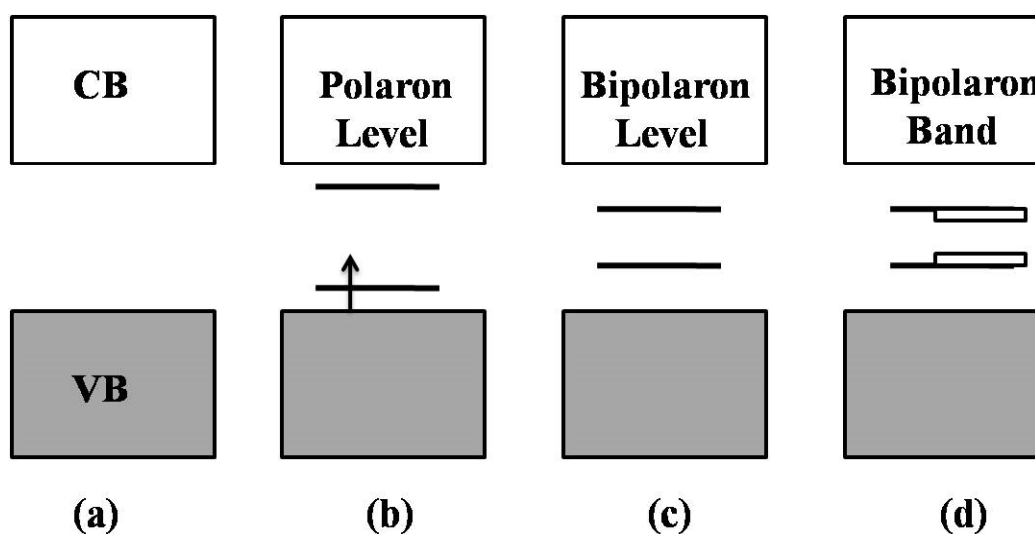
Figure 1.3 Electronic energy level/band diagram of PPy with increased dopant content.

1.2.2 Optical property of conductive polymers

For studying optical property of heterocyclic/aromatic conductive polymers, UV-Visible spectra were useful as a tool. In Figure 1.3, Bredas *et al.* proposed the electronic energy level of PPy from undoped neutral PPy to about 35% doped PPy based the half of the empirical and theoretical calculation. The neutral PPy was expected to show high transition from π-π^* in its valence band (VB) level to the conduction band (CB) level, meaning that the band gap was 3.2 eV [22]. Therefore, difference of energy level between the top of VB and the bottom of the CB called band gap. Generally, this was to be smaller with increase of the dopant content as shown in Figure 1.3a to d. Similarly, every conductive polymers could be with electricity based on this mechanism after be doped. When electronic was removed and formed polaron (radical cations) in

PPy backbone, the special electron levels of PPy was formed and called positive

polaron state (Figure 1.3b). The energy level of polaron was low under partly doped

situation, because many PPy monomeric units shared one polaron. Then, the electron

was removed with progress of the doping and the electron state of the PPy backbone

was charged to be bipolaron state with non spin resonance (Figure 1.3c). Furthermore,

when the doping level was up to 35%, one in three PPy monomeric units could share

one positive charge. Thus, the electronic state of PPy could be combined as bipolaron

band (Figure 1.3d). Other heterocyclic/aromatic conductive polymers also could be

suggested by similar theoretical explanation. According to the above description, the

gradual change of UV-visible spectra of PPy was consistent with the phenomenon of

formation of polaron and replacement of bipolaron band [23]. It was reported that

highly doped PPy showed characteristic bipolaron band and π-π^* absorption band at

about 1240 and 475 nm [24]. Similarly, emeraldine PANI was typical observed in the

π-π^* absorption band around 330 nm, the π-polaron absorption band around 430 nm and

the polaron-π^* transition band around 800 nm [25]. By studying their optical properties,

the location and the shape of the bipolaron band for each ECP could be used to reveal

the conformation of the conjugated backbone and interaction with dopant or solvent,

even with the length of the conjugated backbone [26].
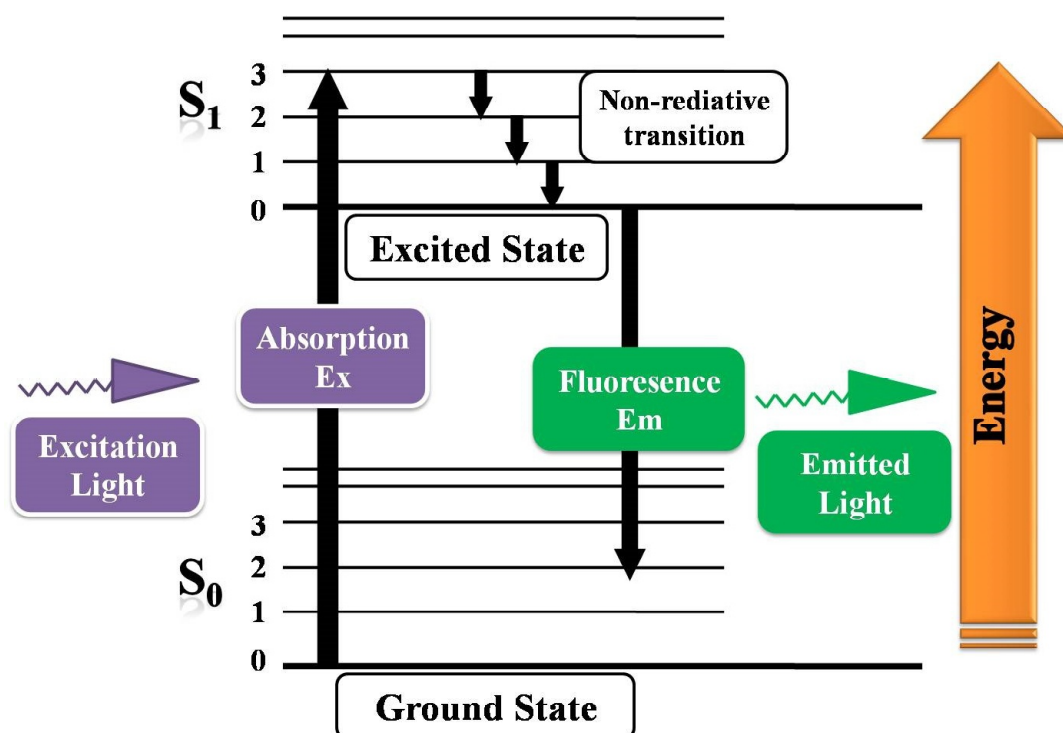
Figure 1.4 Jablonski diagrams of the relaxation mechanisms for excited state molecules

As an emerging class of materials, some of the π-conjugated CEPs have been extensively explored over the past decades for their unique tunable photoluminescence properties, which are potentially applicable in photonic devices [27-28]. Here, photoluminescence (PL) was the spontaneous emission of light from a material under optical excitation for CEPs. The fluorescence spectra described a phenomenon where π-conjugated system absorbed energy, and then emitted light. In absorption high energy light with shorter wavelength lowed excite the chromophor group. So, it could be promoting electron within the π-conjugated to transition from the ground state and then

to the excited state was formed as described by jablonski diagrams (Figure 1.4). In the

excited state, the electrons rapidly relaxed to the lowest available energy state (black

arrow). Once in this state, and after a lag period of several nano-seconds (the

fluorescence lifetime), the electrons would relax back to ground state, releasing their

stored energy in an emitted photon. Due to the higher energy relaxation mechanism this

emitted light energy was than the absorbed light [29-30]. CEPs such as polythiophene,

polyanthracene and theirs derivatives showed photoluminescence in their reduced state,

could be applied in particular photovoltaic devices and organic light-emitting devices

(OLEDs) [31-33].

1.2.3 Thermodynamic and mechanical property of conductive polymers

   For the thermodynamic and mechanical property of heterocyclic/aromatic conductive

polymers, the research of this field was too scarce. Most of the ECPs showed very high

thermostability, such as PTP maintaining stability at about 300℃ in air and over 400℃

in vacuum. For the mechanical property of conductive polymers, only in the film type

and fibrous of heterocyclic/aromatic ECP materials were prepared by electrochemical

polymerization or solution casting methods. This was because that the film type and

fibrous ECP materials were primary to two kinds of forms for their potential

applications duo to the poor solubility and high thermostability. In case of PPy, the

solvent and dopant type could greatly influence the mechanical property of obtained

PPy films. Wynne *et al.* reported that the addition of small amount of water into

acetonitrile could increase the plastic of films [34]. Qian *et al.* revealed the dependency

relationship between the counter-ion type of dopant and the morphology of PPy film

and gave great effect on mechanical property [35]. For PTP, many attempts were carried

out to increase the mechanical behavior by studying the doping effect and the

replacement of alkyl side chain in thiophene aromatic ring [36]. Certainly, improving

solubility of ECPs and mixed other excellent film-forming polymers covered poly

(methyl methacrylate) (PMMA), polyvinyl alcohol (PVA) or polystyrene sulfonate

(PSS) with ECP solution or dispersion. Other usually used methods covered enhance the

mechanical properties of the films using solution casting. Recently, a number of

research investigations was carried out on the synthesis and characterization of

nanoscale ECP materials for improving the morphology of conductive films and

enhance mechanical property [37-39].

In conclusion, as shown in Figure 1.2, the redox reaction of ECPs between different

redox forms could bring a variety of unique properties for widely range of applications,

including the charge and discharge of electron (*e.g.* PPy) as applied for charge storage

devices [40], the electro chromic effect under applied voltage (*e.g.* PANI) applied for

electro chromic display [41], the photons emitting (*e.g.* PTP) under the effect of electric

field applied for organic light emitting diode[42], the photoelectric converting (*e.g.* PPV)

applied for solar cell [43] and the change of the photoelectric performance (*e.g.*

Polyaminoanthraquinone) applied for sensing device [44].

1.3 Preparation Methods of Conductive Polymers

1.3.1 Electrochemical polymerization

   Oxidative electropolymerization was widely used for the preparation of conducting

polymers. Nowadays, a large number of anodically electropolymerizable aromatic ECPs,

PPys, PTPs, and PANIs were mostly studied. By using electrochemical polymerization,

ECP films could be obtained directly on the surface of electrode. Meanwhile, it was

easily to control the surface morphology and properties of the ECP films by changing

the current/voltage, or choosing the appropriate electrode and electrolytic system during

the process of polymerization. However, the resultant films have poorer solubility and

weaker mechanical properties of ECP films prepared by electropolymerization. Thus,

this has given great limitation for their applications. The mechanism of electrical

synthesis of ECPs is not totally understood and is still with controversial discussion [45].

Diaz *et al.* reported the mechanistic concept for the formation of ECPs firstly. In his opinion, the polymerization of PPy could be in analogy with radicalic or ionic polymerization processes as shown in Figure 1.5. During the polymerization, pyrrole dimerized after oxidation on the electrode (Step 1) and the proton elimination occurred from the doubly charged σ-dimer to form an aromatic neutral dimer (Step 2). With the formation of dimers, it was much more easily to oxidize the portion rather than the monomer. Therefore, the dimer was immediately oxidized to the cation and followed to a next coupling step with a monomeric radical cation (Step 3). Then, the similar reaction step repeated and the PPy backbone kept on growth. When the length of the PPy chain was beyond the critical length, the conductive PPy were deposited on the electrode surface because of the poor solubility of the PPy [36]. PTP showed similarly mechanistic concept for the formation of conjugated chain (Figure 1.5) [47]. For other typical ECPs, PANI showed a little different, because the polymerization occurred in the acidic aqueous solution. Here, the addition of acid during the polymerization process was beneficial to have salvation of monomer and serve as dopant into the PANI chains [48]. Recently, advancing attentions focus on employing of electrical methods, including the preparation of nanostructures as well as new strategies for tuning their properties are currently underway with continuous research [49].

1.3.2 Chemical polymerization

On the other hand, most of heterocyclic/aromatic ECPs could be conveniently produced by chemical oxidization polymerization through chemical oxidation of pyrrole, aniline, furan and thiophene without complex electrochemical polymerization system. As mentioned above, ECP films obtained by electrochemical polymerization usually showed better conductivity but weaker physical and mechanical performance as well as complex preparation [50]. Although the primary polymerization mechanism was basically similar in chemical and electrochemical polymerization mechanism (Figure 1.5), it was hard to obtain the ECPs product with similar structure and properties by different polymerization method. Critical parameters in the chemical polymerization such as monomer/oxidant feed, reaction solvent, reaction temperature/time and oxidant type could greatly influence the optimization at their syntheses, especially for film-forming properties, etc [51]. Therefore, chemical polymerization was useful for simple instruments and reaction procedures, but the disadvantages were related to poor solubility and weaker film-formation ability, especially for PPy and PFu [52-53]. Therefore, great attention has been devoted to prepare heterocyclic/aromatic ECPs by using a simple method with economical and stable processes.

Step 1: Oxidation of monomer

Step 2: Radical Coupling and Formation of dimer

PPy: X=N;
PTP: X=S
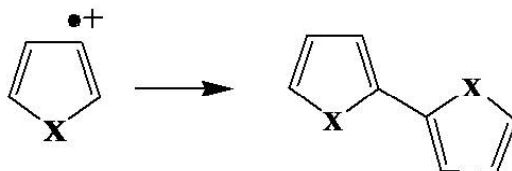
Step 3: Chain Growth

Chain
Growth

Step 1: Oxidation of monomer
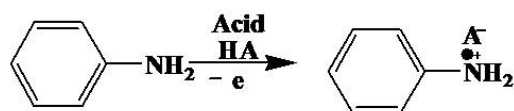
Step 2: Radical Coupling and Formation of dimer
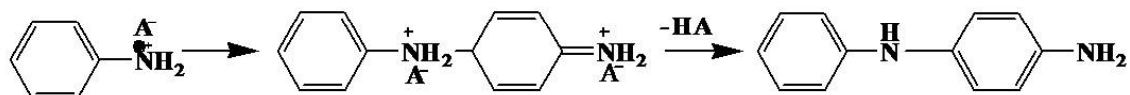
Step 3: Chain Growth

Chain
Growth
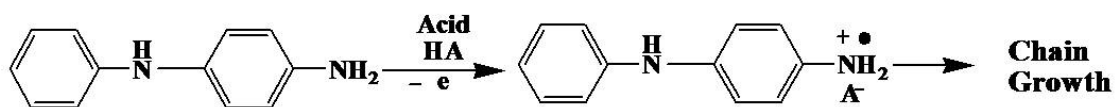
Figure 1.5 Scheme of classical polymerization mechanism of conducvivepolypyrrole,

polythiophene and polyaniline.

Through the employment of chemical polymerization, many new approaches have been presented to improving the solubility and machinability. Emulsion polymerization of heterocyclic/aromatic ECPs such as PPy, PANI and PTP has been attracted broad attention by assistant of emulsifier in the emulsion solution. The obtained polymers usually improved their solubility and enhanced conductivity [54-55]. Osterholm *et al.* reported the fibril PANI with high solubility by polymerized in xylene/water emulsion solution by addition of dodecylbenzene sulfonic acid as emulsifier [56]. One approach was to improve the solubility and discover new performance by preparing the alkyl- or sulfonic-substituted monomers [57-58]. For example, having *et al.* successfully demonstrated the water-solubility of PPy through introduction of the alkylsulfonic function group into 3-substituted pyrrole [59]. Here, the ECPs could realize the self doped by introduced of anionic sulfonic substituent on the heterocyclic/aromatic ring [60]. In addition, relative to homopolymers such as PPy, preparing copolymer systems could have several benefits of different monomers for improvement of physical and electrochemical properties of the conducting polymers. Many copolymers containing two heterocycle monomers such as aniline, pyrrole, and alkyl- or *N*-substituted monomers have been produced using chemical copolymerization method [62-64].

1.3.3 Other polymerization methods

   To obtain ECPs with special and required properties, many unusually used

polymerization methods (such as supercritical–assisted polymerization [65], interfacial

polymerization [66], vapour-depositionpolymerization [67] and template–directed

polymerization [68]) was developed for preparation of novel ECPs with special

properties. Xu *et al* reported a facile strategy to prepare graphene oxide (GO)/ PANI

nanocomposite by in situ polymerization with the assistance of supercritical carbon

dioxide. They confirmed that the PANI nanoparticles uniformly cover the GO sheets,

and the formation mechanism was proposed [65]. Wu *et al*. prepared the conducting

filaments of PANI in the 3-nanometer-wide hexagonal channel system of the

aluminosilicate by adsorption of aniline vapor into the dehydrated host as followed by

reaction with peroxydisulfate. The demonstration of conjugated polymers with mobile

charge carriers in nanometer channels represented a step toward the design of

nanometer electronic devices [67].

1.3.4 Novel conductive films prepared using chemical polymerization

   For the application of the conductive polymer in industrial production, conductive

polymer films are surely needed. Nowadays, this is because of industrial demands in

displays and other electronics are rapidly evolving as they become lighter, cheaper, and

more ergonomic. The next point in this evolution is to increase flexibility to their

properties to substantially reduce their size and increase their usability. Therefore,

conductive polymer films are expected to act as a key component in the function of

electronic devices. In these instances, the conducting polymer was typically formed by a

chemical oxidative polymerization process. However, the processing of electrically

conductive polymers into thin films was often extremely a challenging, because the

highly conductive forms of many of ECP materials were completely insoluble,

intractable, and infusible. Electrospinning and solution casting process by using soluble

conducting polymers was useful methods to produce flexible transparent conductive

films by ECPs. With this process ECPs solution were generated by electrospinning and

partially embedded into transparent films by comsosited with poly (methyl

methacrylate) (PMMA), polyvinyl alcohol (PVA) and cellulose. These films were

subjected to flex testing using a specially developed device and were found to maintain

their conductivity even after repeated flexing [69-72]. Layer-by-layer assemble of

conductive polymer/polystyrene sulfonate is another popular method to formed a

composite films by alternately immersing a surface treated ITO-coated glass substrate

into separate solutions of positively charged CEPs and negatively charged

functionalized polystyrene sulfonate. In these case, carbon nanotubes (CNTs) or

grapheme sheet are sometimes composited in the composite films as shown in Figure

1.6. Here, layer-by-layer (LbL) self-assembly method involved the alternate deposition

of types with complementary chemical interactions for the fabrication of composite

films and had been continuously growing since its rediscovery in the early 1990 [73]. It

occurred due to that sequential adsorption of materials with complementary functional

groups could produce robust films and allowed precise control over the film thickness

and its properties. By combing various functional materials for the formation of

self-assembly multilayer, the LbL technique has lead to a wide range of novel materials

for various applications [74]. Compared with other film-preparation methods, LbL

assembly was unique on controlling the chemical composition and structure of the films

on micro- and nanoscales [75]. Meanwhile, the LbL assembly method is particularly

suitable for film fabrication on non flat surfaces with large areas [76]. The employment

of ECPs using LBL method is well studied when the ECPs applied in microelectronics

[77]. Among conducting polymers of poly (3, 4–ethylenedioxythiophene) and PSS LBL

self–assembly films have been widely investigated [78]. For example, Sookhakian *et al.*

reported the synthesis of a layer-by-layer assembled graphene/zinc sulfide/polypyrrole

thin-film electrode for application of solar cells [79].

Figure 1.6 Illustration of the layer-by-layer assemble of ECPs / carbon nanotubes films.

1.4 Application of Conductive Polymers

Generally, the electrical and physical properties of heterocyclic/aromatic ECPs are influenced by their molecular structure, polymerization procedure and condition and chemical doping, as summarized above. In comparison with the traditional polymer materials, unique and excellent electrical properties, optical and other properties of ECPs are promising cost-effective, lightweight, flexible electrode materials and now becoming commercially available. In the final application, the advance of organic electronics was originated from a research/industrialization to a part of everyday life [80]. In this section, it is necessary to present a brief description of the review and a concise of the basic principles of typical applications of ECPs such as energy storage devices, electroluminescent devices and sensing materials.

1.4.1 Conductive polymers for applications in energy storage devices

Energy storage devices including secondary battery and supercapacitors could be critical to providing electric power for technical applications such as laptops, smartphones, electric vehicles and many other devices. With the development of technology, potentially flexible, lightweight, moldable and excellent electrical performance for energy storage materials is required. Heterocyclic/aromatic ECPs becomes likely candidate to meet the requirement, because the conjugated polymers

could offer not only a means to store energy but also a mean to do so independent of

form factor [81].

The origin of excellent optical and electronic properties including charge storage

capability of ECPs comes from the overlap of adjacent π-orbital. For all of the organic

semiconductors, the bottom of the conduction band (CB) is referred to as the lowest

unoccupied molecular orbital (LUMO), while the top of the valence band (VB) is

referred to as the highest occupied molecular orbital (HOMO) (Figure 1.3). Figure 1.7

demonstrates the illustration of the conductive polymers electronic structure changes

during oxidation (p-doping) and reduction (n-doping). Here, a radical cation (positive

polaron) is formed from oxidation, while a radical anion (negative polaron) is formed

during reduction. High states of charging can lead formation of positive and negative

bipolarons. The values of the HOMO and LUMO energy levels determined whether a

polymer is more likely to be n-type or p-type based on whether they were easily reduced

or oxidized [82]. Electron rich structure with higher HOMO energy level makes

excellent p-type materials depending on the ability to stabilize the positive charge, while

electron poor structure with lower LUMO energy level forms perfect n-type materials

depending on the ability to stabilize the negative charge [83]. The ECPs were expected

to show redox reaction by excitation of π-electron from its valence band (VB) level to

(p-type doping)

Positive Polaron   **Positive Biolaron**

LUMO

Oxidation → Oxidation →

HOMO

[Polymer] + yA⁻ ⟶ [Polymer]$^{y+}$ yA⁻ + ye⁻

(n-type doping)

Negative Polaron   **Negative Biolaron**

LUMO

Reduction → Reduction →

HOMO

[Polymer] + yC⁺ + ye⁻ ⟶ [Polymer]$^{y-}$ yC⁺
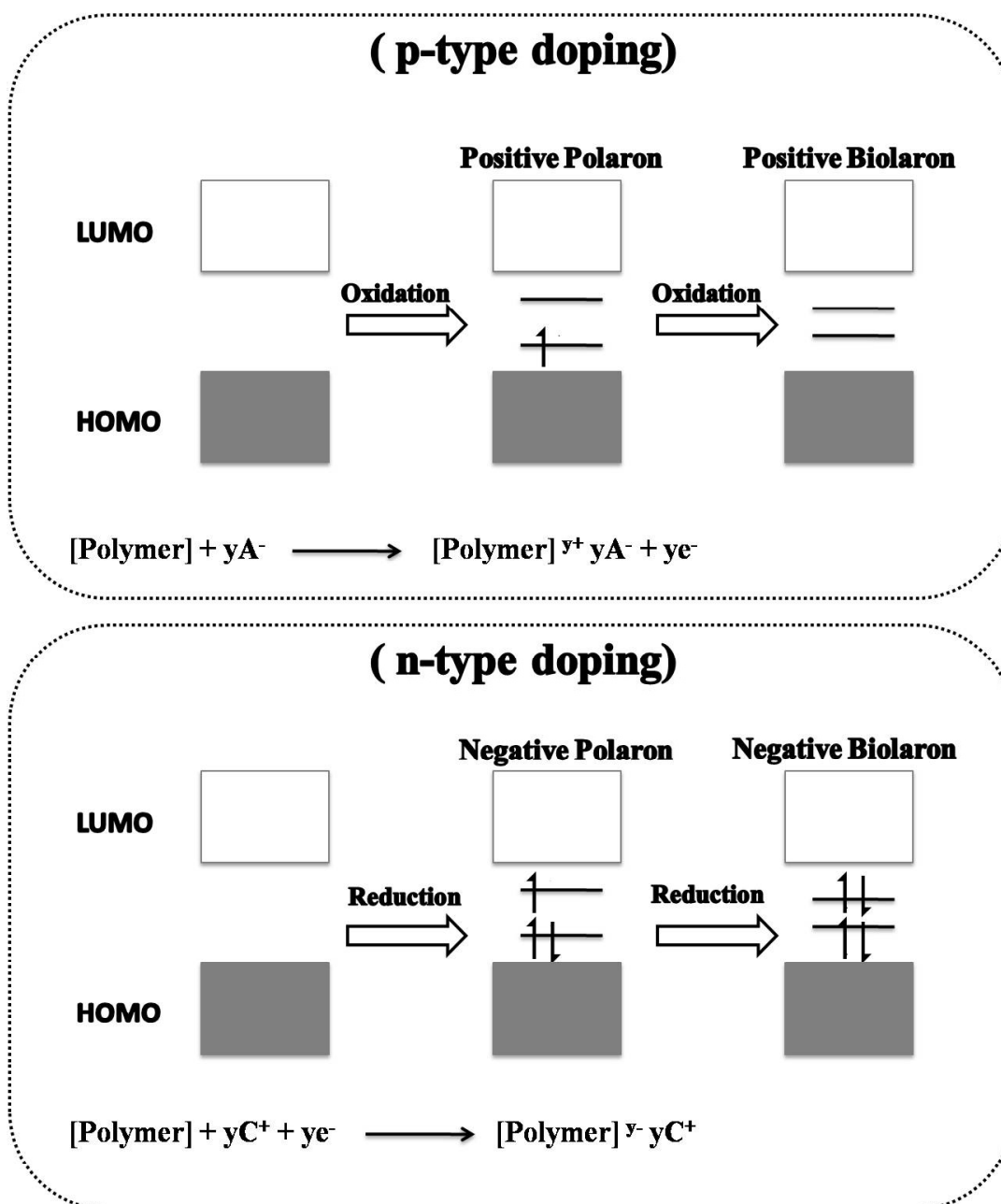
Figure 1.7 Illustration of the conductive polymers electronic structure changes during

oxidation (p-doping) and reduction (n-doping). Cations (C⁺) and anions (A⁻) counter

balance charges in the polymer chain.

the conduction band (CB) level, when it was doped. Doping process could create radical

cations or anions, also referred to as positive and negative polarons and make them

delocalized along the conjugated backbone [84-86]. The redox reaction of ECPs

between different redox forms could bring a variety of unique properties for charge and

discharge of electron. Therefore, this can apply these CEPs for charge storage devices.

The basic principle is shown in Figure 1.8.
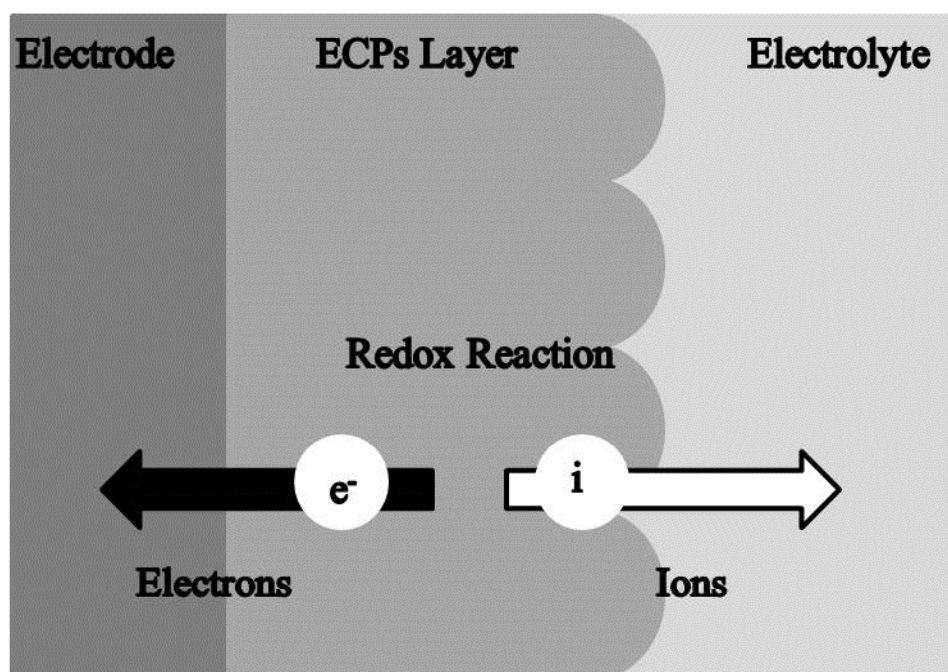
Figure 1.8 Schematic of the movement of electron/ion caused by the redox reaction of

conductive polymers.

Table 1.1 presents the performance characteristics of the typical heterocyclic/aromatic

ECPs as compared to current inorganic Li-ion battery materials ($LiCoO_2$ and $LiFePO_4$).

Although there were some advantages, the oxidative stability, diffusion limitations of

ions of dopants, the lower energy and power density, and low capacity still are several

issues for the full potential of those ECPs [87-88]. Therefore, ECPs with nanostructure

Table 1.1 Performance characteristics of conductive polymers as compared to current

inorganic Li-ion battery materials [81].

Cathode	Operating Voltage	Mw of repeat unit	Theoretical Capacity*	Experimental Capacity	Energy Density	Power Density
	$(vs.Li/Li^+)$		(mAh/g)	(mAh/g)	(mWh/g)	(mWh/g)
$LiCoO_2$	~3.8	97.87	274	135	30-144	100-1000
$LiFePO_4$	~3.2	157.76	170	109	90-100	23-70
PANI	3-4	91.11	294	100-147	300	100
PPy	3-4	65.07	412	82	60	~10
PTP	3.1-4	82.12	326	82	93	89
PEDOT	~2.7-4.2	140.16	191	30-70	1-4	35-2500

* Based on a doping level of 1 electron per monomer unit.

such as nanowires, nanotubes, or nanoparticles could effectively give rise to be capacity

as well as energy and power density. The nanostructure could alleviate problems

associated with ion diffusion by increasing the surface area and porosity [89]. In case of

capacitor applications, according to the classic capacitance (C) formulae of a

parallel-plate capacitor constructed of two parallel plates, C is determined following:

$C=\varepsilon A/4\pi kd$ (C is the capacitance; A is the area of overlap of the two plates; ε is the

dielectric constant of the material between the plates and d is the separation between the

plates). Therefore, if the double layer capacitor plate area is big enough and the distance

between the two plates is small enough, it can obtain very high capacitance.

Supercapacitor is designed based on this principle by using carbon or metal oxide

material with high surface area with a small electrode distance. ECPs were considered

as another c candidate materials applied for supercapacitor, because the oxidative

stability also greatly affected the electrode performance for ECPs, and a higher specific

capacity could be realized with higher level of redox state [90]. For further

improvement of the charge storage ability and the charge cycles stability, grapheme

oxide (GO) or carbon nanotubes, including multi-walled carbon nanotubes (MWCNTs)

and single-walled carbon nanotubes (SWCNTs) were usually composited with ECPs

[91-92]. These nanostructure carbon materials, even carbon black could suffer from

Materials	Synthetic Method	Highest Specific Capacitance	Measurement System (Electrolyte/Scan rate /reference electrode)	Pubilshed Year
PPy [98]	Electrical	~90 F/g	KCl/10 mV/s /2-electrode cells	1999
PPy/MWCNTs [99]	Electrical	~163 F/g	H_2SO_4/5 mV/s /2-electrode cells	2001
PPy/ SWNTs [100]	Electrical	~350 F/g	KOH/50 mV/s /2-electrode cells	2005
PPy/Graphite Fiber [101]	Electrical	~400 F/g	KCl/10 mV/s Ag/AgCl	2002
PPy/MWCNTs [102]	Electrical	~192 F/g	KCl/50 mV/s /SEC electrode	2002
PPy/MWCNTs [103]	Electrical	~243 F/g	KCl/10 mV /2-electrode cells	2012
PPy/MWCNTs [104]	Chemical	~165 F/g	KCl/10 mV /2-electrode cells	2012
PPy/Graphene Oxide [105]	Chemical	~248 F/g	KCl/10 mV/s Ag/AgCl electrode	2012
PPy/Graphene [106]	Electrical	~237 F/g	KCl/10 mV/s Ag/AgCl electrode	2011
PPy/Cladophora Cellulose [107]	Chemical	~180 F/g	NaCl/50 mV/s Ag/AgCl electrode	2012
PPy/Nanocrystal Cellulose [108]	Electrical	~256 F/g	KCl/250mV/s Ag/AgCl electrode	2010
PPy [108]	Electrical	~231F/g	KCl/250mV/s Ag/AgCl electrode	2010
polypyrrole/Stain less steel [109]	Electrical	~281F/g	$NaNO_3$/10 mV/s SCE electrode	2010
PPy/Carbon Black [110]	Chemical	~366F/g	$NaNO_3$/10 mV/s SCE electrode	2011

Table 1.2 Briefly summary of polypyrrole and polypyrrole composites as

supercapacitors materials

lower capacity versus redox active materials due to the non-Faradaic nature of charge

storage [93]. Metal oxide, such as V_2O_5 and MnO_2 was another candidate for high

capacity material that showed promise for battery application but suffered from the poor

electronic conductivity and slow lithium ion diffusion. By composited with PANI or

PPy, the composite can show the improvement in the performance for battery

application than either material alone [94-95]. In addition, to increasing the

processability, stability and charge storage ability of ECPs, porous composites

consisting of cellulose and PPy were fabricated using electrochemical deposition [96] or

chemical polymerization [97]. Table 1.2 shows a brief summary of polypyrrole and

polypyrrole composites as supercapacitors materials. Most research focused on the

electrical polymerization. Only few reports attempted to prepare the supercapacitors

materials through chemical polymerization. All of these efforts greatly promoted the

further application in energy storage field and extended the understanding of ECPs.

1.4.2 Conductive polymers for applications in electroluminescent devices

Electroluminescence (EL) was firstly observed in organic materials in 1963 with

anthracene crystals [111], but it was only with the development of thin films of efficient

organic dye-based LEDs by Tang *et al* in the late 1980s that significant application in

organic EL devices [112]. EL in conductive polymers was first reported as poly

(*p*-phenylenevinylene) (PPV) in 1990 and was then devoted to develop conjugated

materials in organic light-emitting devices (OLEDs) for use in display applications

[113]. As shown in Figure 1.9, in a typical OLED device, a thin film of EL active

polymer was sandwiched between two electrodes. Generally, indium tin oxide (ITO)

glass or transparent polymer substrate was chosen as the anode, and the cathode consists

of a vacuum-deposited metal layer such as Al. Here, EL was defined as the nonthermal

generation of light upon the applied electric field to be conductive substrate and the

production of light was passing electricity through the EL material. The principle of EL

resulted from recombination of charge carriers (holes and electrons) injected into the EL

materials in the presence of an external circuit. If these were excited to give a singlet

excited-state identical to that obtained in photoluminescence (PL) by excitation of an

electron from the HOMO to the LUMO, then symmetrically permitted relaxation to the

ground-state might occurred with emission of a photon. The color of the emission

obviously depended upon the HOMO-LUMO energy gap, which for visible light

(380-780 nm) corresponds to 1.5-3.2 eV [114]. Grimsdale *et al.* reviewed the synthesis

of such adequate conductive polymers and provided a brief introduction to their

applications [114]. Until now, PPV acts as one of the first and most suitable ECPs for
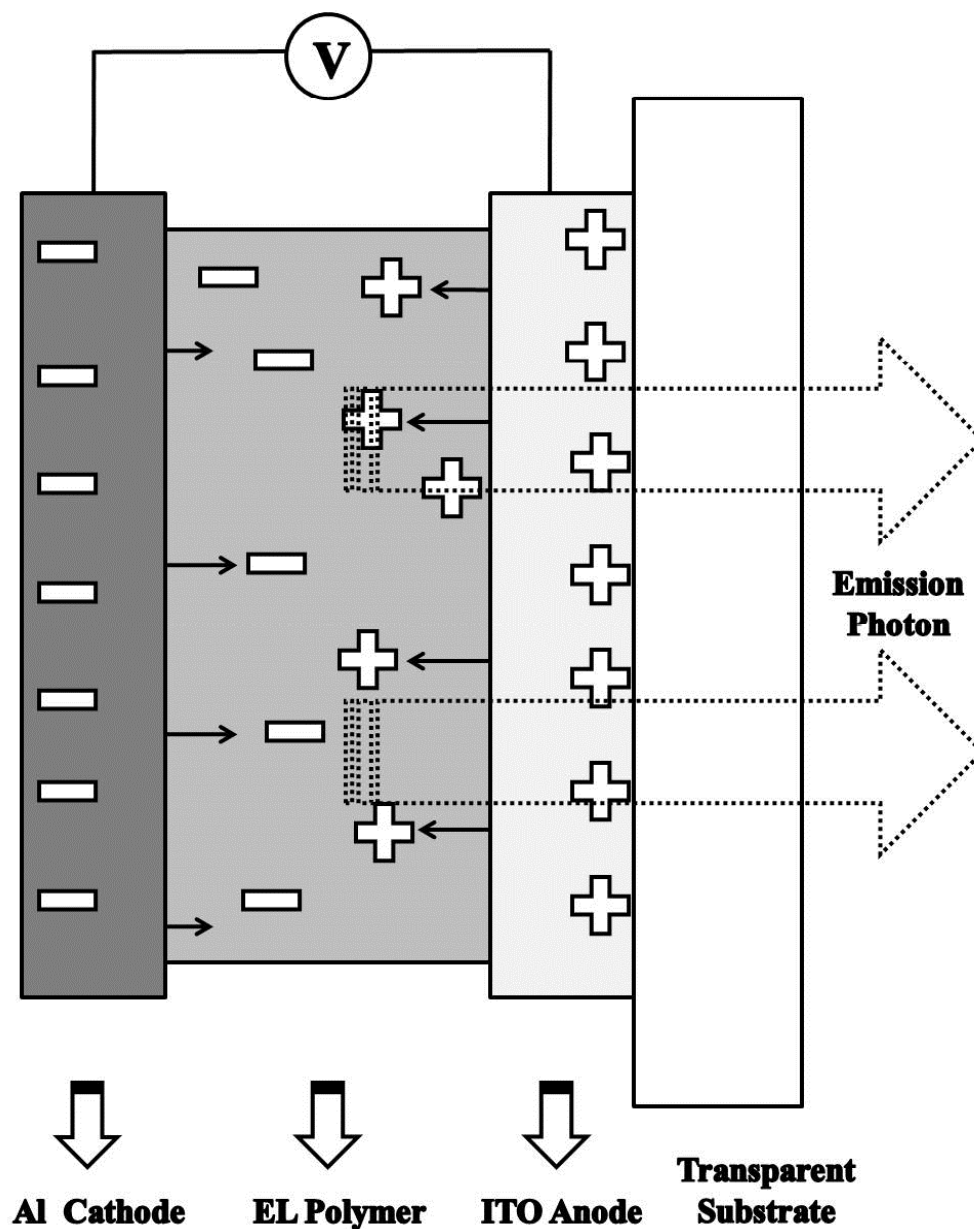
Figure 1.9 Schematic drawing of a single-layer EL device. Double charge injection

through application of a forward bias voltage results in formation of an electron-hole

pair. The singlet excited state which is formed emits a photon by radiative decay to the

ground state.
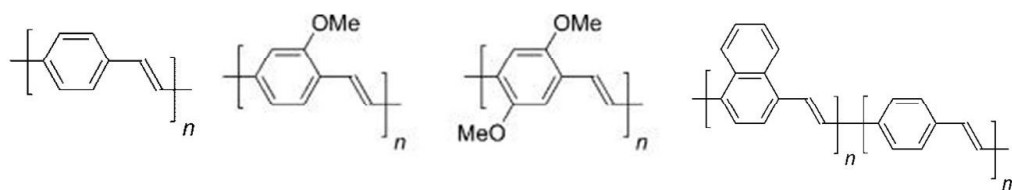
a. PPV and substituents PPVs
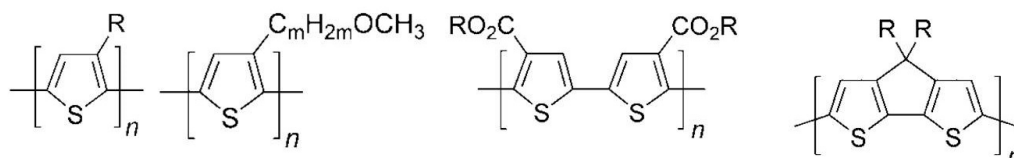
b. PTP and substituents PTPs   **R: Alkyl group**
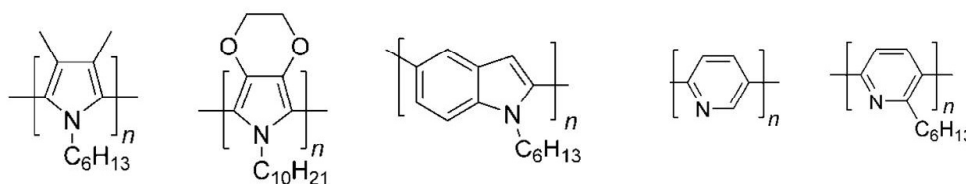
c. N-atom containing PPy derivative and Poly (2,5-pyridine)
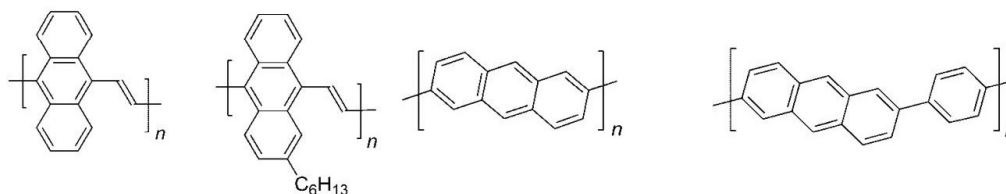
d. Anthracene-containing ECPs
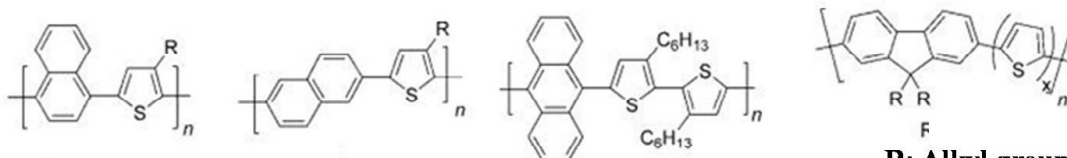
R: Alkyl group

e. Thiophene, naphthalene and anthracene containing copolymers

Figure 1.10 Classification of typical conductive polymers for EL applications.

EL applications by synthesis of its copolymer or derivative to improve the solubility and fluorescence efficiency of PPV, as shown in Figure 1.10a [115]. Polythiophenes (PTPs) acted as another class of hetero ECPs were most widely investigated for luminescence purposes (Figure 1.10b). There are reviews of the synthesis and chemistry of PTPs by Mc-Cullough [116] and on the control of their properties by modifying the substituent by Leclerc [117]. Meanwhile, aromatic heterocycles with nitrogen atoms are expected to be good electron acceptors in the polymer framework. So, these polymers have been studied as both emissive and electron-transporting materials such as Poly (2, 5-pyridine) and substituent PPy (Figure 1.10c) [114]. Anthracene-containing ECPs, such as poly (9, 10-anthracene vinylene) (Figure 1.10d) was also as the quantum efficiency used for emissive and electron-transporting materials [114]. Meanwhile, thiophene, naphthalene and anthracene molecules were usually used as the copolymerization monomer to meet the quality improvement of EL materials (Figure 1.10e) [118-119]. A wide range of conjugated CEPs and copolymers possessing electroluminescent properties suitable for use in OLEDs and related devices have been made by a variety of synthetic methods. Nowadays, the published results demonstrated that polymer LEDs are now commercially viable and may soon be fully competitive with inorganic or molecular organic electroluminescent materials for display applications.
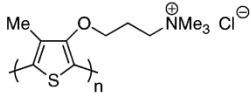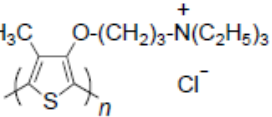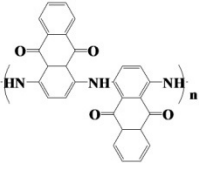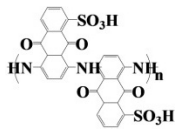
1.4.3 Conductive polymers as chemical sensing materials

The research of chemical sensing materials is becoming ever more dependent upon novel materials. EPCs are expected as one of the most important classes of transduction materials to transform a chemical signal into an easily measured electrical or optical signal. Compared with small molecules sensing materials (macrocyclic compound linking fluorohphore, inorganic hybrid materials), fluorescence-based methods using fluorescent CEPs showed increase of sensitivity due to the amplification derived from the ability of conjugated polymer to serve as highly efficient transport medium [120]. Figure 1.11 illustrates fluorescent signal amplification mechanism for fluorescent molecules and conjugated fluorescent polymers. Here, excited state of conjugated polymers was typical to refer to these excited states as quasiparticles called excitons. The π-conjugated structure led the excitons highly mobile and diffused throughout an isolated polymer chain. Therefore, the fluorescence quenching effect could be amplificated, when the polymer was coordinated or detected target such as the different metal ions [121]. Chemical sensors based on amplifying fluorescent CEPs could use to detect the metal ions, noxious gas and explosives. For example, heterocyclic ECPs having polyfunctional groups, such as O, N or S atoms could show ability to coordinate and detect the different metal ions. CEPs with nitrogen-based fluorophore such as
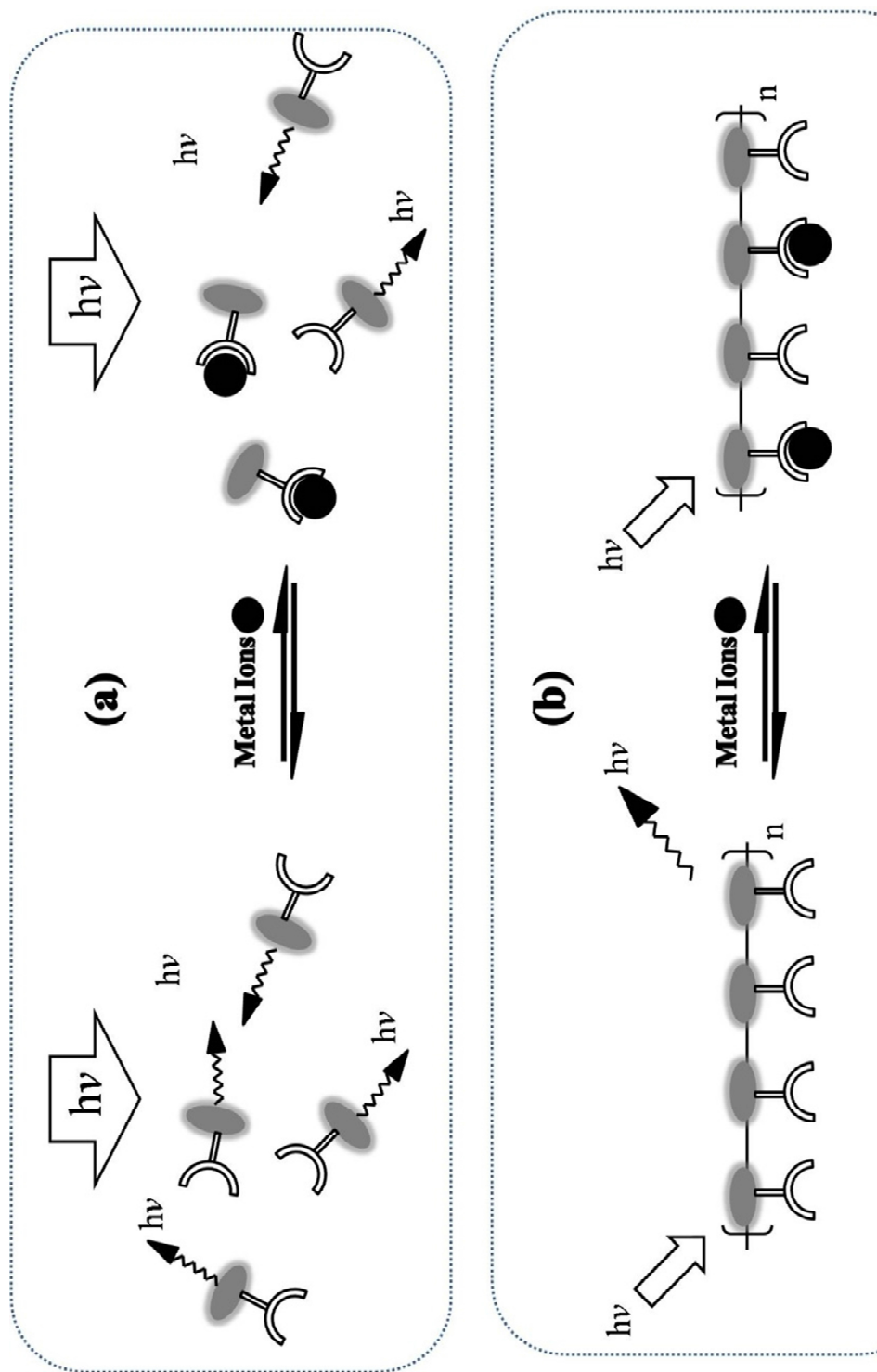
Figure 1.11 Fluorescent signal amplification mechanism for (a): Conjugated fluorescent molecules; (b). Conjugated fluorescent polymers.

Tpye of ECPs	Synthetic Method	Detection Targets	References
PPy	Chemical/Electrical	NO_2	[125, 126]
PPy	Electrical	NH_3	[127]
PPy/CNTs	Chemical	H_2	[128]
PANI and PANI/Graphene	Chemical	Toluene	[129]
PANI/TiO$_2$	Chemical	O_2/NH_3	[129]
PANI/PSS	Chemical	NH_3	[131]
Poly (thiophene)s derivative	Chemical	Adenosine triphosphate	[133]
Poly(3-alkoxy-4-methylthiophene)s	Chemical	DNA	[123]
Poly(aminoanthraquinone)s	Chemical	Heavy Metal Ions (Pb^{2+})	[44]
Polysulfoaminoanthraquinones	Chemical	Heavy Metal Ions (Pb^{2+})	[133]

Table 1.3 Classical of typical conductive polymers for chemicals sensing materials.

pyridine-based moieties and other multidentate amine-containing ligands effectively

coordinate a variety of metal ions [122]. It was also used as biosensors to detect the

proteins and DNA. PTP was the commonly used ECPs. Leclerc *et al.* found that the

water soluble imidazolium-substituted poly (thiophene), which was oxidatively

synthesized using $FeCl_3$, was highly sensitive to the presence of DNA [123]. In addition,

PPy and PANI, though their poor fluorescence property, could also transport charge

when they were oxidized or reduced. This feature was expected to provide signal gain in

the form of resistivity changes. There have been a lot of reports on the gas sensing

materials based on PPy or PANI [124-125]. PPy was mostly studied among them,

because the conductivity of PPy exhibited a long-term irreversible decay due to the

irreversible attack of oxygen present in the ambient, and the long response time due to

the highly ordered structure [126]. Table 1.3 summarizes the classical of typical

conductive polymers for chemicals sensing materials, including PPy, PANI, PTP and so

on. The field of amplifying fluorescent CPEs is far from mature, and the future

promises interesting new discoveries and commercial technologies to effectively impact

the environmental sensing, and healthcare.

Rather than the examples listed above, conductive polymer exhibits multifunctional

and unique properties and is expected to find applications in many extra fields, such as

nanoelectronic devices, catalysis or electrocatalysis, energy, microwave absorption and

electro-magnetic interference (EMI) shielding, and biomedicine.

1.5 Outline of The Thesis

The preparation of several kinds of novel heterocyclic aromatic conductive polymers

of such poly (pyrrole–*co*–formylpyrrole), poly (pyrrole–*co*–furfural) and PANI

derivatives (polyaminoanthracenes) was described having economical/stable processes

in chemical polymerization. Their composite functional films are demonstrated to be

smart materials for fascinating applications in this thesis. To promote the understanding

of these kinds of conductive polymers, the neat polymers and functional films is

prepared and characterized for their potential industrial application including energy

storage materials and ion sensing materials. This thesis is constructed in seven chapters

as followed.

Chapter 1 presents a brief introduction to related topics to electrically conductive

polymers. The synthetic method, basic property, main application fields of heterocyclic

aromatic conductive polymers are summarized in this chapter.

Chapter 2 describes investigation on the facile syntheses of P(Py-*co*-FFr) film by

chemical copolymerization of pyrrole (Py) and Furfural (FFr). Critical parameters such

as the solvents, the catalyst acid and the molar ration of the Py/FFr in copolymerization

and properties of novel film are investigated in detail. The positive effect of introduction

the methine group between the PPy conjugated backbones was studied. Meanwhile, the

formation of density and smooth surface and the thebenefitof better reflection of the

incident light is used to reveal the origination of metal-like luster for this novel PPy

films.

Chapter 3 focuses on the fabrication of composite films consisting of poly

(pyrrole–*co*–formylpyrrole) copolymers (P(Py-*co*-FPy)) and multiwall carbon

nanotubes (MWCNTs). The effect of addition MWCNTs on the improved electrical and

physical performance of P(Py-*co*-FPy) fims are revealed. The surface morphology and

the capacitance behavior of the composite films are studied for the effect of the addition

amount of MWCNTs on the surface morphology and the capacitance behavior.

In Chapter 4, the novel capacitance films are presented as facile syntheses of poly

(pyrrole–*co*–formylpyrrole) prepared on poly (4–styrenesulfonate acid) (PSS) with

electrostatic self–assembly layer–by–layer process. Surface analysis confirms that the

multilayer of the P(Py–*co*–FPy) and the PSS contained homogeneous particulate layers

with the changed morphology, depending on the number of layer or the concentration of

PSS. Cyclic voltammetry and impedance measurement are used to the evidence that the

capacitance of the LBL films is influenced by the increasing of the number of layers or

the concentrations of PSS.

Chapter 5 focuses facile synthesis of polyaminoanthrcaenes (PAAs) by chemical

oxidation polymerization of 1-aminoanthrcaen and 9-aminoanthracene. The electrical

and optical properties of the obtained PAAs are investigated. In addition, in the effect of

the molecular formation on the fluorescence lifetime the solvent effect of fluorescence

emission on fluorophore in different solvents is also demonstrated. In addition, the

fluorescent composite films consisting of P1AA and PVA/PSS are prepared to study the

electrostatic interaction between the P1AA and sulfo group, which is expected to show

greatly effect on the surface morphology and the optical properties for composite films.

Chapter 6 deals with the comparative investigations of adsorption behaviors revealed

that the obtained soluble PAAs, and the results suggest the detection capacity towards

several heavy metal ions and implied their potential applications for sensitive

fluorometric detection of heavy metal ions, especially in detection of Pb^{2+}.

Finally, Chapter 7 is the summary of this thesis.

1.6 References

[1]. Noel, S. H. An Overview of the first half-century of molecular electronics. *Annals of the New York Academy of Sciences.* **2003**, 1006, 1.

[2]. Herbert, N. Polymers, electrically conductive. *Ullmann's Encyclopedia of Industrial Chemistry.***2000**, doi: 10.1002/14356007.a21_429.

[3]. Young, R. J.; Lovell, P. A. Introduction to polymers. *CRC: Printing Press*. **2011**, ISBN 978-0-8493-3929-5.

[4]. Bolto, B. A.; McNeill, R.; Weiss, D. E. Electronic Conduction in Polymers. III. Electronic properties of polypyrrole. *Australian Journal of Chemistry.* **1963**, *16*, 1090.

[5]. De Surville, R.; Jozefowicz, M.; Yu, L. T.; Pepichon, J.; Buvet, R. Electrochemical chains using protolytic organic semiconductors. *Electrochimica. Acta.* **1968**, *13*, 1451.

[6]. Shirakawa, H; Louis, E. J.; MacDiarmid, A. G.; Chiang, C. K.; Heeger, A. J. Synthesis of electrically conductive organic polymers: Halogen derivatives of polyacetylene, $(CH)_x$. *J. Chem. Soc., Chem. Commun.* **1977***, 16*, 578.

[7]. Rajesh, B.; Thampi, K. R.; Bonard, J. M.; Xanthopoulos, N., Mathieu, H. J.; Viswanathan, B. Carbon nanotubes generated from template carbonization of polyphenyl acetylene as the support for electrooxidation of methanol. *J. Phys. Chem. B* **2003**, *107*, 2701.

[8]. Xu, Q.; Lee, S.; Cho, Y.; Kim, M. H.; Bouffard, J.; Yoon, J. Polydiacetylene-based colorimetric and fluorescent chemosensor for the detection of carbon dioxide. *J. Am. Chem. Soc.* **2013**, *135*, 17751.

[9]. Waltman, R. J.; Bargon, J.; Diaz, A. F. Electrochemical studies of some conducting polythiophene films. *J. Phys. Chem.***1983**, *87*, 1459.

[10]. Ohsawa, T.; Kaneto, K.; Yoshino, K. Electrical and optical properties of electrochemically prepared polyfuran. *Jpn. J. Appl. Phys*. **1984**, *23*, 663.

[11]. Moon, D. K.; Osakada, K.; Maruyama, T.; Kubota, K.; Yamamoto, T. Synthesis of poly(1-aminonaphthalene) and poly(1-aminoanthracene) by chemical oxidative polymerization and characterization of the polymers. *Macromolecules* **1993**, *26*, 6992.

[12]. Neuert, G.; Hugel, T.; Netz, R. R.; Gaub, H. E. Elasticity of poly(azobenzene−peptides). *Macromolecules* **2006**, *39*, 789.

[13]. Tong, L.; Ho, D. M.; Vogelaar, N.J.; Schutt, C. E.; Jr, P. The albatrossenes: Large, cleft-containing, polyphenyl polycyclic aromatic hydrocarbons. *J. Am. Chem. Soc.* **1997**, *119,* 7291.

[14]. Huang, F.; Wu, H.; Wang, D.; Yang, W.; Cao, Y. Novel electroluminescent conjugated polyelectrolytes based on polyfluorene. *Chem. Mater.* **2004**, 16, 708.

[15]. Tanemura, K.; Suzuki, T.;Horaguchi, T. Synthesis of sulfonated polynaphthalene,

polyanthracene, and polypyrene as strong solid acids via oxidative coupling polymerization. *J. Appl. Polym. Sci*. **2013**, *127*, 4524.

[16]. Liao, L.; Ding, L.; Karasz, F. E. Blue-emitting poly [(*m*-phenylenevinylene)-*alt*-(*o*-phenylenevinylene)]s: The effect of regioregularity on the optical properties. *J. Polym. Sci: Polym. Chem.* **2003**, *41*, 2650.

[17]. Chen, W.; Xue, G. Low potential electrochemical syntheses of heteroaromatic conducting polymers in a novel solvent system based on trifluroborate–ethyl ether. *Prog. Polym. Sci.* **2005**, *30*, 783.

[18]. Wong, B. M.;Cordaro, J. G. Electronic properties of vinylene-linked heterocyclic conducting polymers: Predictive design and rational guidance from DFT calculations. *J. Phys. Chem. C* **2011**, *115*, 18333.

[19]. MacDiamid, A. G. Synthetic met als': a novel role for organic polymers (Nobel lecture). *Angew. Che. Int. Ed*. **2001**, *40*, 2581.

[20]. Negi, Y. S.;Ashyapak, P. V. Development in polyaniline conducting polymers. *J. Macromol. Sci. Polym. Rev.* **2002**, *42*, 35.

[21]. Chan, H. S, O.; Ng,S. O. Synthesis, characterization and applications of thiophene-based functional polymers. *Prog. Polym. Sci.* **1998**, *23*, 1167.

[22]. Bredas, J. L.; Street, G. B. Polarons, bipolarons, and solitons in conducting

polymers. *Acc. Chem. Res*. **1985**, *18*, 309.

[23]. Furukawa, Y.; Tazawa, S.; Fuji, Y.; Harada, I. Raman spectra of polypyrrole and its 2,5-^{13}C-substituted and C-deuterated analogues in doped and undoped states. *Synth. Met*. **1988**, *24*, 329.

[24]. Hu, Y.; Yang, R.; Evans, D. F.; Weaver, J. H. Direct measurements of bipolaron-band development in doped polypyrrole with inverse photoemission. *Phys. Rev B*. **1991**, *44*, 13660.

[25]. Zhuang, L.; Zhou, O.; Lu, J. Simultaneous electrochemical–ESR–conductivity measurements of polyaniline. *J. Electroanal. Chem*. **2000**, *493*, 135.

[26]. McCullough, R. D. The chemistry of conducting polythiophenes. *Adv. Mat*. **1998**, *10*, 93.

[27]. Asati, A.; Lehmkuhl, D.; Diaz, D.; Perez, J. M. Nanoceria facilitates the synthesis of poly (*o*-phenylenediamine) with pH-tunable morphology, conductivity, and photoluminescent properties. *Langmuir*. **2012**, *28*, 13066.

[28]. Lu, X. F.; Zhang, W. J.; Wang, C.; Wen, T. C.; Wei, Y. One-dimensional conducting polymer nanocomposites: Synthesis, properties and applications. *Prog. Polym. Sci*. **2011**, *36*, 671.

[29]. Liu, I. S.; Chen, Y. F.; Su, W. F. Modulating the photoluminescence of conducting

polymer by the surface plasmon of Au colloids. *J. Photochem. Photobio A: Chem*. **2008**, *199*, 291.

[30]. Donald, S.; Marcus, J.; Garry, R.; Yu, P.; Jovan, N.; Shaheen, S.   Quenching of semiconductor quantum dot photoluminescence by a -conjugated polymer. *J. Phys. Chem. B* **2005**, *109*, 15927.

[31]. Ji, J. S.; Lin, Y. J.; Lu, H P.; Wang, L.; Rwei, S. P. Synthesis and photoluminescence of poly (3-hexylthiophene) / titania nanostructured hybrids. *Thin Solid Films.* **2006**, *511*, 182.

[32]. Wang, X.; Li, H. D.; Liu, P. Well-defined aniline-triphenylamine copolymer nanotubes: Preparation, photoluminescent, and electrochemical properties. *Electrochimica. Acta.* **2014**, *125*, 630.

[33]. Tao, Y. J.; Zhou, Y. J.; Xu, X. H.; Zhang, Z. Y.; Cheng, H .F.; Zheng, W. W.   A multi electrochromic copolymer based on anthracene and thiophene via electrochemical copolymerization in boron trifluoride diethyl etherate. *Electrochimica. Acta.* **2012**, *78* 353.

[34]. Wynne, K. J.; Street, G. B. Poly (pyrrol-2-ylium tosylate), electrochemical synthesis and physical and mechanical properties. *Macromolecules* **1985**, *18*, 2361.

[35]. Moutet, J. C.; Saint-Aman, E.; Tran-Van, F.; Angibeaud, P.; Utille, J .P. Poly

(glucose-pyrrole) modified electrodes: A novel chiral electrode for enantioselective recognition. *Adv. Mater*. **1992**, *4*, 511.

[36]. Moulent, J.; Simth, P. Electrical and mechanical properties of oriented poly (3-alkylthiophenes): 2. Effect of side-chain length. *Polymer*. **1992**, *33*, 2340.

[37]. Chew, S. Y.; Guo, Z. P.; Wang, J. Z.; Chen, J.; Munroe, P.; Ng, S. H.; Zhao, L.; Liu, H. K. Novel nano-silicon/polypyrrole composites for lithium storage. *Electrochem. Comm.* **2007**, *9*, 941.

[38]. Jang, J., Oh, J. H.; Stucky, G. D. Fabrication of ultrafine conducting polymer and graphite nanoparticles. *Angew. Chem. Int. Ed*., **2002**, *41*, 4016.

[39]. Stejskal, J.; Omastová, M.; Fedorova, S.; Prokes, J.; Trchova, M. Polyaniline and polypyrrole prepared in the presence of surfactants: A comparative conductivity study. *Polymer*, **2003**, *44*, 1353.

[40]. Soon. Y. L, Wim. T., Darren. W. Electrochemical capacitance of nanocomposite polypyrrole/cellulose films. *J. Phys. Chem. C* **2010**, *114*, 17926.

[41]. Zhao, L.; Zhao, L.; Xu, Y.; Qiu, T.; Zhi, L.; Shi, G. Polyaniline electrochromic devices with transparent graphene electrodes. *Electrochimica. Acta*. **2009**, *55*, 491.

[42]. Ohshita, J.; Tada, Y.; Kunai, A.; Harima, Y.; Kunugi, Y. Hole-injection properties of annealed polythiophene films to replace PEDOT–PSS in multilayered OLED systems.

Synth. Met. **2009**, *159*, 214.

[43].Wang, M.; Wang, X. PPV/TiO2 hybrid composites prepared from PPV precursor reaction in aqueous media and their application in solar cells. *Polymer*. **2008**, *49*, 1587.

[44]. Li, X. G; Li, H.; Huang, M. R.; Moloney, M. G. Synthesis and multifunctionality of self-stabilized poly (aminoanthraquinone) nanofibrils. *J. Phys. Chem. C* **2011**, *115*, 9486.

[45]. Heinze, J.; Frontana-Uribe, B. A.; Ludwigs, S. Electrochemistry of conducting polymers-persistent models and new concepts. *Chem. Rev*. **2010**, *110*, 4724.

[46]. Diaz, A. F.; Castillo, J. I.; Logan, J. A.; Lee, W. Y. J. Electrochemistry of conducting polypyrrole films. *Electroanal. Chem*. **1981**, *129*, 115.

[47]. Wei, Y.; Chan, C. C.; Tran, J.; Jang, G. W.; Hsueh, K. F. Electrochemical polymerization of thiophenes in the presence of bithiophene or terthiophene: kinetics and mechanism of the polymerization. *Chem. Mat.* **1991**, *3*, 888.

[48]. Zotti, G.; Cattrain, S.; Comisso, N. J. Cyclic potential sweep electropolymerization of aniline: The role of anions in the polymerization mechanism. *Electroanal. Chem.* **1988**, *239*, 387.

[49]. Pron, A.; Rannou, P. Processible conjugated polymers: from organic semiconductors to organic metals and superconductors. *Prog. Polym. Sci.* **2002**, *27*, 135.

[50]. Kaplin, D. A.; Qutubuddin, S. Electrochemically synthesized polypyrrole film: effects of polymerization potential and electrolyte type. *Polymer*. **1995**, *36*, 1275.

[51]. Li, X. G.; Huang, M. R.; Duan, W.; Yang, Y. L. Novel multifunctional polymers from aromatic diamines by oxidative polymerizations. *Chem. Rev*. **2002**, *102*, 2925.

[52]. Kudoh, Y. Properties of polypyrrole prepared by chemical polymerization using aqueous solution containing $Fe_2(SO4)_3$ and anionic surfactant. *Synth. Met*. **1996**, *79*, 17.

[53]. Hoshina, Y. E.; Contreras, A. Z.; Farnood, R.; Kobayashi, T. Nanosized polypyrrole affected by surfactant agitation for emulsion polymerization. *Polym. Bull*. **2012**, *68*, 1689.

[54]. Shen, Y.; Wan, M. Counter-ion induced processibility of conducting polymers: 2. Acid-assisted oxidative polymerization, doping and solubilization. *Synth. Met*. **1997**, *87*, 141.

[55]. Lee, J. Y.; Kim, D. Y.; Kim, C. Y. Poly (cyclopentadienylenevinylene)s: synthesis via ROMP, chemical and physical properties. *Synth. Met*. **1995**, *74*, 103.

[56]. Osterholm, J. E.; Cao, Y.; Klavetter, F.; Smith, P. Emulsion polymerization of aniline. *Polymer*. **1994**, *35*, 2902.

[57]. Macinnes, D.; Funt, B. L. Poly-*o*-methoxyaniline: A new soluble conducting polymer. *Synth. Met*. **1988**, *25*, 235.

[58]. Shoji, E.; Freund, M. S. Poly (aniline boronic acid): A new precursor to substituted poly (aniline)s. *Langmuir*. **2001**, *17*, 7183.

[59]. Havinga, E. E.; Ten Hoeve, W.; Meijer, E. W.; Wynberg, H. Water-soluble self-doped 3-substituted polypyrroles. *Chem. Mater*. **1989**, *1*, 650.

[60]. Yamaguchi, I.; Higashi, H.; Sato, M. Synthesis and chemical properties of photoluminescent self-doped polyanilines.*J. Mater. Sci.* **2009**, *44*, 6408.

[61]. Mu, S. Synthesis and electronic properties of poly (aniline-*co*-2-amino-4 hydroxybenzenesulfonic acid). *J. Phys. Chem. B* **2008**, *112*, 6344.

[62]. Jinish, A. M.; Jayakannan, M. Role of anionic micellar template on the morphology, solid state ordering and unusual non-linear conductivity of polyaniline-*co*-polypyrrole nanomaterials*J. Phys. Chem. B* **2011**, *115*, 6427.

[63]. Rao, P. S.; Sathyanarayana, D. N. Synthesis of electrically conducting copolymers of aniline with *o/m*-aminobenzoic acid by an inverse emulsion pathway. *Polymer*. **2002**. *43*, 5051.

[64]. Kabasakaloglu, M.; Talu, M.; Yildirim, F.; Sari, B. The electrochemical homopolymerization of furan and thiophene and the structural elucidation of their biopolymer films. *Appl. Surf. Sci*. **2003**, *218*, 84.

[65]. Xu, G. H.; Wang, N.; Wei, J. Y.; Lv, L.; Zhang, J. N.; Chen, Z. M.; Xu, Q.

Preparation of graphene oxide/polyaniline nanocomposite with assistance of supercritical carbon dioxide for supercapacitor electrodes. *Ind. Eng. Chem. Res.* **2012**, *51*, 14390.

[66]. Han, Y. Q.; Shen, M. X.; Lin, X. C.; Ding, B.; Zhang, L. G.; Tong, H.; Zhang, X. J. Ternary phase interfacial polymerization of polypyrrole/MWCNT nanocomposites with core–shell structure. *Synth. Met.* **2012**, *162*, 753.

[67]. Wu, C. G.; Bein, T. Conducting polyaniline filaments in a mesoporous channel host. *Science*, **1994**, *264*, 1757.

[68]. Zhang, D.; Dong, Q. Q.; Wang, X.; Yan, W.; Deng, W.; Shi,L. Y. Preparation of a three−dimensional ordered macroporous carbon nanotube/polypyrrole composite for supercapacitors and diffusion modeling. *J. Phys. Chem. C* **2013**, *117*, 20446.

[69]. Chen, Z. D.; Okimoto, A.; Kiyonaga, T.; Nagaoka, T. Preparation of soluble polypyrrole composites and their uptake properties for anionic compounds. *Anal. Chem.* **1999**, *71*, 1834.

[70]. Li, Y.; Yinga, B. Y.; Honga, L. J.; Yang, M. J. Water-soluble polyaniline and its composite with poly(vinyl alcohol) for humidity sensing. *Synth. Met.* **2010**, *160*, *455*.

[71]. Sata, T.; Funakoshi, T.; Akai, K. Preparation and transport properties of composite membranes composed of cation exchange membranes and polypyrrole. *Macromolecules*

1996, *29,* 4029.

[72]. Nikpour, M.; Chaouk, H.; Mau, A.; Chung, D. J.; Wallace, G. Porous conducting membranes based on polypyrrole–PMMA composites. *Synth. Met.* **1999**, *99*, 121.

[73]. Fou, A. C.; Rubner, M. F. Molecular–level processing of conjugated polymers. 2. layer–by–layer manipulation of in–situ polymerized p–type doped conducting polymers. *Macromolecules* **1995**, *28*, 7115.

[74]. Zhang, X.; Chen, H.; Zhang, H. Y. Layer-by-layer assembly: from conventional to unconventional methods. *Chem. Commun*. **2007**, 1395.

[75]. Srivastava, S.; Kotov, N. A. Composite layer-by-layer (LBL) assembly with inorganic nanoparticles and nanowires. *Acc. Chem. Res*. **2008**, *41*, 1831.

[76]. Thierry, B.; Winnik, F. M.; Merhi, Y.; Tabrizian, M. Nanocoatings onto arteries via layer-by-layer deposition: Toward the in vivo repair of damaged blood vessels. *J. Am. Chem. Soc*. **2003**, *125*, 7494.

[77]. Lee, J.; Ryu, J.; Youn, H. J. Conductive paper through LbL multilayering with conductive polymer: dominant factors to increase electrical conductivity. *Cellulose*. **2012**, *19*, 2153.

[78]. Schrote, K.; Frey, M. W. Effect of irradiation on poly (3, 4–ethylenedioxythiophene): poly (styrenesulfonate) nanofiber conductivity. *Polymer*.

2013, *54*, 737.

[79]. Sookhakian, M.; Amin, Y. M, Baradaran, S.; Tajabadi, M.T.; Moradi Golsheikh, A.; Basirunb, W. J. A layer-by-layer assembled graphene/zinc sulfide/polypyrrole thin-film electrode via electrophoretic deposition for solar cells. *Thin. Solid. Films.* **2014**, *552*, 204.

[80]. Kertesz, M.; Choi, C. H.; Yang, S. Conjugated polymers and aromaticity. *Chem. Rev.* **2005**, *105*, 3448.

[81]. Mike, J. F.; Lutkenhaus, J. L. Recent advances in conjugated polymer energy storage. *J. Polym. Sci. Part B: Polm. Phys.* **2013**, *51*, 468.

[82]. Heeger, A. G. Semiconducting and metallic polymers: The fourth generation of polymeric materials (Nobel Lecture). *Angew. Chem. Int. Ed. Engl.* **2001***, 40,* 2591.

[83]. Michinobu, T. Adapting semiconducting polymer doping techniques to create new types of click postfunctionalization. *Chem. Soc. Rev.* **2011***, 40,* 2306.

[84]. Bredas, J. L.; Street, G. B. Polarons, bipolarons, and solitons in conducting polymers. *Acc. Chem. Res.* **1985**, *18*, 309.

[85]. Bredas, J. L.; Beljonne, D.; Coropceanu, V.; Cornil, J. Charge-transfer and energy-transfer processes in π-conjugated oligomers and polymers: A molecular picture. *Chem. Rev.* **2004**, *104*, 4971.

[86]. Fesser, K.; Bishop, A. R.; Campbell, D. K. Optical absorption from polarons in a model of polyacetylene. *Phys. Rev. B* **1983**, *27*, 4804.

[87]. Pasquier, D. A.; Plitz, I.; Menocal, S.; Amatucci, G. A comparative study of Li-ion battery, supercapacitor and nonaqueous asymmetric hybrid devices for automotive applications. *J. Power. Sources.* **2003**, *115*, 171.

[88]. Dubarry, M.; Liaw, B. Y. Identify capacity fading mechanism in a commercial LiFePO4 cell. *J. Power. Sources.* **2009**, *194*, 541.

[89]. Cho, S. I.; Lee, S. B. Fast electrochemistry of conductive polymer nanotubes: Synthesis, mechanism, and application. *Acc. Chem. Res.* **2008**, *41*, 699.

[90]. Levi, M. D.;Aurbach, D.A short review on the strategy towards development of π-conjugated polymers with highly reversible p- and n-doping. *J. Power. Sources.* **2008**, **180**, 902.

[91]. Lee, S. W.; Gallant, B. M.; Byon, H. R.; Hammond, P. T.; Shao-Horn, Y. Nanostructured carbon-based electrodes: bridging the gap between thin-film lithium-ion batteries and electrochemical capacitors. *Energy. Environ. Sci.* **2011**, *4*, 1972.

[92]. Zhang, L. L.; Zhou, R.; Zhao, X. S. Graphene-based materials as supercapacitor electrodes. *J. Mater. Chem.* **2010**, *20*, 5983.

[93]. Dumitrescu, I.; Unwin, P. R.; Macpherson, J. V. Electrochemistry at carbon

nanotubes: perspective and issues. *Chem. Commun.* **2009**, *45*, 6886.

[94]. Ferreira, M.; Huguenin, F.; Zucolotto, V.; Silva, P.; Torresi, C.; Temperini, M. L. A.; Torresi, R. M.; Oliveira, O. N. Electroactive multilayer films of polyaniline and vanadium pentoxide. *J. Phys. Chem. B* **2003**, *107*, 8351.

[95]. Chen, W.; Fan, Z.; Gu, L.; Bao X.; Wang, C. Enhanced capacitance of manganese oxide via confinement inside carbon nanotubes. *Chem. Commun.* **2010**, *46*, 3905.

[96]. Liew, S. Y.; Thielemans, W.; Walsh, D. A. Electrochemical capacitance of nano composite polypyrrole/cellulose films. *J. Phys. Chem. C* **2010**, *114*, 17926.

[97]. Jradi, K.; Bideau, B.; Chabot, B.; Daneault, C. Characterization of conductive composite films based on TEMPO-oxidized cellulose nanofibers and polypyrrole. *J. Mater. Sci.* **2012**, *47*, 3752.

[98]. Conway, B. E. (Ed.), Electrochemical supercapacitors, *Kluwer Academic Publishers/Plenum Press, New York,* **1999**.

[99]. Jurewicz, K.; Delpeux, S.; Bertagna, V.; Beguin, F.; Frackowiak, E. Supercapacitors from nanotubes/polypyrrole composites. *Chem. Phys. Lett.* **2001**, *347*, 36.

[100]. Zhou, C. F.; Kumar, S. Functionalized single wall carbon nanotubes treated with pyrrole for electrochemical supercapacitor membranes. *Chem. Mater.* **2005**, *17*, 1997.

[101]. Park, J .H.; Ko, J. M.; Park, O. O. Capacitance properties of graphite/polypyrrole composite electrode prepared by chemical polymerization of pyrrole on graphite fiber. *J. Power. Sources.* **2002**, *105*, 20.

[102]. Hughes, M.; Chen, G. Z.; Shaffer, M. S. P.; Fray, D. J.; Windle, A. H. Electrochemical capacitance of a nanoporous composite of carbon nanotubes and polypyrrole. *Chem. Mater*. **2002**, *14*, 1610.

[103]. Sun, X.; Xu, Y.; Wang, J.; Mao, S. The composite film of polypyrrole and functionalized multi–walled carbon nanotubes as an electrode material for supercapacitors. *Int. J. Electrochem. Sci.* **2012**, *7*, 3205.

[104]. Paul, S.; Choi, K. S.; Lee, D. J.; Sudhagar, P.; Kang, Y. S. Factors affecting the performance of supercapacitors assembled with polypyrrole/multi–walled carbon nanotube composite electrodes. *Electrochimica. Acta*. **2012**, *78*, 649.

[105]. Zhang, J.; Zhao, X. S. Conducting polymers directly coated on duced grapheme oxide sheets as high performance supercapacitor electrodes. *J. Phys. Chem. C* **2012**, *116*, 5420.

[106]. Davies, A.; Audette, P.;Farrow, B.; Hassan, F.; Chen, Z.; Choi, J. Y.; Yu, A. P. Graphene-based flexible supercapacitors: pulse-electropolymerization of polypyrrole on free-standing graphene films. *J. Phys. Chem. C* **2011**, *115*, 17612.

[107]. Olsson, H.; Carlsson, D.; Nyströ¨m, G.; Sjo¨din, M.; Nyholm, L.; Strømme, M. Influence of the cellulose substrate on the electrochemical properties of paper-based polypyrrole electrode materials. *J. Mater. Sci.* **2012**, *47*, 5317.

[108]. Zhang, J.; Kong, L. B.; Li, H.; Luo, Y. C.; Kang, L. Synthesis of polypyrrole film by pulse galvanostatic method and its application as supercapacitor electrode materials. *J. Mater. Sci.* **2010**, *45*, 1947.

[109]. Liew, S. Y.; Thielemans, W.; Walsh, D. A. Electrochemical capacitance of nanocomposite polypyrrole/cellulose films. *J. Phys. Chem. C* **2010**, *114*, 17926.

[110]. Yang, C.; Liu, P.; Wang, T. Well-defined core-shell carbon black / polypyrrole nanocomposites for electrochemical energy storage. *ACS Appl Mater Interfaces.* **2011**, *3*, 1109.

[111]. Pope, M.; Kallmann, H. P.; Magnante, P. Electroluminescence in organic crystals. *J. Chem. Phys.* **1963**, *38*, 2042.

[112]. Tang, C. W.; VanSlyke, S. A. Organic electroluminescent diodes. *Appl. Phys. Lett.* **1987**, *51*, 913.

[113]. Burroughes, J. H.; Bradley, D. D. C.; Brown, A. R.; Marks, R. N.; Mackay, K.; Friend, R. H.; Burn, P. L.; Holmes, A. B. Light-emitting diodes based on conjugated polymers. *Nature.* **1990**, *347*, 539.

[114]. Grimsdale, A. C.; Chan, K. L.; Martin, R. E.; Jokisz, P. G.; Holmes, A. B. Synthesis of light-emitting conjugated polymers for applications in electroluminescent devices. *Chem. Rev*. **2009**, *109*, 897.

[115]. Schenk, R.; Gregorius, H.; Meerholz, K.; Heinze, J.; Mu̇llen, K. Novel oligo (phenylenevinylenes): models for the charging of extended .pi. chains**.** *J. Am. Chem. Soc.* **1991**, *113*, 2634.

[116]. McCullough, R. D.The Chemistry of Conducting Polythiophenes. *Adv. Mater.* **1998**, *10*, 93.

[117]. Leclerc, M.; Faı̈d, K. Electrical and optical properties of processable polythiophene derivatives: structure-property relationships. *Adv. Mater.* **1997**, *9*, 1087.

[118]. Lee, J.-I.; Klaerner, G.; Miller, R. D. Structure-property relationship for excimer formation in poly (alkylfluorene) derivatives. *Synth. Met.* **1999**, *101*, 126.

[119]. Kreyenschmidt, M.; Klaerner, G.; Fuhrer, T.; Ashenhurst, J.; Karg,S.; Chen, W. D.; Lee, V. Y.; Scott, J. C.; Miller, R. D. Thermally stable blue-light-emitting copolymers of poly (alkylfluorene). *Macromolecules* **1998**, *31*, 1099.

[120]. McQuade, D. T.; Pullen, A. E.; Swager, T. M. Conjugated polymer-based chemical sensors. *Chem. Rev.* **2000**,*100*, 2537.

[121]. Zhou, Q.; Swager, T. M. Method for enhancing the sensitivity of fluorescent

chemosensors: energy migration in conjugated polymers. *J. Am. Chem. Soc.* **1995**, *117*, 7017.

[122].   Wang, B.; Wasielewski, M. R. Design and synthesis of metal ion-recognition-induced conjugated polymers: An approach to metal ion sensory materials. *J. Am. Chem. Soc.* **1997**, *119*, 12.

[123]. Ho, H.-A.; Boissinot, M.; Bergeron, M. G.; Corbeil, G.; Doré, K.; Boudreau, D.; Leclerc, M. Colorimetric and fluorometric detection of nucleic acids using cationic polythiophene derivatives. *Angew. Chem., Int. Ed.* **2002**, *41*, 1548.

[124]. Kincal, D.; Kumar, A.; Child, A. D.; Reynolds, J. R. Conductivity switching in polypyrrole-coated textile fabrics as gas sensors. *Synth. Met.* **1998**, *92*, 53.

[125]. Ram, M. K.; Yavuz, O.; Aldissi, M. NO_2 gas sensing based on ordered ultrathin films of conducting polymer and its nanocomposite. *Synth. Met.* **2005**, *151*, 77.

[126]. Karin, P. K. Chemical gas sensors based on organic semiconductor polypyrrole. *Crit. Rev. Anal. Chem.* **2002**, *32*, 121.

[127]. Patois, T.; Sanchez, J. B.; Berger, F.; Rouch, J. Y.; Fievet, P.; Lakard, B. Ammonia gas sensors based on polypyrrole films: Influence of electrodeposition parameters. *Sensors and Actuators B: Chemical*. **2012**, 171, 431.

[128]. Park, S. J.; Kwon, O. S. Jang, J. A high-performance hydrogen gas sensor using

ultrathin polypyrrole-coated CNT nanohybrids. *Chem. Commun.*, **2013**,*49*, 4673.

[129]. Parmar, M.; Balamurugan, C.; Lee, D. W. PANI and Graphene/PANI nanocomposite films-comparativetoluene gas sensing behavior. *Sensors*. **2013**, *12*, 16611.

[130]. Huyen, D. N.; Tung, N, T.; Thien, N, D.; Thanh, L. H. Effect of TiO_2 on the gas sensing feature of TiO_2/PANI nanocomposites. *Sensors*. **2011**, *11*, 1924.

[131]. Jang, J.; Cho, J. Fabrication of water-dispersible polyaniline-poly (4-styrenesulfonate) nanoparticles for inkjet-printed chemical-sensor applications. *Adv. Mater*. **2007**, *19*, 1772.

[132]. Li, C.; Numata, M.; Takeuchi, M.; Shinkai, S. A sensitive colorimetric and fluorescent probe based on a polythiophene derivative for the detection of ATP. *Angew. Chem., Int. Ed.* **2005**, *44*, 6371.

[133]. Huang, M. R.; Huang, S. J.; Li, X. G. Facile synthesis of polysulfoaminoanthraquinone nanosorbents for rapid removal and ultrasensitive fluorescent detection of heavy metal ions. *J. Phys. Chem. C* **2011***, 115*, 5301.

Chapter 2

Novel Metal-like Luster Conductive Film Made of Pyrrole and Furfural in Straightforward Chemical Copolymerization

ABSTRACT: Novel metal-like luster conductive films were prepared using straightforward chemical copolymerization of pyrrole (Py) and furfural (FFr). Critical parameters in the copolymerization such as monomer feed, reaction solvent, acid catalyst were studied to optimize their syntheses, film-forming properties, etc. These films showed a metal-like black luster and exhibited excellent mechanical properties with flexibility. The conjugate chemical bonds obtained from methine group were revealed in the copolymer film by FT-IR, UV-vis and H NMR spectra. DSC and CV results implied that these copolymers showed better thermo and electrochemical stability. The density and smooth surface of the copolymer films contributed to the performance of metal-like luster, presenting the benefit of better surface reflect into the incident light.

2.1 Introduction

In recent years, electronically conductive polymers have attracted much attention from scientific and technological perspective [1-5]. Among those polymers, polyheterocyclic polymers such as polypyrrole (PPy), polyaniline, and polythiophene are common materials containing hetero atom in the aromatic structure, which engenders unique electrical and optical properties and numerous potential applications such as capacitor [6-7], sensors [8-10], electromagnetic shielding [11], transparent conductors [12] and so on. However, polyfuran (PFu) containing oxygen atom in the conjugated structure has attracted less attention because of the difficulty for PFu when synthesized with a regular structure. The different arises from the furan (Fu) monomer, which has low reactivity relatively existing high oxidation potential up to 1.85 V/SCE, in contrast to pyrrole (Py) as 0.8 V/SCE in acetonitrile solution [13]. In spite of the difficulty for synthesis of PFu, a lot of efforts have been conducted and some superior properties of PFu in electrochromic effect and good redox ability have been mentioned [14]. For instance, González *et al.* reviewed PFu in terms of syntheses, properties and applications, even though most of the reviewed contents dealt with electrochemical polymerization at a high electropolymerization voltage (1.8–2.5 V) [15]. In case of chemical oxidation polymerization, high oxidation potential of Fu monomer required a

stronger oxidant. However, such an oxidant brought Fu monomer ring to open much more easily in the polymerization process, implying poor stability, lower conductivity and degree of polymerization which mean a larger limit of application [16]. Meanwhile, conductive polymer films show better conductivity but weaker physical and mechanical performance obtained by electrochemical polymerization [17]. Conductive polymers prepared through chemical polymerization are useful for simple instruments and reaction procedures, but the disadvantages are related to poor solubility and weaker film-formation ability, especially for PPy and PFu [18-20]. Therefore, great attention has been devoted to preparation of conductive polymer films using a simple method with economical and stable processes. Relative to homopolymers such as PPy, preparing copolymer systems can combine several benefits of different monomers to improve physical and electrochemical properties of the conducting polymers, which can appear as novel property [21]. Many copolymers containing two heterocycle monomers such as aniline, pyrrole, and alkyl- or *N*-substituted monomers have been produced using chemical or electrochemical method [22-25]. For Fu and Py copolymers, Xue *et al.* studied electrochemical copolymerization to investigate the influences of the monomer feed ratio of Fu and Py on the copolymers. McConnell *et al.* described oxidative polymerization method for copolymers of Fu and Py with the aim of

increasing polymer stability [26-27]. In addition, Glenis et al. used terfuran monomer

for reduction of the oxidation potential of furan [28]. However, these copolymers

retained inconvenient properties such as stability and poor film-forming.
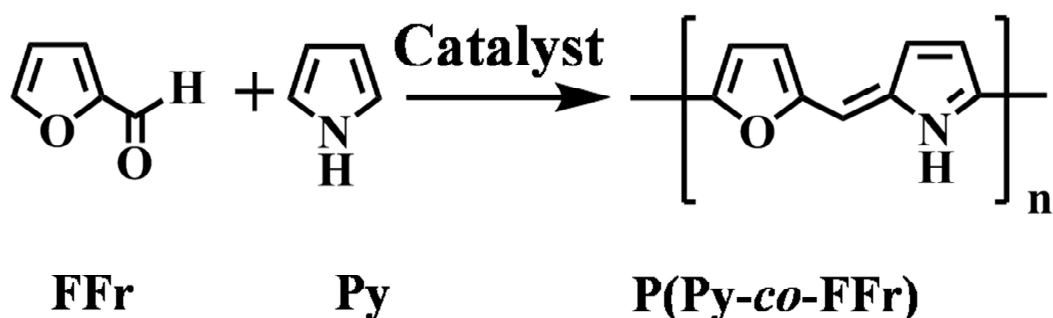
Scheme 2.1 Nominal chemical oxidative polymerization of P(Py-*co*-FFr) as copolymer.

On the other hand, furfural (FFr) as industrially manufactured for a long time through

hydrolysis of pentose can be produced from agricultural raw materials including

corncobs, wheat bran or sawdust, unlike other heterocyclic compounds which are

produced from fossil resources [29]. Electropolymerization of FFr has been reported to

obtain novel conductive films. However, the films obtained with weak mechanical

behavior still cannot satisfy demands for the potentially application [30]. From our

previous investigation, it was reported that facile syntheses of P(Py-*co*-FPy) in chemical

copolymerization of Py and formyl pyrrole (FPy) was conducted in the presence of

trifluoroacetic acid (TFA) catalyst [31]. The obtained films showed a metallic greenish

black color with better electrical conductivity in addition to good film formation. In this

case, the formyl group was able to form methine group in the presence of acidic catalyst

in mild condition. Therefore, for FFr, copolymer between Py and FFr might be expected

to extend the conjugated structure through the formation of a methine group (Scheme

2.1). In the present work, the straightforward chemical copolymerization of Py and FFr

was investigated to obtain novel conductive copolymers having Fu segment and to

examine details of their characteristics. Critical polymerization parameters such as the

monomer ratio, reaction solvent, acid catalyst, and the electrical and film-forming

properties of copolymer were investigated systematically.

2.2 Experimental Section

2.2.1 Reagents

Pyrrole (Py) and furfural (FFr) used as monomers were purchased from Tokyo

Chemical Industry Co. Ltd. and distilled under reduced pressure before use. Acid

catalyst reagents including trifluoroacetic acid (TFA), acetic acid (AA), formic acid

(FA), difluoroacetic acid (DFA), hydrochloric acid (HCl), and sulfuric acid (H_2SO_4)

were obtained from Nacalai Tesque Inc. Trichloroacetic acid (TCA), dodecyl

benzenesulfonic acid (DBSA) were obtained from Tokyo Chemical Industry Co. Ltd.

The chemical dopant iodine (I_2) was a product of Nacalai Tesque Inc. Tetrahydrofuran

(THF), chloroform (CHCl$_3$), acetonitrile (CH$_3$CN) and other solvents were purchased

and used as received.

2.2.2 Preparation of P(Py-*co*-FFr) copolymers

   The chemical oxidative polymerization of Py and FFr was carried out with different

catalysts in several solvents by following a typical procedure: Py (200 mg, 3 mmol) and

FFr (286 mg, 3 mmol) were dissolved respectively in 2 mL CHCl$_3$ and mixed in a

sample tube (20 mL) under continuous stirring. Then, CHCl$_3$ (2 mL) containing TFA

(13 mmol) as catalyst was added to the mixed monomer solution at room temperature.

When the TFA solution was added, the mixture color changed immediately from

transparent to yellowish red and gradually turned to dark brown. The mixed solution

was spin-coated onto a petri dish at 200 rpm using a spin coater (Opticoat MS-A100;

Mikasa Co. Ltd., Japan). After this coating process, the polymerization was carried out

for about 24 hour at room temperature. Finally, with the evaporation of solvent, the

resultant film was formed on the petri dish. Figure 2.1 presents typical image of the

P(Py-*co*-FFr) films prepared under different monomer ratio in the present of the TFA

catalyst. The obtained films present a metal-like black luster, which was insoluble in

several solvents, such as THF, CHCl$_3$, CH$_3$CN, dimethylformamide, and toluene. After

copolymerization of Py and FFr, the resultant films were ground down completely and

washed well with water and acetone several times under suction filtration until the

filtrate was colorless. The precipitates were stirred in 3 wt% of aqueous NaOH solution

for 30 min to remove the acid catalyst. Then they were stirred in 2 N HCl aqueous

solutions for 30 min to convert copolymers medium to an acidic one. Finally, the

obtained black precipitates were dried in a vacuum oven at room temperature for 12

hours and then measured.

Py:FFr =7:3   **Py:FFr =5:5**   **Py:FFr =3:7**
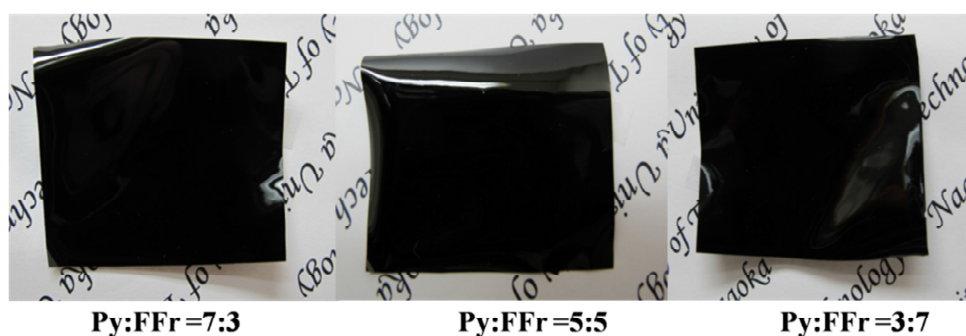
Figure 2.1 Images of P(Py-*co*-FFr) using various mole fractions of FFr with TFA as
catalyst.

2.2.3 Measurements

To measure electrical conductivity, each film was washed with excess water and put

in a sealed vessel containing a small amount of I_2 for chemical doping during 24 hours.

Then, the electrical conductivity of the doped film was determined using a typical

four-point method (Roresta-GP MCP-T610; Mitsubishi Chemical Analytec Co. Ltd., Japan) at room temperature. The measurement was conducted with attachment to the film surface at five different points. The tensile strength of the film was measured using a load cell (LTS-500N; Minebea Co. Ltd., Japan) with the sample specimen (2.5 cm × 7.5 cm). FT-IR spectra of the resultant films were recorded on IR spectrophotometer (Prestige, Shimadzu Corp) with KBr pellets under the transmittance mode. An elemental analyzer (CHN Corder MT-6; Yanaco Analytical Inc., Japan) was used to determine the mass percentage of hydrogen (H), carbon (C), and nitrogen (N) of the films. The UV-visible absorption spectra of the thin films with less than 10 μm thickness on the quartz glass were measured using a UV-vis-NIR spectrophotometer (V-570; Jasco Corp., Japan) under transmittance mode. The thermal decomposition performance of the copolymers was determined in a nitrogen atmosphere with 4 mg sample at temperatures of 30 °C to 500 °C with a heating rate of 20 °C min^{-1} using a DSC thermal analyzer (Thermo Plus EVO DSC8230; Rigaku Corp. Ltd., Japan). For other electrical electric property of the films, cyclic voltammetry (CV) was recorded in a 0.1 M LiPF$_6$ (lithium hexafluorophosphate)/acetonitrile solution with Pt wire as the working electrode (HSV-110 Automatic Polarization System; Hokuto Denko Corp., Japan). Voltammograms quoted against Ag/Ag$^+$ counter electrode were obtained at a scanning

rate of 30 mV s^{-1} and scanning range from -1 V to 1 V. To investigate the

copolymerization process, H NMR spectra of monomers in the presence of TFA were

measured using a spectrometer (AL-400 NMR; JEOL Ltd., Japan) with deuterated

chloroform (CDCl$_3$) as solvent. For surface analysis of the films, the UV-visible spectra

of thick films were measured suing a UV-vis-NIR spectrophotometer in reflection mode.

Scanning probe microscopy (SPM, Nanocute; SII Investments, Inc., Japan) was applied

in a 750 × 750 nm area of the film to obtain the AFM images. A silicon probe mounted

on a cantilever (Micro cantilever Si-DF40P2; SII Investments Inc., Japan) was used.

The surface roughness was calculated using root mean squares values (RMS) in the

Z-range images. In FE-SEM measurement for the surface morphology observation, the

film coated with 5 nm thickness of Au, then it was observed (JSM-7000F; JEOL Ltd.,

Japan) at 5 keV.

2.3 Results and Discussions

2.3.1 Preparation of P(Py-*co*-FFr) copolymer films

   As shows in Tables 2.1, various acidic catalysts were used to prepare the copolymer

films in equal mole ratio to optimize the synthesis and film-forming properties. The

yields of copolymer were low in cases of HCl and H$_2$SO$_4$. Similar situations were

occurred when AA and FA were used. Additionally, these incomplete films were not

applicable for the tensile strength and electrical conductivity measuring because they

were quite porous and fragile. In the case of DBSA, the yield was as high as 98.6%,

although the films had been washed well to remove the remaining DBSA. No additional

evaluation was carried out because obtained film was porous and showed brittleness.

When TFA, DFA, and TCA were used, the polymer yields reached to around 70%. This

tendency meant that the carboxylic acids had benefits for the film formation. The

obtained films showed an excellent tensile strength of greater than 34.6 N/mm^2 in the

case of TFA because of the dense structure of the copolymer film, as shown in Figure

2.1. In Figure 2.2, FT-IR spectra of copolymers prepared using different catalysts are

shown. In cases of HCl and H_2SO_4, washing was performed until the water pH was

neutral. From the FT-IR spectrum of the copolymer obtained by H_2SO_4, the peak of

S=O stretching at about 1150–1300 cm^{-1} was only slightly observed and indicated the

film purity. Two peaks of phenyl ring stretching appeared at 729, 760 cm^{-1} and S=O

stretching appeared at 1280 cm^{-1} for using DBSA, which indicated the existence of

DBSA in the copolymer, even though the film was washed completely. For TFA, the

peak of –COOH stretching at about 1578 cm^{-1} strongly suggested the existence of TFA

acid in the copolymer film. Table 1 also shows the data for the electrical conductivity of

Table 2.1 Polymerization yield, tensile strength and electrical conductivity of

P(Py-*co*-FFr) synthesized in the present of acidic catalysts[a].

Acidic Catalyst [b]	Acid type	Yield[c] (%)	Tensile strength (N/mm^2)	Electrical Conductivity[d] (S/cm)
HCl	Inorganic	4.0	*e*	*e*
H$_2$SO$_4$	Inorganic	2.1	*e*	*e*
DBSA	Sulfonic	98.6	*e*	*e*
AA	Carboxylic	22.3	*e*	*e*
FA	Carboxylic	35.9	*e*	*e*
DFA	Carboxylic	68.9	19.8	7.6×10^{-4}
TCA	Carboxylic	74.5	21.1	9.3×10^{-4}
TFA	Carboxylic	85.1	34.6	1.5×10^{-3}

[a]Within CHCl$_3$ .Mole ratio of Py/FFr was equal.

[b]Catalyst amount was 13 mmol.

[c]Yield (%) = amount of P(Py-*co*-FFr) copolymer (g) / amount of Py and FFr (g) $\times$ 100.

[d]Conductivity of film was measured after I$_2$ was doped at room temperature.

[e]In case of films were prepared with FA, AA, DBSA and inorganic acid, the films could not measure by tensile strength and conductivity due to the porous and fragile film formation.

Table 2.2 Polymerization yield, tensile strength and electrical conductivity of

P(Py-*co*-FFr) synthesized in various solvents[a].

Solvent	Solvent type	Yield[b] (%)	Tensile strength (N/mm^2)	Electrical Conductivity[c] (S/cm)
Chloroform	Nonpolar	85.1	34.6	1.5×10^{-3}
Diethyl ether	Nonpolar	80.1	8.6	7.5×10^{-4}
Benzene	Nonpolar	75.6	9.7	4.9×10^{-4}
Methanol	Polar-protic	24.1	*d*	*d*
Ethanol	Polar-protic	19.5	*d*	*d*
THF	Polar-aprotic	76.1	17.6	2.5×10^{-4}
Acetonitrile	Polar-aprotic	73.5	25.3	9.8×10^{-4}

[a]Within 3 mmol of TFA. Mole ratio of Py/FFr was equal.

[b]Yield (%) = amount of P(Py-*co*-FFr) copolymer (g) / amount of Py and FFr (g) $\times$ 100.

[c]Conductivity of film was measured after I_2 was doped at room temperature.

[d]In case of films were prepared with polar-protic solvent, the films could not measure by tensile strength and conductivity due to the porous and fragile film formation.
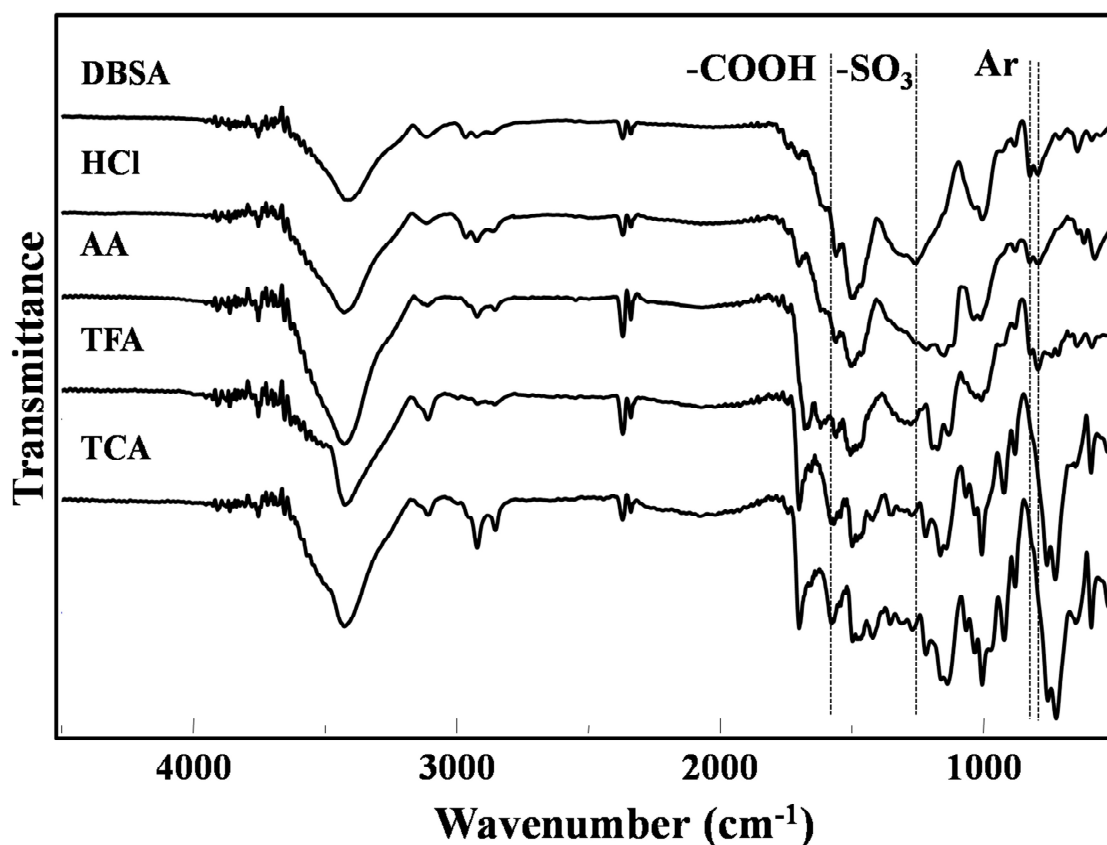
Figure 2.2 FT-IR spectra of P(Py-*co*-FFr) films prepared in the present of various acidic

catalysts.

the films. The value of electrical conductivity was changed in the range of $1.5 \times$

10^{-4}–7.6×10^{-3} S/cm, when different acidic catalysts were used. When the TFA catalyst

was used, the electrical conductivity became higher. The film also showed better tensile

strength. These results suggested that TFA was a suitable catalyst for copolymer film

preparation. Table 2.2 presents solvent data for the copolymer films preparation when

TFA was used as catalyst. For methanol and ethanol, the obtained films showed porous

and fragile film formation with low yield. When a weaker polarity solvent such as THF

and CH_3CN was used, the value of tensile strength and conductivity was remarkable enhanced with the increase of yield relative to these of methanol and ethanol. In the case of $CHCl_3$, the obtained film became much flexible without fragile features and showed a better tensile strength than 34.6 N/mm^2. Therefore, copolymerization with TFA and $CHCl_3$ were regarded as optimized for use as the catalyst and solvent, respectively. Then, the polymerization was performed with TFA in $CHCl_3$ for different mole fractions of FFr to optimize the monomer feed. Without FFr, the Py solution changed from transparent to a brownish black color slowly, and then a fragile film was obtained without a perfect metal-like luster. When the mole fraction of FFr increased from 0.1 to 0.9, the color of the solution changed rapidly. Figures 2.3(a) show the influence of mole fraction of FFr against Py in feed on the polymerization yield and tensile strength, respectively. The values of copolymerization yield increased concomitantly with the increase of FFr feeds until 0.5. However, when the mole fraction was increased more than 0.5, the value of yield decreased gradually. The tensile strength and the polymerization yield showed a similarly trend, meaning that 0.5 mole fraction presented maximum values in polymerization yield, tensile strength. Figure 2.3(b) present the electrical conductivity of the copolymer films doped with I_2. For electrical conductivity, without doping with I_2 it was lower than the measuring range (10^{-7} S/cm) of the

instrument that it was unable to obtain the data. After I_2 doping, the values was

increased clearly with increased of FFr feeds from 10^{-4} to 10^{-3} S/cm. Compared with

references concerning chemical polymerization of PFu or PFu copolymers, those

obtained copolymers were typically varied from 10^{-5} to 10^{-6} S/cm [32-33]. The

P(Py-*co*-FFr) copolymers showed improved conductivities, suggesting the formation of

a higher developed conjugated backbone. To examine the influence of oxygen for the

polymerization, the reaction was carried out in a nitrogen atmosphere for 24 hours after

the monomer solution was bubbled into nitrogen for about 30 min. Compared with the

films prepared in air,, higher conductivity was observed as shown in Figure 2.3(b). This

can be considered that the lower electrical conductivity in air was attributable to shorter

conjugation lengths or less developed conjugated backbones because of the increasing

ring-opining probability through the oxidation reaction.
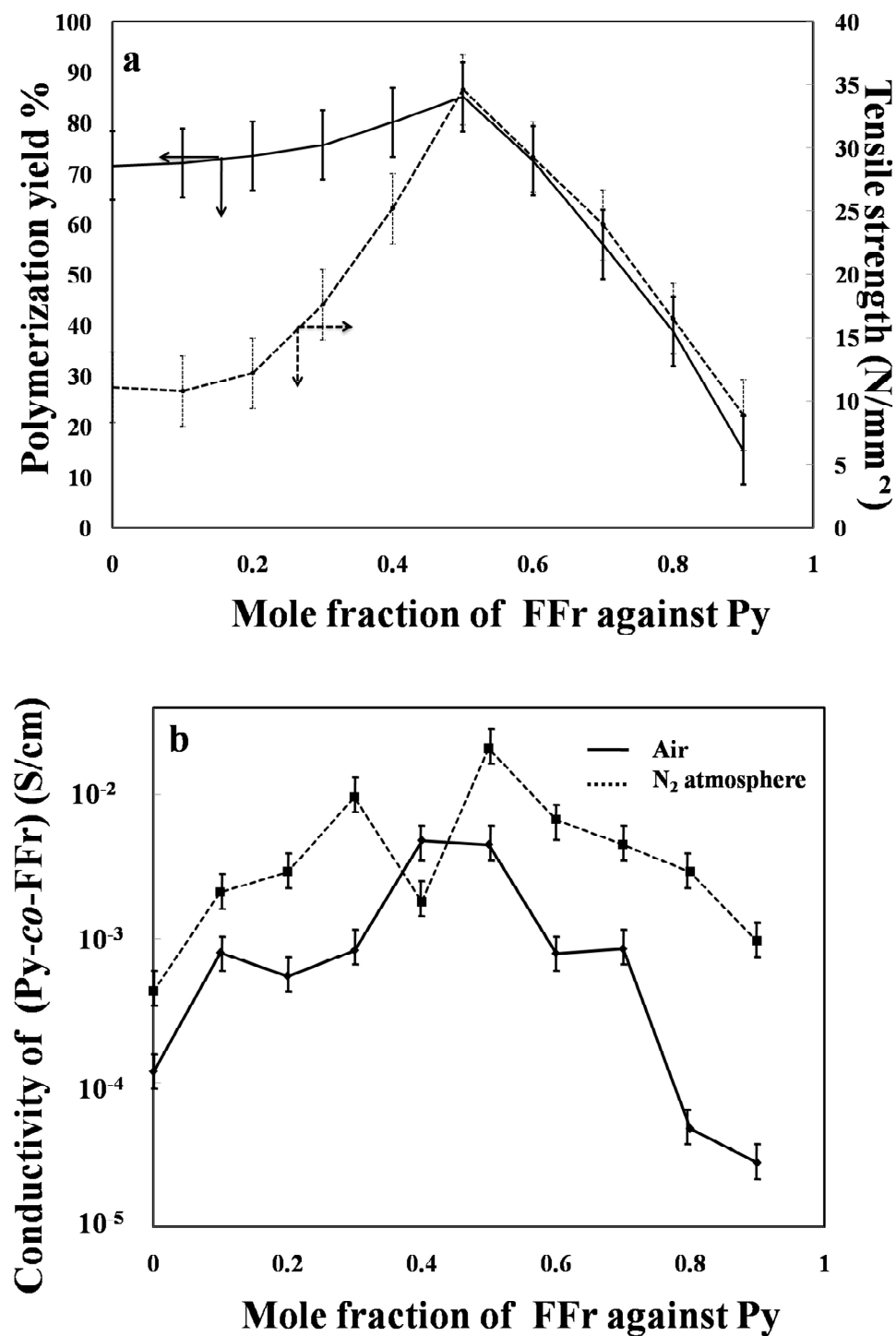
Figure 2.3 Polymerization yields, tensile strength (a) and electrical conductivity (b) of

I_2 doped P(Py-*co*-FFr) synthesized with various mole fractions of FFr.

2.3.2 Characteristics of P(Py-*co*- FFr) copolymer films

To confirm the copolymerization with Py and FFr monomer, H NMR spectroscopy was conducted in CDCl$_3$ with TFA at room temperature, as shown in Figure 2.4. Thereby, at 0 min the solution contained 0.5 mole fraction of Py and FFr without TFA, so the several characteristic peaks were observed at a certain position. When the catalyst was added, the solution in NMR tube became yellowish red immediately. It was measured as quickly as possible at around 1 min. Then, every 30 min the gradual transformation to dark brown of the mixture solution was determined. With the increased of reaction time from 0 min to 120 min, the formyl group at 9.57 ppm disappeared and the methine proton at about 4.16 and 4.11 ppm was observed immediately. For the spectra shown the disappearance of the formyl group, the TFA addition meant the consumption of monomers with the formation of soluble dimer or oligomers in the initial stage of the copolymerization, as shown in Scheme 2.2 [31]. It was important to note that several small broad peaks between 7–8 ppm were observed. This also meant that the remaining proton of the formyl group might be shifted to a high magnetic field side with increasing time. Large shift of the characteristic peak of TFA toward the high magnetic field side became evident as the reaction time increased. Reportedly, when the methine structure connected with Fu, Py rings or aromatic dimer, the proton signal appeared at 8 to 6 ppm

[34]. Therefore, in the 8–6 ppm region, these peaks of the oligomer were confirmed. It

was confirmed that the peaks at 10.73 and 10.7 ppm were the NH group of oligomers

for the existing Py [35]. A notable observation was that the peaks appeared at 9.24, 9.32,

and 9.34 ppm, respectively corresponding to reaction times of 30, 60, and 120 min. This

correspondence suggested that five-membered heterocyclic groups were mutually

connected through the methine group to form long conjugated polymer chains.
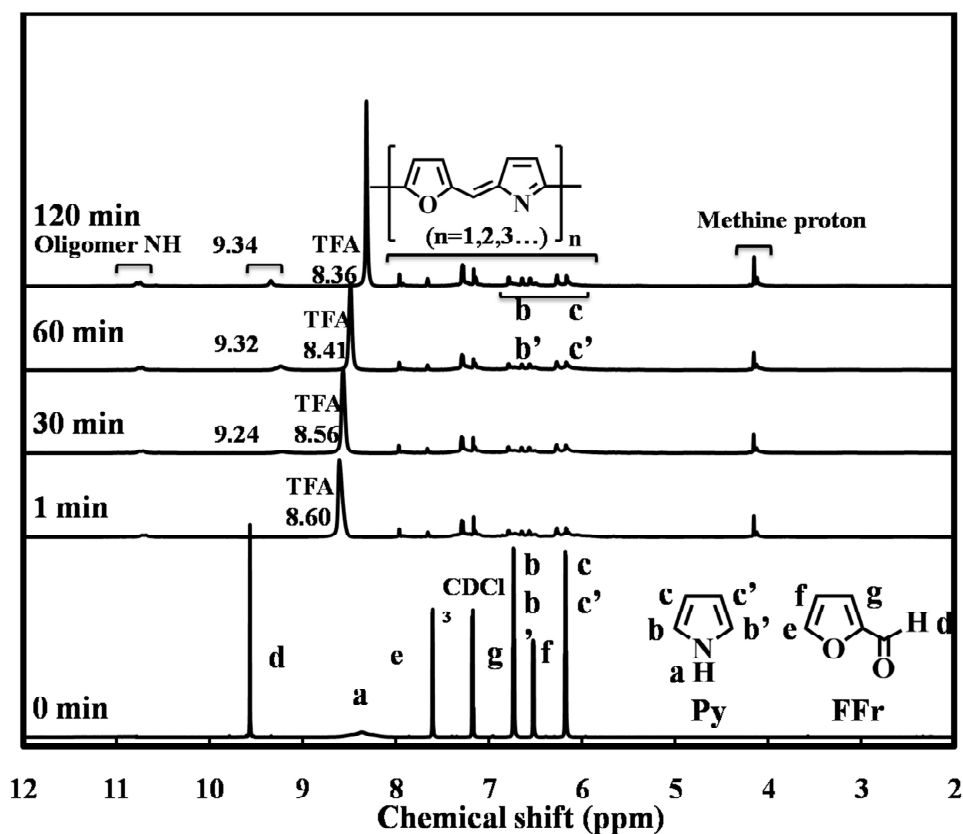
Figure 2.4 H NMR spectra of the reaction solution with 0.5 mole fractions of FFr in

CDCl$_3$ in the presence of TFA.
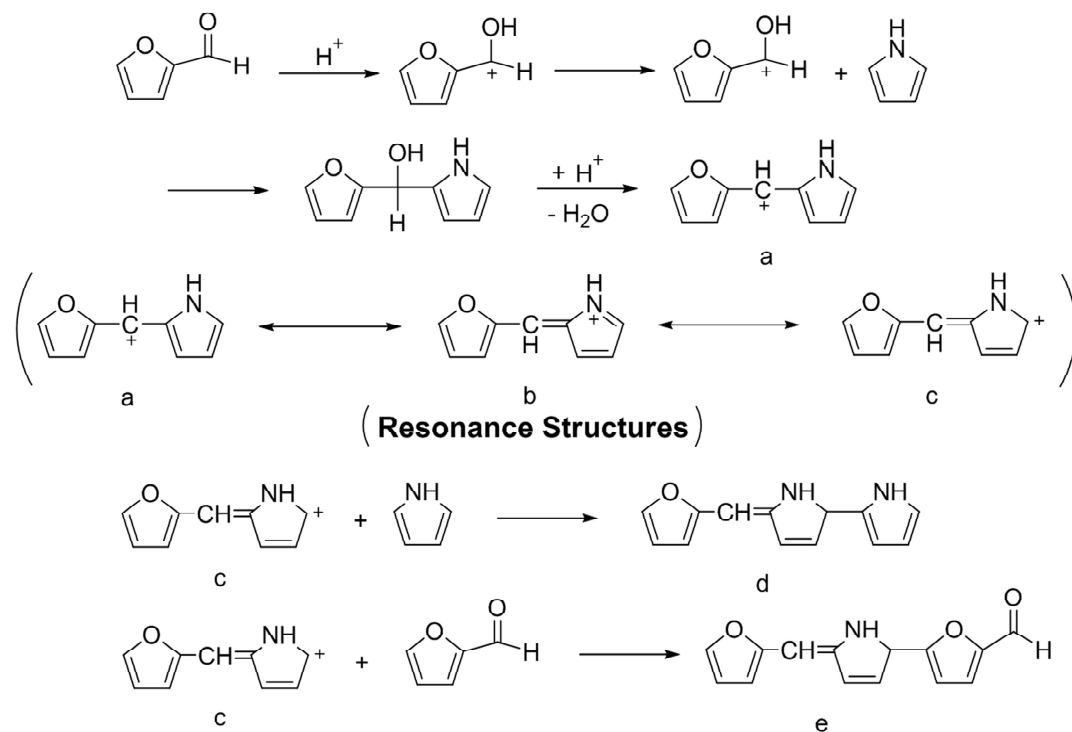
Scheme 2.2 Nominal dimerization mechanism between Py and FFr.

Therefore, Figure 2.4 showed the copolymerization proceeded during about 120 min, with disappearance of the formyl group and appearance of the conjugated methine group in oligomer main chains. Results roughly suggested a reaction mechanism between Py and FFr, as shown in Scheme 2.2. These peaks completely disappeared when the reaction time became longer than 120 min and meant that insoluble copolymer was produced.

To obtain the copolymer composition, the C/H/N elemental analysis was measured. As Table 2.3 shows, the value of the C/N component ratio in the copolymer film increased concomitantly with the increasing component of FFr. This tendency suggested that the film contained copolymerization segments of FFr, as shown in Scheme 2.1. However, the calculated C/N value showed much higher contents relative to those of the measurement result when the feed ratio of FFr was 0.5. This result implied that the content of Py segments was much more than FFr segments in the copolymer films because the oxidation potential of FFr was higher than Py, as described above [13]. After the dimer formation (Scheme 2.2), results suggested a priority selection to react to Py for the growth of the backbone. Therefore, the Py segment content was much greater than FFr segments in the copolymer films, even though the feed ratio of Py and FFr monomers was 1:1. The total contents of the C/H/N elements were less than 100%, even the feed ratio of FFr was 0. This result indicated the presence of TFA catalyst or other oxides through the oxidation of Py or FFr because Py and FFr were oxidized easily. For the estimation of quantities of the TFA catalyst from the calculated values, it was inferred that the catalyst was present in half molecules in the chemical structure, as shown in Scheme 2.1. Therefore, the flexible characteristics of the films might result from the presence of the TFA catalyst.

Table 2.3 Elemental composition of P(Py-*co*-FFr) synthesized from each mole fraction

of Py against FFr.

Mole fraction of FFr[a]	Elemental composition (wt %)			C/N
	H	C	N	
0	5.69	57.36	11.35	5.05
0.1	4.98	54.78	10.77	5.09
0.2	4.80	56.82	9.39	6.05
0.3	4.53	52.01	8.47	6.14
0.4	4.28	56.82	7.82	7.27
0.5	3.86	57.44	7.02	8.18
0.6	3.66	58.83	5.20	11.31
0.7	3.55	59.77	4.76	12.56
0.8	3.60	59.09	3.96	14.92
0.9	3.59	58.41	3.89	15.02
Calculated(0.5)[b]	3.50	75.52	9.79	7.71

[a]Total monomer content in each feed solution was 6 mmol in 2ml CHCl$_3$ in the presence of 13 mmol TFA.

[b]The values were calculated by the nominal structure of P(Py-*co*-FFr) as shown in Scheme 1.

Figure 2.5 shows FT-IR spectra of the copolymers prepared at different mole fraction

of FFr. As shown by line (a), two peaks of N–H stretching vibrations of at 3410 and

3110 cm^{-1} were presented. It was also apparent that line (b) for the saturated C–H

stretching vibrations at 2935 and 2866 cm^{-1} showed decreased peaks when the mole

fraction of FFr was added. This decrease might indicate that the conjugated structure of

the resultant copolymers was increased in the polymer backbone when the mole fraction

of FFr increased. The peaks (c) for 1626, 1558, and 1502 cm^{-1} were attributed to the

C=C double bond stretching of the Py and Fu rings. In line (d), it was noted that the

broad peak observed at 1280 cm^{-1} might be assigned to -C=CH- stretching from methine

group. The C–O–C plane deformation of the Fu segments was indicated by the band at

1012 cm^{-1} and the C–H out-of-plane bending of the furan rings was indicated by the

band at 790–720 cm^{-1}. It can be observed that the furan ring band characteristics were

increased with increasing of FFr feed [36]. In addition, the peak (e) of C–H out-of-plane

deformation vibration from methine group appeared at 1008 cm^{-1}, indicating that the

increase of the mole fraction of FFr became high contents of the methine group in the

films. It increased concomitantly with increasing mole fraction of FFr and was almost

disappeared when there was no existence of FFr.
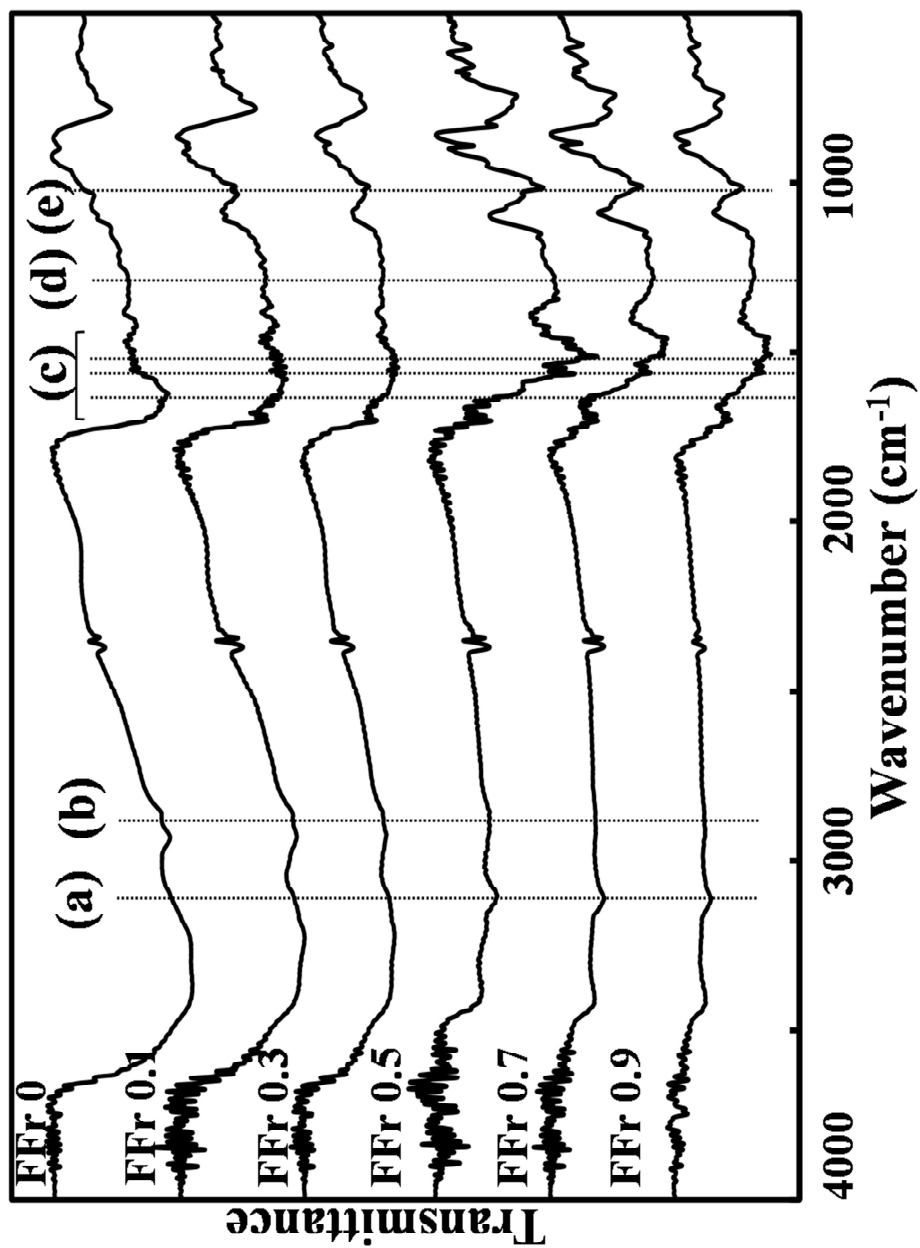
Figure 2.5 FT-IR spectra of P(Py-*co*-FFr) films prepared with various mole fractions of

FFr in CHCl$_3$ in the present of TFA.
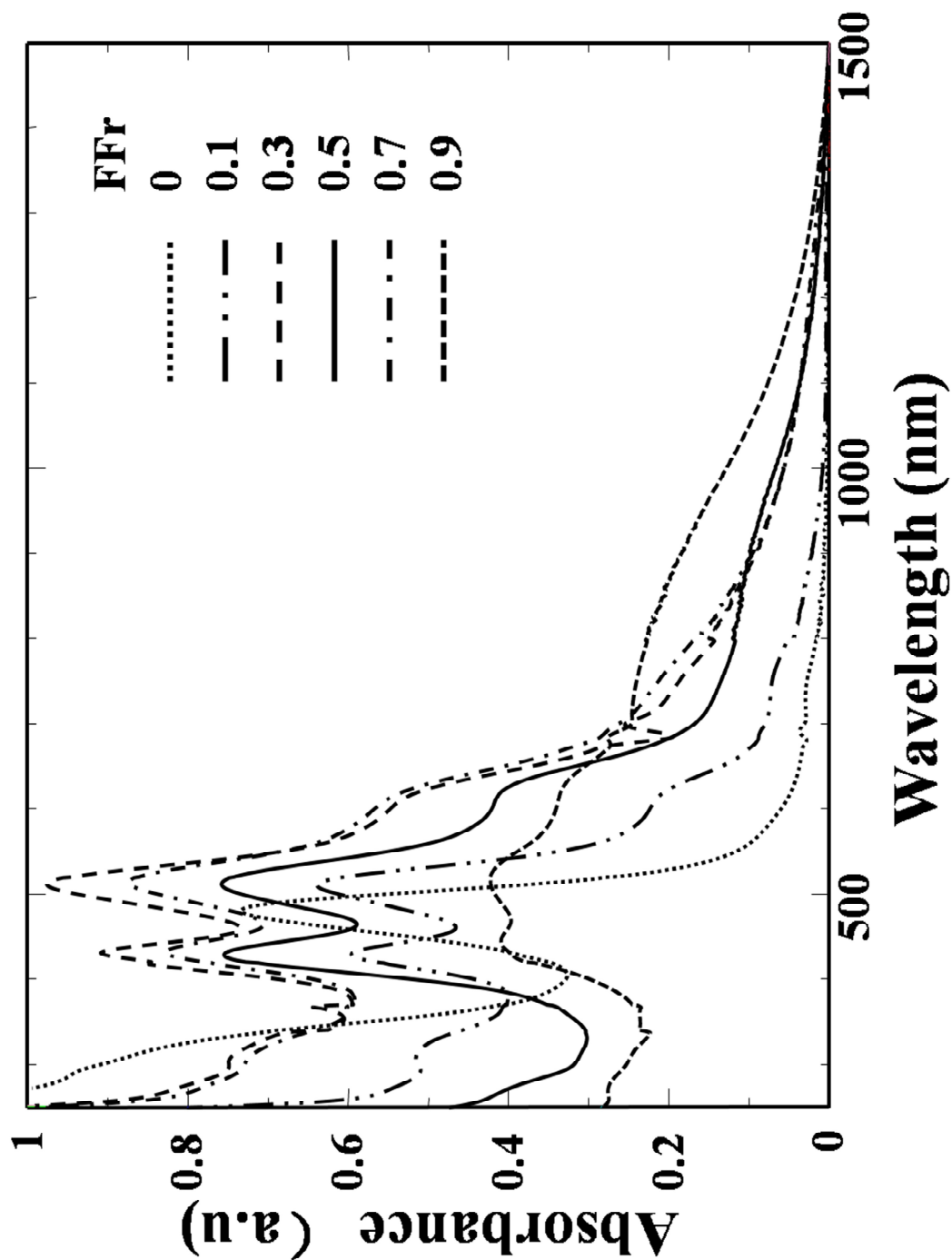
Figure 2.6 UV-vis spectra of P(Py-*co*-FFr) films prepared at various mole fractions of

FFr in CHCl$_3$ in the present of TFA.

Figure 2.6 shows UV-vis spectra of thin films prepared by copolymerization for each mole fraction of FFr. The obtained UV-vis spectra reflected the presence of the characteristic absorption band of the π-π* transition of PPy segment, which was apparent at 473 nm. However, the band intensity decreased with the increasing mole fraction of FFr. Alternatively, the peaks at 430 nm were increased indicating the former of π-π* transition of PFu segment. When the PFu film was illuminated at 488 or 514 nm, the resonance effect greatly enhanced the Raman lines of undoped parts, and the 514 nm absorption band disappeared after doping [37]. Therefore, the shoulder peaks at 517 nm indicated that the Fu having conjugate methine group was incorporated into the conjugated polymer chains. A marked change of the spectra at mole fractions of 0.7 and 0.9 was obtained, with weaker and broader absorption appearing near 750–1500 nm. This result strongly suggested that the bipolaron state of copolymer was present in the films. Therefore, the introduction of the FFr monomer caused formation of the conjugated methine structure in the backbone. Thereby, these well corresponded with high electrical conductivity might be attributed by the formation of more developed conjugated structure in polymer backbone [31].

For these films, DSC measurements were conducted at 30–400 °C to ascertain the

thermal properties of copolymer. The DSC curves of P(Py-*co*-FFr) copolymer are shown

in Figure 2.7. These data exhibited that the first endothermic processes appeared at

53 °C for evaporation of the residual solvent in each film for $CHCl_3$ (Teb＝81 °C) and

acid catalyst TFA (Teb ＝72 °C) [38]. In addition, marked changes at around 100 °C for

the endothermic processes were visible with mole fractions of FFr from 0.1and 0.9,

which might be attributable to the removal of units with low molecular weights [32].
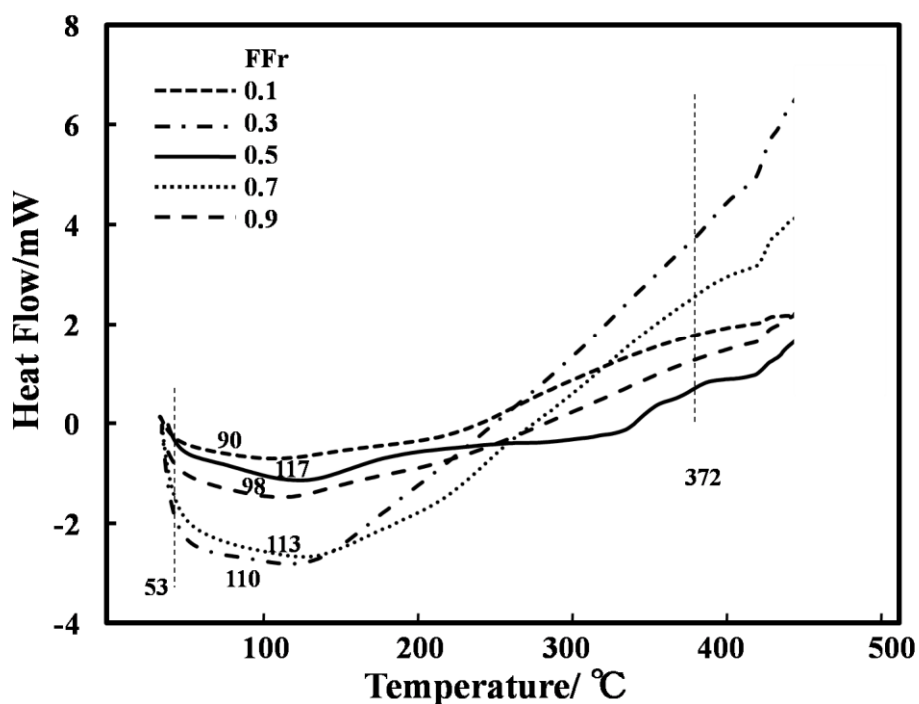
Figure 2.7 DSC thermograms of P(Py-*co*-FFr) copolymers synthesized at various mole

fractions of FFr with a heating rate of 20 °C min^{-1} in a nitrogen atmosphere.
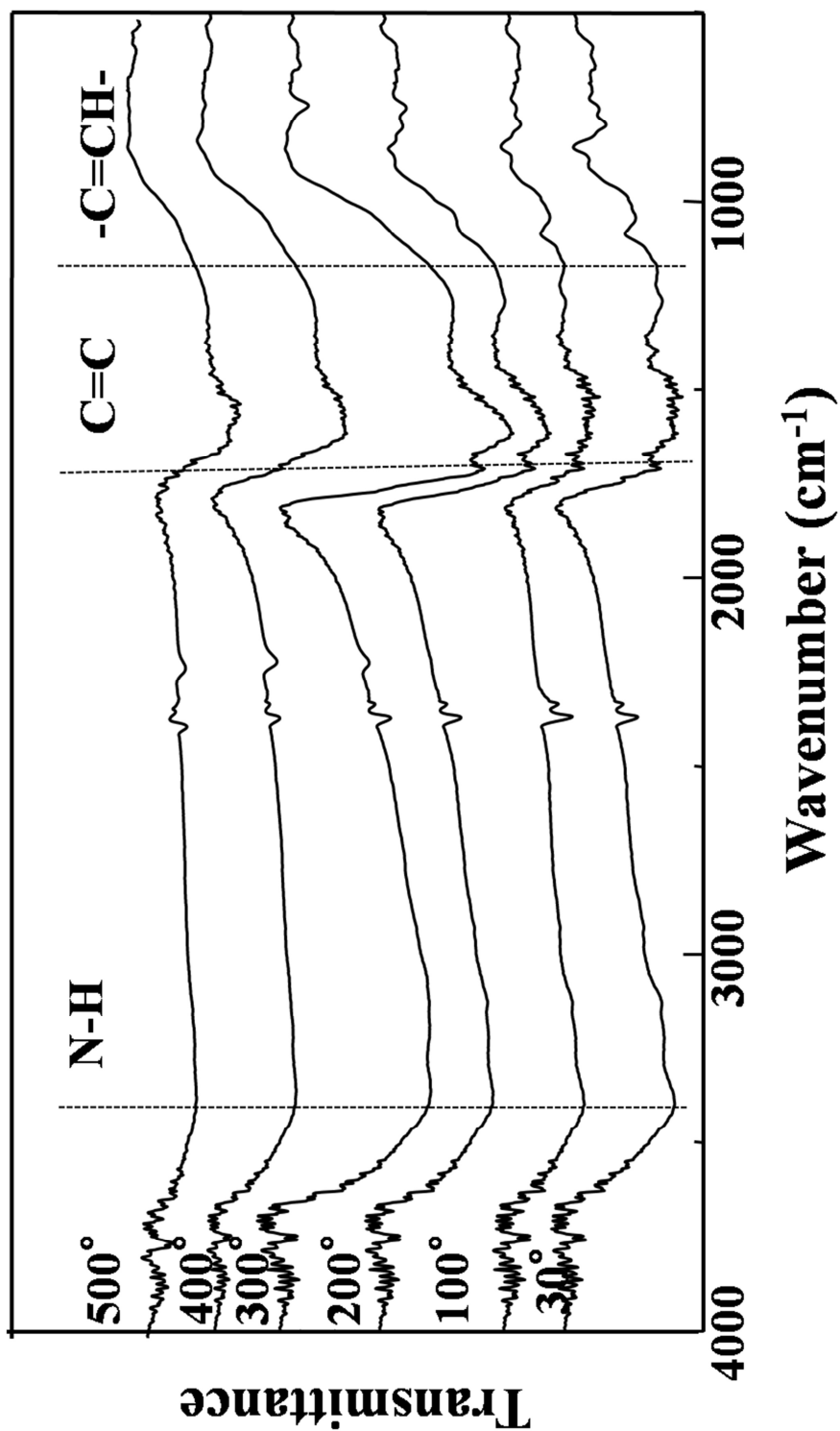
Figure 2.8 FT-IR spectra of P(Py-*co*-FFr) with 0.5 mole fractions of FFr at different

temperatures.

For 0.5 mole fraction of FFr, the higher endothermic transition at 117 °C than any other films proved that the film with the high polymerization degree, which improved the electrical conductivity and the mechanical performance. These copolymers exhibiting a small endothermic process at 372 °C were related to the loss of dopant bound to the polymer chain [39]. In order to elucidate the decomposition process of copolymers, FT-IR spectra were measured at different heating temperatures for the copolymers with 0.5 mole fraction of FFr, as shown in Figure 2.8. The FT-IR spectra of the P(Py-*co*-FFr) copolymers showed that the peaks observed at 1280 cm^{-1} assigned to the -C=CH- stretching from methine group and the peaks around 1626 cm^{-1} from the C=C double bond stretching of the Py. Results demonstrated that the furan rings disappeared gradually after 300 °C. Meanwhile, new peaks observed at 2216 cm^{-1} were assigned to the -C=C=O stretching of the Fu ring opening. The DSC results indicated that the copolymer films involved TFA and had better thermal stability up to 300 °C.

To investigate the electrochemical property of the P(Py-*co*-FFr) films, cyclic voltammetry (CV) was recorded. Figure 2.9(a) shows respective CV profiles of the P(Py-*co*-FFr) films obtained with different mole fractions of FFr at 0, 0.5, 0.7 and 0.9. For the film without FFr, no anodic or cathodic peaks were observed. The obtained PPy
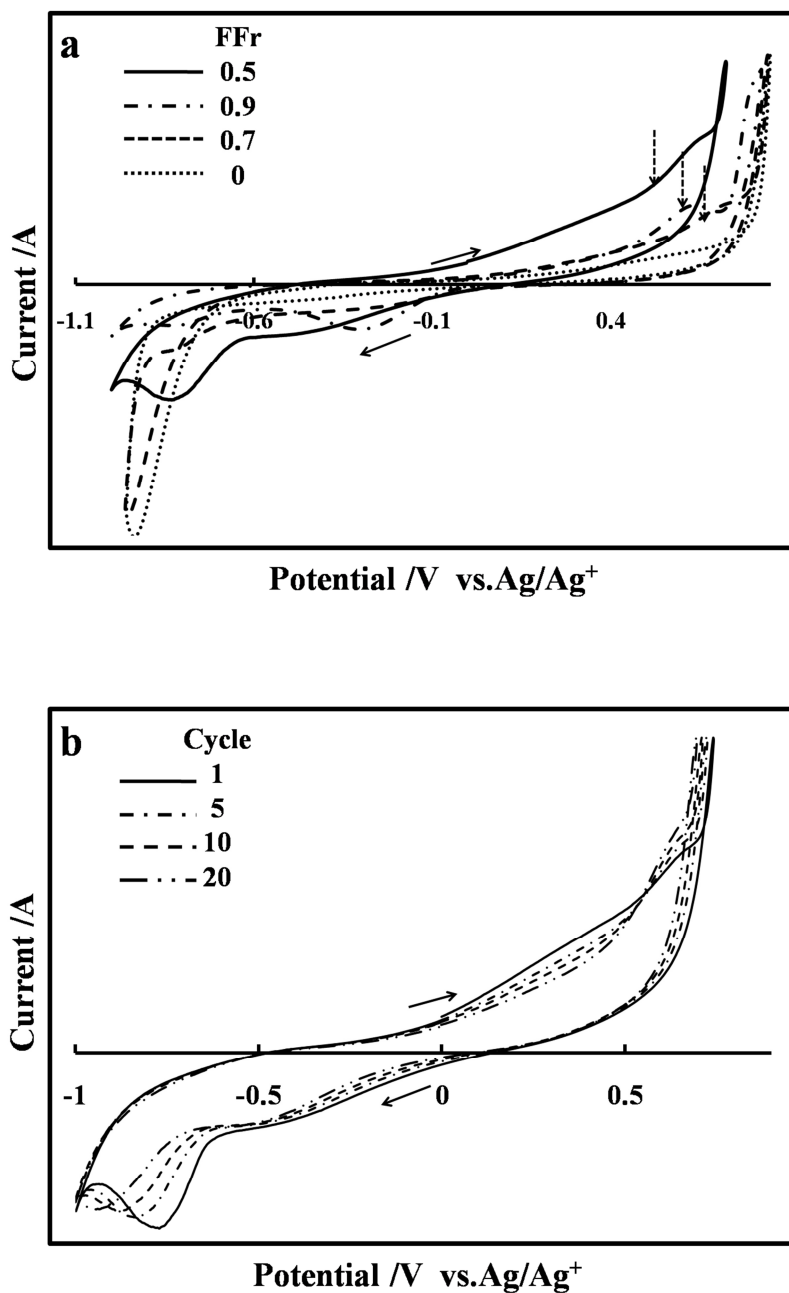
Figure 2.9 The CV recorded in 0.1M Lithium hexafluorophosphate (LiPF6)/acetonitrile

solution and scan rate at 30mV/s: (a) P(Py-*co*-FFr) films at different FFr mole fractions

of 0, 0.5, 0.7 and 0.9 at first scan cycle; (b) different scan cycle of P(Py-*co*-FFr)

copolymers synthesized at 0.5 mole fraction of FFr.

film exhibited a sharply crowded area, showing close similarity with the electrochemical behavior of the platinum electrode in an appropriate potential window. With increasing of FFr mole fraction in the copolymers, inconspicuous anodic peaks appeared at 0.71, 0.63, and 0.62 V, respectively, for mole fractions of FFr at 0.9, 0.7, and 0.5. It was noteworthy that the cathodic peaks were observed at -0.27 and -0.7 V respectively, when the FFr feeds were 0.7 and 0.5. Reportedly, an anodic peak appeared at around 0.6 V in PFu film synthesized using electropolymerization [30]. In addition, a cathodic peak appeared at around -0.65 V when furan and 2-methylfuran were used for electropolymerization [16]. Formation of the copolymer film with FFr was confirmed as the feed was increased. The cathodic peak current around -0.65 V decreased rapidly during the added of FFr feed, probably because the added fraction of FFr in polymer main chain effectively led a lower oxidation potential because of the electron release characteristics of the methine [16]. To evaluate their electrochemical stabilities, different scan cycles of P(Py-*co*-FFr) copolymers for the 0.5 mole fraction of FFr were conducted as shown in Figure 2.9(b). The voltammograms both showed an inconspicuous anodic peak at around 0.6 V with a tiny shift to low potential. However, a noteworthy cathodic peak was observed at -0.74, -0.76, and -0.81 V, corresponding respectively to the first, fifth, and tenth scans with a decrease in the current. The oxidation and reduction peaks

shifted gradually toward the low potential side, perhaps because the residual catalyst,

monomer, or oligomer inside of the copolymer film gradually came into the electrolyte

with the increasing of scan times. With the tiny shift of the peaks, the scan area

decreased slightly. However, the curves did not change markedly over 20 cycles,

indicating that the film was coated tightly on the Pt wire surface and that it had a

suitable electrostability [40]. The curve areas of the films gradually decreased with an

increasing number of cycles, perhaps indicating that the capacitance of the films did not

change greatly with the increasing scan times [41]. Results suggested that the

electrochemical stability of copolymer films was partially explained by the tight

adhesion of the well-formed films and the dense and smooth surface.

2.3.3 Surface morphology and metal-like luster properties

   As noted in Figure 2.1, P(Py-*co*-FFr) films obtained with different mole fractions of

FFr exhibited a metal-like luster surface. Reportedly, some π-conjugated polymers

showed metal-like luster with donor and acceptor groups connected by π-conjugated

linkages [42-42]. Additionally, it was usually assumed that the metal-like luster

originated from the microstructure on the scale of the visible region light or other

factors such as the smoothness of the film surface with strong reflection in the visible

region [44]. Therefore, FE-SEM (Figure 2.10) was used to observe the surface (a, b, d, e)

and cross-section (c, f) of P(Py-*co*-FFr) films prepared with 0 and 0.5 mole fractions of

FFr. It was observed that the film showed a continuous smooth and dense morphology

both on the surface and cross-sectional, with none of the fibrous or nanoparticle

structures that were invariably observed in other similar conductive films [45-46]. The

film thickness was 54 μm with a dense and smooth surface that might contribute to the

metal-like luster, which was beneficial to the better reflection of incident light.
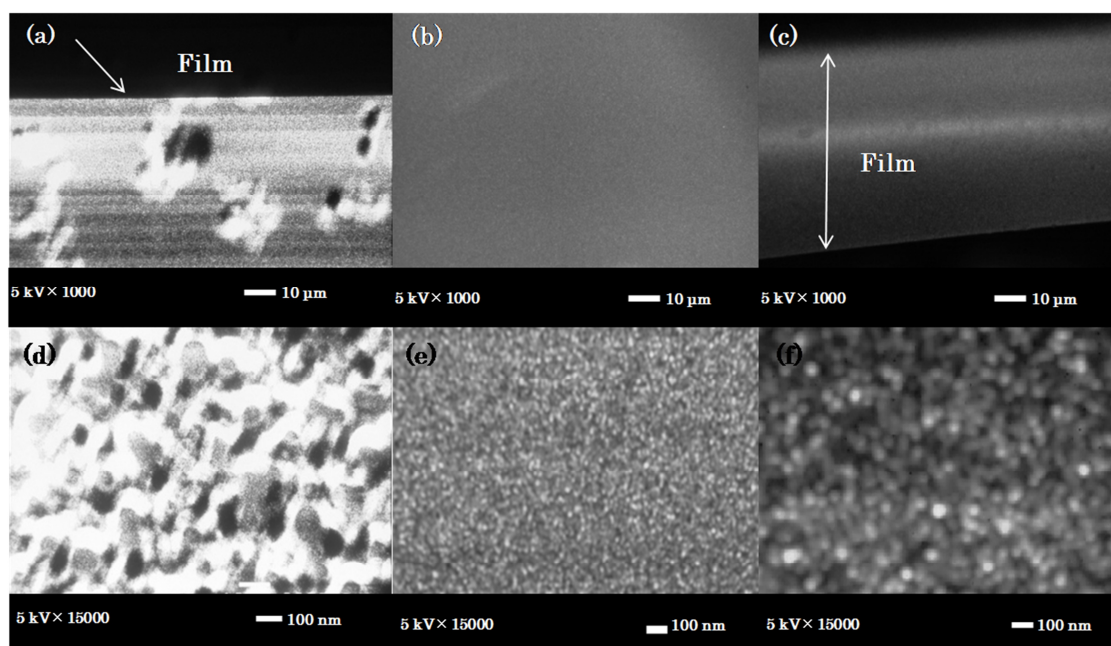
Figure 2.10 SEM images of surface of the P(Py-*co*-FFr) films with Py/FFr= (a, d) 1/0,

(b, c) 0.5/0.5.and cross-section (c, f) prepared with 0.5 mole fraction of FFr.

To reveal such surface morphology, the copolymer films were analyzed using AFM.

Figure 2.11 shows AMF images of surface topographic and phase shift for these films.

Results suggested that both copolymers exhibited a very smooth surface. The values of

roughness parameter (RMS) on P(Py-*co*-FFr) films were obtained, as 3.3 ± 1.6 nm, 2.3

± 0.9 nm and 1.6 ± 0.3 nm with the mole fraction of FFr at 0, 0.1, and 0.5, respectively.

The film prepared with 0.5 mole fraction of FFr became a flatter surface relative to other

films. Phase imaging revealed that the AMF results presented almost only one phase at

the film surface. This indicated the absence of any marked color contrast in the phase

image for the films prepared with FFr at 0.1 and 0.5 mole fractions. Therefore, these

results suggested that the enhancement of homogeneity of the copolymerized film with

the FFr at several nanometer scales to form a smooth surface.

Figure 2.12 presents UV-visible spectra of P(Py-*co*-FFr) films (a) with different mole

fractions of FFr and (b) at various incident angles prepared with 0.5 mole fraction of FFr.

All copolymer films showed a broad reflectance band around 400–800 nm, suggesting

strong light absorption in the visible region. Without FFr, the π-π^* transition was

observed at 405 nm in addition to appearance of 539 and 653 nm bands. However, when

the film prepared with FFr, the π-π^* transition was shifted toward a more red region side

near 463 nm. The results suggested that the reflectance was quite high, probably
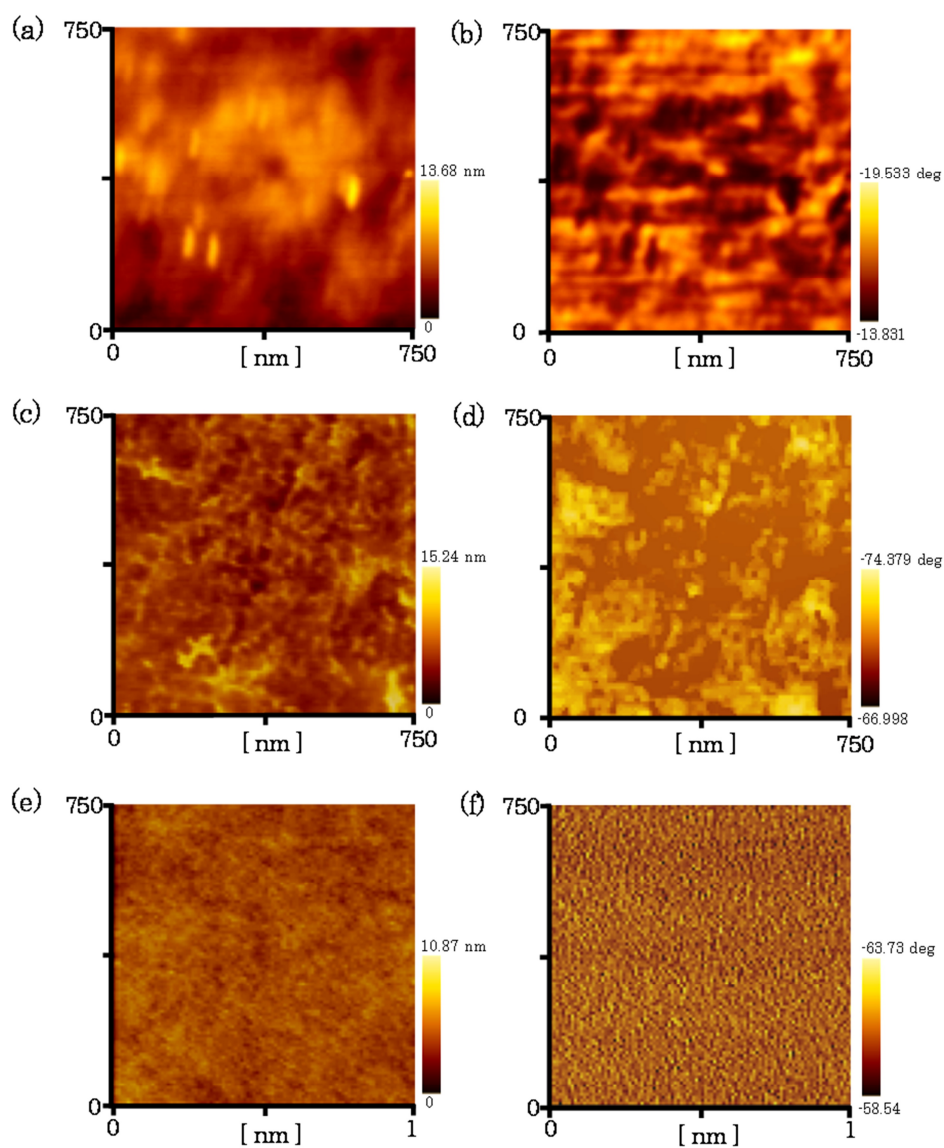
Figure 2.11 AFM topological (a, c, e) and phase (b, d, f) images of the copolymer films

with Py/FFr= (a, b) 1/0, (c, d) 0.9/0.1 and (e, f) 0.5/0.5.
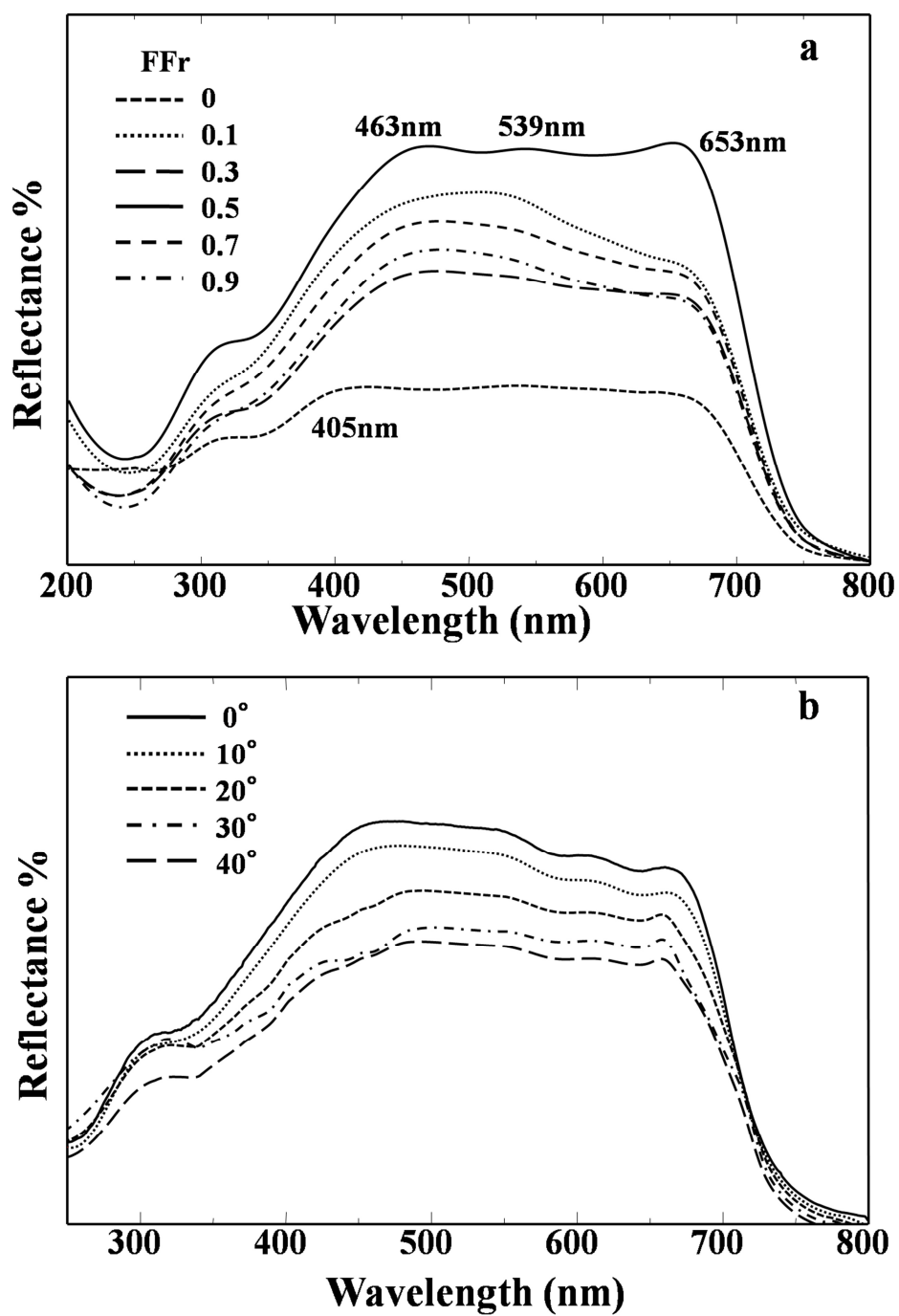
Figure 2.12 Reflectance UV-vis spectra of P(Py-*co*-FFr) films: (a) at different mole

fractions of FFr and (b) at various incident angles prepared with 0.5 mole fraction of

FFr.

because of the strong light absorption attributed to the π-π^* transition of conjugated

structure in copolymers and better film formation of containing FFr segments. In Figure

2.12(b), the reflectance spectra of P(Py-*co*-FFr) films were measured at various incident

angles from 0 ° to 40 °. The films were prepared with 0.5 mole fraction of FFr. The π-π^*

transition was observed at 463 nm in addition to the appearance of 539 and 653 nm

bands at various incident angles. It was observed that reflection peaks did not depend on

the angle of incident light. They only showed changes of the reflection intensity. It was

quite different with the angle dependence of incident light with the nanoscale structural

color [44, 47]. Therefore, it seemed that the origin of the metal-like luster should be the

film surface smoothness, strong light absorbance in the visible region, and the similar

formation of donor (Py) and acceptor (methine group) structures in the copolymer

backbone [47].

2.4 Conclusion

This report is the first describing syntheses of metal-like luster electrical conductive films containing FFr segments. Critical polymerization parameters such as the monomer ratio, reaction solvent, and acid catalyst of the P(Py-*co*-FFr) films were studied to optimize the syntheses and film-formation. Results revealed that the copolymer films were synthesized effectively at 0.5 mole fraction of FFr in the presence of TFA as catalyst. Moreover, better polymerization yield and tensile strength were observed in addition with the electrical conductivity of the copolymer films doped by I_2 from 10^{-4} to 10^{-3} S/cm. Results show that the methine group from FFr was formed in the copolymers, which improved the conjugate structure in the main chain. The metal-like lustrous films were analyzed using SEM and AMF to confirm the formation of a dense and smooth surface. The obtained conductive film exhibited interesting properties such as enhanced conjugated backbone, good thermal/electrical stability, and a smooth surface that can be regarded as a new conductive polymeric material providing benefits for industrial applications.

2.5 References

[1]. MacDiarmid, A. G. Synthetic metals: a novel role for organic polymers. *Angew. Chem. Int. Ed*. **2001**, *40*, 2581.

[2]. Li, X. G.; Huang, M. R.; Duan, W.; Yang, Y. L. Novel multifunctional polymers from aromatic diamines by oxidative polymerizations. *Chem. Rev*. **2002**, *102*, 2925.

[3]. TrippM, G.; Derf, F. L.; Lyskawa, J.; Mazari, M. J.; Gorgues, A.; Levillain, E.; SallM, M. Crown-tetrathiafulvalenes attached to a pyrrole or an EDOT unit: synthesis, electropolymerization and recognition properties. *Chem. Eur. J*. **2004**, *10*, 6497.

[4]. Chao, Y; Liu, P. Water-dispersed conductive polypyrroles doped with lignosulfonate and the weak temperature dependence of electrical conductivity. *Ind. Eng. Chem. Res*. **2009**, *48*, 9498.

[5]. Li, X. G.; Li, H.; Huang, M. R.; Moloney, M. G. Synthesis and multifunctionality of self-stabilized poly (aminoanthraquinone) nanofibrils. *J. Phys. Chem. C* **2011**, *115*, 9486.

[6]. Kudoh, Y.; Fukuyama, M.; Yoshimura, S. Stability study of polypyrrole and application to highly thermostable aluminum solid electrolytic capacitor. *Synth. Met*. **1994**, *66*, 157.

[7]. Wang, Y.; Su, F.; Wood, C.; Lee, J. Y.; Zhao, X. S. Preparation and

characterization of carbon canospheres as cnode caterials in lithium-ion secondary batteries. *Ind. Eng. Chem. Res*. **2008**, *47*, 2294.

[8]. Aquino-Binag, C.; Kumar, N.; Lamb, R. Fabrication and characterization of a hydroquinone-functionalized polypyrrole thin-film pH sensor. *Chem. Mater*. **1996**, *8*, 2579.

[9]. Li, Y.; Ying, B. Y.; Hong, L. J.; Yang, M. J. Water-soluble polyaniline and its composite with poly(vinyl alcohol) for humidity sensing. *Synth. Met*. **2010**, *160*, 455.

[10]. Paul, S.; Amalraj, F.; Radhakrishnan, S. CO sensor based on polypyrrole functionalized with iron porphyrin. *Synth. Met*. **2009**, *159*, 1019.

[11]. Hakansson, E.; Amiet, A.; Nahavandi, S.; Kaynak, A. Electromagnetic interference shielding and radiation absorption in thin polypyrrole films. *Euro. Polym. J*. **2007**, *43*, 205.

[12]. Groenendaal, L. B.; Jonas, F.; Freitag, D.; Pielartzik, H.; Reynolds, J. R. Poly(3,4-ethylenedioxythiophene) and its derivatives: past, present, and future. *Adv. Mater*. **2000**, *12*, 481.

[13]. Tourillon, G.; Garnier, F. New electrochemically generated organic conducting polymers. *J. Electroanal. Chem*. **1982**, *135*, 173.

[14]. Shilabin, A. G.; .Entezami, A. A. Electrochemical behavior of conducting

polyfuran derivatives containing pyrrole, thiophene and ethylenic spacers. *Eur. Polym. J.* **2000**, *36*, 2005.

[15]. González-Tejera, M. J.; Sánchez de la Blanca, E.; Carrillo, I. Polyfuran conducting polymers: synthesis, properties, and applications. *Synth. Met*. **2008**, *158*, 165.

[16]. Demirboga, B.; Onal, M. A. Electrochemical polymerization of furan and 2-methylfuran. *Synth. Met*. **1999**, *99*, 237.

[17]. Kaplin, D. A.; Qutubuddin, S. Electrochemically synthesized polypyrrole film: effects of polymerization potential and electrolyte type. *Polymer*. **1995**, *36*, 1275.

[18]. Kudoh, Y. Properties of polypyrrole prepared by chemical polymerization using aqueous solution containing $Fe_2(SO_4)_3$ and anionic surfactant. *Synth. Met*. **1996**, *79*, 17.

[19]. Hoshina, Y. E.; Contreras, A. Z.; Farnood, R.; Kobayashi, T. Nanosized polypyrrole affected by surfactant agitation for emulsion polymerization. *Polym. Bull*. **2012**, *68*, 1689.

[20]. Gok, A.; Sari, B.; Talu, M. Polymer, composites, and characterization of conducting polyfuran and poly (2-bromoaniline). *J. Appl. Poly.Sci*. **2005**, *98*, 2048.

[21]. Mu, S. Synthesis and electronic properties of poly(aniline-*co*-2-amino-4 hydroxybenzenesulfonic acid). *J. Phys. Chem. B* **2008**, *112*, 6344.

[22]. Antony, M. J.; Jayakannan, M. Molecular template approach for evolution of

conducting polymer nanostructures: Tracing the role of morphology on conductivity and solid state ordering. *J. Phys. Chem. B* **2012**, *114*, 1314.

[23]. Jinish, A. M.; Jayakannan, M. Role of anionic micellar template on the morphology, solid state ordering and unusual non-linear conductivity of polyaniline-*co*-polypyrrole nanomaterials. *J. Phys. Chem. B* **2011**, *115*, 6427.

[24]. Rao, P. S.; Sathyanarayana, D. N. Synthesis of electrically conducting copolymers of aniline with o/m-aminobenzoic acid by an inverse emulsion pathway. *Polymer*. **2002**. *43*, 5051.

[25]. Kabasakaloglu, M.; Talu, M.; Yildirim, F.; Sari, B. The electrochemical homopolymerization of furan and thiophene and the structural elucidation of their biopolymer films. *Appl. Surf. Sci*. **2003**, *218*, 84.

[26]. Wan, X, B.; Zhang, W.; Jin, S.; Xue, G.; You, Q. D.; Che, B. The electrochemical copolymerization of pyrrole and furan in a novel binary solvent system. *J. Electroanal. Chem*. **1999**, *470*, 23.

[27]. McConnell, R. M.; Godwin, W. E.; Baker, S. E.; Powell, K.; Baskett, M.; Morara, A. Polyfuran and co-polymers: a chemical synthesis. *J. Undergraduate Chem. Res*. **2002**, *3*, 121.

[28]. Glenis, M.; Benz, M.; LeGoff, E.; Schindler, J. L.; Kannewurt, C. R.; Kanatzidis,

M. G. Polyfuran: a new synthetic approach and electronic properties. *J. Am. Chem. Soc*. **1993**, *115*, 12519.

[29]. Guo, H.; Yin, G. Catalytic aerobic oxidation of renewable furfural with phosphomolybdic acid catalyst: an alternative route to maleic acid. *J. Phys. Chem. C* **2011**, *115*, 17516.

[30]. Hallal, J. J. L; Lucho, A. M. S.; Gonçalves, R. S. Electrochemical polymerization of furfural on a platinum electrode in aqueous solutions of potassium biphthalate. *Mat. Res*. **2005**, *8*, 1439.

[31]. Hoshina, Y.; Kabayashi, T. Electrically conductive films made of pyrrole-formyl pyrrole by straightforward chemical copolymerization. *Ind. Eng. Chem. Res.* **2012**, *51*, 5961.

[32]. Gök, A.; Sari, B.; Talu, M. Chemical preparation of conducting polyfuran/poly (2-chloroaniline) composites and their properties: a comparison of their components, polyfuran and poly(2-chloroaniline). *J. App. Poly. Sci*. **2003**, *88*, 2924.

[33]. Ballav, N.; Biswas, M. Preparation and evaluation of nanocomposites of polyfuran with Al_2O_3 and montmorillonite clay. *Polym. Int*. **2004**, *53*, 1467.

[34]. Yamamoto, O; Suzuki, T; Yanagisawa, M; Hayamizu, K. Graphic representation of nuclear magnetic resonance proton chemical shifts for the acyclic methine group. *Anal.*

Chem. **1968**, *40*, 568.

[35]. Thompson, A.; Rettig, S. J.; Dolphin D. Self-assembly of novel trimers using dipyrromethene ligands. *Chem. Commum.* **1999**, *7*, 631.

[36]. Benvenuti, F.; Galletti, A. M. R.; Carlini, C.; Sbrana, G. Synthesis, structural characterization and electrical properties of highly conjugated soluble poly(furan)s. *Polymer.* **1997**, *38*, 4973.

[37]. Alakhras, F.; Holze, R. Redox thermodynamics, conductivity and Raman spectroscopy. *Electrochimica. Acta*. **2007**, *52*, 5896.

[38]. Fusalba, F.; Be´langer, D. Electropolymerization of polypyrrole and polyaniline−polypyrrole from organic acidic medium. *J. Phys. Chem. B* **1999**, *103*, 9045.

[39]. Palaniappan, S.; Narayana, B. H. J. Temperature effect on conducting polyaniline salts: thermal and spectral studies. *Polym. Sci.* **1994**, *32*, 2431.

[40]. Sun, H. C.; Luo, Y. H.; Zhang, Y. D.; Li, D. M.; Yu, Z. X.; Li, K. X.; Meng, Q. B. In situ preparation of a flexible polyaniline/carbon composite counter electrode and its application in dye-sensitized solar cells. *J. Phys. Chem. C* **2010**, *114*, 11673.

[41]. Chen, H. L.; Chen, Guo, L. H.; Ferhan, A. R.; Kim, D. H. Multilayered polypyrrole-coated carbon nanotubes to improve functional stability and electrical

properties of neural electrodes. *J. Phys. Chem. C* **2011**, *115*, 5492.

[42]. Morikita, T.; Yamaguchi, I.; Yamamoto, T. New charge transfer-type p-conjugated poly(aryleneethynylene) containing benzo[2,1,2]thiadizaole as the electron-accepting unit. *Adv. Mater*. **2001**. *13*, 1862.

[43]. Yamaguchi, I.; Kado, A.; Fukuda, T.; Fukumoto, H.; Yamamoto, T.; Sato, M. Ionic polymers and oligomers with expanded π-conjugation system derived from through-space interaction in piperazinium ring. *Eur. Polym. J.* **2010**, *46*, 1119.

[44]. Kinoshita, S.; Yoshioka, S.; Fujii, Y.; Okamoto, N. Photophysics of structural color in the morpho butterflies. *Forma.* **2002**, *17*, 103.

[45]. Weatherspoon, M. R.; Cai, Y.; Crne, M.; Srinivasarao, M.; Sandhage K. H. 3D rutile titania-based structures with morpho butterfly wing scale morphologies. *Angew. Chem. Int. Ed*. **2008**, *47*, 7921.

[46]. Han, Y.; Qing, X.; Ye, S.; Lu, Y. Conducting polypyrrole with nanoscale hierarchical structure. *Synth. Met*. **2010**, *160*, 1159.

[47]. Kukino, M.; Kuwabara, J.; Matsuishi, K.; Fukuda, T.; Kanbara, T. Synthesis and metal-like luster of novel polyaniline analogs containing azobenzene unit. *Chem. Lett*. **2010**, *39*. 1248.

Chapter 3

Poly (Pyrrole–*co*–Formylpyrrole) / Multi–Wall Carbon Nanotubes Composite Films Prepared in Straightforward Chemical Polymerization

ABSTRACT: In this study, the preparation of composite films consisting of poly (pyrrole–*co*–formylpyrrole) copolymers (P(Py-*co*-FPy)) and multiwall carbon nanotubes (MWCNTs) through straightforward chemical polymerization in the presence of trifluoroacetic acid was revealed. The P(Py-*co*-FPy) coated on the MWCNTs surface uniformly during the chemical copolymerization and formed a homogeneous particulate structure to the composite films with rough surface. The composite films exhibited better film–forming ability as well as improved conductivity due to the conjugated backbone of the copolymer interacted with MWCNTs. Results of cyclic voltammetry suggested that the P(Py-*co*-FPy) /MWCNTs composites showed better capacitance with 184 F/g, when the scan rate was 10mV/s. The electrochemical behavior of the composite films could be improved as the MWCNTs amount was increased in the film.

3.1 Introduction

Recently, polypyrrole (PPy) and its derivatives have been attracted widely attention for application of fuel cells, sensors, and energy storage devices including batteries or electrochemical supercapacitors [1-4]. During the development of energy storage devices with employment of conductive PPy, the addition of cellulose, graphene and carbon nanotubes could greatly improve the physical and electrochemical performance of PPy [5-7]. Among them, carbon nanotube (CNT) is considered as the most potential candidate for electrochemical supercapacitor electrodes due to the excellent properties, including high surface area, well conductivity and stable electrochemical behavior [8-9]. Therefore, great attention has been devoted to fabrication of composited conductive PPy and CNT. In the composite materials, highly porous nanostructure exhibited unique electrochemical properties as promising candidate for electrochemical supercapacitor materials or other applications [10-12]. Thus, many works have been performed to prepare the PPy/CNT composites as applied for supercapacitor material such as incorporation of CNT into PPy by using electrochemical polymerization, template–directed polymerization, supercritical–assisted polymerization, interfacial polymerization and other facile chemical oxidative polymerization [13-16]. As reported, Hughes *et al*. studied the capacitive properties of catalytically grown MWCNTs and

PPy composites via electrochemical route and found that the film showed 192 F/g for

capacitance [17]. Sun and coworkers then studied PPy/MWCNTs composite prepared

by electrochemical polymerization. They successfully achieved high capacitance of 243

F/g [18]. Paul *et al*. reported PPy/MWCNTs composites synthesized by chemical

oxidative polymerization with highest capacitance of 165 F/g and found that the

synthesis method, electrolyte type, and binder compositions had profound effects on the

overall performance of the capacitor behavior [19]. Among these approaches, facile

chemical polymerization was preferable in comparison with electrochemical

polymerization and had the merit for the preparation of large area films by alternative

procedures. However, conductive PPy prepared through in situ chemical polymerization

are generally related to poor solubility, weaker film–formation ability. Therefore, it

would be needed to add quite an amount of film former fabrication as composited with

CNTs [20-22]. It is attractive to develop a simple method with economical and stable

processes for the PPy/CNT composites through chemical polymerization. On the other

hand, in our previous research, a simple method involving economical and stable

processes using chemical copolymerization of pyrrole (Py) and formyl pyrrole (FPy)

was developed to alleviate difficulties, which benefited of the formation of conjugated

methine group in the backbone arising from the use of FPy [23]. It was reported that

such self–standing film of the Py/FPy copolymer films (Scheme 3.1) had well–defined

nanostructures that showed a metal–like luster greenish color. In addition, excellent

mechanical properties were characteristics of the conjugated copolymer. For much

better development of the potential application of such films, the present study reports a

facile method to prepare the composite films of poly (pyrrole–*co*–formylpyrrole)

composited with multiwall carbon nanotube (MWCNT) and the influences of the

MWCNTs amount on the performance of the composite films. Characterization of the

obtained composite films was performed in the film–forming ability, electrical

conductivity and electrochemical behaviors. Evidence of the composite film exhibited

better physical property and electrochemical performance than pure PPy and

P(Py-*co*-FPy) films, suggesting its further application in electrochemical devices.
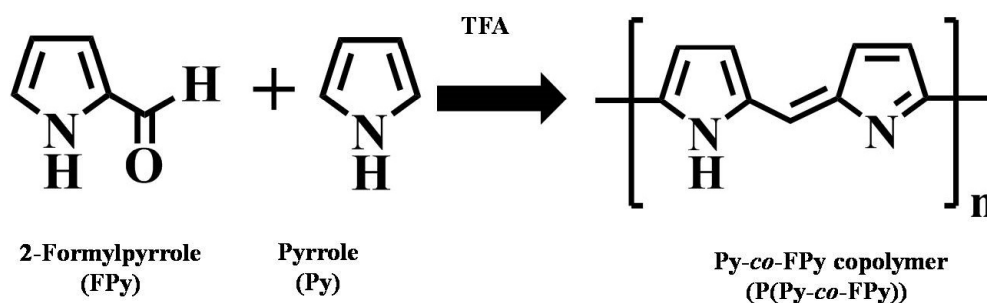
Scheme 3.1 Chemistry structures of Py, FPy and synthesis route and P(Py–*co*–FPy)

copolymer.

3.2 Experimental Section

3.2.1 Reagents

   Pyrrole (Py) and Pyrrole–2–carboxaldehyde (FPy), which were used as monomers, were purchased from Tokyo Chemical Industry Co. Ltd. Trifluoroacetic acid (TFA) and nitric acid sulfuric acid (HNO_3) were obtained from Nacalai Tesque Inc. Tetrabutylammonium Perchlorate (TBAP) were purchased from Tokyo Chemical Industry Co. Ltd. Multiwalled carbon nanotubes (MWCNTs) with a diameter of approximately 6–9 nm and a length of approximately 5 µm and indium tin oxide (ITO, 60 Ω/square) coated glass were purchased from Aldrich Chemical Co. Ltd. Other reagents were purchased and used as received.

3.2.2 Preparation of Treated MWCNTs

   Since suspension of MWCNTs in organic solvents such as $CHCl_3$ facilitated electrostatic adsorption of the MWCNTs on PPy group, acid treatment of the MWCNTs was carried out according with a previously described report, which can attach functional groups such as hydroxyl, carbonyl, and carboxylic groups to the MWNT with surface modification [24]. The MWCNTs were dispersed in 1 M HCl under ultrasonic irradiation (MUC–38, Askul Corp., Japan) for 30 min to remove residue from the metallic catalyst particles. The resulting MWCNTs were dispersed in 2.6 M HNO_3 and

refluxed for 24 hours at 140 ℃. The MWCNTs dispersion was filtered and washed

with amounts of deionized water and ethanol several times until the pH became neutral.

The treated MWCNTs were dried under vacuum and dispersed in CHCl$_3$ under

ultrasonic irradiation with different concentration for further used. Figure 3.1 shows the

images of MWCNTs (left) and treated MWCNTs (right) dispersed in deionized water

after standing for 24 hours.

MWCNTs   Treated-MWCNTs
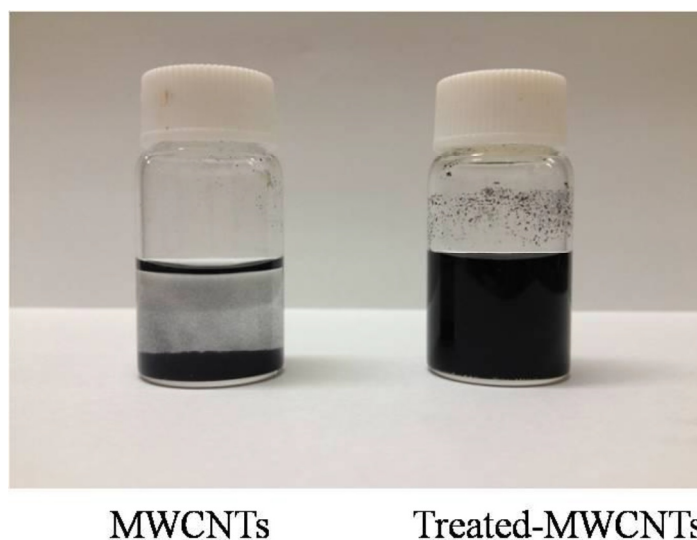
Figure 3.1 Pictures of MWCNTs and treated MWCNTs dispersed in deionized water

after standing for 24 hours.

3.2.3 Preparation of P(Py–*co*–FPy)/MWCNTs films

Three different films were prepared for comparative experiments in the present study.

According to experimental procedure described in our previous research, the chemical

oxidative polymerization of P(Py–*co*–FPy) copolymer (named P(Py-co-FPy)) film was carried out at optimum condition when 0.5 mole fraction of FPy was presented with the addition of TFA in $CHCl_3$ [23, 25]. For the preparation of P(Py-*co*-FPy) films, Py (200 mg, 3 mmol) and FPy (286 mg, 3 mmol) were dissolved and mixed under continuous stirring in 2 ml of $CHCl_3$. Then, $CHCl_3$ (4 ml) containing TFA (13 mmol), which was used as polymerized catalyst, was added to the solution at room temperature. The mixed solution was then coated onto ITO–coated glass (5 mm× 10 mm) or slide glass to determine the electrochemical performance and surface morphology, respectively. After the coating process, copolymer film was obtained within 24 hour at room temperature. Finally, solvent was evaporated for forming the films. The obtained films were washed by deionized water several times until the pH became neutral and dried under vacuum for 24 hour. Composite of P(Py-*co*-FPy) and MWCNTs carried out as followed: Py (200 mg, 3 mmol) and FPy (286 mg, 3 mmol) were dissolved in 2 ml $CHCl_3$ and mixed together. Then, treated MWCNTs was dispersed in 2 ml $CHCl_3$ with different weight percentage (1, 3, and 5 wt%, which was designated for 1%MWCNTs-P(Py-*co*-FPy), 3%MWCNTs-P(Py-*co*-FPy) and 5%MWCNTs-P(Py-*co*-FPy), respectively) under ultrasonic operation for 30 min and then each MWCNTs solution was mixed with the monomer. After that $CHCl_3$ (2 ml) containing TFA (13 mmol) as catalyst was added to

the mixture solution containing monomers and MWCNTs. Then, the mixed solution

was coated onto substrate and the composite films were prepared and dried under the

same conditions. The schematic illustration of the process for formation of the

composite films during the copolymerization is shown in Scheme 3.2. In comparison of

the copolymer, PPy film was also prepared by addition of Py monomer (400 mg, 6

mmol) with TFA (13 mmol) in total 4 ml CHCl$_3$ as well as operated step similarly with

the copolymer and MWCNTs. Figure 3.2 shows the composite films preparation on the

ITO substrate.
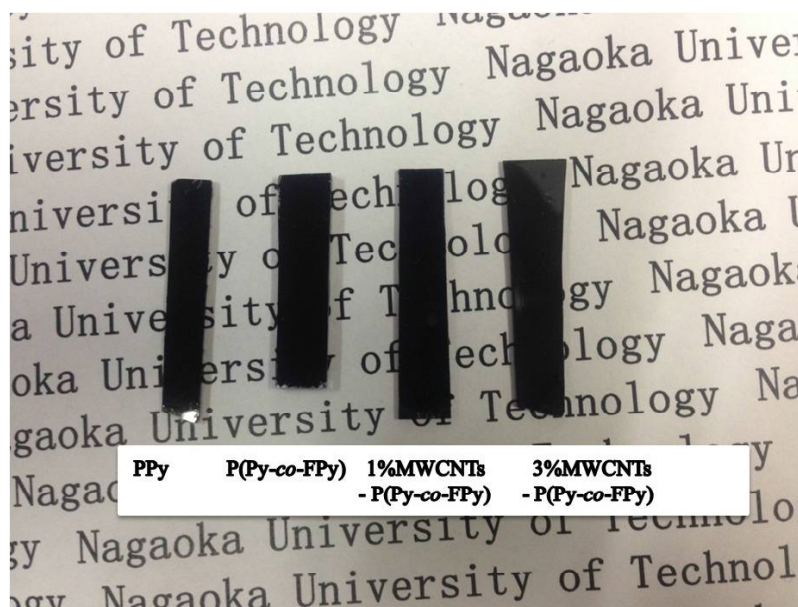
Figure 3.2 Images of PPy, P(Py-*co*-FPy) copolymer and 1%MWCNTs-P(Py-*co*-FPy)

and 3%MWCNTs-P(Py-*co*-FPy) composited films.

3.2.4 Characterization of composite films

FT–IR spectra were obtained on an IR spectrophotometer (Prestige; Shimadzu Corp.) under the transmittance mode. Zeta potential results were determined by using zeta–potential/particle size analyzer (ELSZ–1; Otsuka Electronics Corp., Japan). The UV–visible absorption spectra of the each film on the quartz glass substrate were measured using a UV–vis–NIR spectrophotometer (V–570; Jasco Corp., Japan) under transmittance mode. To measure electrical conductivity, the resultant films were put in a sealed vessel containing a small amount of I_2 for chemical doping during 24 h and determined at room temperature using a typical four–point method (Roresta–GP MCP–T610; Mitsubishi Chemical Analytec Co. Ltd., Japan). The tensile strength of the films was measured using a load cell (LTS–500N; Minebea Co., Ltd., Japan) with the sample specimen (2.5 cm × 7.5 cm). For SEM measurements, surface morphology of the films was observed after coating with about 5 nm thickness of Au. Then, the surface and cross–section of the films were observed (JSM–7000F; JEOL Ltd., Japan) at 15 keV. For the surface analysis of the films, scanning probe microscopy (SPM, Nanocute; SII Investments, Inc., Japan) was applied in a 500 × 500 nm area of the film to produce AFM images. A silicon probe mounted on a cantilever (Micro cantilever Si–DF40P2; SII Investments Inc., Japan) was used. The surface roughness was calculated using root mean square values (RMS) in the Z–range images. Rrms was calculated according to the following equcation:

$$R_{rms} = \sqrt{\frac{\sum_{n=1}^{n}(h(x_i) - h)^2}{n}}$$

Here, n was the measurement points; $h(x_i)$ was the height of the point x_i; h was the average height.

To determine the electrochemical behavior of each film, cyclic voltammetry (CV) of films with an ITO–coated substrate was recorded in a 0.1 M tetrabutylammonium perruthenate (TBAP) / acetonitrile supporting electrolyte solution (HSV–110; Hokuto Denko Corp., Japan). Voltammograms quoted against a Ag/Ag^+ counter electrode were obtained at a scanning rate of 1 mV s^{-1} and scanning range of –1.0 V to 1.0 V. The electrochemical impedance spectroscopy (EIS) was performed over a range of frequencies (10 mHz – 100 kHz) with a signal amplitude of 5 mV in 0.1 M TBAP / acetonitrile supporting electrolyte solution using an impedance analyzer (IM3590; Hioki Co. Ltd., Japan).

3.3 Results and Discussions

3.3.1 Formation of the P(Py-*co*-FPy)/MWCNTs composite films

Table 3.1 presents the polymerization yield, tensile strength, and the electrical conductivity of each composite film. As seen in Table 3.1, it was noted that the values of tensile strength and electrical conductivity was remarkable enhanced with the increase of yield relative to these of pure PPy and P(Py-*co*-FPy) after the addition of MWCNTs. The conductivity of the P(Py-*co*-FPy)/MWCNTs films was increased with a narrow range from 10^{-4} to 10^{-3} S/cm than P(Py-*co*-FPy) films. However, as the

MWCNTs content increased from 1 to 5 wt %, the conductivity was irregularly changed.

The tensile strength of the P(Py-*co*-FPy)/MWCNTs could increased from 108 to 114

N/mm^2, as the content of MWCNTs was more than 7 wt% in the dispersion solution, the

viscosity of MWCNTs interfered the uniformly mixing with Py and FPy monomer.

Table 1. Copolymerization yield, tensile strength, and the electrical conductivity of each

PPy film.

	PPy	P(Py-*co*-FPy)	1%MWCNTs-P(Py-*co*-FPy)	1%MWCNTs-P(Py-*co*-FPy)	1%MWCNTs-P(Py-*co*-FPy)
Molar ratio of Py/FPy	1/0	1/1	1/1	1/1	1/1
MWCNTs content [a] (wt %)	0	0	1	3	5
Yeild [b] (%)	13.6	83.3	86.5	90.2	87
Tensile strength (N/mm^2)	16.7	84.6	108.5	106.8	114.2
Electrical conductivity [c] (S/cm)	2.1×10^{-5}	8.2×10^{-4}	3.8×10^{-3}	5.6×10^{-3}	4.5×10^{-3}

[a] The MWCNTs content mean the originally weight percentage of MWCNTs in the

dispersion solution before addition with Py monomer solution.

[b] In case of the addition of MWCNTs, the yield (%) = amount of obtained powder(g) /

amount of Py /FPy/MWCNTs (g) × 100.

[c] Conductivity of each film was measured after I$_2$ was doped at room temperature.
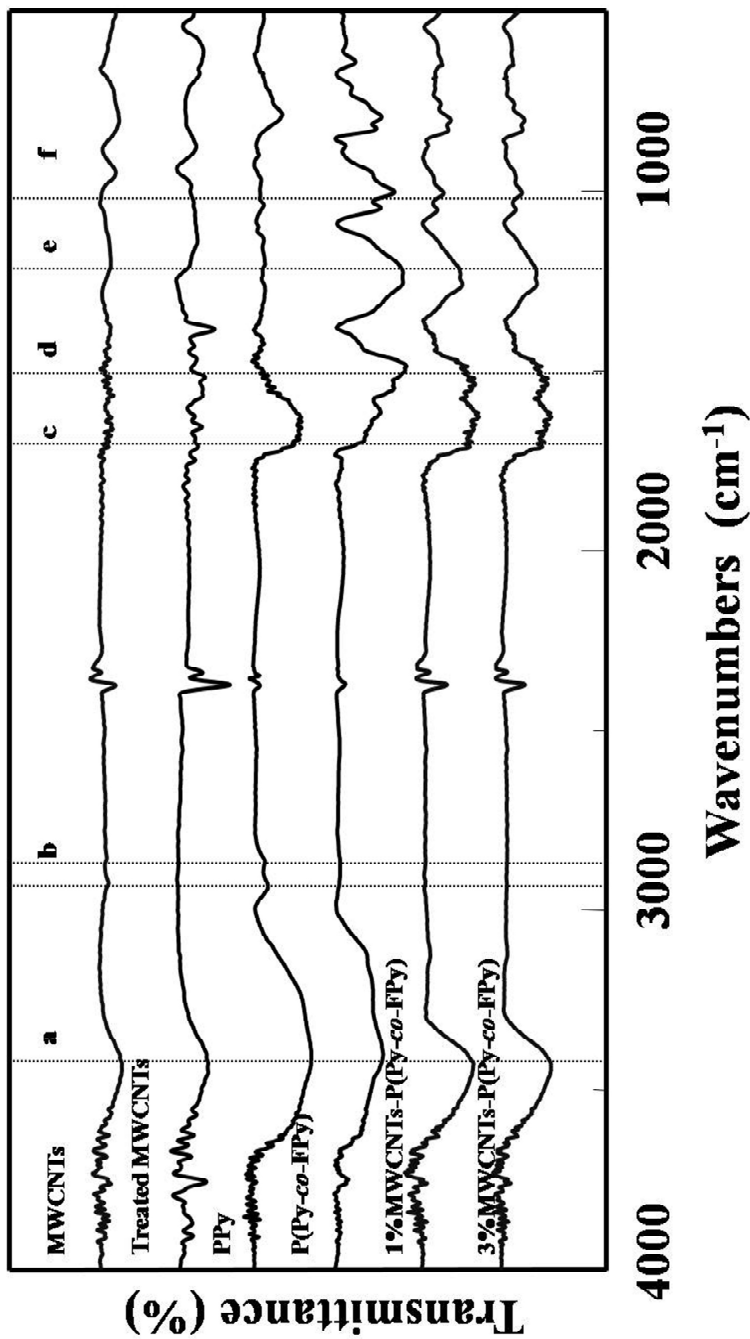
Figure 3.3 FT–IR spectra of MWCNTs, Treated MWCNTs, PPy, P(Py-*co*-FPy), and P(Py-*co*-FPy)

/MWCNTs composite films with different MWCNTs content.

To confirm the composition of the MWCNTs in the composite films, UV–vis and FT–IR analysis were implemented. Figure 3.3 showed the FT–IR spectra of the composited P(Py-*co*-FPy) and MWCNTs/P(Py-*co*-FPy) films. To compare each of them, the spectra of the treated MWCNTs and PPy were shown additionally. The treated MWCNTs exhibited the peak at around 1700 cm^{-1} as indicated by line c, which corresponded to the C=O stretching vibration of the carboxylic acid groups. This indicated the existence of the carboxylic acid groups at the surface of MWNCTs after
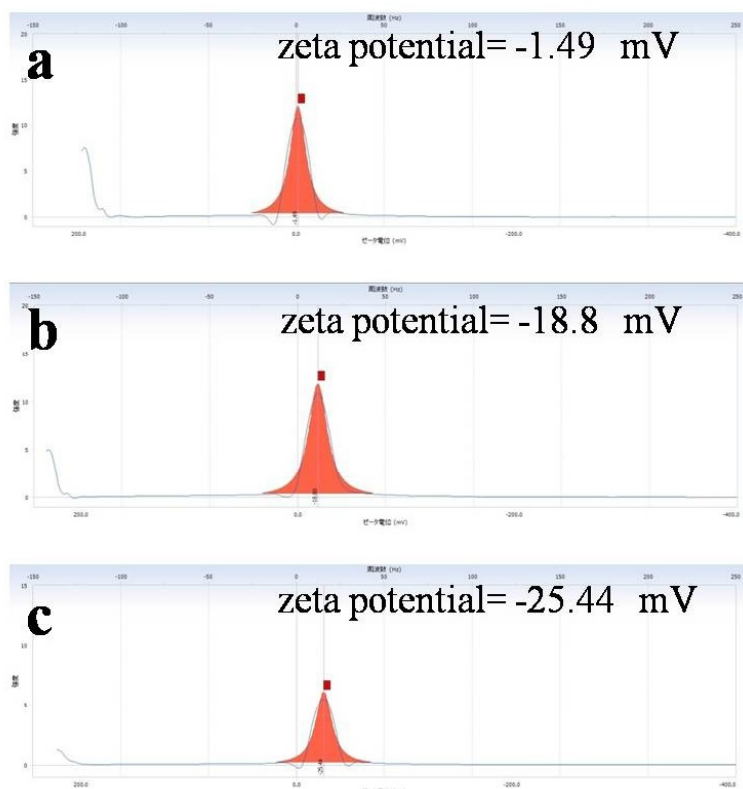
Figure 3.4 Zeta potential patterns of the treated–MWCNTs with different component of 1(a), 3 (b) and 5 (c) wt% treated–MWCNTs in deionized water dispersion.

the acid treatment process [19, 26]. In addition, zeta potentials could provide further

evidence for the identification of treated MWCNTs (Figure 3.4), which resulted in a

negative potential due to the presence of carboxylic acid groups on the surface. The

treated MWCNTs showed a zeta potential of –1.49, –18.80 and – 25.44 mV for 1, 3 and

5wt% content of MWCNTs in deionized water dispersion (pH = 7), respectively.
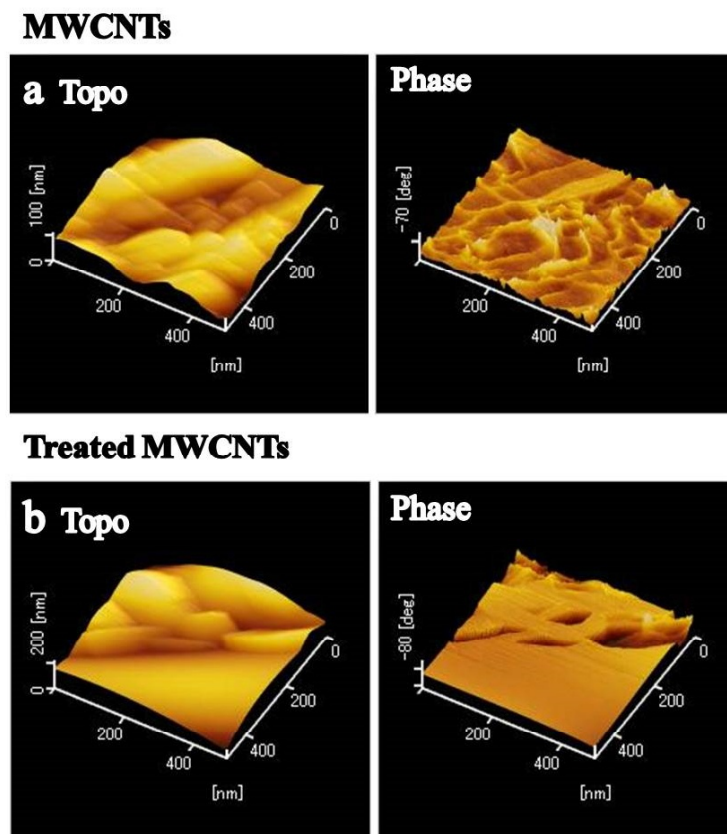
Figure 3.5 Topological and phase AFM imagesof MWCNTs and treated MWCNTs.

It should be pointed that after acid treatment, the average surface roughness parameter values (*Rrms*) was almost same for the MWCNTs and treated MWCNTs as 1.47 ± 0.1 nm and 1.68 ± 0.1 nm, respectively (Figure 3.5). However, the average surface area of the particulate aggregate structure on a nanoscale (500 nm × 500 nm area) was increased from 2.0×10^3 nm^2 for MWCNTs to 3.8×10^4 nm^2 for treated MWCNTs. Meanwhile, the electrical conductivity of MWCNTs before and after the acid treatment showed a slight decrease from 5.2×10^1 S/cm to 1.6×10^1 S/cm, probable due to the oxidation by the nitric acid. For both PPy and P(Py-*co*-FPy), the N–H stretching vibrations originated from Py were observed at 3404 cm^{-1} (line a). It was apparent that the lines (b) for the saturated C−H stretching vibrations at 2938 and 2868 cm^{-1} were appeared in PPy but the P(Py-*co*-FPy) had weaker one. This decrease indicated that the conjugated structure for the polymer backbone [23]. Additionally, the peaks for C=C double bond stretching of the pyrrole ring, peaks (d) for C–N stretching and the peak (f) of C–H out–of–plane deformation vibration from methine group appeared at 1651, 1498, and 1008 cm^{-1}, respectively. These were attributed to the formation of conjugated structure in the copolymer films. It was noted that the broad peak (e) observed around 1250 cm^{-1} was assigned to –C=CH– stretching from the methine group of PFy for P(Py-*co*-FPy) and P(Py-*co*-FPy)/MWCNTs films. It was also

apparent that the peaks at 1489 cm^{-1} in the P(Py-*co*-FPy) shown tiny shifted in the

P(Py-*co*-FPy) /MWCNTs composites as indicated with line d. It was reported that peaks

near 1254 (line e) and 1000 cm^{-1} indicated the doping state of polypyrrole [25]. Both of

these peaks appeared in P(Py-*co*-FPy) and P(Py-*co*-FPy)/MWCNTs films but could not

observe in neat PPy. Meanwhile, it was observed that with the increasing of MWCNTs

content, the integrated absorption intensities around 1500-1600 became broader and

bigger. According to Tian et al reports, polymers with short conjugation lengths show

high values of I_{1620}/I_{1487}, whereas polymers with long conjugation lengths show low

values of I_{1620}/I_{1487}. The calculated ratios of the integrated absorption intensities of the

peak 1620 and 1487 cm^{-1} (I_{1620}/I_{1487}) of P(Py-*co*-FPy) and 1, 3, 5 wt% MWCNTs

contents P(Py-*co*-FPy)/MWCNTs films are 0.7, 1.06, 1.1 and 1.78, respectively. It was

consider that the changes revealed that the chain of P(Py-*co*-FPy) deposited directly

onto the surface of MWNTs with a shorter conjugation length, probably because of the

interaction between the MWCNTs and the conjugated structure of PPy [27]. UV–vis

absorption measurement is used to characterize the interfacial interaction between

P(Py-*co*-FPy) and MWCNTs for the composite films. The UV–vis spectra of each film

were shown in Figure 3.6. The obtained UV−vis spectra had a typical characteristic

absorption band of the π−π* transition of conjugated PPy at 478 and 495 nm for PPy
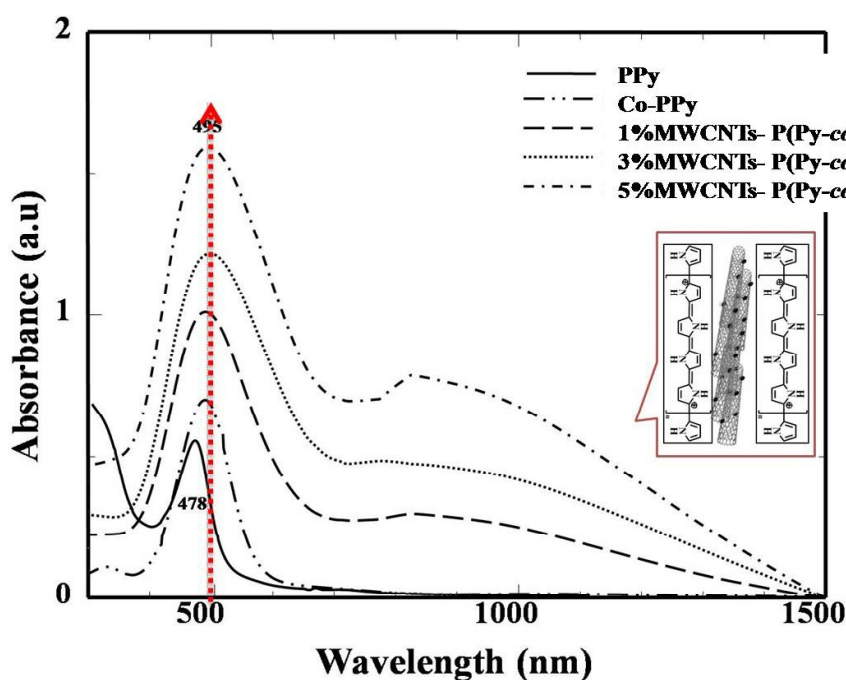
Figure 3.6 UV–visible absorption spectra of PPy, P(Py-*co*-FPy) and

P(Py-*co*-FPy)/MWCNTs composite films for 1, 3 and 5 wt% MWCNTs content.

and P(Py-*co*-FPy), respectively [23]. With addition of MWCNTs to P(Py-*co*-FPy), slight

shift was observed for the π−π* transition absorption of the P(Py-*co*-FPy), and the bond

intensity increased gradually with the increase of the MWCNTs content. Meanwhile, it

was noted that a stronger and broader absorption peak was appeared from 700 and 1500

nm for the composites. When the MWCNTs content was high, the intensity was

increase remarkably. It was considered that the formation of bipolaron of P(Py-*co*-FPy)

conjugated   chain   in   the   composite   films,   especially   effective   for   the

5%MWCNTs–P(Py-*co*-FPy). It could be probable considered that the PPy was absorbed by π–π interaction during the polymerization process and uniformly coated on MWCNTs [20, 26].

3.3.2 Surface morphology of the composite films

Figure 3.7 presented the SEM images of the surface and cross–section of PPy (a, b), P(Py-*co*-FPy) (c, d), 1%MWCNTs-P(Py-*co*-FPy) (e, f), and 3%MWCNTs-P(Py-*co*-FPy) films (g, h). The P(Py-*co*-FPy) film exhibited a metallic greenish–black color that has excellent film–forming ability, whereas the Py film without adding FPy exhibited a black color. In the P(Py-*co*-FPy) films, a relatively smooth and dense morphology was observed. In e and f, the surface of the 1%MWCNTs-P(Py-*co*-FPy) and 3%MWCNTs-P(Py-*co*-FPy) films had much rougher than the P(Py-*co*-FPy) and the trend became gradually increased. The irregular aggregation structure was appeared with the addition of MWCNTs. In g and h, the SEM images of the cross section of the composite film exhibited a particulate aggregate structure for these films. This was probably due to that the formation of Py and FPy oligomer/polymer was attracted by the π–π interaction and uniformly coated on the treated MWCNTs as well as the interfacial interaction between P(Py-*co*-FPy) conjugated chain and MWCNTs promoted the
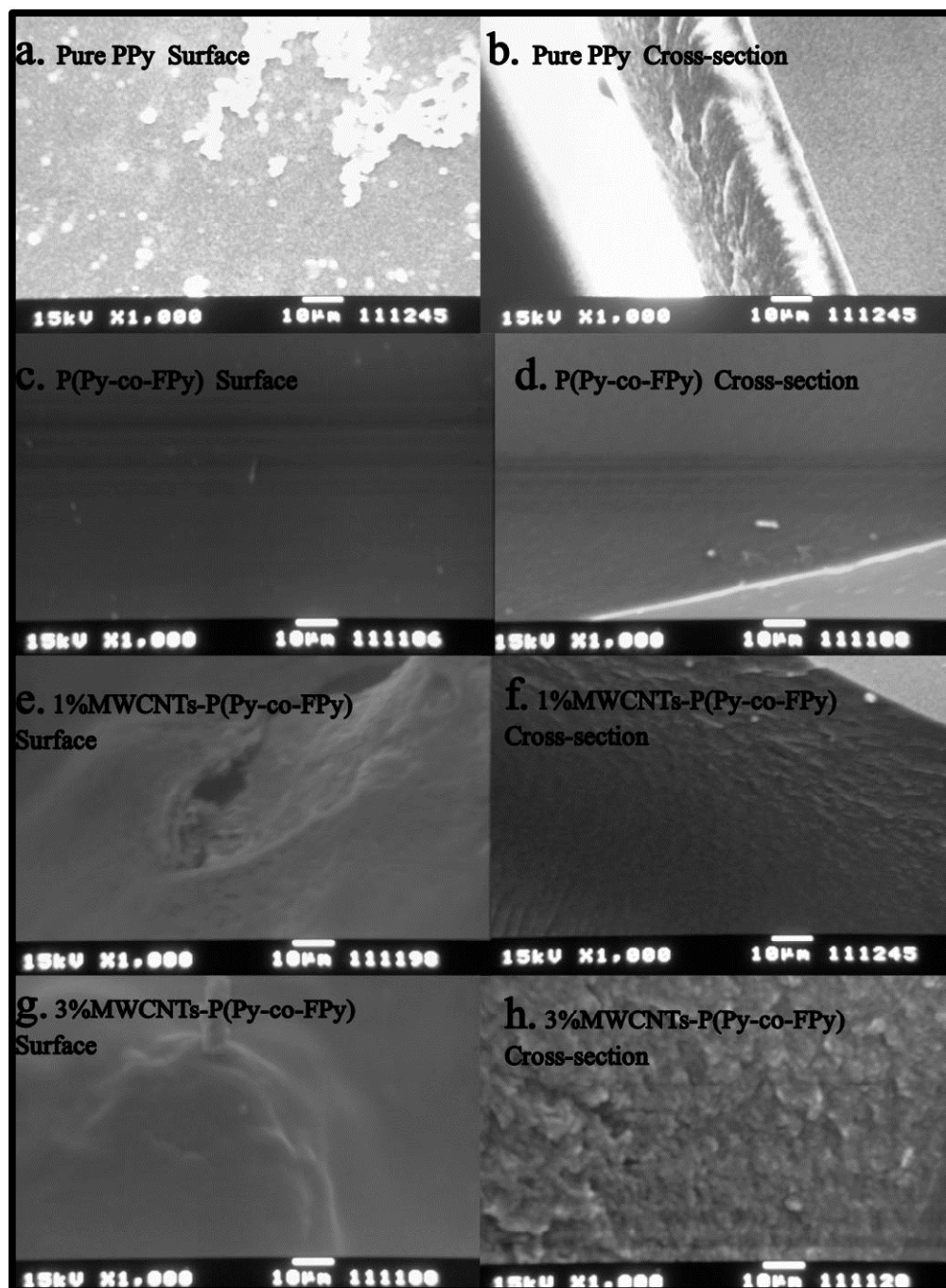
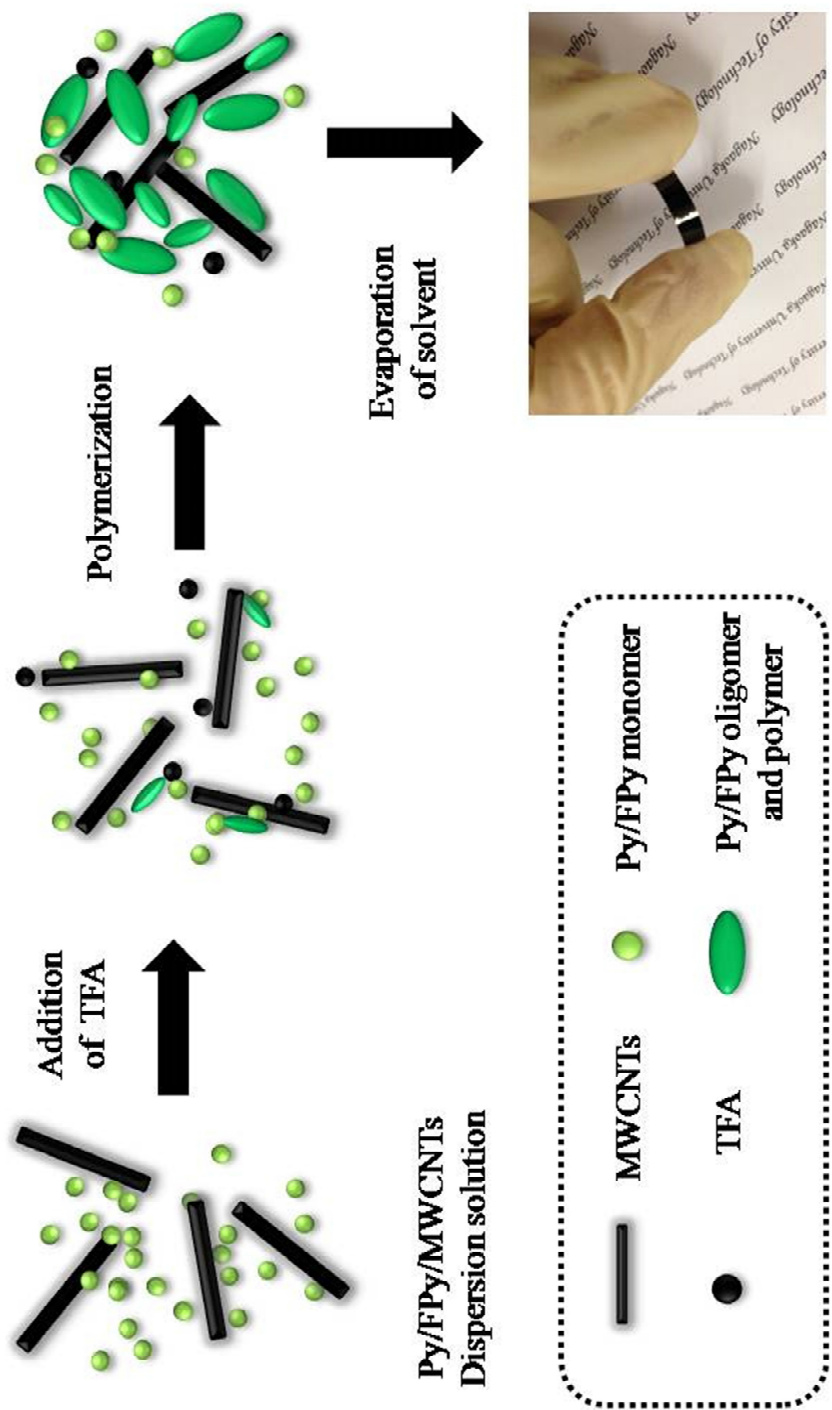**Figure 3.7** SEM images of surface and cross–section of PPy (a,b), P(Py-*co*-FPy) (c, d),

1%MWCNTs-P(Py-*co*-FPy) (e, f), and 3%MWCNTs– P(Py-*co*-FPy) films (g, h).

Scheme 3.2 Schematic illustration of the process for formation of

P(Py-*co*-FPy)/MWCNTs composite in the chemical oxidative polymerization.
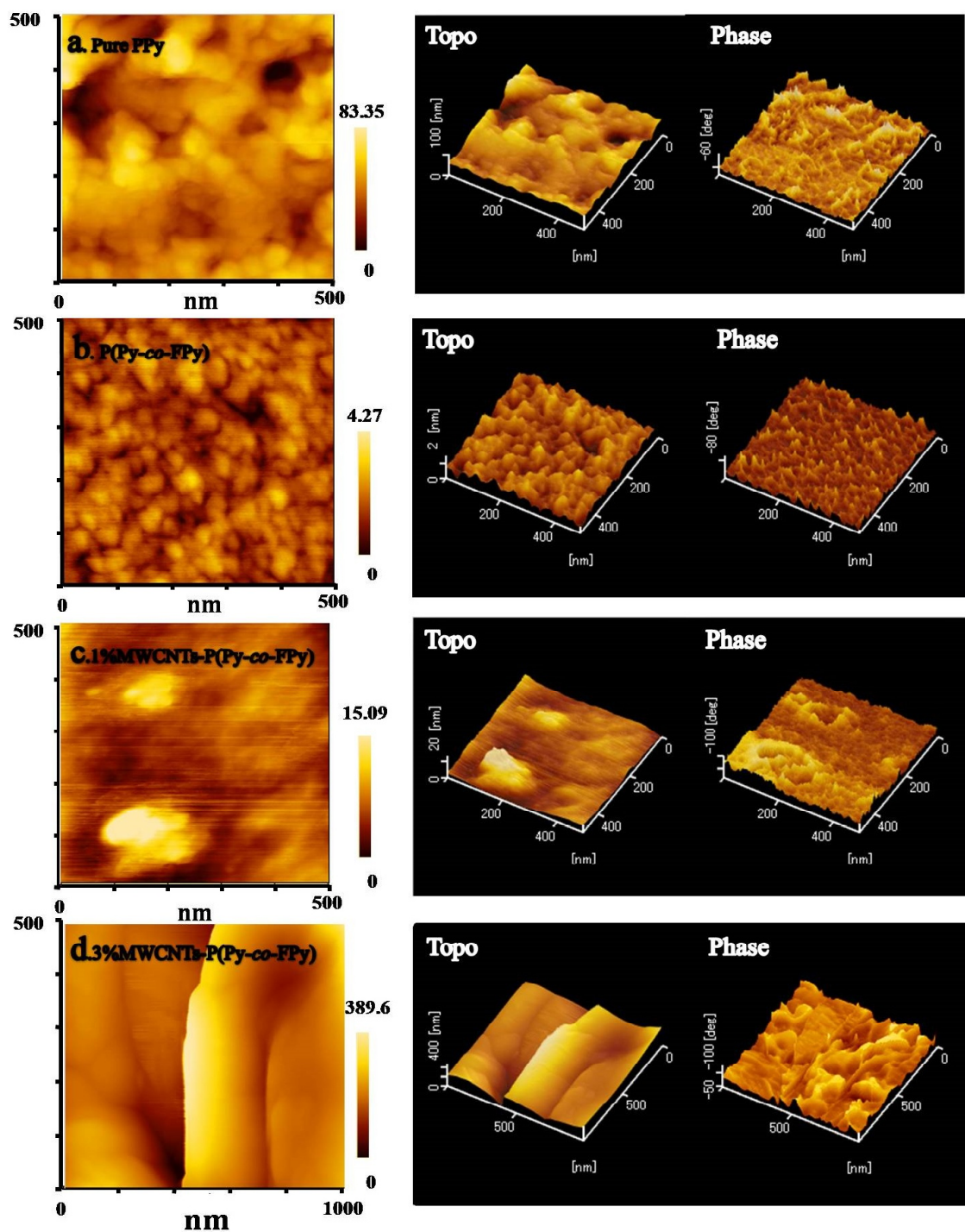
Figure 3.8 Topological and phase AFM imagesof each films: (a) PPy; (b) P(Py-*co*-FPy);

(c) 1%MWCNTs-P(Py-*co*-FPy); (d) 3%WMCNTs-P(Py-*co*-FPy).

uniformly coated of P(Py-*co*-FPy) on MWCNTs during the polymerization. With the

slowly evaporation of the solvent and TFA during polymerization, the single PPy

coated-MWCNTs particulate were agglomerated together to form irregular aggregation

of films. It was consider that the well-dispersed MWCNTs could prevent the self

aggregation of MWCNTs and the polymerized P(Py-*co*-FPy). In addition, Chen *et al*.

reported that the positive effect of trifluoroacetic acid as a co–solvent for the dispersion

of MWNTs in a conjugated polymer (poly 3–hexylthiophene) through a solution

process [29]. The results revealed the better dispersion of CNTs in polymer matrixes

whereas the hydrophilic head group induced electrostatic repulsions and prevented the

self aggregation of MWCNTs [30]. On the basis of these reports, the polymerization of

the P(Py-*co*-FPy) in the presence of MWCNTs was preceded as illustrated in Scheme

3.2. It was probable to consider that the interaction between MWCNTs and Py

oligomer/polymer was enhanced in the uniform dispersion of MWCNTs benefit by the

assistance of trifluoroacetic acid and surface treatment of MWCNTs. Then, the Py

oligomer and polymer coated on the MWCNTs homogeneously to form the particulate

aggregate structure during the polymerization [28, 31].

AFM topographic and phase–shift images for each film are shown for 500 nm × 500

nm area in Figure 3.8. The Pure PPy film (3.8a) showed a rough surface, whereas the

copolymer films (3.8b) showed homogeneous particulate surfaces with nanodomains.

The 3D topographic and phase imaging of P(Py-*co*-FPy) film also indicated that almost

only one phase on the film surface with different surface morphology was seen,

suggesting that the enhancement of homogeneity of the copolymerized films [25, 32].

With addition of MWCNTs, it was obviously observed that the surface of composite

films became much rougher than P(Py-*co*-FPy) film, as shown in Figure 3.8c and 3.8d.

To evaluate the surface roughness and the average surface area of particulate aggregate

structure on a nanoscale for each film, the roughness parameter values (R_{rms}) was

calculated for the PPy and P(Py-*co*-FPy) as 9.9 ± 0.4 nm and 0.41 ± 0.1 nm,

respectively. In cases of the composite films, the values of the R_{rms} were increased as

1.91± 0.3 nm, 9.7 ± 0.5 nm to 44.8 ± 1.2 nm for the 1%MWCNTs-P(Py-*co*-FPy),

3%MWCNTs-P(Py-*co*-FPy) and 5%MWCNTs-P(Py-*co*-FPy) films, respectively.

Herein, the composite films had a much rougher surface with porous morphology with

the increasing of MWCNTs content. The average surface area of the particulate

aggregate structure on a nanoscale (500 nm × 500 nm area) for composite films was 8.8

× 10^3, 2.5× 10^4, 5.7× 10^4 nm^2 for 1, 3 and 5 wt% contents of the MWCNTs, respectively.

All this results were summarized in Figure 3.9. The particulate structure and increased

average surface area of the particulate structure for composite film surface was expected
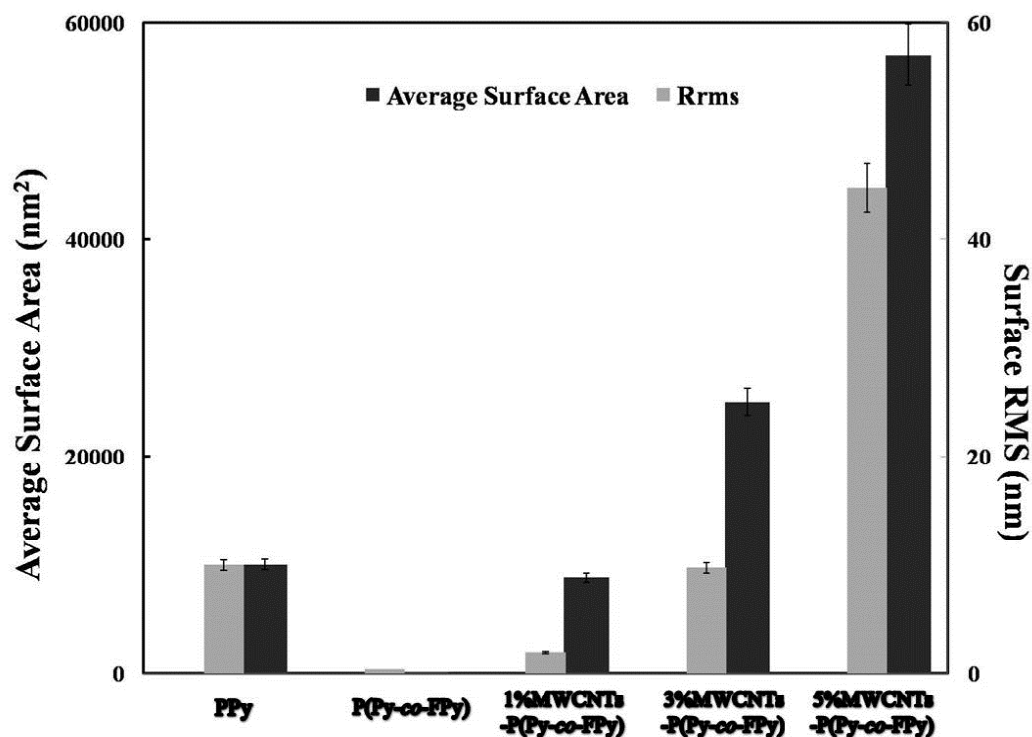
Figure 3.9 AFM parameters of surface roughness and average surface area of the

particulate aggregate structure surface area for each film.

to provide great benefits for applications in electrode materials [33].

3.3.3 Electrochemical properties of the composite films

   To evaluate the electrochemical performance of the composite films, cyclic

voltammetry (CV) and electrochemical impedance spectroscopy (EIS) were employed

for each film. These characteristics were measured with an ITO–coated substrate and

recorded in a 0.1 M tetrabutylammonium perruthenate (TBAP) / acetonitrile supporting

electrolyte. Figure 10a shows CV curves of PPy, P(Py-*co*-FPy) and composite films
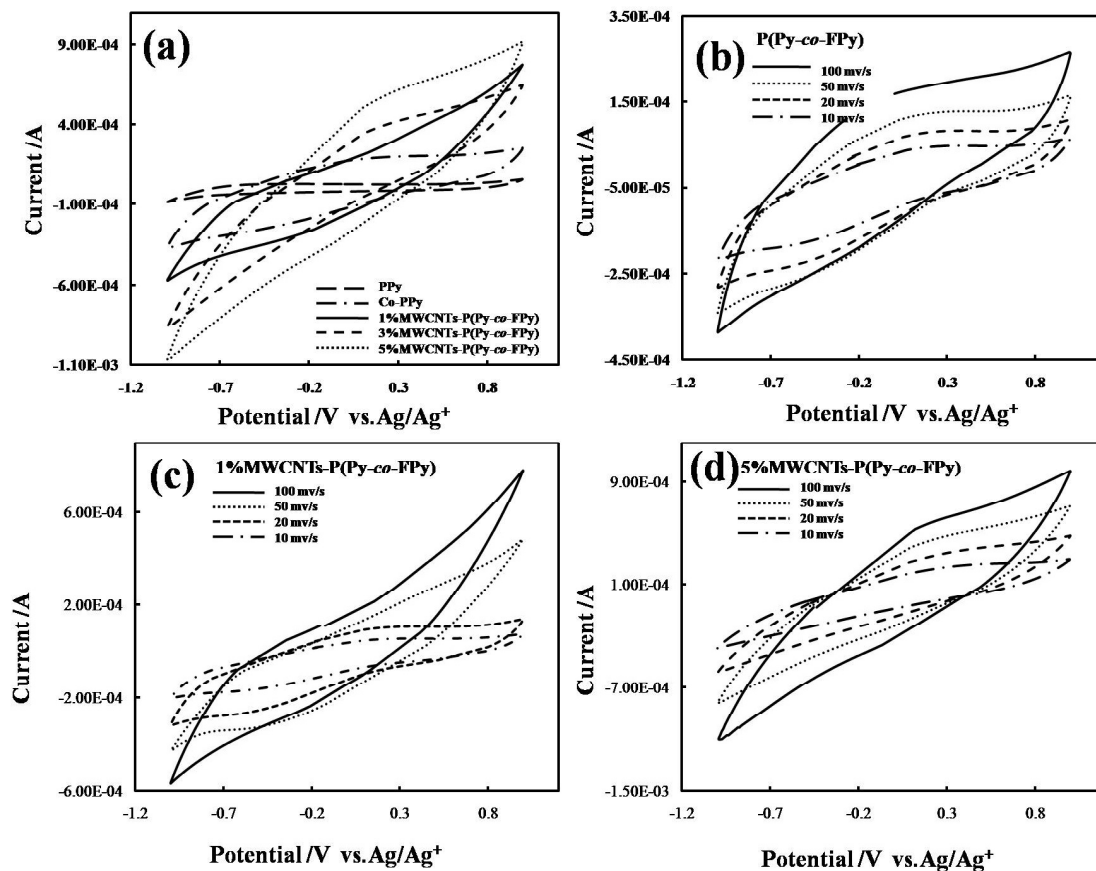
Figure 3.10 Cyclic voltammogram curves of each PPy films at 100 mVs^{-1} in 0.1 M

solution 0.1M TBAP /acetonitrile solution (a) and scan rate dependence of the

P(Py-*co*-FPy), 1%MWCNTs-P(Py-*co*-FPy) , and 5%MWCNTs-P(Py-*co*-FPy) in 0.1 M

solution 0.1M TBAP /acetonitrile with scan rate at 100, 50, 20, 10 mV/s(b ,c, and d).
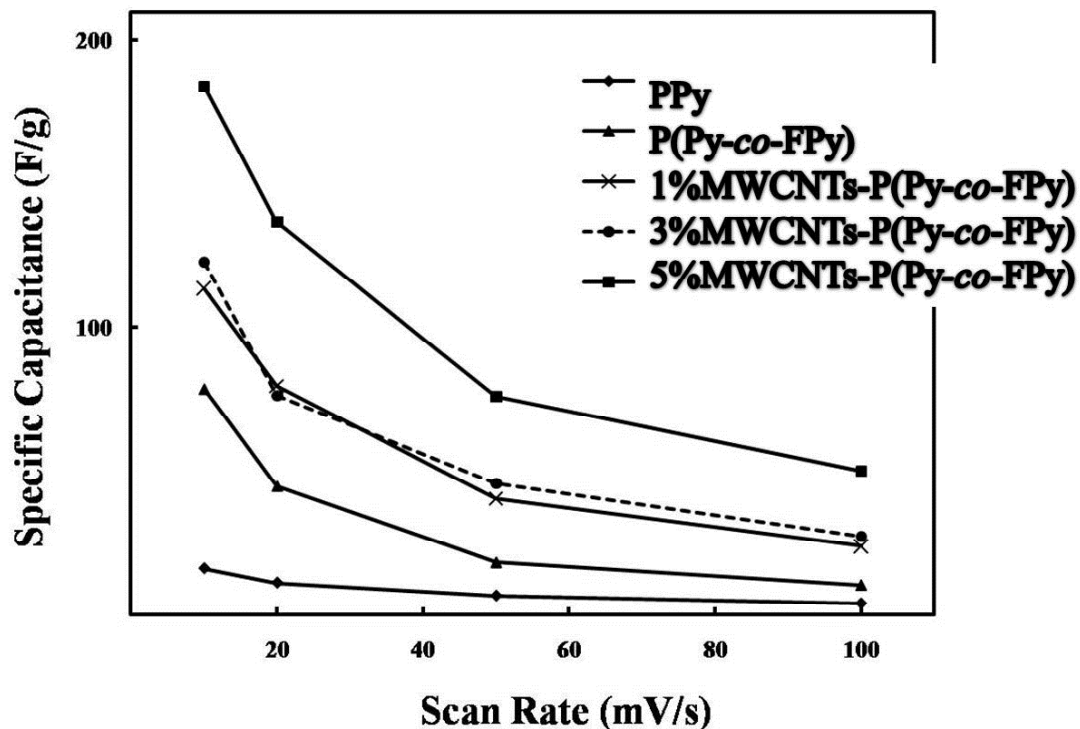
Figure 3.11 Specific capacitance of PPy, P(Py-*co*-FPy) and P(Py-*co*-FPy)/MWCNTs

composites films with scan rate at 100, 50, 20, 10 mV/s.

were examined within the applied voltage range of –1 V to +1 V at 100 mV/s scan rates.

As observed in Figure 3.10, pure PPy showed a lower current density response,

suggesting the poor conductivity of the PPy films. In the case of the composite films, it

was observed that the current density response was apparently larger than those of the

P(Py-*co*-FPy) and PPy films. In addition, as increased with the MWCNTs content in the

composite films, the current density became high. The CV curves within the different

scan of 10, 20, 50, and 100 mV/s for each film is shown in b, c, and d for the

P(Py-*co*-FPy),   1%MWCNTs-P(Py-*co*-FPy)   and   5%MWCNTs-P(Py-*co*-FPy),

respectively. In case of the P(Py-*co*-FPy) film, the CV curve had unconspicuous

negative and the positive current region, this presented the reduction peak at 0.3V and

the oxidation peak was observed at –0.2 V, as similarly reported [10]. This indicated the

cathodic reduction and anodic oxidation due to the redox reaction of the P(Py-*co*-FPy)

in the electrode/electrolyte surface, respectively [14]. With an decreasing scan rate from

100 to 10 mV/s, the cathodic peaks shifted positively and the anodic peaks did

negatively. This was due to the existing resistance of the electrode materials [33]. In

contrast the composite films showed the nonrectangular shape of the CV curves,

suggesting the more effective electron transport. This might be due to the surface of

MWCNTs showing the existence of redox reaction with P(Py-*co*-FPy) and electron

transport all at once [10]. With the increasing of scan rates, the similar tendencies were

observed for composite films. It was easily noted that the addition of MWCNTs

enhanced the current density response at each scan rate, indicating higher specific

capacitance (*C*). It was considering that the CV curves were not the mirror symmetry in

the CV shape. The area inside of CV curve/scan rate was used to represent the total of

anodic and cathodic voltammetric charges [34-35]. Herein, the specific capacitance was

calculated according to the following equation:

$$C = \int_{E1}^{E2} I(E)\,dE \; / \, 2\,(E_2 - E_1)\,mv = \text{Area in side CV curve} \, / \, 2\,mv$$

where *C* is the specific capacitance of each film. E_1 and E_2 were the cutoff potentials in

CV curve. *I (E)* was the instantaneous current. $\int_{E1}^{E2} i(E)\,dE$ was the total voltammetric

charge obtained by integration of positive and negative sweep in CV curves. Here, the

term of $E_2 - E_1$ meant the potential window width and *m* was for the mass of active PPy

or PPy/MWCNTs within the electrode. *v* was the potential scan rate. Based on the

above equation, the value of *C* for the composite films showed that much higher of 23.7,

27.2 and 50.2 F/g for 1%MWCNTs-P(Py-*co*-FPy), 3%MWCNTs-P(Py-*co*-FPy) and

1%MWCNTs-P(Py-*co*-FPy) was observed than 4 F/g of PPy and 10.3 F/g of

P(Py-*co*-FPy) at 100 mV/s scan. Figure 11 summarizes the specific capacitance at

different scan rate at 100, 50, 20, 10 mV/s. With the increasing of MWCNTs content in

the composite films, the *C* values remarkable increased to be 16, 78.6, 113.5, 122.6 and

184   F/g   for   PPy,   P(Py-*co*-FPy),   1%MWCNTs-P(Py-*co*-FPy),

3%MWCNTs-P(Py-*co*-FPy) and 5%MWCNTs-P(Py-*co*-FPy), respectively, when the

scan rate was 10mV/s. It was probably considered that there were two different kinds of

capacitive contributions in the composite films. One was the double–layer capacitance

behavior of the MWCNTs and other was the pseudocapacitance behavior of the

P(Py-*co*-FPy) [36-37]. Therefore, it was reasonable to consider that the addition of the

MWCNTs into the P(Py-*co*-FPy) films improved the specific capacitance effectively.

For more information about the ability of such P(Py-*co*-FPy)/MWCNTs films, electrochemical impedance spectroscopy (EIS) was employed to determine the electrochemical behaviors in electrolyte for electrode materials. Figure 3.12 showed the Nyquist plots of the composite films within a frequency range of 10 mHz – 100 kHz in 0.1 M TBAP / acetonitrile electrolyte. The internal set represented the corresponding model for ideal capacitors. Therein, a solution resistance (Rs) refers to the resistance from the electrolyte and R_1 refers to the double layer capacitance connected in parallel with a pseudocapacitance ability of the electrode materials (C_1) and a charge transfer resistance (R_{CT}). The R_{CT} corresponded to the resistance between the electrode and the electrolyte interface [38-39]. In Figure 3.12, an unconspicuous arc in the high–frequency region could be observed, implying the transition from frequency dependent diffusion resistance to capacitive charging behavior. In the low–frequency region, straight lines with the angle of 45° in the medium–to–low frequency region were seen, suggesting the existence of Warburg impedance in the system for a limiting diffusion process in the electrolyte [36]. It was obviously observed that the real–part impedance (Z') was increased with the increase of the MWCNTs content in the composite films. Such tendency could be related to the particulate structure and much
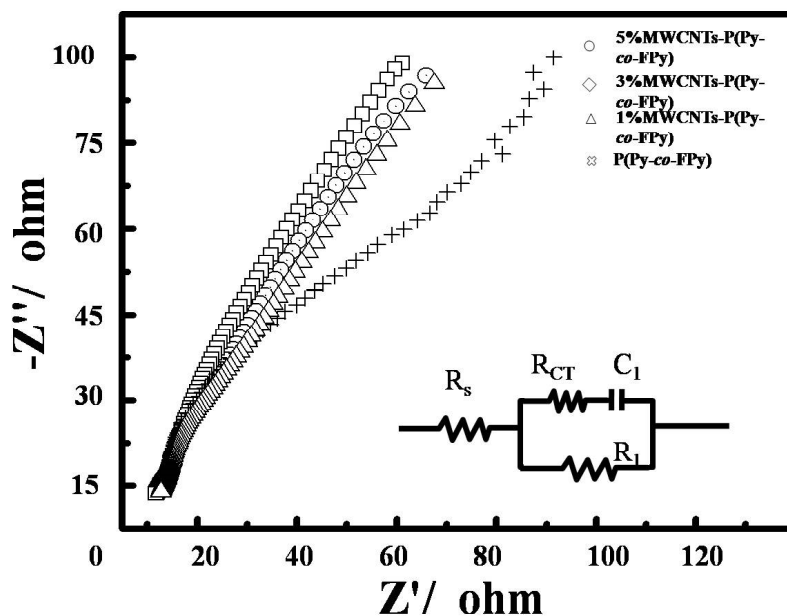
Figure 3.12 Complex plane impedance (Nyquist plot) of results of P(Py-*co*-FPy) and

P(Py-*co*-FPy) /MWCNTs composite films (Inset: the corresponding model and the

equivalent circuit for an ideal capacitors).

rough surface of the composite films, or the composites/electrolyte interface with the

increasing of MWCNTs content [40-41]. Compared with P(Py-*co*-FPy), the composite

films were favorable for charge transfer. This indicated that the composites had an

improved capacitive behavior and were suitable as a candidate for application on

electrode material of supercapacitor. Meanwhile, according to the analysis of the

equivalent circuit   by the chemical impedance analyzer, the solution resistance of each

film was obtain, it was changed from about 3.35 KΩ to 8.8 KΩ.

3.4 Conclusions

In conclusion, we have successfully prepared the composite films consisted of P (Py-*co*-FPy) and MWCNTs in a facile chemical oxidative polymerization in presence of TFA. The composite films could improve the interfacial interaction between the copolymer and the MWCNTs during the polymerization and enhance the P(Py-*co*-FPy) coating on the MWCNTs surface with relatively uniform to form a homogeneous particulate structure and rough surface. The obtained composite films exhibited better film–forming ability and higher conductivity due to the enhanced conjugated backbone and the interaction between P(Py-*co*-FPy) and MWCNTs. The performance of such composites films could be improved by increasing the addition mount of MWCNTs. Moreover, electrochemical measurement results suggested that the composite films had a good electrical capacitance property and higher specific capacitance than pure PPy and P(Py-*co*-FPy) without MWCNTs. The content of MWCNTs could influence the electrochemical performance of composite films by influencing the surface morphology and irregular aggregation particulate structure of composite films. All these results are expected to promote the understanding of such multilayer film for their potential applications.

3.5 References

[1]. Lua, X. F.; Zhanga, W. J.; Wanga, C.; Wen, T. C.; Wei, Y. One–dimensional conducting polymer nanocomposites: synthesis, properties and applications. *Prog. Polym. Sci*. **2011**, *36*, 671.

[2]. Hatchett, D. W.; Josowicz, M. Composites of intrinsically conducting polymers as sensing nanomaterials. *Chem. Rev*. **2008**, *108*, 746.

[3]. Wang, C. Y.; Zheng, W.; Yue, Z. L.; Too, CO.; Wallace, G. G. Buckled, stretchable polypyrrole electrodes for battery applications. *Adv. Mater*. **2011**, *23*, 3580.

[4]. Zhou, C. F.; Kumar, S.; Doyle, C. D.; Tour, J. M. Functionalized single wall carbon nanotubes treated with pyrrole for electrochemical supercapacitor membranes. *Chem. Mater.* **2005**, *17,* 1997.

[5]. Olsson, H.; Carlsson, D. O.; Nystrom, G.; Sjodin, M.; Nyholm, L.; Strømme, M. Influence of the cellulose substrate on the electrochemical properties of paper–based polypyrrole electrode materials. *J. Mater. Sci*. **2012**, *47*, 5317.

[6]. Liu, Y.; Wang, H.; Zhou, J.; Bian, L.; Zhu, E.; Hai, J.; Tang, J.; Tang, W. Graphene/polypyrrole intercalating nanocomposites as supercapacitors electrode. *Electrochimica Acta*. **2013**, *112*, 44.

[7]. Byrne, M. T.; Gun'ko, Y. K. Recent advances in research on carbon

nanotube–polymer composites. *Adv. Mater.* **2010**, *22*, 1672.

[8]. Hu, L. B.; Hecht, D. S.; Gruner, G. Carbon Nanotube Thin Films: fabrication, properties, and applications. *Chem. Rev.* **2010**, *110,* 5790.

[9]. Lu, W.; Dai, L. Nanocomposite electrodes for high–performance supercapacitors. *J. Phys. Chem. Lett.* **2011**, *2*, 655.

[10]. Dhibar, S.; Sahoo, S.; Das, C. K. Fabrication of transition–metal–doped polypyrrole/multiwalled carbon nanotubes nanocomposites for supercapacitor applications. *J. Appl. Polym. Sci*. **2013**, *130*, 554.

[11]. Chen, H.; Guo, L. H.; Ferhan, A R.; Kim, D. H. Multilayered polypyrrole–coated carbon nanotubes to improve functional stability and electrical properties of neural electrodes. *J. Phys. Chem. C* **2011**, *115*, 5492.

[12]. Lien, T. T. N.; Lam, T. D.; An, V. T. H.; Hoang, T. V.; Quang, D. T.; Khieu, D. Q.; Tsukahara, T.; Lee, Y. H.; Kim, J. S. Multi–wall carbon nanotubes (MWCNTs)–doped polypyrrole DNA biosensor for label–free detection of genetically modified organisms by QCM and EIS. *Talanta*. **2010**, *80*, 1164.

[13]. Zhang, D.; Dong, Q. Q.; Wang, X.; Yan, W.; Deng, W.; Shi, L. Y. Preparation of a three−dimensional ordered macroporous carbon nanotube/polypyrrole composite for supercapacitors and diffusion modeling. *J. Phys. Chem. C* **2013**, *117*, 20446.

[14]. Xu, G. H.; Wang, N.; Wei, J. Y.; Lv, L.; Zhang, J. N.; Chen, Z. M.; Xu, Q. Preparation of graphene oxide/polyaniline nanocomposite with assistance of supercritical carbon dioxide for supercapacitor electrodes. *Ind. Eng. Chem. Res.* **2012**, *51*, 14390.

[15]. Wang, J.; Dai, J.; Yarlagadda, T. Carbon nanotube conducting polymer composite nanowires. *Langmuir*. **2005**, *21*, 9.

[16]. Han, Y. Q.; Shen, M. X.; Lin, X. C.; Ding, B.; Zhang, L. G.; Tong, H.; Zhang, X. J. Ternary phase interfacial polymerization of polypyrrole/MWCNT nanocomposites with core–shell structure. *Synth. Met*. **2012**, *162*, 753.

[17]. Hughes, M.; Chen, G. Z.; Shaffer, M. S. P.; Fray, D. J.; Windle, A. H. Electrochemical capacitance of a nanoporous composite of carbon nanotubes and polypyrrole. *Chem. Mater*. **2002**, *14*, 1610.

[18]. Sun, X.; Xu, Y.; Wang, J.; Mao, S. The composite film of polypyrrole and functionalized multi–walled carbon nanotubes as an electrode material for supercapacitors. *Int. J. Electrochem. Sci*. **2012**, *7*, 3205.

[19]. Paul, S.; Choi, K. S.; Lee, D. J.; Sudhagar, P.; Kang, Y. S. Factors affecting the performance of supercapacitors assembled with polypyrrole/multi–walled carbon nanotube composite electrodes. *Electrochimica Acta*. **2012**, *78*, 649.

[20]. Wu, T. M.; Lin, S. H. Synthesis, characterization, and electrical properties of polypyrrole/multiwalled carbon nanotube composites. *J. Polym. Sci. Part A: Polm. Chem.* **2006**, *44*, 6449.

[21]. Grover, S.; Shekhar, S.; Sharma, R. K.; Singh, G. Multiwalled carbon nanotube supported polypyrrole manganeseoxide composite supercapacitor electrode: role of manganese oxidedispersion in performance evolution. *Electrochimica Acta.* **2014**, *116*, 137.

[22]. Fang, Y. P.; Liu, J. W.; Yu, J. D.; Wicksted, J. P.; Kalkan, K.; Topal, CO.; Flanders, B. N.; Wu, J.; Li, J. Self–supported supercapacitor membranes: polypyrrole–coated carbon nanotube networks enabled by pulsed electrodeposition. *J. Power. Sources.* **2010**, *195*, 674.

[23]. Hoshina, Y.; Kabayashi, T. Electrically conductive films made of pyrrole–formyl pyrrole by straightforward chemical copolymerization. *Ind. Eng. Chem. Res.* **2012**, *51*, 5961.

[24]. Soon. Y. L, Wim. T., Darren. W. Electrochemical capacitance of nanocomposite polypyrrole/cellulose films. *J. Phys. Chem. C* **2010**, *114*, 17926.

[25]. Wang, K.; Hoshina, Y.; Cao, Y.; Kabayashi, T. Novel metal−like luster conductive Film made of pyrrole and furfural in straightforward chemical copolymerization. *Ind.*

Eng. Chem. Res. **2013**, *52,* 2762.

[26]. Jeon, I. Y.; Choi, H. J.; Tan, L. S.; Baek, J. B. Nanocomposite prepared from in Situ grafting of polypyrrole to aminobenzoyl−functionalized multiwalled carbon nanotube and its electrochemical properties. *J. Polym. Sci. Part A: Polm. Chem.* **2011**, *49*, 2529.

[27]. Zhang, X. T.; Lu, Z.; Wen, M. T.; Liang, H.; Zhang, J.; Liu, Z. F. Single–walled carbon nanotube–based coaxial nanowires: synthesis, characterization, and electrical properties. *J. Phys. Chem. B* **2005**, *109*, 1101.

[28]. Tian, B.; Zerbi, G. Lattice dynamics and vibrational spectra of pristine and doped polypyrrole: effective conjugation coordinate. *J. Chem. Phys.* **1990**, *92*, 3892.

[29]. Chen, H.; Muthuraman, H.; Stokes, P., Zou, J.; Liu, X.; Wang, J.; Huo, Q.; Khondaker, S.; Zhai, L. Dispersion of carbon nanotubes and polymer nanocomposite fabrication using trifluoroacetic acid as a co-solvent. *Nanotechnology*, **2007**, *18*, 415606. doi:10.1088/0957-4484/18/41/415606

[30]. Sahoo, N. G.; Rana, S.; Cho, G. W.; Li, L.; Chan, H. S. Polymer nanocomposites based on functionalized carbon nanotubes. *Prog. Polym. Sci.* **2010**, *35*, 837.

[31]. Yu, Y.; Ouyang, C.; Gao, Y.; Si, Z.; Chen, W.; Wang, Z.; Xue, J. Synthesis and characterization of carbon nanotube/polypyrrole core–shell nanocomposites via in situ

inverse microemulsion *J. Polym. Sci. Part A: Polm. Chem.* **2005**, *43*, 6105.

[32]. Tagaya, M.; Hoshina, Y.; Ogawab, N.; Takeguchic, M.; Kobayashia, T. Nanostructural analysis of self–standing pyrrole/2–formylpyrrole Copolymer. *Micron.* **2013**, *46*, 22.

[33]. Wang, Y. G.; Li, H. Q.; Xia, Y. Y. Ordered whisker like polyaniline grown on the surface of mesoporous carbon and its electrochemical capacitance performance. *Adv. Mater.* **2006**, *18*, 2619.

[34]. Li, H.; Wang, J.; Chu, Q.; Wang, Z.; Zhang, F.; Wang, S. Theoretical and experimental specific capacitance of polyaniline in sulfuric acid. *J. Power. Sources.* **2009**, *190*, 578.

[35]. Wang, C. C.; Hu, C. C. Electrochemical catalytic modification of activated carbon fabrics by ruthenium chloride for supercapacitors. *Carbon.* **2005**, *43*, 1926.

[36]. Yang, C.; Liu, P.; Wang, T. Well–defined core–shell carbon black/polypyrrole nanocomposites for electrochemical energy storage. *ACS Appl. Mater. Interfaces.* **2011**, *3*, 1109.

[37]. Frackowiak, E.; Khomenko, V.; Jurewicz, K.; Lota, K. Supercapacitors based on conducting polymers/nanotubes composites. *J. Power. sources.* **2006**, *153*, 413.

[38]. Li, X.; Rong, J.; Wei, B. Electrochemical behavior of single–walled carbon nanotube supercapacitors under compressive stress. *ACS Nano* **2010**, *4*, 6039.

[39]. Davies , A.; Audette, P.; Farrow, B.; Hassan, F.; Chen, Z.; Choi, J. Y.; and Yu, A. P. Graphene–based flexible supercapacitors: pulse–electropolymerization of polypyrrole on free–standing graphene films. *J. Phys. Chem. C* **2011**, *115*, 17612.

[40]. Marchesi, L. F. Q. P.; Simoes, F. R., Pocrifka, L. A., Pereira, E. C. Investigation of polypyrrole degradation using electrochemical impedance spectroscopy. *J. Phys. Chem. B* **2011**, 115, 9570.

[41]. Garcia–Belmonte, G.; Bisquert, J. Impedance analysis of galvanostatically synthesized polypyrrole films: Correlation of ionic diffusion and capacitance parameters with the electrode morphology. *Electrochim Acta* **2002**, *47*, 4263.

Chapter 4

Electrochemical Capacitance of Poly (Pyrrole–*co*–Formylpyrrole) / Sulfonated Polystyrene Layer–by–Layer Assembled Multilayer Films

ABSTRACT: Poly (pyrrole–*co*–formylpyrrole), P(Py–*co*–FPy) was prepared on poly (4–styrenesulfonate acid) (PSS) using layer–by–layer (LBL) self–assembly process in the presence of TFA through straightforward chemical polymerization. The P(Py–*co*–FPy) and PSS multilayer contained homogeneous particulate surfaces with a hierarchical porous structure, depending on the number of layers and the PSS concentration. The layer cycles gave rise to increased electrical conductivity from 2.8×10^{-4} S/cm at 2 layers to 3.2×10^{-3} S/cm at 10 layers, implying the benefit of the doping effect of the sulfonic group on the improvement of electrical conductivity for multilayer films. The electrostatic interaction between the P(Py–*co*–FPy) and the PSS layer was confirmed from UV–visible spectra and enhanced by the number of layers and PSS concentration. Cyclic voltammetry and electrochemical impedance measurements showed that the electrochemical capacitance of those multilayer films is influenced by the increase of the number of layers and the PSS concentration, suggesting that the multilayer film morphology affects the electrochemical behavior.

4.1 Introduction

Conducting polymers such as polyaniline (PANI), polypyrrole (PPy), and their derivatives have attracted attention recently for application to organic light–emitting diodes, sensors, and energy storage devices including batteries and electrochemical supercapacitors [1–4]. This rising interest derives from their characteristics of higher conductivity, better stability, and cost effectiveness on conductive polymers [5]. Nevertheless, various shortcomings such as poor physical and mechanical properties for film preparation have been found. These characteristics greatly limit conducting polymers' application. When conductive polymer films fabricated by electrochemical polymerization on an electrode surface, it is usually shown high electrochemical behavior in contrast with weaker physical and mechanical performance [6–7]. For chemical polymerization, the film fabrication presents difficulties because of the obtained powdery conductive polymer. Many efforts have been done to synthesis the conductive polymer films through a facile chemical polymerization, such as the preparation of the cellulose or grapheme sheet and conductive polymer composite films [8–9]. On the other hand, layer–by–layer (LBL) self–assembly processes using different polymers was developed based on electrostatic interaction [10], hydrogen bonding [11], and covalent bonding [12]. Originally developed by Decher et al for polyelectrolytes,

LBL self–assembly was later extended by Rubner et al for use with doped conjugated polymers [13–14]. Such processing promotes the understanding of surface morphology formation, electrostatic effects, and the kinetics of deposition during LBL layer processing [15–16]. Moreover, molecular–level processing of conductivity polymers using LBL methods is known to be applicable for LBL multilayers in microelectronics such as optoelectronics and energy storage devices [17–18]. Among conducting polymers, a polythiophene derivative, poly (3, 4–ethylenedioxythiophene) and poly (styrene sulfonic acid) LBL self–assembly films have been widely investigated and used [19]. Another extensive study of PPy film for electronic materials has received considerable interest [20]. Nevertheless, little is known about chemically polymerized PPy films produced using LBL technology for basic and applied research. As reported from our previous research, a simple method involving economical and stable processes using chemical copolymerization of pyrrole (Py) and formyl pyrrole (FPy) was developed to alleviate difficulties arising from the use of PPy. Such self–standing Py/FPy copolymer films were prepared (Scheme 3.1) with well–defined nanostructures that showed a metal–like luster greenish color and good film formation with excellent mechanical properties and improved conjugated structure, which benefited by the formation of methine group from FPy in the copolymers [21–22]. For much better

development of such films, the LBL process was applied for fabrication of P(Py–*co*–FPy)/PSS multilayer films for which PSS layers would act as a dopant layer.

In this study, the fabrication and characterization of the P(Py–*co*–FPy)/PSS multilayer films were investigated to elucidate electrostatic interactions between the copolymer layers and the PSS layers. The relation between morphological characteristics and electrochemical behaviors of the P(Py–*co*–FPy)/PSS multilayer film was studied to assess the degree to which electrochemical behavior is influenced by the increase of the number of layers or the concentration of PSS and to enrich the knowledge of potential applications for capacitor electrode materials for these novel multilayer films.

4.2 Experimental Section

4.2.1 Reagents

Pyrrole (Py) was purchased from Tokyo Chemical Industry Co. Ltd. and was distilled under reduced pressure before use. Pyrrole–2–carboxaldehyde (FPy) and tetrabutylammonium perchlorate (TBAP) were purchased from Tokyo Chemical Industry Co. Ltd. and were used with no further purification. Trifluoroacetic acid (TFA), iodine (I_2), ammonia aqueous solution (28%), and hydrogen peroxide aqueous solution

(35% of H_2O_2) were obtained from Nacalai Tesque Inc. Poly(sodium 4–styrenesulfonate) (PSS, 70000 Mw), *N*–2–aminoethyl–3–aminopropyltrimethylvinylsilane (TMS) and indium tin oxide (ITO, 60 Ω/square) coated glass were purchased from Aldrich Chemical Co. Inc. Other reagents were purchased and used as received.

4.2.2 Preparation of LBL P(Py–*co*–FPy) / PSS films

   Indium tin oxide (ITO) glass substrates were pretreated using a reported procedure [23–24] to produce a surface with a covalently bonded amine group, as shown in Figure 1. The pretreatment of the glass substrates to produce a positively charged surface resulted from the introduction of –NH_2 group for interaction with PSS. First, a glass slide was treated for 2 h with sulfuric acid and hydrogen peroxide mixture solution (H_2SO_4:H_2O_2=7:3). It was subsequently treated with diluted ammonia aqueous solution/hydrogen peroxide mixture solution (NH_3:H_2O_2=1:1) for another 2 h to create a hydrophilic surface. The treated substrates were washed with deionized water and dried in vacuum. Then, the hydrophilic substrate was washed in sequence carefully with ethanol, methanol/toluene mixture solution (1:1), and toluene. Finally, the substrate was immersed in a TMS toluene solution (5 wt %) for 24 h to create a positively charged surface. The treated substrates were washed with deionized water before the deposition

of electrostatic self–assembled LBL films. Before measuring the electrochemical properties, the ITO glass was washed carefully with a methanol/toluene mixture solution and was then immersed in a diluted ammonia aqueous solution/hydrogen peroxide mixture solution (NH_3:H_2O_2=1:1) for 2 h to create a hydrophilic surface. The positively charged surface on the pretreated ITO glass plate was created similarly to the glass treatment.

Then, the LBL layers were fabricated on the pretreated substrate as shown in Figure 4.1, which presented a schematic drawing of the LBL films of P(Py–*co*–FPy)/PSS. To enhance the doping effect of the conductive polymer layer by PSS, the sodium salt of PSS aqueous solution was converted to –SO_3H in a sealed semipermeable membrane with a dialyzed process for 7 days. Ion–exchanged PSS was used for the following experiment for LBL film fabrication.

The copolymer layer was fabricated using Py (200 mg, 3 mmol) and FPy (286 mg, 3 mmol), which were dissolved in 50 ml of acetonitrile (CH_3CN) in a sample tube (20 ml). Then the solution containing TFA acid catalyst (13 mmol) in 2 ml CH_3CN was added to the monomer solution at room temperature. Results showed that the solvent color changed gradually from transparent brown to yellowish red. After 15 min, the mixed solution of Py and FPy was filtered using a filter having 0.45 μm pore size. It was then
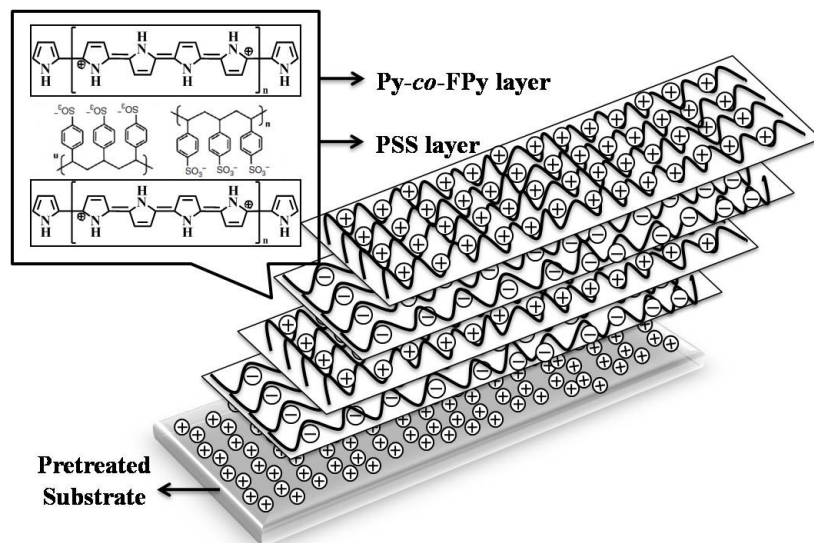
Figure 4.1 Schematic of electrostatic self–assembled LBL films of P(Py–*co*–FPy)

copolymer with PSS.

polymerized with *in situ* polymerization. At this condition, simultaneously, the

positively charged substrate was dipped into acidic PSS solution for 10 min to obtain a

negatively charged surface. Various concentrations of the dipping solutions of acidic

PSS solution were tested between 2, 4, and 6 mg/ml for each concentration. The first

PSS layer was washed carefully using deionized water and was then dried. Then, the

PSS coated substrate was dipped into P(Py–*co*–FPy) reacting solution for 5 min to

obtain the second PPy layer and dried. The processes of washing and drying were

repeated similarly after LBL formation in each deposition cycle. After several

repetitions, the multilayer film was dried in vacuum for future measurements.

4.2.3 Measurements

FT–IR spectra were recorded on an IR spectrophotometer (Prestige; Shimadzu Corp.) under the reflection mode. The UV–visible absorption spectra of the P(Py–*co*–FPy)/PSS multilayer films on the quartz glass substrate were measured using a UV–vis–NIR spectrophotometer (V–570; Jasco Corp., Tokyo, Japan) under transmittance mode. In SEM measurements, the films' surface morphology was observed after the film coated with 5 nm thickness of Au. Then the surface and cross–section of the films were observed (JSM–7000F; JEOL Ltd., Japan) at 15 keV. For surface analysis of the films, scanning probe microscopy (SPM, Nanocute; SII Investments, Inc., Japan) was applied in a 500×500 nm area of the film to produce AFM images. A silicon probe mounted on a cantilever (Micro cantilever Si–DF40P2; SII Investments Inc., Japan) was used. The surface roughness was calculated using root mean square values (RMS) in the Z–range images. Rrms was calculated according to the following equcation:

$$\mathrm{R}_{rms} = \sqrt{\frac{\sum_{n=1}^{n}(h(x_i) - h)^2}{n}}$$

Here, n was the measurement points; $h(x_i)$ was the height of the point x_i; h was the average height. To measure the electrical conductivity, the resultant P(Py–*co*–FPy)/PSS multilayer film was put in a sealed vessel containing a small amount of I_2 for chemical doping during 24 h. It was determined at room temperature using a typical four–point method (Roresta–GP MCP–T610; Mitsubishi Chemical Analytec Co. Ltd., Japan). Cyclic voltammetry (CV) of multilayer films with an ITO–coated glass substrate was recorded in a 0.1 M tetrabutylammonium perruthenate (TBAP) / acetonitrile supporting electrolyte solution (HSV–110; Hokuto Denko Corp., Japan). Voltammograms quoted against a Ag/Ag$^+$ reference electrode were obtained at a scanning rate of 1 mV s^{-1} and

scanning range of –1.5 V to 1.5 V. Then, electrochemical impedance spectroscopy (EIS) was performed over a range of frequencies (10 mHz – 100 kHz) with a signal amplitude of 5 mV in 0.1 M TBAP / acetonitrile supporting electrolyte solution using an impedance analyzer in the a Cole-Cole plot analytical model to obtain the Nyquist diagrams (IM3590; Hioki Co. Ltd., Japan).

4.3 Results and Discussions

4.3.1 Fabrication of the P(Py–*co*–FPy)/PSS multilayer films

   To confirm the fabrication of the multilayer of the P(Py–*co*–FPy)/PSS, FT–IR spectra of each layer were measured using the reflection model (Figure 4.2). Each P(Py–*co*–FPy) layer exhibited similar characteristic peaks, but each was quite different from PSS layers. The inconspicuous peaks of N–H stretching vibrations of at 3380 cm^{-1} are shown in line (a). Each Py–*co*–FPy layer shows peaks observed at 1258 cm^{-1} (line d) assigned to the –C=C– stretching attribute to the methine group [21]. The peaks appeared at 1008 cm^{-1} of C–H out–of–plane deformation vibration from the methine group polymerized between Py and FPy monomer. In addition, the peak at 1626 and 1538 cm^{-1} (line b, c)

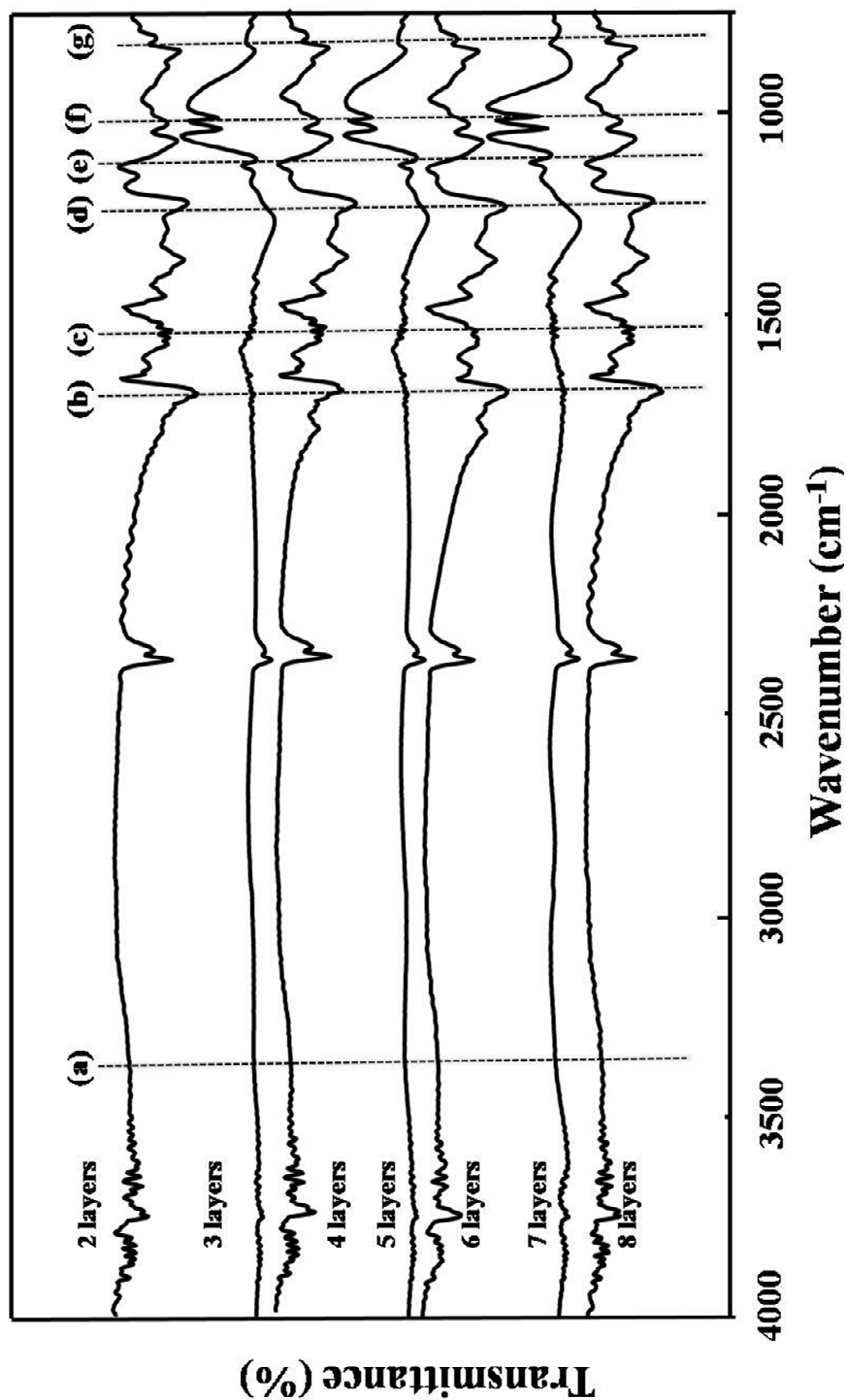**Figure 4.2** Reflection FT–IR spectra of the different P(Py–*co*–FPy) / PSS multilayer films.

from the C=C double bond stretching of the aromatic ring originates from the Py conjugated backbone [25]. For the PSS layers, the peak of the phenyl ring stretching appeared at 829 cm^{-1} only (line g), originating from the formation of PSS layers. The characteristic peaks of the sulfonic group stretching at about 1134 and 1026 cm^{-1} (lines e, f) were observed from the 3, 5, and 7 layers of PSS layer [26]. These indicate that the LBL multilayer film formation was attained.

Furthermore, absorption spectroscopy of the LBL film was conducted. UV–visible (UV–Vis) spectroscopy was chosen to analyze the optical bands of the chromophore species of each multilayer film. Figure 4.3a depicts UV–Vis absorption spectra of the characteristic absorption peak of PSS layers for the wavelength band at 227 nm. With increasing deposition cycles from 1 to 7 layers, the band intensity was increased. In contrast, the UV–Vis absorption spectra of the LBL films in Figure 4.3b are shown for the P(Py–*co*–FPy) layer deposited on the top surface. The spectra showed a broad absorption peak at 496 nm with conditions similar to typical PPy segments, which indicates that the characteristic absorption band of the π–π* transition of the P(Py–*co*–FPy) is presented in the film [21]. In addition, weaker and broader absorption appearing near 750–1500 nm was observed in the near infrared region, which strongly suggests that the bipolaron state of copolymer segment was formed in the LBL process
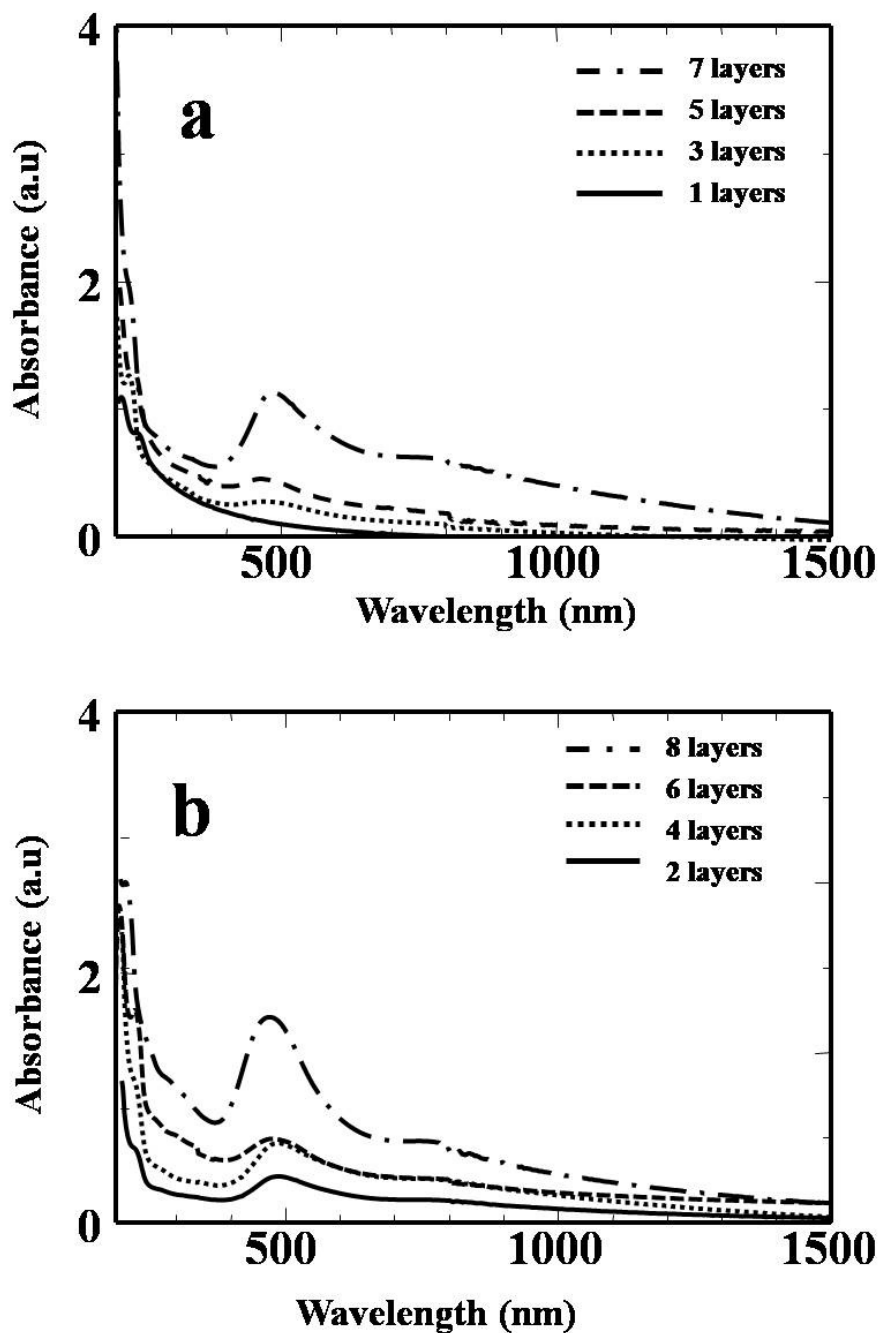
Figure 4.3 UV–Vis absorption spectra of the P(Py–*co*–FPy) / PSS multilayer films: (a) PSS layers of multilayer films prepared with the PSS concentration of 2mg/ml; (b) P(Py–*co*–FPy) layers of multilayer films prepared with the PSS concentration of 2mg/ml.
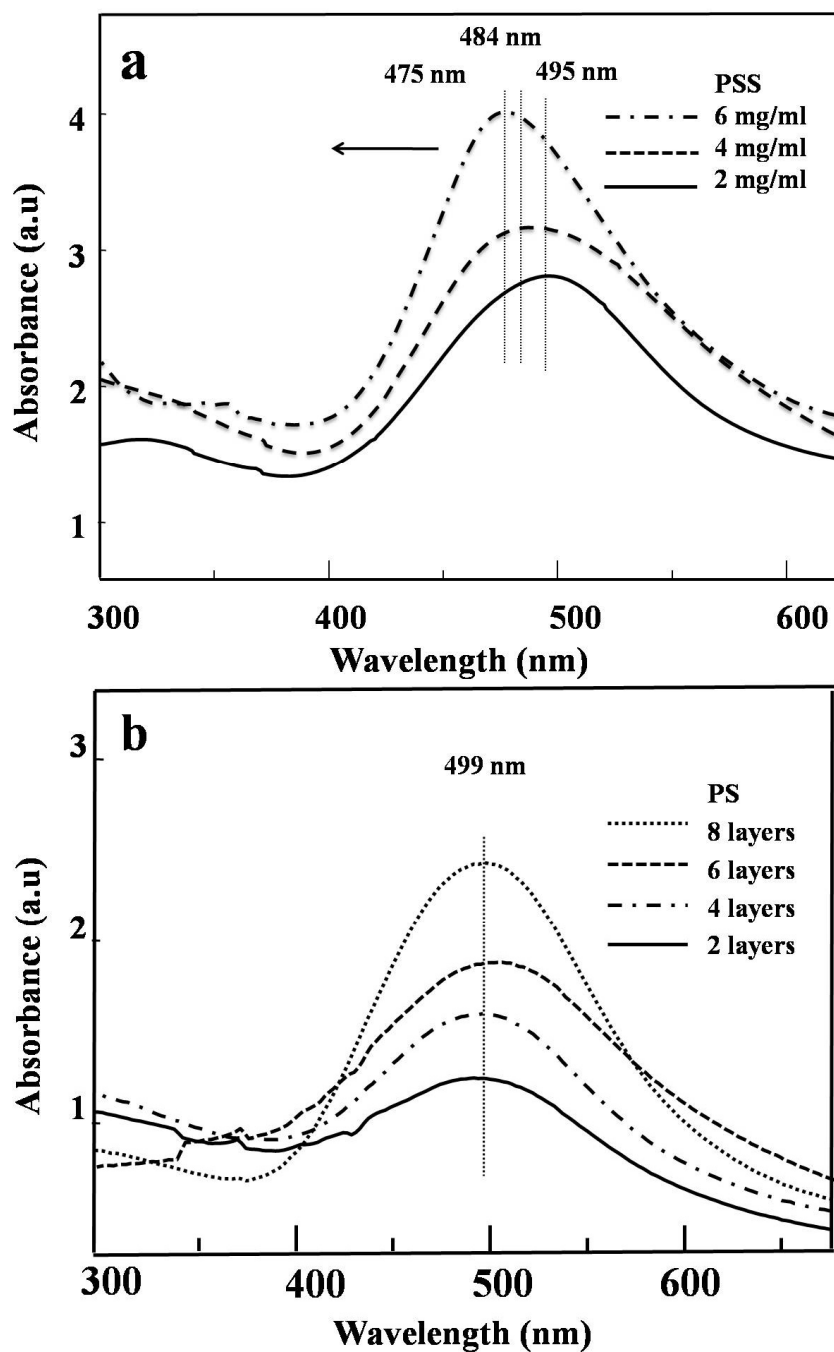
Figure 4.4 UV–Vis absorption spectra of (a) the 8th P(Py–*co*–FPy) / PSS layer of the multilayer films prepared with PSS concentration of 2, 4, 6 mg/ml; (b) the P(Py–*co*–FPy) / PS multilayer films with the PS concentration of 6mg/ml.

because of the introduction of the FPy monomer causing the formation of the conjugated methine structure in the backbone. The UV absorbance intensity increased with the increasing number of the P(Py–*co*–FPy) layers. Furthermore, UV–Vis absorption spectra were measured at different PSS amounts to examine the π–π^* band region (Figure 4.4a). With the increase of the PSS concentration from 2 to 6 mg/ml, the characteristic absorption band of PPy was shifted to the shorter wavelength side from 484 nm to 475 nm. This fact might be attributed to the electrostatic interaction between the PSS layer and Py–*co*–FPy layer as well as the doping effect with the sulfonic group of the PSS. In addition, the multilayer improved the degree of electron delocalization of the P(Py–*co*–FPy) chains. To verify this, a comparison was made in the UV–vis spectra of the multilayer films with the polystyrene (PS) concentration of 6 mg/ml (Figure 4.4b). Results show that the π–π^* transition of PPy was observed at 499 nm, but the band peak was not shifted as much as at the PSS having a sulfonic group. These results corresponded well with the result shown for the existence of electrostatic interaction between the P(Py–*co*–FPy) and PSS layers [27–29]. Therefore, the doping effect of the sulfonic group of PSS implies a benefit of the improvement of electrical conductivity for multilayer films.

Figure 4.5 portrays the surface morphology of the P(Py–*co*–FPy)/PSS multilayer films for 1 (a), 3 (b), and 5 (c) layer of PSS layers and 2 (d), 4 (e), 6 (f) layer of PPy layers on glass substrates. All PSS layers had an aggregated structure on the surfaces. With the increased number of layers, the top surface of PSS layer became much rougher. The area of the particulate aggregate structure was increased. In contrast, after deposition of the P(Py–*co*–FPy) on the PSS layer, a relatively smooth surface was observed, benefited by the formation of methine group from FPy in the copolymers similar like we reported [21, 30]. With the increase of the layer number, the top surface of the P(Py–*co*–FPy) layer became rougher gradually and the particulate aggregate structure appeared under the influence of PSS layers. In Figure 4.6, cross–sectional SEM images of multilayer films are shown. The multilayer film thickness increased from 3 μm to 12 μm when the number of layers was increased from 2 to 7. From the LBL film thickness, it was concluded that the formation of LBL films was partly depended on physical adsorption due to the excellent mechanical properties of the self–standing copolymer films except the electrostatic self–assembly. The cross–section of the films shows hierarchical phenomena for the respective layers, especially in Figures 4.6b, c and f. Actually, such a hierarchical porous structure provided great benefits for applications in electrode materials, as discussed hereinafter [31].
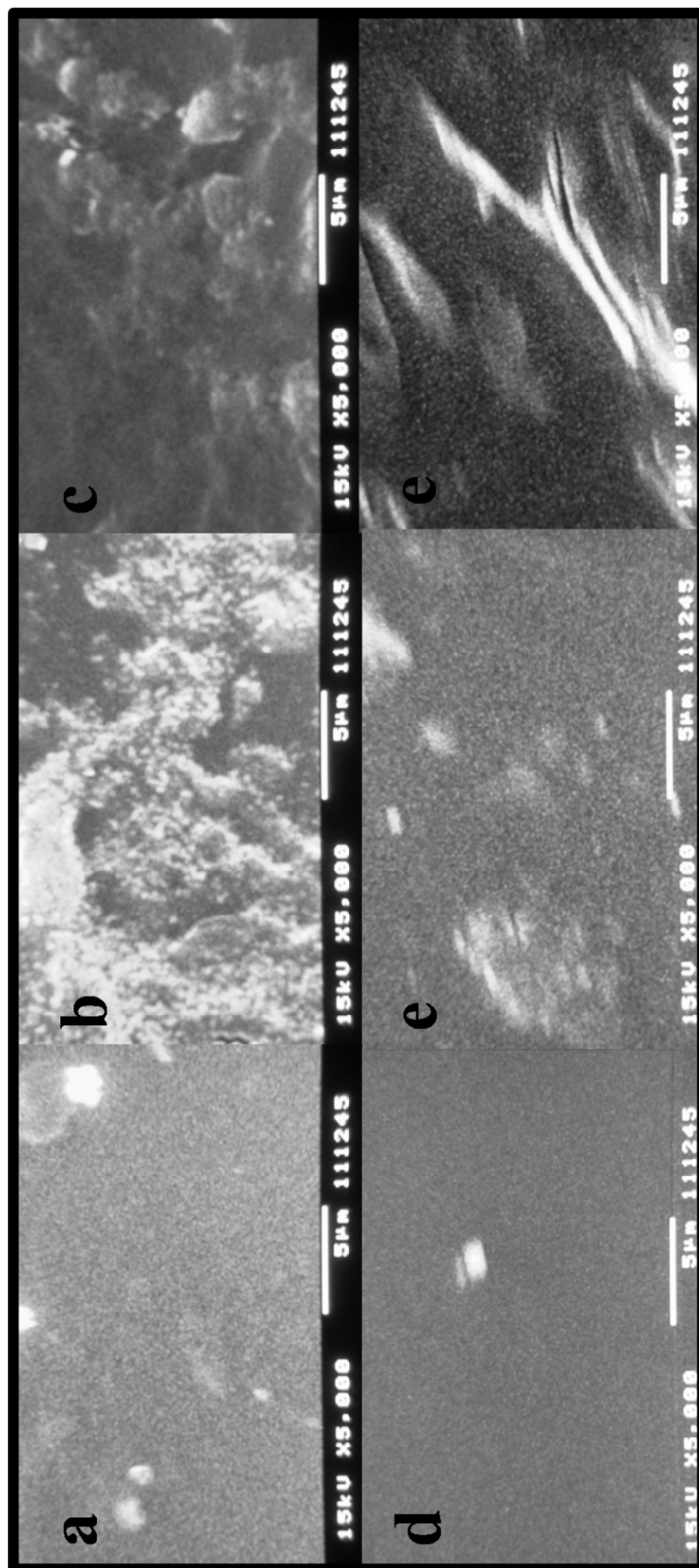
Figure 4.5 Surface SEM images of P(Py–*co*–FPy) / PSS multilayer films for 1 (a), 3(b), 5(c) r of PSS layers and 2 (d),4 (e),6 (f) of PPy layers.
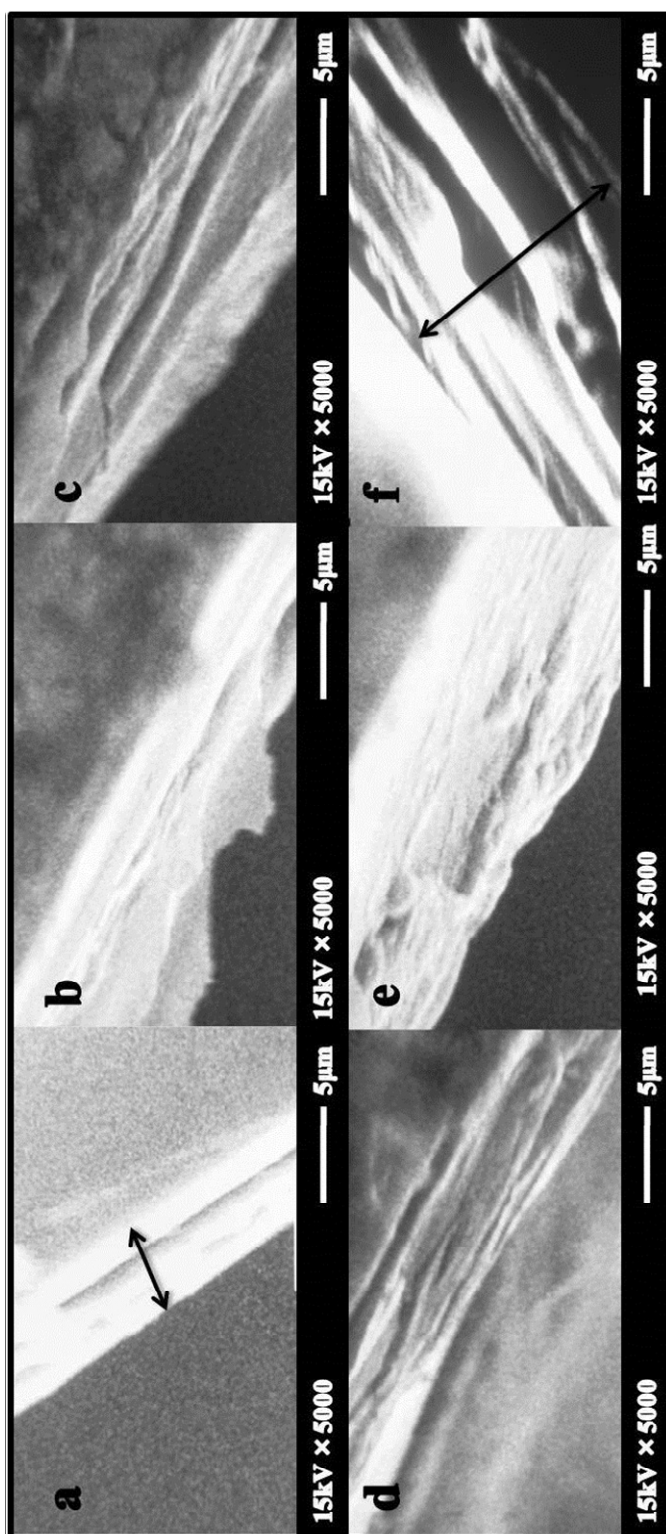
Figure 4.6 Cross–sectional SEM images of multilayer thin films P(Py–*co*–FPy) / PSS multilayer films for 2(a),3(b),4(c), and 5(d),6(e),7(f) layers.

To calculate the multilayer film surface roughness, AFM topographic and phase–shift images were applied. Figure 4.7 portrays the surface morphology of the P(Py–*co*–FPy) layer fabricated on the concentration of 2 mg/ml PSS on glass substrate for different numbers of layers. The AFM images suggest that the top P(Py–*co*–FPy) layer showed the presence of homogeneous particulate surfaces, exhibiting a dense morphology with nanoscale on the surface at the top (first) PPy layer. When the layer cycles were increased from 2 to 4 or 6, the roughness parameter values (R_{rms}) on the top P(Py–*co*–FPy) layer became 2.3 ± 0.1 nm, 2.5 ± 0.1 nm, and 2.4 ± 0.2 nm, respectively. Those data demonstrate that the value of R_{rms} had no great change with the increase of the deposited layers. In case of second PPy layer, the topolopical and phase imaging indicated that the P(Py–*co*–FPy) layers presented only one phase at the P(Py–*co*–FPy) layers surface. However, with the deposition of layers, the fourth and sixth P(Py–*co*–FPy) layers showed enhanced particulate structure on the surface, as shown in Figure 4.7 b and c. In phase imaging, the delay of phase was related to the local viscoelasticity and the hardness on the surface of the sample. Li *et al.* reported that the influence of the wedge cavity and tip slip artificial effect on the particles and the concave valley between the particles of the sample surface could make the similarly contour feature for the AFM topological and phase images [32]. It can be compared the

maximum and the minimum phase shift to evaluate the physical properties on the surface. The second P(Py-*co*-FPy) layer showed a uniform surface morphology and homogeneous viscoelastic behavior(Figure 4.7d). With the increase of the deposition layer of P(Py-*co*-FPy), the phase shift increased and suggested the uneven deposition on the surface leading to uniformly viscoelasticity (Figure 4.7e). However, all of the phase imaging of the PSS layer showed a larger difference value between the maximum and the minimum phase shift revealing the rough distribution of particles on the PSS layers (Figure 4.8d, e, f). Therefore, the top layer constructed with PSS on the P(Py–*co*–FPy) layers had a much rougher surface with porous morphology at a certain scale with the R_{rms} on the 3, 5, and 7 layers of 8.4 ± 0.1 nm, 17.0 ± 0.2 nm, and 14.1 ± 0.1 nm, as presented in Figure 4.8. However, the P(Py–*co*–FPy) layers were between about 2–4 nm in the R_{rms}. Figure 4.9 shows the obtained AFM parameters of such deposited multilayer films, including the surface R_{rms} and the average surface area of the nano–particulates. The values of R_{rms} on each top surface were increased or decreased regularly depending on the deposited P(Py–*co*–FPy) or PSS layer during the LBL processes. In contrast, the average surface area of the nano–particulates for each top layer shows no large changes with the increase of deposited processes, suggesting that similar surface morphology of each layer is fabricated independently during the deposition process.
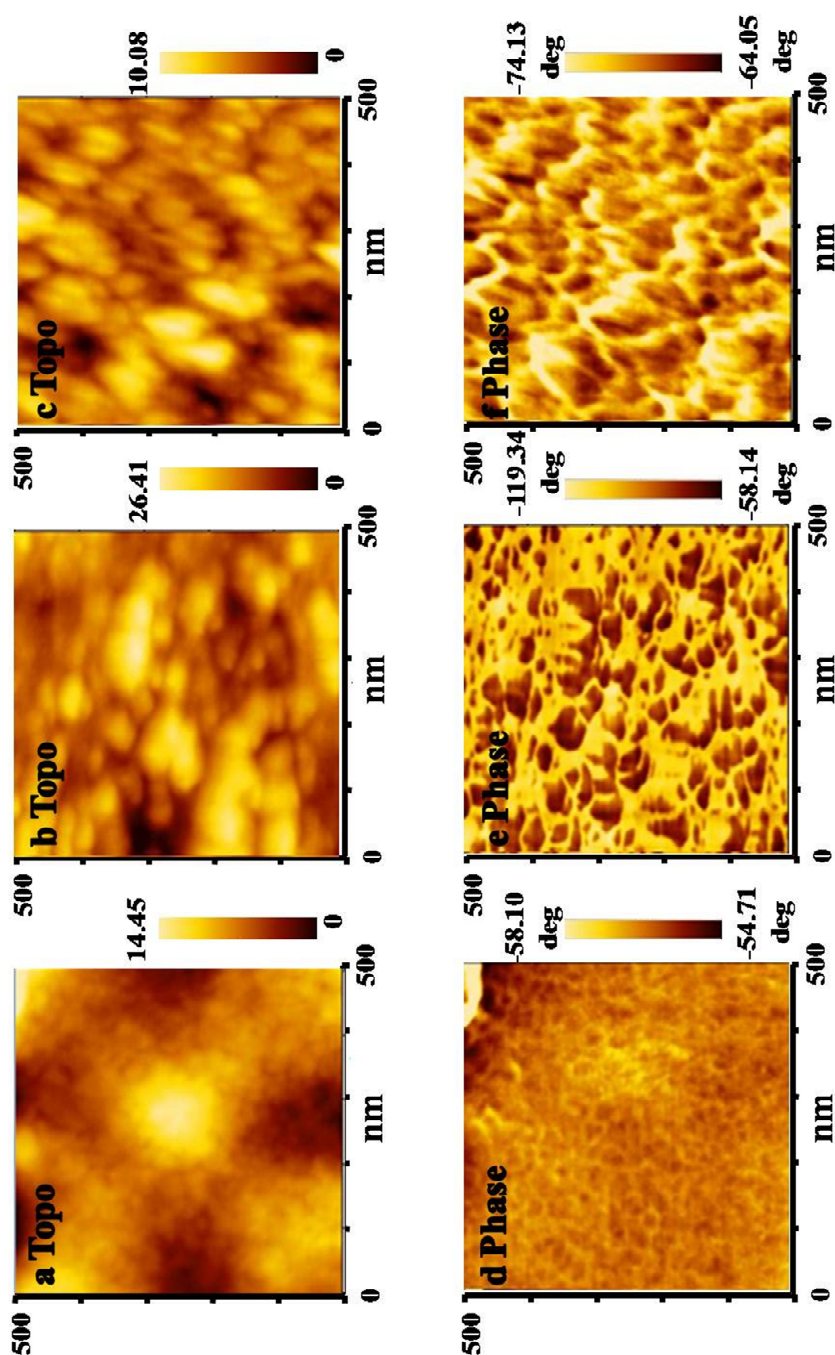
Figure 4.7 AFM topological and phase images of the multilayer films surfaces in the 2

(a, d), 4 (b, e), 6 (c, f) of P(Py–*co*–FPy) layers.
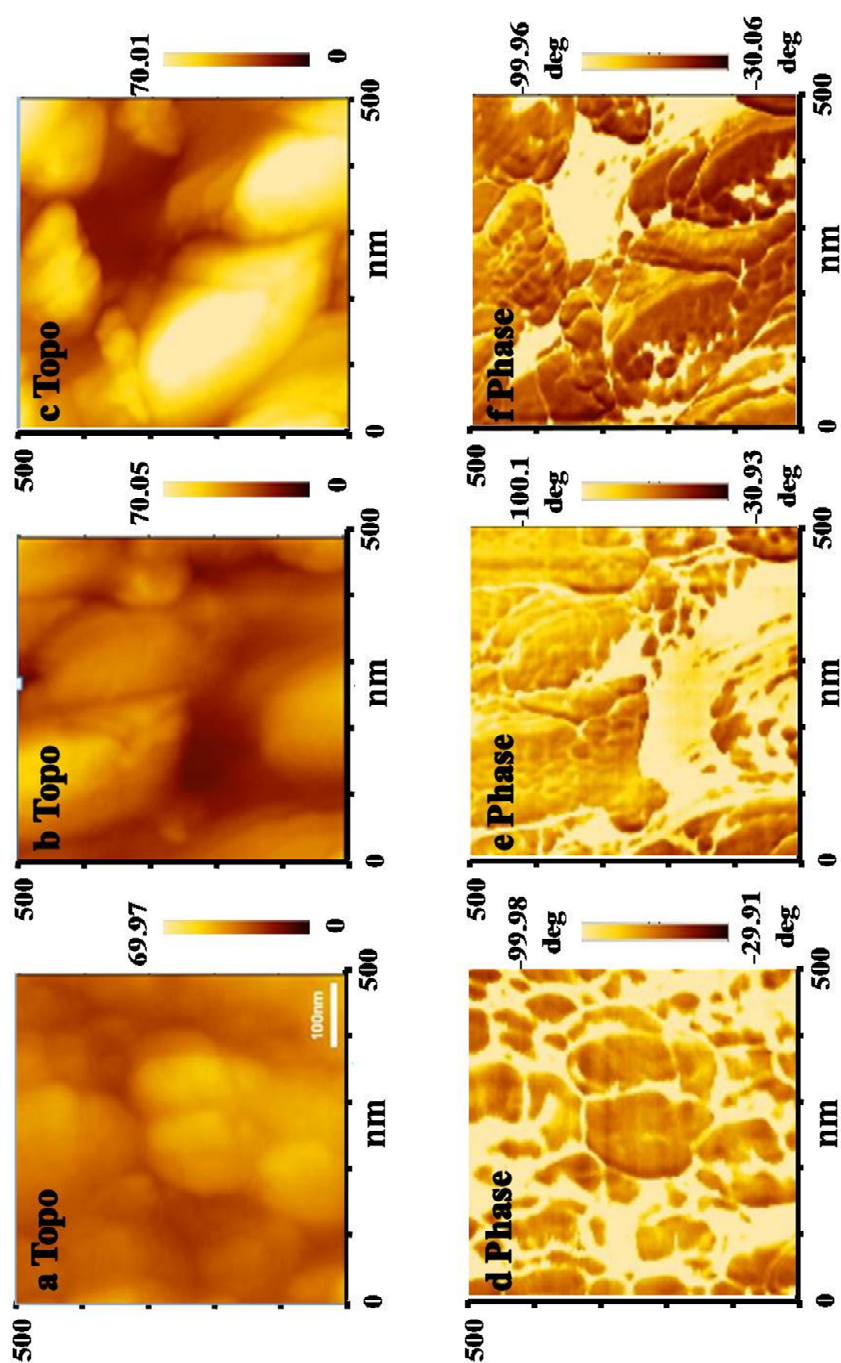
Figure 4. 8 AFM topological and phase images of the multilayer films surfaces in the 3

(a, d), 5 (b, e), 7 (c, f) of PSS layers.
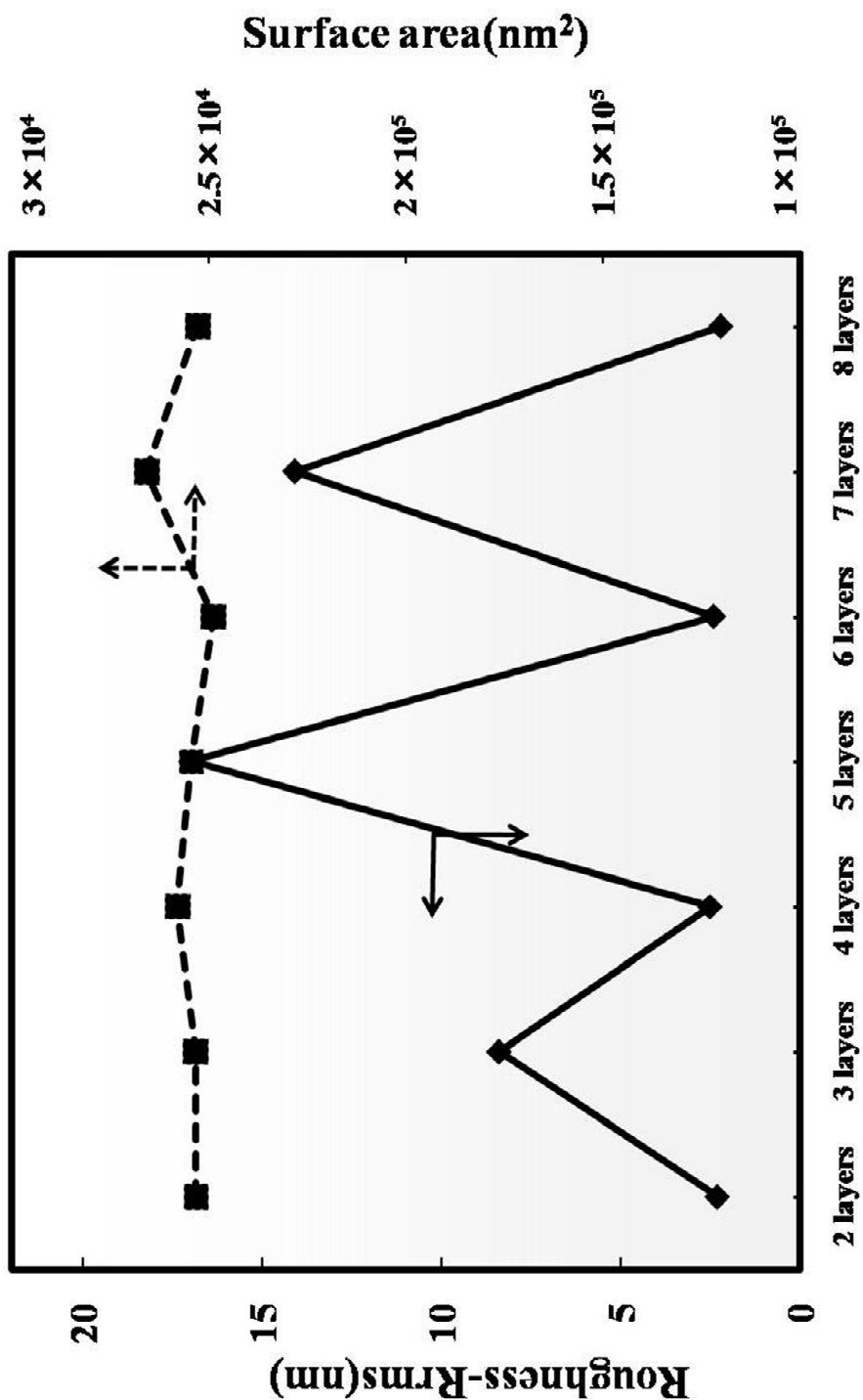
Figure 4.9 AFM parameters of roughness and surface area for each deposited of the

P(Py–*co*–FPy) / PSS multilayer films.

4.3.2 Electrochemical properties of the LBL multilayer films

    The effect of the LBL multilayer on the electrochemical behavior of the P(Py–*co*–FPy)/PSS films was assessed. For the LBL multilayer films at each deposition cycle, Figure 4.10 presents results of the electrical conductivity of the films measured simply by contacting five points after the doped I_2. There, the P(Py–*co*–FPy)/PS multilayer films were also prepared as comparative references. As shown there, reasonable conductivity was observed in the P(Py–*co*–FPy)/PSS in the 10^{-3} S/cm region. For P(Py–*co*–FPy)/PSS multilayer films, the values of the electrical conductivity increased markedly with the increase of the deposited cycle. Compared with the reference in the P(Py–*co*–FPy)/PS multilayer films, the P(Py–*co*–FPy)/PSS films showed better conductivity, which indicated a dopant effect of the sulfonic group of PSS attributable to electrostatic interaction between the PSS and P(Py–*co*–FPy) layers.

    In addition, the electroactivity of the multilayer was characterized using cyclic voltammetry (CV) recorded in 0.1M TBAP /acetonitrile supporting electrolytes with a scan rate at 1 mV/s. Figure 4.11 presents the respective CV profiles of P(Py–*co*–FPy)/PSS multilayer films in addition to 2 (a), 4 (b), and 6 mg/ml (c) of the PSS. These CV profiles present a multi–peaked cycle within the scan range. Obvious oxidation peaks at around 1.1 V and reduction peaks at around –0.4 V were observed in
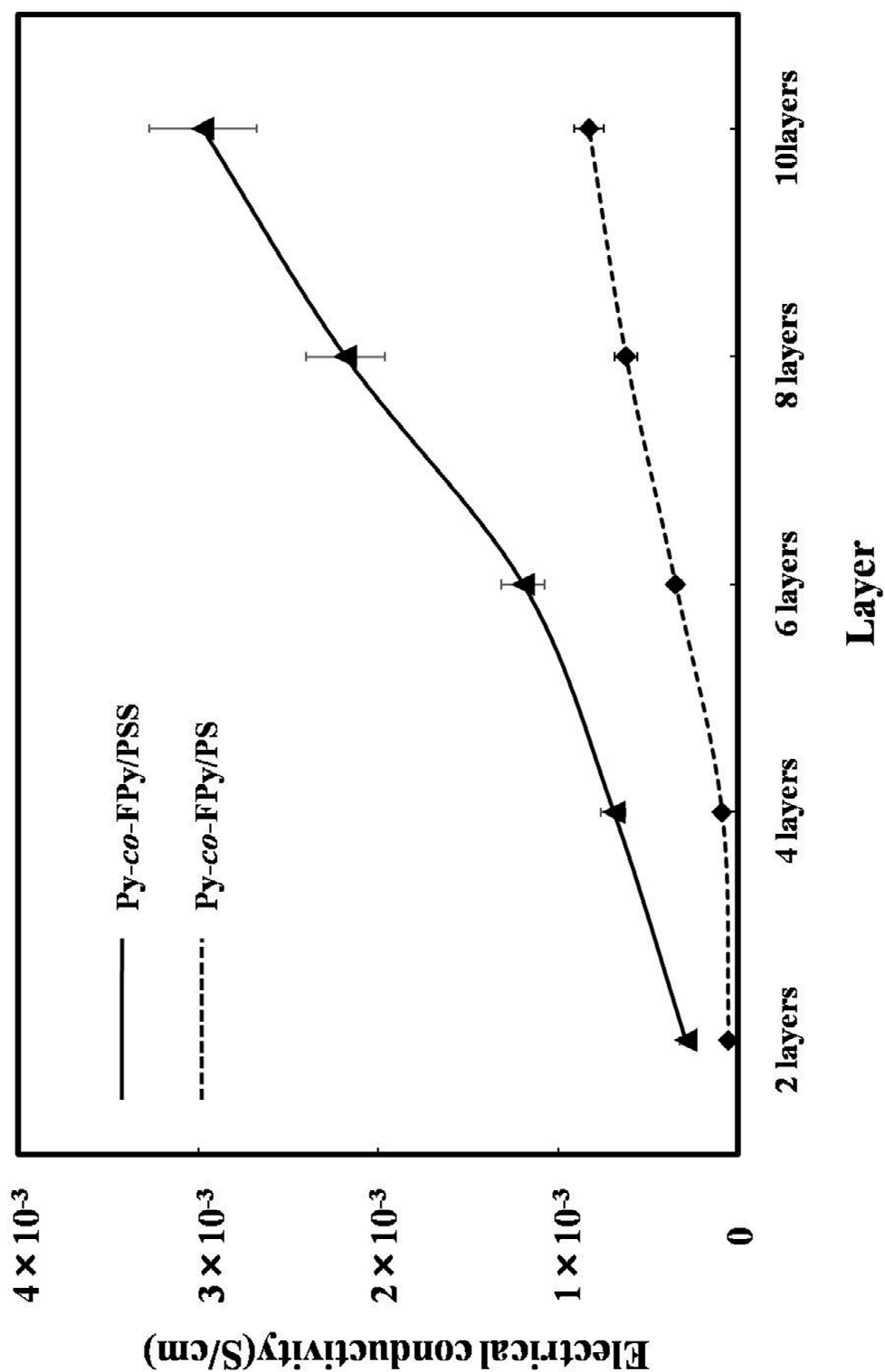
Figure 4.10 The electrical conductivity of P(Py–*co*–FPy) / PSS and P(Py–*co*–FPy) / PS

multilayer films with different layers after doped with I_2.

each system. In the PSS concentration with 2 mg/ml, the CV profiles were changed in

the redox peaks with the increase of deposition cycles. The peak potentials at 1.1 V for

the two layers were shifted to 0.9 V for the 10 layers. The redox peaks differed slightly

from those of pure PPy films, as reported [33–34]. This difference was assumed to

reflect the dedoping effect, confirming the anionic PSS connections [34]. In CV (b) and

(c), a similar phenomenon was observed when 4 and 6 mg/ml concentrations of PSS

were used. It was also apparent that, with the increased numbers of multilayers, the

current intensity increased greatly because confirmation of the conductivity was

enhanced with the increase of layers. The porosity surface is expected to engender more

efficient ion storage capability within the structure, which is expected to enhance the

charge storage capacity in higher cycle numbers [36]. The CV profiles imply a

completely continuous cycle during the scan range, meaning that the charge storage

capacity can be estimated from the area inside CV curve divided by the scan rate, as

charge storage capacitance (C) = area inside CV curve / 2 × scan rate [34]. The

capacitance related to the calculated results for the multilayer films with different PSS

concentration is presented in Figure 4.12. The charge storage capacitance of the

multilayer films increased concomitantly with the number of layers: as the number of

layers increased, the charge storage capacity increased, showing an almost linear
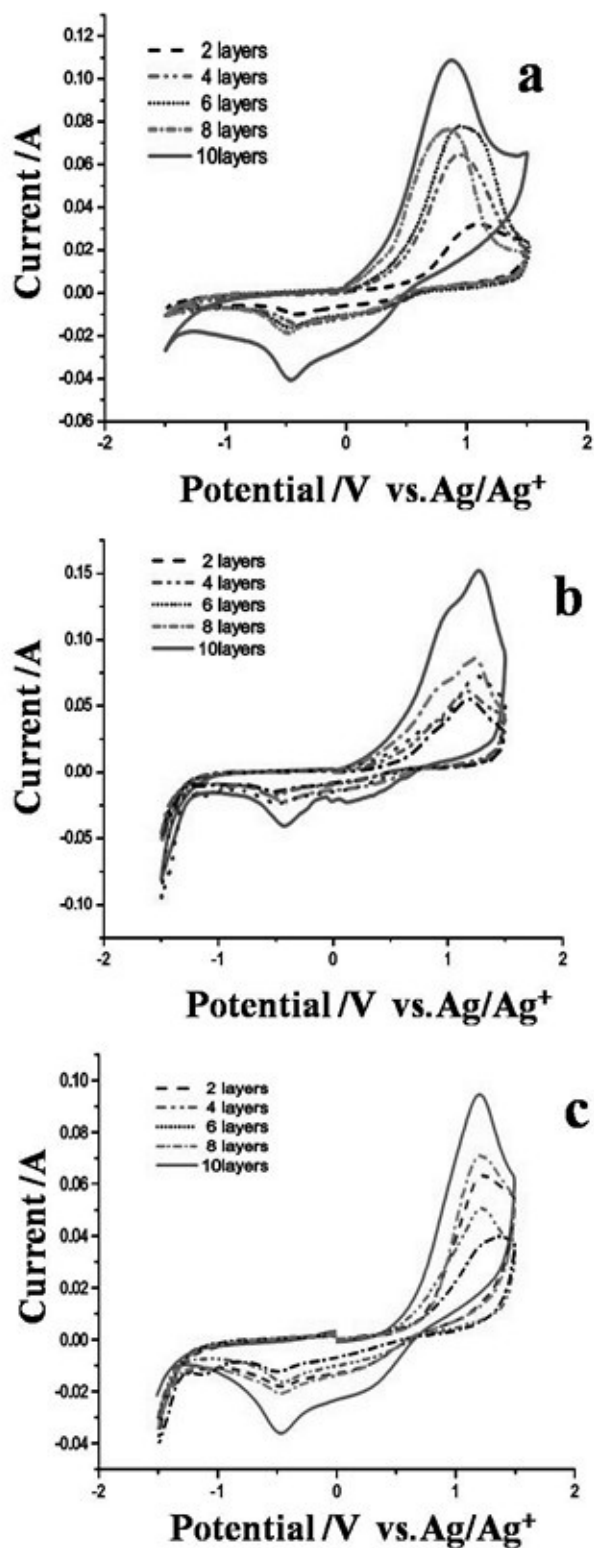
Figure 4.11 The CV recorded of the P(Py–*co*–FPy) / PSS multilayer films in 0.1M
TBAP /acetonitrile solution and scan rate at 1mV/s with the PSS concentration of 2 (a),
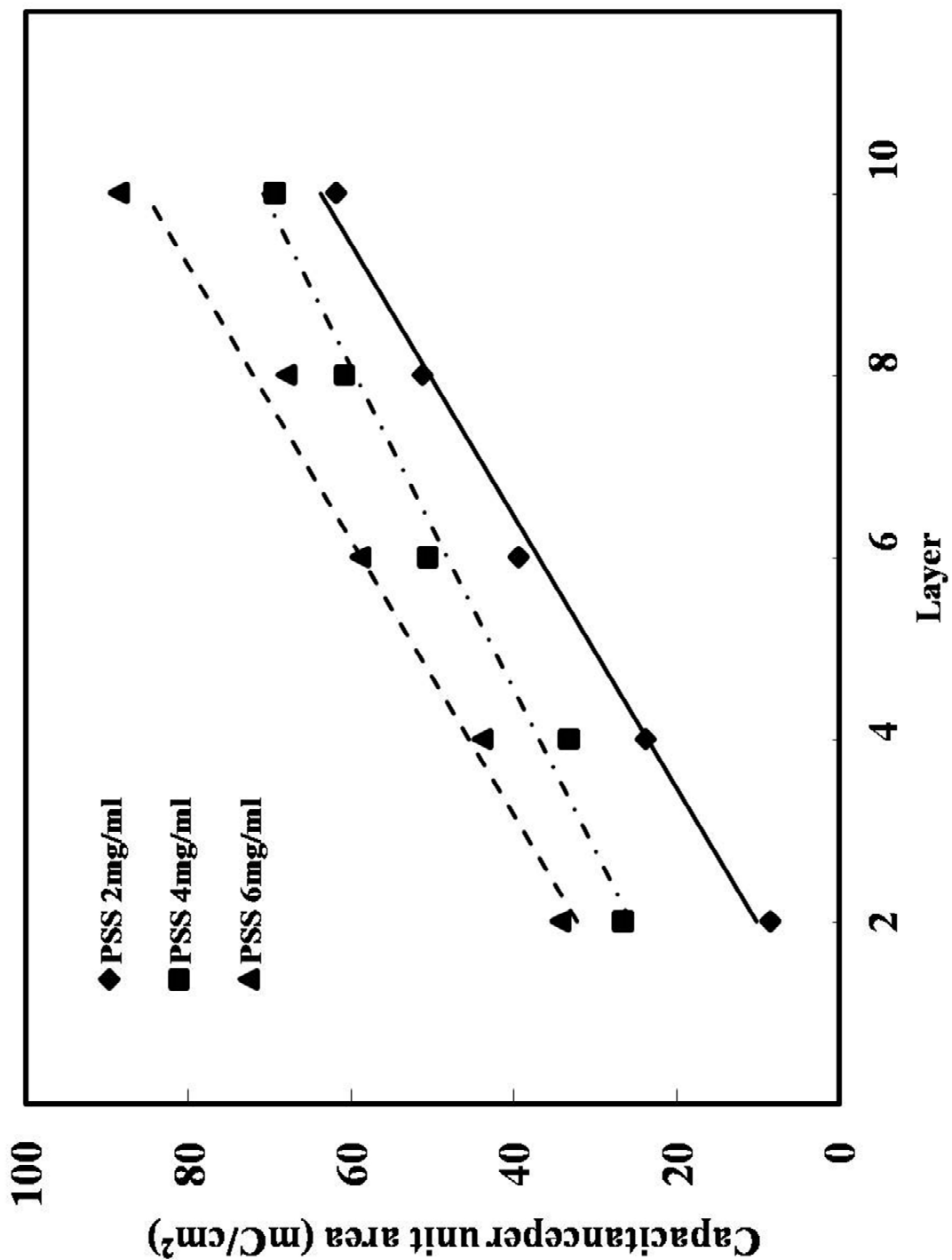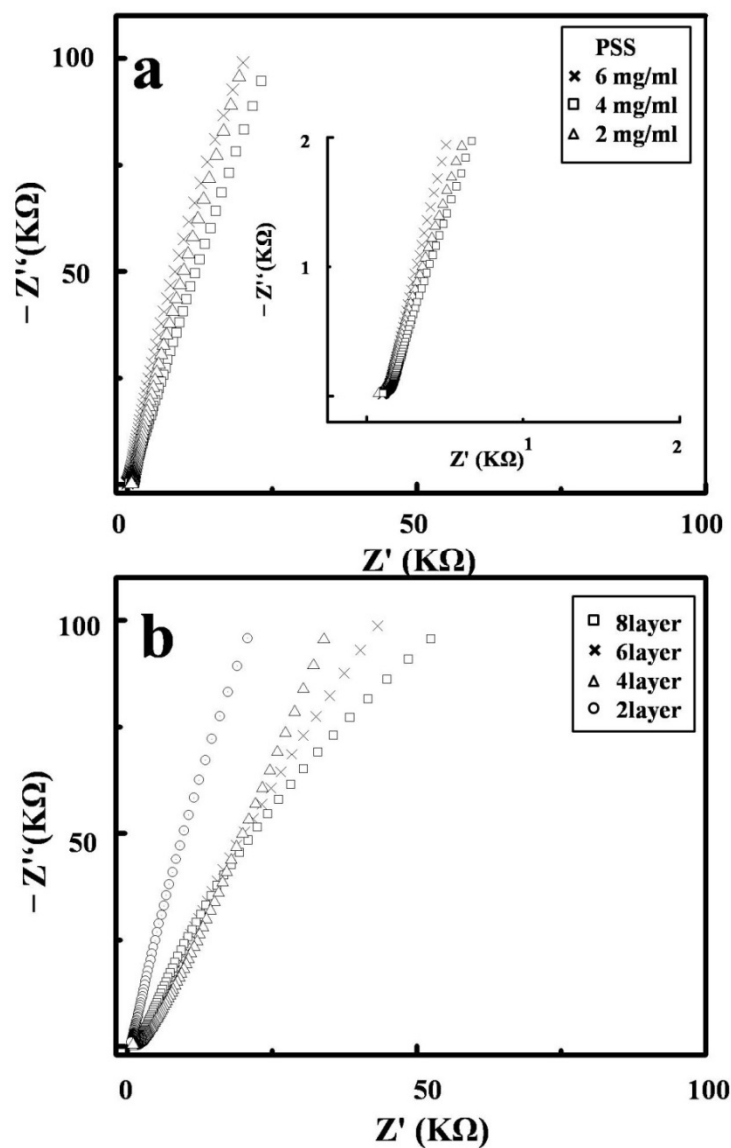4 (b) and 6mg/ml (c).

Figure 4. 12 Comparison of charge storage capacity of P(Py–*co*–FPy) / PSS multilayer

films with different layers.

tendency with the layer number. Furthermore, the capacitance value became higher with higher PSS concentration. Reportedly, the electrode surface roughness and hierarchical porous structure are related with capacitance because they strongly affect the shape of CV and peak currents [37]. Results show that the reversibility of the redox reaction influenced the sensitivity of the peak current on the surface roughness and hierarchical porous structure of these multilayer films.

In order to further investigate the electrochemical performance of the P(Py–co–FPy)/PSS multilayer films, electrochemical impedance spectroscopy (EIS) measurement was employed. Figure 13 and its inset show Nyquist plots of the obtained P(Py–co–FPy)/PSS multilayer films within a frequency range of 10 mHz – 100 kHz in 0.1 M TBAP / acetonitrile electrolyte using the a Cole–Cole plot analytical model. Nyquist plots could suggest the frequency response of the multilayer films/electrolyte system and are a plot of the imaginary component (Z'') of the impedance versus the real component (Z') by collecting data at a different frequency and showing the lower left portion of the curve corresponding to higher frequencies. In Figure 13a, both of the Nyquist plots for the multilayer films with different PSS concentration are nearly vertical and no obviously semicircle in the high–frequency region, suggesting their approach to well capacitance behavior [38]. Because of the high conductivity of these

films, the internal resistances of the films (including solution resistance and charge transfer resistance) at high–frequency were so small that the arc cannot be observed with inconspicuous knee frequency, implying a transition from frequency–dependent diffusion resistance to capacitive charging behavior [39]. With increasing PSS concentration in multilayer films, EIS results changed irregularly, suggesting the less obvious effect of PSS concentration on the electrochemical performance of the LBL films. However, EIS curve of the 8th layers of the film is more vertical than those of 2, 4 and 6 layers, indicating that the better capacitive performance based on increasing layers, as shown in Figure 13b. It was reported that the hierarchically porous structure and the high electrical conductivity of the multilayer films could promote the ion transport in the multilayer film surface and the formation of the electric double layers at the interface between film and electrolyte. Therefore, it is considered that the better capacitive performance might be related to the easy charge storage in the multilayer matrix during the increasing of layers, as caused by the hierarchical porous structure and roughness surface [40].

Figure 4.13 Complex plane impedance (Nyquist plot) of P(Py–*co*–FPy) / PSS multilayer films at (a) 2th layer with the PSS concentration of 2, 4 and 6mg/ml and (b) different layers with the PSS concentration of 2 mg/ml.

4.4 Conclusions

This was the first report to describe a simple and cost–effective approach for fabrication of novel P(Py–*co*–FPy)/PSS multilayer films using LBL self–assembly with the enhanced conjugated bond in PPy backbone. Results revealed that the multilayer films formed a homogeneous particulate and dense morphology on the surface for the first P(Py–*co*–FPy) layer, whereas the hierarchical porous structure and roughness surface was observed with the increase of deposited cycles. The existence of electrostatic interaction between P(Py–*co*–FPy) and PSS layers was confirmed by UV–vis results to reveal the doping effect of sulfonic group on the benefit of the improvement of electrical conductivity for these multilayer films. Regarding electrochemical behavior, the charge storage capacitance of the multilayer films increased with the increase of deposited cycles and PSS concentration. The CV and impedance results suggested that the deposited cycles influence the electrochemical performance of multilayer films by influencing the surface morphology and hierarchical porous structure of multilayer films. All of these results are expected to promote the understanding of such multilayer film for their potential applications.

4.5 References

[1]. Mike, J. F.; Lutkenhaus, J. L. Recent advances in conjugated polymer energy storage. *J. Polym. Sci B: Polm. Phys*. **2013**, *51*, 468.

[2]. Du, H. Y.; Wang, J.; Yao, P. J.; Hao, Y. W.; Li, X. G. Preparation of modified MWCNTs-doped PANI nanorods by oxygen plasma and their ammonia-sensing properties. *J. Mater. Sci*. **2013**, *48*, 3597.

[3]. Zhou, C. F.; Kumar, S.; Doyle, C. D.; Tour, J. M. Functionalized single wall carbon nanotubes treated with pyrrole for electrochemical supercapacitor membranes. *Chem Mater*. **2005**, *17*, 1997.

[4]. Zhang, J.; Kong, L. B.; Li, H.; Luo, Y. C.; Kang, L. Synthesis of polypyrrole film by pulse galvanostatic method and its application as supercapacitor electrode materials. *J. Mater. Sci*. **2010**, *45*, 1947.

[5]. Lu, X. F.; Zhang, W.; Wang, C.; Wen, T. C.; Wei, Y. One–dimensional conducting polymer nanocomposites: Synthesis, properties and applications. *Prog. Polym. Sci*. **2011**, *36*, 671.

[6]. Wang, L. X.; Li, X. G.; Yang, Y. L. Preparation, properties and applications of polypyrroles. *React. Funct. Polym*. **2001**, *47*, 125.

[7]. Kaplin, D. A.; Qutubuddin, S. Electrochemically synthesized polypyrrole film:

effects of polymerization potential and electrolyte type. *Polymer*. **1995**, *36*, 1275.

[8]. Jradi, K.; Bideau, B.; Chabot, B.; Daneault, C. Characterization of conductive composite films based on TEMPO-oxidized cellulose nanofibers and polypyrrole. *J. Mater. Sci.* **2012**, *47*, 3752.

[9]. Liu, Y.; Wang, H.; Zhou, J.; Bian, L.; Zhu, E.; Hai, J.; Tang, J.; Tang, W. Graphene/polypyrrole intercalating nanocomposites as supercapacitors electrode *Electrochimica Acta*. **2013**, *112*, 44.

[10]. Ai, H.; Gao, J. Size-controlled polyelectrolyte nanocapsules via layer–by–layer self–assembly. *J. Mater. Sci*. **2004**, *39*, 1429.

[11]. Gesquie`re, A.; Jonkheijm, P.; Hoeben, F. J. M.; Schenning, A. P. H. J.; De Feyter, S.; De Schryver, F. C.; Meijer, E. W. 2D–Structures of quadruple hydrogen bonded oligo(p-phenylenevinylene)s on graphite: self–assembly behavior and expression of chirality. *Nano. Lett*. **2004**, *4*, 1175.

[12]. Manna, U.; Dhar, J.; Nayak, R.; Patil, S. Multilayer single–component thin films and microcapsules via covalent bonded layer–by–layer self–assembly. *Chem. Comm.* **2010**, *46*, 2250.

[13]. Fou, A. C.; Rubner, M. F. Molecular–level processing of conjugated polymers. 2. layer–by–layer manipulation of in–situ polymerized p–type doped conducting polymers.

Macromolecules **1995**, *28*, 7115.

[14]. Ferreira, M.; Cheung, J. H.; Rubner, M. F. Molecular self–assembly of conjugated polyions: a new process for fabricating multilayer thin film heterostructures. *Thin. Solid. Films.* **1994***, 244*, 806.

[15]. Lowack, K.; Helm, C. A. Molecular mechanisms controlling the self–assembly process of polyelectrolyte multilayers. *Macromolecules* **1998**, *31*, 823.

[16]. Simoes, F. R.; Marchesi, L. F. Q. P.; Pocrifka, L. A.; Pereira, E. C. Investigation of electrochemical degradation process in polyaniline/polystyrene sulfonated self–assembly films by impedance spectroscopy. *J. Phys. Chem B* **2011**, *115*, 11092.

[17]. Lee, J.; Ryu, J.; Youn, H. J. Conductive paper through LbL multilayering with conductive polymer: dominant factors to increase electrical conductivity. *Cellulose.* **2012**, *19*, 2153.

[18]. Feng, X.; Yan, Z.; Li, R.; Liu, X.; Hou, W. The synthesis of shape–controlled polypyrrole/graphene and the study of its capacitance properties. *Polym. Bull.* **2013**, *70*, 2291.

[19]. Schrote, K.; Frey, M. W. Effect of irradiation on poly (3, 4–ethylenedioxythiophene): poly(styrenesulfonate) nanofiber conductivity. *Polymer.* **2013**, *54*, 737.

[20]. Mihranyan, A.; Esmaeili, M.; Razaq, A.; Alexeichik, D.; Lindstrom, T. Influence of the nanocellulose raw material characteristics on the electrochemical and mechanical properties of conductive paper electrodes. *J. Mater. Sci.* **2012**, *47*, 4463.

[21]. Hoshina, Y.; Kabayashi, T. Electrically conductive films made of pyrrole–formyl pyrrole by straightforward chemical copolymerization. *Ind. Eng. Chem. Res*. **2012**, *51*, 5961.

[22]. Tagaya, M.; Hoshina, Y.; Ogawa, N.; Takeguchic, M.; Kobayashia, T. Nanostructural analysis of self–standing pyrrole/2–formylpyrrole copolymer. *Micron.* **2013**, *46*, 22.

[23]. Hong, H.; Davidov, D.; Avany, Y.; Chayet, H.; Faraggi, E. Z.; Neumann, R. Electroluminescence, photoluminescence and X–ray reflectivity studies of self–assembled ultra–thin films. *Adv. Mater*. **1995**, *7*, 846.

[24]. Ram, M. K.; Salerno, M.; Adami, M.; Faraci, P.; Nicolini, C. Physical properties of polyaniline films: Assembled by the layer–by–layer technique. *Langmuir*. **1999**, *15*, 1252.

[25]. Xie, Y. B.; Du, H. G. Electrochemical capacitance performance of polypyrrole–titania nanotube hybrid. *J. Solid. State. Electrochem*. **2012**, *16*, 2683.

[26]. Chen, N. P.; Hong, L. A. A study on polypyrrole–coated polystyrene sulfonic acid

microspheres – a proton electrolyte. *Eur. Polym. J.* **2001**, *37*, 1027.

[27]. Li, D.; Ding, W. Y.; Wang, X.; Lu, L.; Yang, X. J. Modifying substrate surfaces with self–assembled polyelectrolyte layers to promote the formation of uniform polypyrrole films. *Appl. Surf. Sci.* **2001**, *183*, 259.

[28]. Qu, L.; Shi, G. Hollow microstructures of polypyrrole doped by poly(styrene sulfonic acid). *J. Polym. Sci A: Polm. Chem.* **2004**, *42*, 3170.

[29]. Dominis, A. J.; Spinks, G. M.; Kane–Maguire, L. A. P.; Wallace, G. G. A. A de–doping/re–doping study of organic soluble polyaniline. *Synth. Met.* **2002**, *129*, 165.

[30]. Wang, K.; Hoshina, Y.; Cao, Y.; Kabayashi, T. Novel metal-like luster conductive Film made of pyrrole and furfural in straightforward chemical copolymerization in straightforward chemical copolymerization. *Ind. Eng. Chem. Res.* **2013**, *52*, 2762.

[31]. Fan, L. Z.; Hu, Y. S.; Maier, J.; Adelhelm, P.; Smarsly, B.; Antonietti, M. High electroactivity of polyaniline in supercapacitors by using a hierarchically porous carbon monolith as a support. *Adv. Funct. Mater.* **2007**, *17*, 3083.

[32]. Li, F. B.; Thompson, G. E.; Newman, R. C. Force modulation atomic force microscopy: background,development and application to electrodeposited cerium oxide films. *App. Surf. Sci.* **1998**, *126*, 21.

[33]. Mostany, J.; Scharifker, B. R. Impedance spectroscopy of undoped, doped and

overoxidized polypyrrole films. *Synth. Met*. **1997**, *87*, 179.

[34]. Chen, H.; Guo, L. H.; Ferhan, A. R.; Kim, D. H. Multilayered polypyrrole–coated carbon nanotubes to improve functional stability and electrical properties of neural electrodes. *J. Phys. Chem C* **2011**, *115*, 5492.

[35]. Ren, X. M.; Pickup, P. G. Impedance spectroscopy of polypyrrole/poly (styrenesulphonate) composites. Simultaneous anion and cation transport. *J. Electrochim. Acta*. **1996**, *41*,1877.

[36]. Suppes, G. M.; Deore, B. A.; Freund, M. S. Porous conducting polymer/heteropolyoxometalate hybrid material for electrochemical supercapacitor applications. *Langmuir*. **2008**, *24*, 1064.

[37]. Menshykau, D.; Streeter, I.; Compton, R G. Influence of electrode roughness on cyclic voltammetry. *J. Phys. Chem C* **2008**, *112*, 14428.

[38]. Jiang, L.; Yan, J W.; Xue, R.; Hao, L. X.; Jiang, L.; Sun, G. Q.; Yi, B. L. Hierarchically porous carbons with partially graphitized structures for high rate supercapacitors. *J. Mater. Sci*. **2014**, *49*, 363.

[39]. Yang, C.; Liu, P.; Wang, T. Well–defined core–shell carbon black/polypyrrole nanocomposites for electrochemical energy storage. *ACS. Appl. Mater. Interfaces*. **2011**, *3*, 1109.

[40]. Marchesi, L.; Simoes, F. R.; Pocrifka, L. A.; Pereira, E. C. Investigation of polypyrrole degradation using electrochemical impedance spectroscopy. *J. Phys. Chem B* **2011**, *115*, 9570.

Chapter 5

Synthesis of Conjugated Polyaminoanthracenes by Chemical Polymerization and Composite Films for The Fluorescent Properties

ABSTRACT: Conjugated poly (9–aminoanthracene) (P9AA) and poly (1–aminoanthracene) (P1AA) were synthesized through a facile chemical oxidative polymerization in the presence of $FeCl_3$. The chemical structure of the polymers was confirmed by H NMR and FT–IR. The obtained polymers showed suitable solubility in common organic solvents. The fluorescence spectra showed that their polymers had strong anthranyl emission, especially for the P1AA in excimer band. The existence of solvent effect on the maximum emission peak was seen with slight change in THF, DMF and DMSO. The fluorescent composite films consisting of P1AA and polystyrene sulfonate (PSS) were also prepared by the electrostatic interaction between the poly P1AA and SO_3^- group in PSS. This revealed that the surface morphology and the optical properties for each composite film was quite different in the behavior of only P1AA in the PSS absent case. This meant that the electrostatic interaction of PSS and P1AA influenced to interfere the excimer formation of the anthranyl groups.

5.1 Introduction

Recently, conjugated electrical conducting polymers had been widely investigated due to their increasing number of applications, such as solar cells, sensors and organic light emitting diode materials and so on [1-3]. Polyaniline (PANI) is one of the most studied conducting polymers because of its low cost, excellent stability, and relative ease of the synthesis. However, due to the poor solubility of those conductive materials, there have been fewer reports on such PANI investigation of their optical properties [4-5]. Herein, 1–aminonathracene (1AA) and 9–aminoanthracene (9AA) have similarly chemical structure than aniline. It is attractive to obtain polyaniline–like conjugated polyaminoanthracenes (PAAs) with excellent fluorescence behaviors by a simple chemical polymerization [6]. On the other hand, anthracene–containing polymers have attracted considerable scientific and industrial interests, due to their attractive features as fluorescent probes, photon harvesters and electro– and photo-luminescent materials [7-9]. However, most researches concerning chemical synthesis of anthracene–containing structure on backbone are confined within metal coupling reaction or other complex polymerization methods, as required with metallic catalyst. The extreme reaction conditions seriously limit the facile preparation and application of these polymers [10-11]. Only few reports pay attention to the simple chemical

polymerization of anthracene–containing conjugated polymers, though their optical studies have not yet been studied adequately [12-13]. Ikedu *et al.* investigated the effect of the side chain anthracene substitution position on excited state intermolecular proton transfer by the emissive properties of anthracene derivatives [14]. Mori *et al.* investigated the optoelectronic properties of alternating copolymers containing anthracene unit in the backbone [15]. Horaguchi *et al.* showed the facile synthesis and activities of sulfonated polyanthracene [16]. It was also reported that anthracene moieties was easily affected by the π–π stacking between anthracene moiety, the stereo–hindrance effect of the chemical structure or the solvent effect of the solution, which could be a greatly influenced on the formation of dimer or excimer [17-18]. Therefore, it is necessary to enrich the knowledge of the optical property of such kind of anthracene–containing conjugated polymers. Meanwhile, conductive polymers with anthracene–containing structure including PAAs could present distinct chromogenic and fluorescent property. There are considerable as fluorescence materials applied on analytical chemometrics and provided sensitive and became quick methods for the sensing of dangerous substances or optical devices such as organic light emitting diode [19]. Many researches involving conjugated polymers as a fluorophore have been conducted to evaluate the substituent effects, fluorophore arrangement, or solvent

effects to evaluate the corresponding changes in structural and optical feature of this anthracene–containing structure, improving its ability to act as an electron acceptor or donor [20-22].

The present work reports successful chemical oxidative polymerization of 1AA and 9AA by a facile chemical oxidative polymerization method. The chemical structure and optical property of the obtained PAAs is investigated (Scheme 5.1). The solvent effect of fluorescence emission on fluorophore in different solvents is determined in various organic solvents. The fluorescent composite films consisting of poly (1–aminoanthracene) and polyvinyl alcohol (PVA) and polystyrene sulfonate (PSS) were prepared. Results suggested that the electrostatic interaction between the poly (1–aminoanthracene) and the SO_3^- group was greatly influence on the surface morphology and the optical properties for P1AA/PSS composite films.
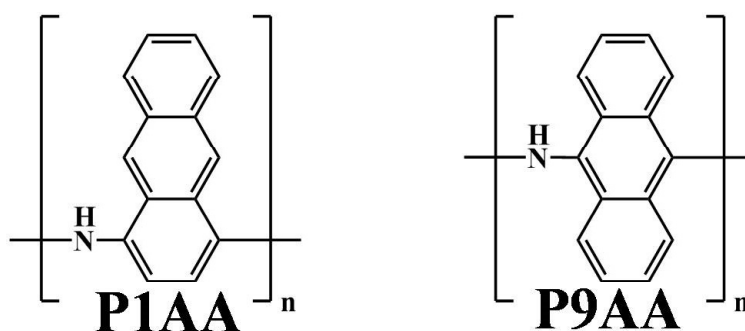
Scheme 5.1 Calculated structures of poly (1–aminoanthracene) and poly (9–aminoanthracene)

5.2 Experimental Section

5.2.1 Reagents

Anthracene, 1–aminoanthraquinone, dodecylbenzenesulphonic acid (DBSA) and zinc powder were purchased from Tokyo Chemical Industry Co., Ltd., and used as received. Nitric acid (HNO_3), hydrochloric acid (HCl) and anhydrous tin chloride, iron chloride ($FeCl_3$) were purchased from Nacalai tesque Chemical Industry Co., Ltd. Polyvinyl alcohol (PVA, hydrolyzed) and sodium polystyrenesulfonate (PSS, 70000 Mw) were purchased from Aldrich Chemical Co. Inc. Other chemicals were purchased and used as received. The monomer of 1-aminoanthracene (1-AA) and 9-aminoanthracen (9-AA) were synthesized according to the previously reported procedures [23-24].

5.2.2 Measurments

The electrical conductivity of doped and undoped samples was determined with bars and prepared from pressed pellets of the sample using a typical four–probe method (Roresta–GP MCP–T610; Mitsubishi Chemical Analytec Co. Ltd., Japan) at room temperature. The measurement was conducted with attachment to the compacted sample surface at three different points. To determine the molecular weight, gel permeation chromatograms (GPC) were recorded with a column of TSK gel G2000 using

polystyrene standards and using THF as eluent (SPD–20A; Shimadzu Corp., Japan).

FT–IR spectra of the polymers were recorded on an IR spectrophotometer (Prestige–21,

Shimadzu Corp., Japan) with KBr pellets under the transmittance mode. To confirm the

structure of the polymers, H NMR spectra of PAAs were measured using a spectrometer

(AL–400 NMR; JEOL Ltd., Japan) with deuterated dimethylsulfoxide (d_6–DMSO) as

solvent. The UV–visible absorption spectra of the polymer solutions were measured

using a UV–vis–NIR spectrophotometer (V–570; Jasco Corp., Japan) under

transmittance mode. Fluorescence property of polymers doped with various dopants was

studied using spectrophotometer (FP–5300PC; Shimadzu Corp., Japan) at room

temperature. For surface analysis of the films, scanning probe microscopy (SPM,

Nanocute; SII Investments, Inc., Japan) was applied in a 500×500 nm area of the film

to produce AFM images. A silicon probe mounted on a cantilever (Micro cantilever

Si–DF40P2; SII Investments Inc., Japan) was used. The surface roughness was

calculated using root mean square values (RMS) in the Z–range images.

5.2.3 Preparation of 1–aminoanthracene

10g of 1–aminoanthraquinone was stirred with 100 ml of 10% sodium hydroxide

(100 ml) and 8g zinc dust at room temperature for about 30 min in a 500–ml three–neck

round–bottomed flask under nitrogen atmosphere. It was slowly heated and the temperature of the reaction mixture was maintained around 90°C. Zinc dust (10 g) was then introduced into the reaction mixture in two equal installments at an interval of 30 min each, and heating was continued with constant stirring for 24 h at 90 °C. The solid material from the reaction mixture was collected and washed several times with water. The crude 1–aminoanthracene was purified by using soxhelet extraction with acetone. The residue was dissolved in ethanol and recrystallized in a rotary evaporator under reduced pressure several times and gave 5.82g 1–aminoanthracene as greenish–yellow plates (68% in yield).

FT–IR (KBr disc): 3380, 3060 cm^{-1} (NH$_2$ stretch).

H NMR (d_6–DMSO, 399 MHz), δ: 4.25 (2H, NH$_2$), 7.36 (2H, anthryl), 7.48 (1H, anthryl), 7.97 (2H, anthryl), 8.59ppm (2H, anthryl).

5.2.4 Preparation of 9–nitroanthracene

   In a 300 ml three–neck round–bottomed flask, 10 g (0.056 mmole) anthracene was suspended in 40 ml glacial acetic acid at room temperature under a nitrogen atmosphere with continuous stirring. Then, 3.50 g (55.40 mol) concentrated nitric acid was added slowly from a dropping funnel during 10 min. The reaction was continued under stirring

for 12 h. A mixture of 25 ml concentrated HCl and 25 ml glacial acetic acid was added slowly to the reaction solution and a pale–yellow precipitate of 9–nitro–10–chloro–9, 10–dihydroanthracene was appeared gradually during the stirring. After that, the suspension was filtered and washed by water several times until the filtrate was neutral. The product was triturated thoroughly 60 ml of warm 10% sodium hydroxide solution with strong agitation. Crude 9–nitroanthracene was filtered and washed by water until neutral. The crude 9–nitroanthracene was recrystallized from ethanol to afford 9.80 g yellow powder (78% in yield).

FT–IR (KBr disc): 1518 cm^{-1} (NO$_2$ stretch).

H NMR (d_6–DMSO, 399 MHz), δ: 7.56 (2H, anthryl), 7.63 (2H, anthryl), 7.92 (2H、 anthryl), 8.05ppm (2H、 anthryl), 8.59ppm (1H, anthryl).

5.2.5 Preparation of 9–aminoanthracene

In a 300 ml three–neck round–bottomed flask, 12.00 g (53.74 mmol) of 9–nitroanthracene was suspended in 100 ml glacial acetic acid at 70 °C under a nitrogen atmosphere with continuous stirring until it completely dissolved. Then, 42.4 g (0.22 mol) tin (II) chloride dissolved in 150 ml concentrated HCl was added slowly to the 9–nitroanthracene from a dropping funnel during 1 hour. A yellow precipitate was

gradually appeared after 75 ml tin (II) chloride in HCl solution was added. The rest of

the tin solution was added and the solution stirred at 80 °C for half an hour, then it was

cooled to room temperature. The light yellow solid was filtered and washed with small

amounts of concentrated HCl and a lot of water until the filtrate was neutral. The

product was triturated thoroughly 100 ml of warm 10% sodium hydroxide solution with

strong agitation. The residue was collected, and the crude 9–aminoanthracene was

recrystallized from ethanol to afford 10.16 g yellow powder (90.3% in yield).dried in

vacuo at 80 °C to give 9.49 g (91% in yield) of yellow crystals.

FT–IR (KBr disc): 3411, 3490 cm^{-1} (NH$_2$ stretch).

H NMR (d_6–DMSO, 399 MHz), δ: 4.85 (2H, NH$_2$), 7.40~7.44 (4H, anthryl), 7.67~7.75

(1H, anthryl), 7.87 (2H, anthryl), 7.94ppm (2H, anthryl).

5.2.6 Polymerization of Polyanimanthracenes

   1AA/9AA (1g, 5.18mmol) was dissolved in acetonitrile (100ml) and then the

anhydrous ferric chloride (FeCl$_3$) (3.36g, 20.72mmol) methanol suspension solution

was added slowly under continuous stirring. The solution was stirred under nitrogen

atmosphere for 24h at room temperature. Most of solvent was removed by evaporation

and the residue was filtered. Methanol (200ml) was added to make a dispersion solution

and refluxed for other 4hours, and then filtered. After that the solid was washed by

methanol and distilled water several times until the filtrate was colorless. Finally, the

products were dried under vacuum. The synthesis and calculated chemical structure of

PAAs was summarized in Scheme 5.2.

5.2.7 Preparation of P1AA/PSS and P1AA/PVA composite films

   Composite films of P1AA and PSS carried out as followed: P1AA (10 mg) was

dissolved in 10 ml DMSO to obtain the 1 mg/ml P1AA solution. Then, PSS was

dissolved in deionized water to prepare the 1, 3, 5 and 10wt% PSS aqueous solution,

respectively. The mixture solution was prepared by addition 1 ml P1AA solution (1

mg/ml) into each concentration of PSS aqueous solution (5 ml) under constantly stirring.

Then, 2 ml of mixture solution of P1AA/PSS was coating on with quartz glass substrate

under atmosphere at 80 ℃ for 1 hour. With the evaporation of the solvent, the each

PSS concentration of composite film was obtained on the quartz glass for future

measurement. In case of PVA composite films, the same process was done to prepare

the composite films with 1, 3, 5, 10 wt% of PVA content. Meanwhile, the 1 wt% PSS

and PVA aqueous solution was prepared to make the neat PSS and PVA film as a

contrast experiment.
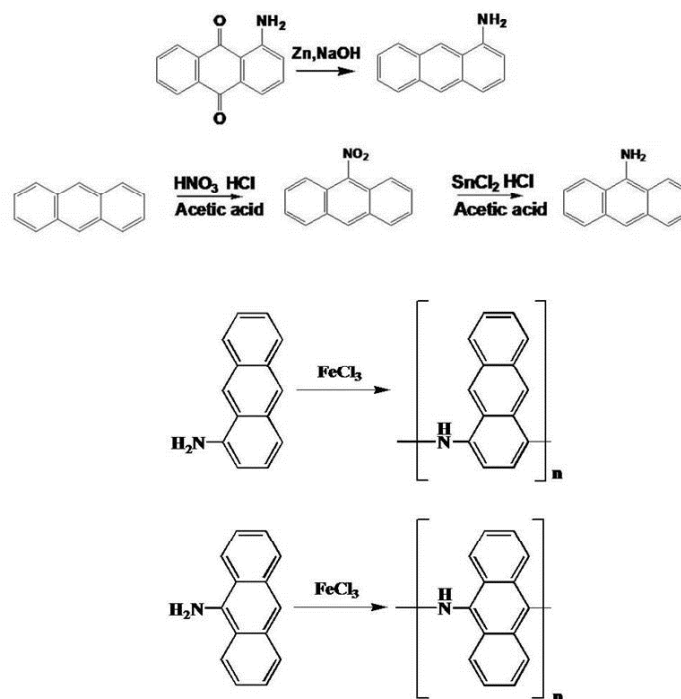
Scheme 5.2 Synthesis route to monomer and polymers and estimated structure of

Polyaminoanthracenes.
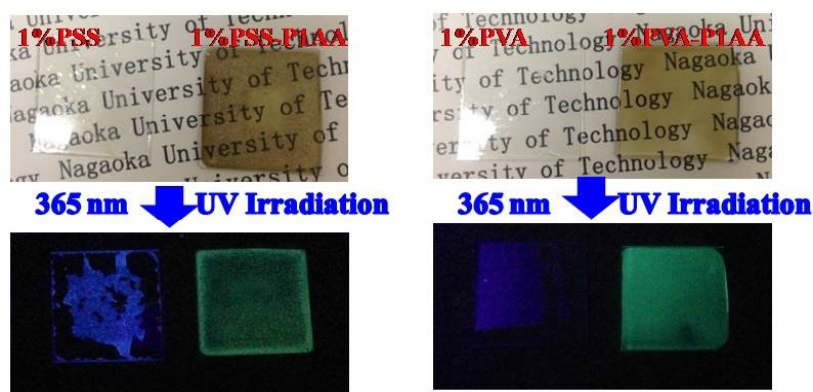
Figure 5.1 Images of P1AA/PSS and P1AA/PVA composite films irradiated under

365 nm ultraviolet light.

Figure 5.1 shows the picture of P1AA/PSS and P1AA/PVA composite films as irradiated under 365 nm ultraviolet light. It was obviously observed the yellow-green fluorescence emission for both of the composite films.

5.3 Results and Discussions

5.3.1 Chemical structure of Polyanimanthracenes

Figure 5.2 shows the FT-IR spectra of monomer and PAAs. Both PAAs give rise to mixed bands assigned to skeletal vibration of the aromatic ring and the quinoid imine moiety in a region from 1660 to 1440 cm^{-1} and the N–H stretching vibration at about 3400cm^{-1}. The FT-IR spectrum of polyaniline also exhibits the absorption bands in the same region for the N-H band. The absorption peaks at around 900 cm^{-1} were observed that both FT-IR spectra of P1AA and P9AA seemed to be assigned to the out–of–plane vibrations for four adjacent H atoms and those of around 810cm^{-1} to the two adjacent H atoms as references [25-26].

In Figure 5.3, the H NMR spectra of P1AA (a) and P9AA (b) were obtained in d_6–DMSO. It was reported that the H NMR spectrum of polyaniline–like polymer had its protonation to change the redox states of the conjugated backbone [27]. In the case of polyaniline, there was consideration that the three peaks around 7 ppm having almost

equal intensity attributed to the free radical NH^+ proton resonance. The presence of ^{14}N with unit spin was to be split in the proton attached to it into a 1/1/1 triplet [28]. Therefore, a broad mixture peak could be assigned from 7 ppm to 7.95 ppm for the P1AA. Three unconspicuous spaced lines of equal intensity around 6.97 ppm, 7.09 ppm, and 7.22 ppm were indicative protonated NH^+ proton resonance. The peaks around 7.5–8.5 ppm could be considerable to assign to the proton resonance of the aromatic ring, because the chemical shift for the aromatic protons of the monomer commonly was observed in the region of 6.9–7.4 ppm [28]. Meanwhile, the aromatic proton resonance could be supposed to shift toward a range from7.5 ppm to 8.2 ppm and split to many tiny unconspicuous peaks. This was due to the influence of the asymmetry for the anthracene ring connection. For P9AA, three sharp lines of equal intensity 6.89 ppm, 7.09 ppm, and 7.29 ppm, showing equal space in the chemical shift were indicative of the free protonated NH^+ resonance. The peak was split in the proton attached to it into three lines. Instead, two obvious peaks were appeared at 8.24 and 8.55 ppm for P1AA and 8.25 and 8.60 for P9AA as shown in Figure 5.3. These complex peaks would be attributed to the aromatic proton resonance of PAAs aromatic rings [27, 29]. According to the above results, the chemical structure of the obtained PAAs could be determined.
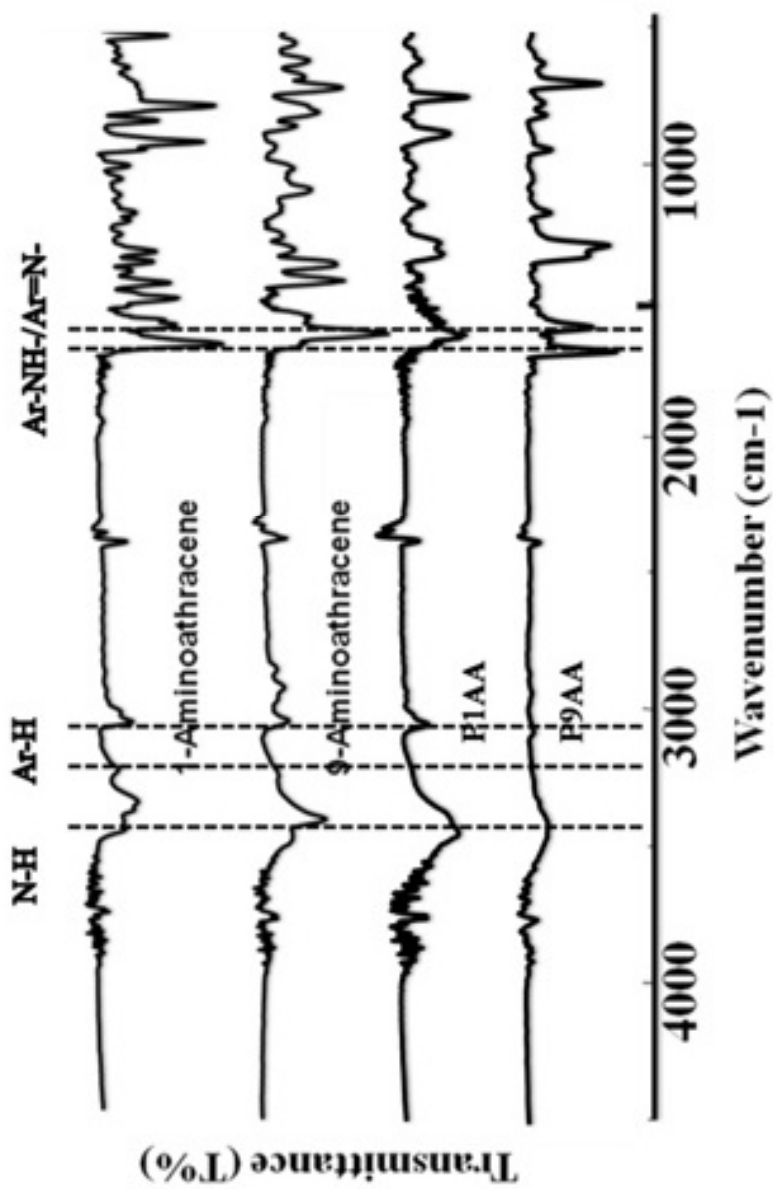
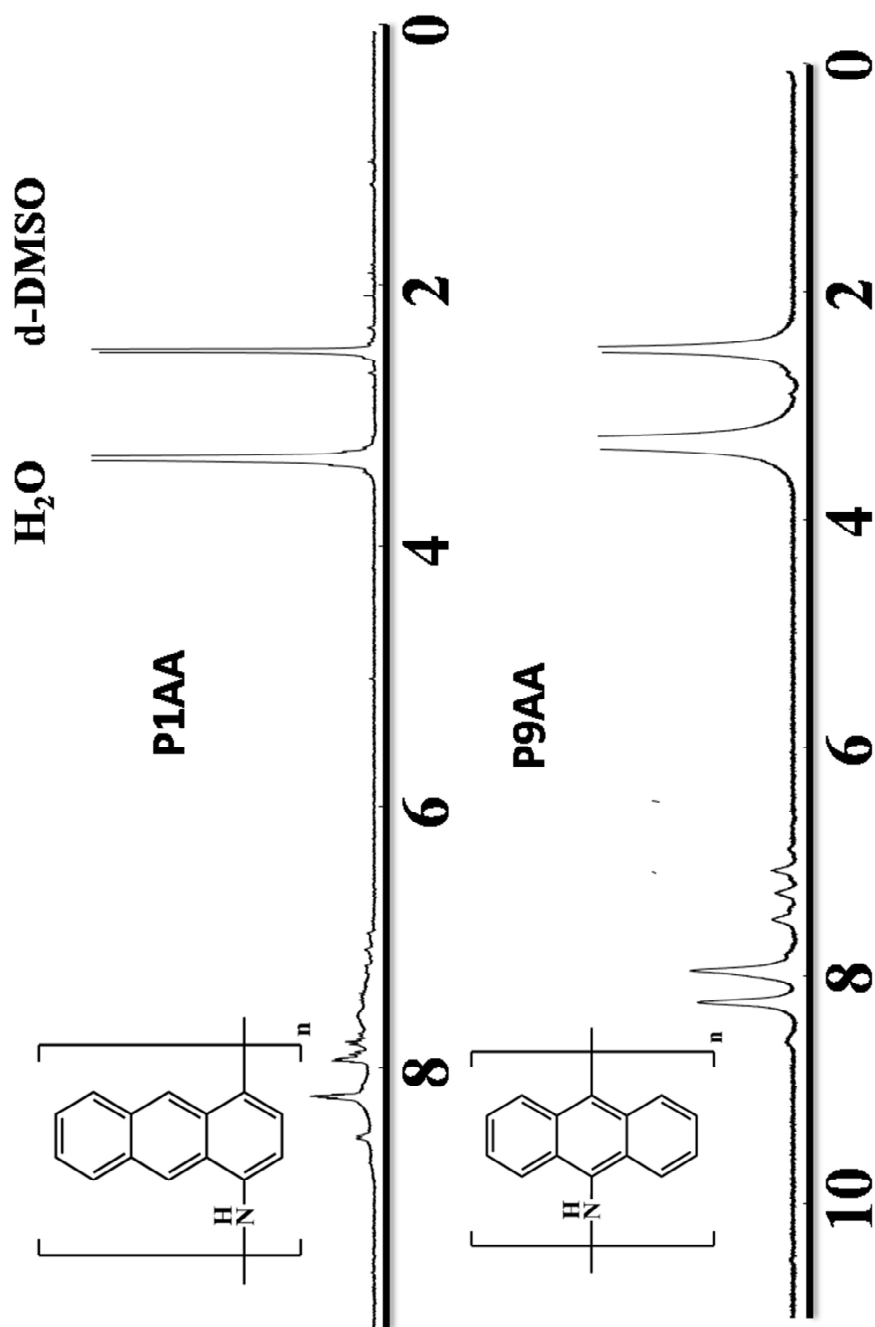**Figure 5.2** FT-IR spectra of PAAs (d_6-DMSO).

Figure 5.3 H NMR spectra of PAAs (*d₆*-DMSO).

Table 5.1 Electrical conductive, yield and weight molecule weight of PAAs.

		P1AA	P9AA
Conductivity before doping (S/cm)		1.3×10^{-6}	3.2×10^{-7}
Conductivity doping with HCl (S/cm)		2.6×10^{-3}	4.2×10^{-3}
Conductivity doping with DBSA (S/cm)		4.6×10^{-4}	1.3×10^{-4}
Average weight molecule weight (Mw, 10^3)		4.2	5.3
Yield (%)		76.2	66.7
UV-vis Absorption	λ/max/nm	255	256
	ε/Lmol^{-1}cm^{-1}	5.6×10^4	5.0×10^4

### 5.3.2 Properties of Polyanimanthracenes

The conductivity of the PAAs doped with different dopants lists in Table 5.1. P1AA and P9AA both showed semiconductivity without doping and the values of conductivity for P1AA and P9AA were in the range of $10^{-7} \sim 10^{-6}$ S/cm. The electrical conductivity of PAAs could rise to $10^{-4} \sim 10^{-3}$ S /cm by doping with HCl or DBSA. It was also confirmed that the molecular weight distribution of the PAAs was determined using gel permeation chromatography in the range of Mw $\approx$ 5000 $\sim$ 6000. Both samples were observed only one broad peak for distribution of molecular weights. It always was shown that the low Mw fraction dominated to be contrasted with conventional

chemically polymerized PANI [30]. However, due to that the steric hindrance of anthracene exited in polymer main chain, the segments led to a resistance effect. This led a direct impact both on the molecular weight and conductive rate raising more.

Figure 5.4 describes the UV–vis absorption spectra of monomers and PAAs taken in DMSO solution with decreased concentration as compared with the UV–vis absorption spectra of monomers. Both PAAs exhibited the first absorption band around 255 nm assigned to the π–π^* transition of anthracene moiety [31]. It was reported that anthracene and anthracene derivatives usually showed three well–defined and shaped absorption bands between 330 and 430nm. This was observed in the absorption spectra of the monomers. Therein, both P1AA and P9AA solution presented a widely absorption mixed peaks at 330–430nm as originated from the n-π^* transition adjacent anthracene moieties and proved the exited of anthracene unit in the main chain [32]. Figure 5.5 displays typical emission and excitation fluorescence spectra of P1AA and P9AA when exited at 360 nm in DMSO (up) and DMF (down) solution with the concentration of anhtracene concentration [Ar] at 2, 1, 0.5, 0.25, 0.12 $\times$ 10^{-4} M. In addition to these peaks for P1AA, a broad peak from 450 to 650 nm with a maximum at 527 nm showed a typical yellow–green emission, which was assigned to the formation of anthracene dimer or excimer emission. It is well known that the anthracene molecule

was easily to form the relatively stable excimer by π–π stacking between different anthracene moieties originated from the interaction of anthracene moieties in different molecular chain [33-34]. In case of P9AA, broad tailing peaks were observed around 430, 450 nm and another broad peak at around 510 nm were visible, corresponding to a green–yellow emission for P9AA. There, the strong peaks appeared over 510 nm could probably be caused by the formation of excimer of anthracene moieties on the backbone originated from the interaction of anthracene moieties in different molecular chain. Here, it was noted that the monomer emission band was observed at 450 nm in the excited state for P9AA. Therefore, it could be supposed that the P1AA might show high possibility to form stable anthracene excimer relative to that of P9AA, possibly due to the inter chain interactions of anthracene moiety. However, P9AA was considered to show a better planarity to form the unstable face to face excimer between relative anthracene moieties [35]. The comparison of the UV and emission spectra of P1AA and P9AA indicated the importance of optical property affected by the chemical structure.
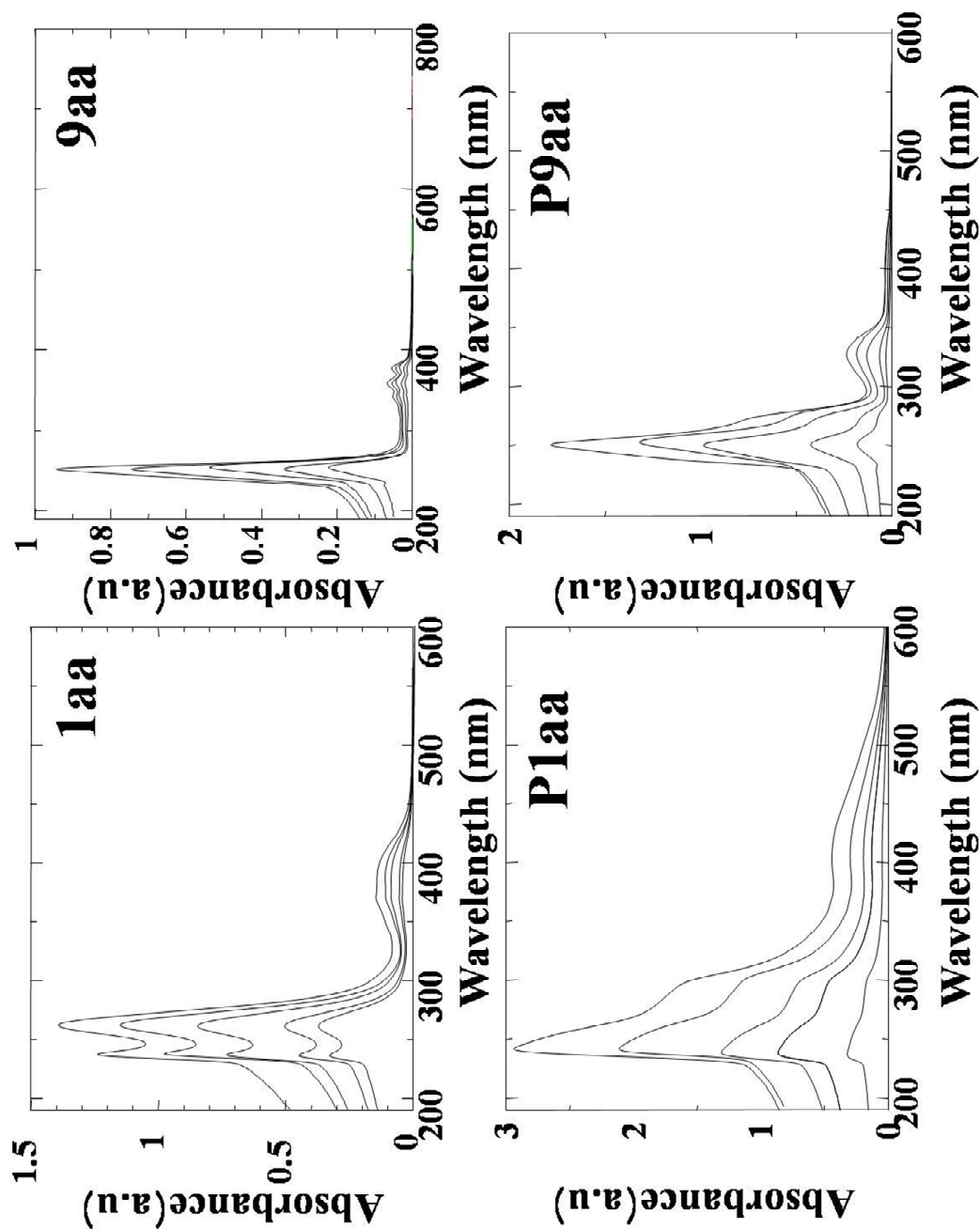
Figure 5.4 UV-vis spectra of monomers (([Ar]= 2, 1, 0.5, 0.25, 0.12 × 10^{-5} M) and PAAs ([Ar]= 2, 1, 0.5, 0.25, 0.12 × 10^{-4} M) in DMSO solution.
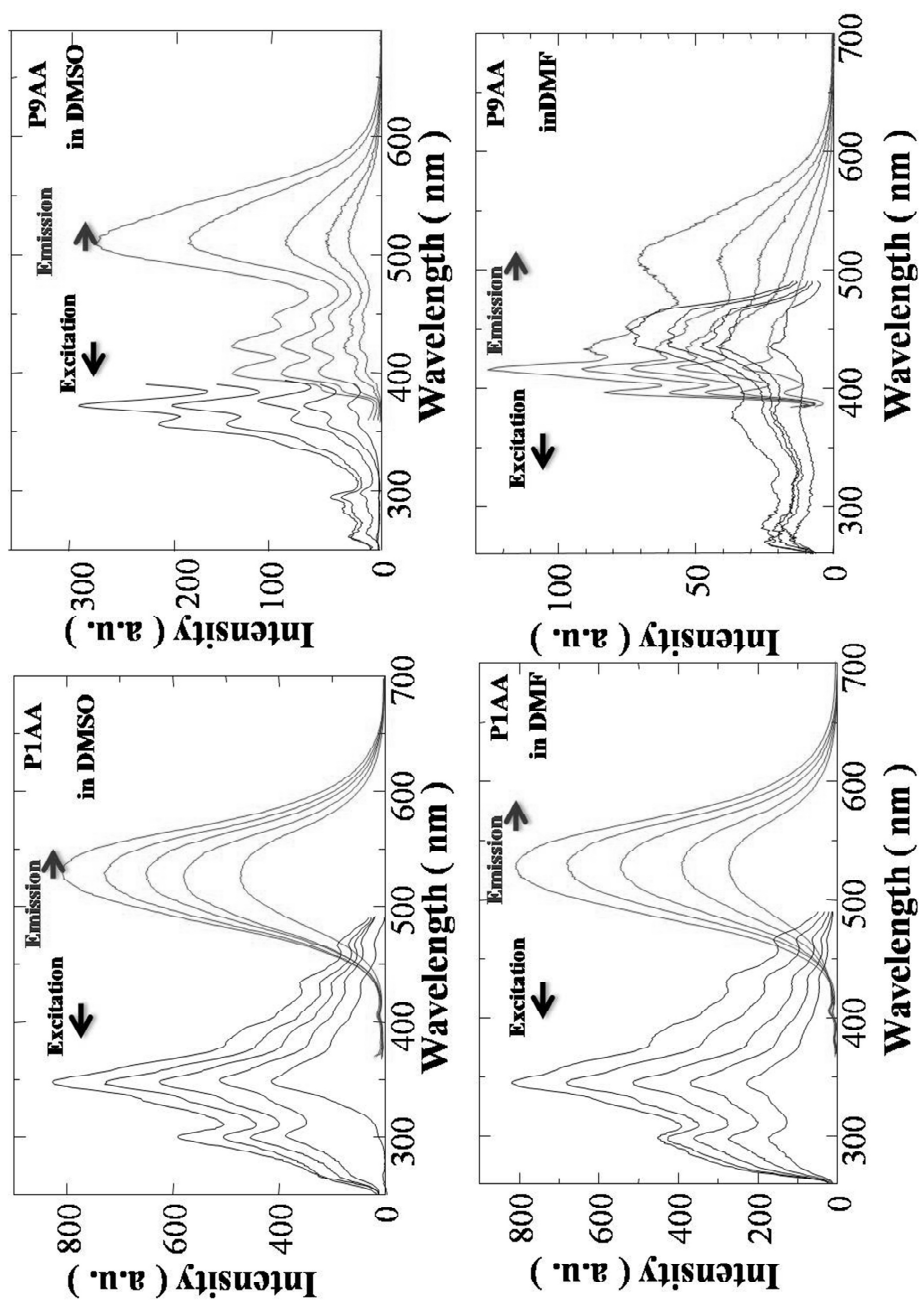
Figure 5.5 The fluorescence spectra of PAAs exited at 360 nm in DMSO and DMF solution ([Ar]= 2, 1, 0.5, 0.25, 0.12 × 10^{-4} M).

**Table 5.2** Solubility and fluorescence data of P1AA and P9AA in different solvents [a]

Solvent	Dielectric Constant	P1AA	Emission λ_{max} (nm)	P9AA	Emission λ_{max} (nm)
DMSO	47.24	s	527	s	510
DMF	38.25	s	526	s	514
NMP	32.2	s	527	s	518
THF	11.6	ss	521	ss	514
Benzene	2.283	i	−	i	−
Toluene	2.4	i	−	i	−
Hexane	1.9	i	−	i	−

a: s, soluble; ss, slightly soluble; i, insoluble.

To determine the solubility of PAAs, 1 mg obtained sample was dissolved in 20 ml solvent under ultrasonic for 10 min until no precipitation was observed. Then, additional 1 mg sample was added to the translucent homogenous solution successively under ultrasonic and observed whether it could completely dissolve. The powdery PAAs were soluble in common organic solvent of dimethyl sulfoxide (DMSO), dimethylformamide (DMF), *N*–methyl–2–pyrrolidone (NMP), tetrahydrofuran (THF). Therefore, it was supposed that the torsion structure of rigidity π–conjugated anthracene moieties in backbone might be greatly influenced by the solvent effect as we introduced [21]. To consider the influence of different solvent on the fluorescence behavior of PAAs, the fluorescence spectra were examined in several organic solvents with different dielectric constant (Figure 5.6). As summarized in Table 5.2, maximum emission wavelength

(λ_{max}) was listed. It is observed that as the dielectric constant of solvents increasing there was tendency of the λ_{max} of PAAs to show a slightly shift toward a longer wavelength, meaning that the salvation decades the excited level. The dielectric constant is an important parameter for solvent and represents the ability of salvation for solute with a general influence on the fluorescence properties. It was reported that when the conjugated aromatic polymers is excitant with the π–π* transition, the excitation state could be much stable and existed for a longer time in solvent with a higher polarity [36-37]. In case of PANI–like polymer, the shift on emission spectra could be described as solvatochromic stokes shift [38]. Although the solvatochromic on emission λ_{max} is little, it could be observed that the relationship between dielectric constant and emission λ_{max} for each solvent showed poor linearity (Figure 5.6). The dependence of fluorescence emission on fluorophore concentration in different solvents was also determined. In Figure 5.7, the relationship between I_0/I and the fluorophore concentration of [Ar] at 2, 1, 0.5, 0.25, 0.12 $\times$ 10^{-4} M is plotted. Here, I_0 means the original fluorescence intensity, which is taken as the fluorescence intensity at the maximum emission wavelength. Both results showed a nearly linearity with the fluorophore concentration of the P9AA, especially for the THF solvent system. From these absorbance and fluorescence study, it was reasonable to consider that the main
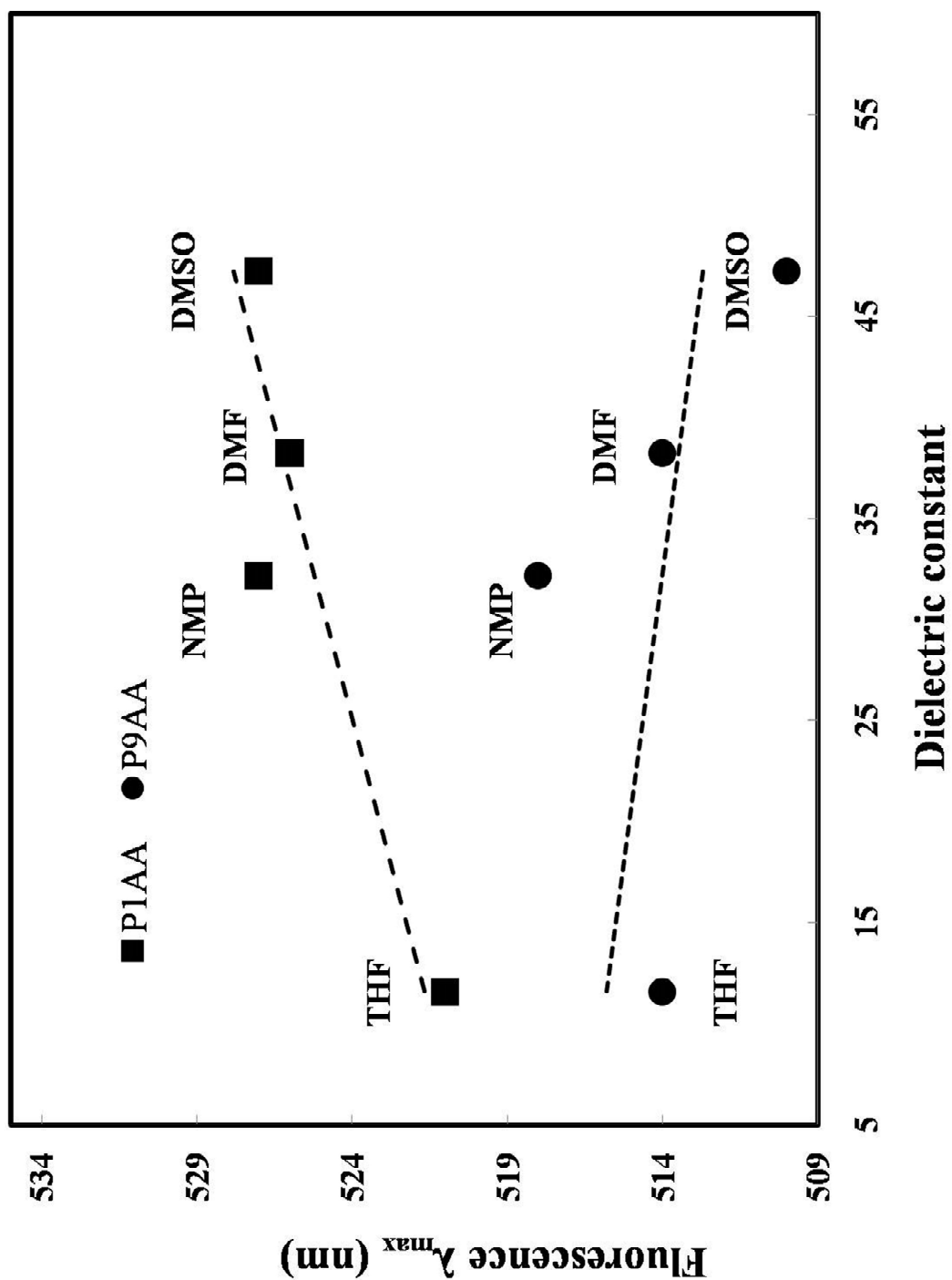
Figure 5.6 Fluorescence maximum wavelengths (λ_{max}) of PAAs measured in several

solvents with different dielectric constant.
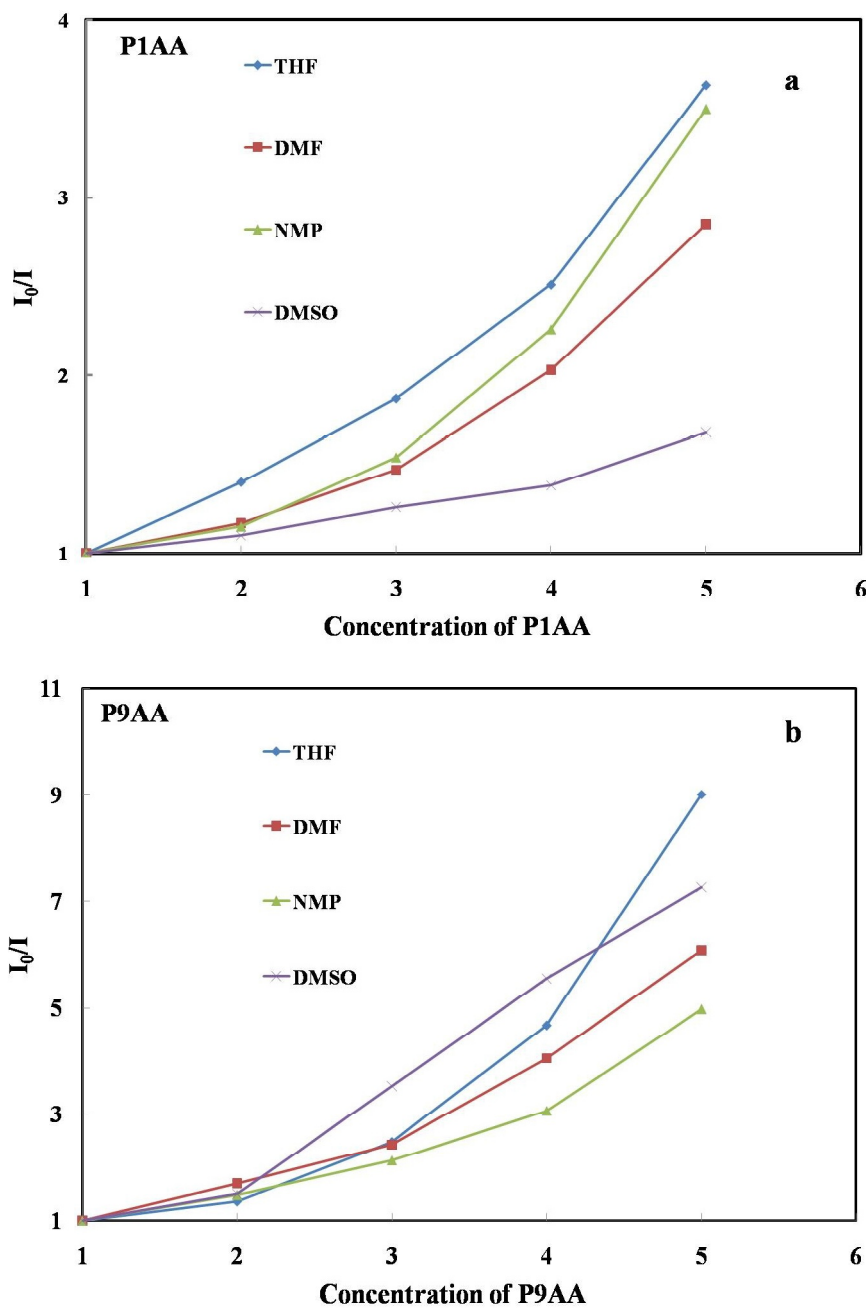
Figure 5.7 Summary of the Stern–Volmer plots associated with the PAAs in the several organic solvents. ([Ar]= (2, 1, 0.5, 0.25, 0.12)×10^{-4} M, Excitation at 360 nm).

chain anthracene moieties in PAAs were close enough to produce π–π stacking interaction by the forming of excimer in their solutions, especially in cases of P1AA [39-40].

5.3.3 Characterization of P1AA/PSS and P1AA/PVA composite film.

As described in Chapter 4, PSS became good polymeric dopant in the polypyrrole copolymers. In addition, the film forming could be supported by the addition of PSS. It was known that the PVA and PSS were suitable film-former applied for preparation composite films with conductive polymers [42, 43]. Because P1AA shows better and stable fluorescence emission than P9AA, P1AA was chosen to be a suitable fraction for the film formation.

Figure 5.8 shows the UV-vis spectra for the PSS/P1AA composite film (a) and PVA/P1AA composite film (b) at 1, 3, 5, 10 wt% amount of PSS or PVA in the casting solution. Under the affect of strong π-π stacking between anthracene moieties, the powdery P1AA (red solid line) showed greatly red shift to weaker absorption around 295 nm [18, 24]. For the composite films, compared with the UV spectra of neat P1AA solution (red dotted line), PSS composite films shows a tiny red shift at the peak of
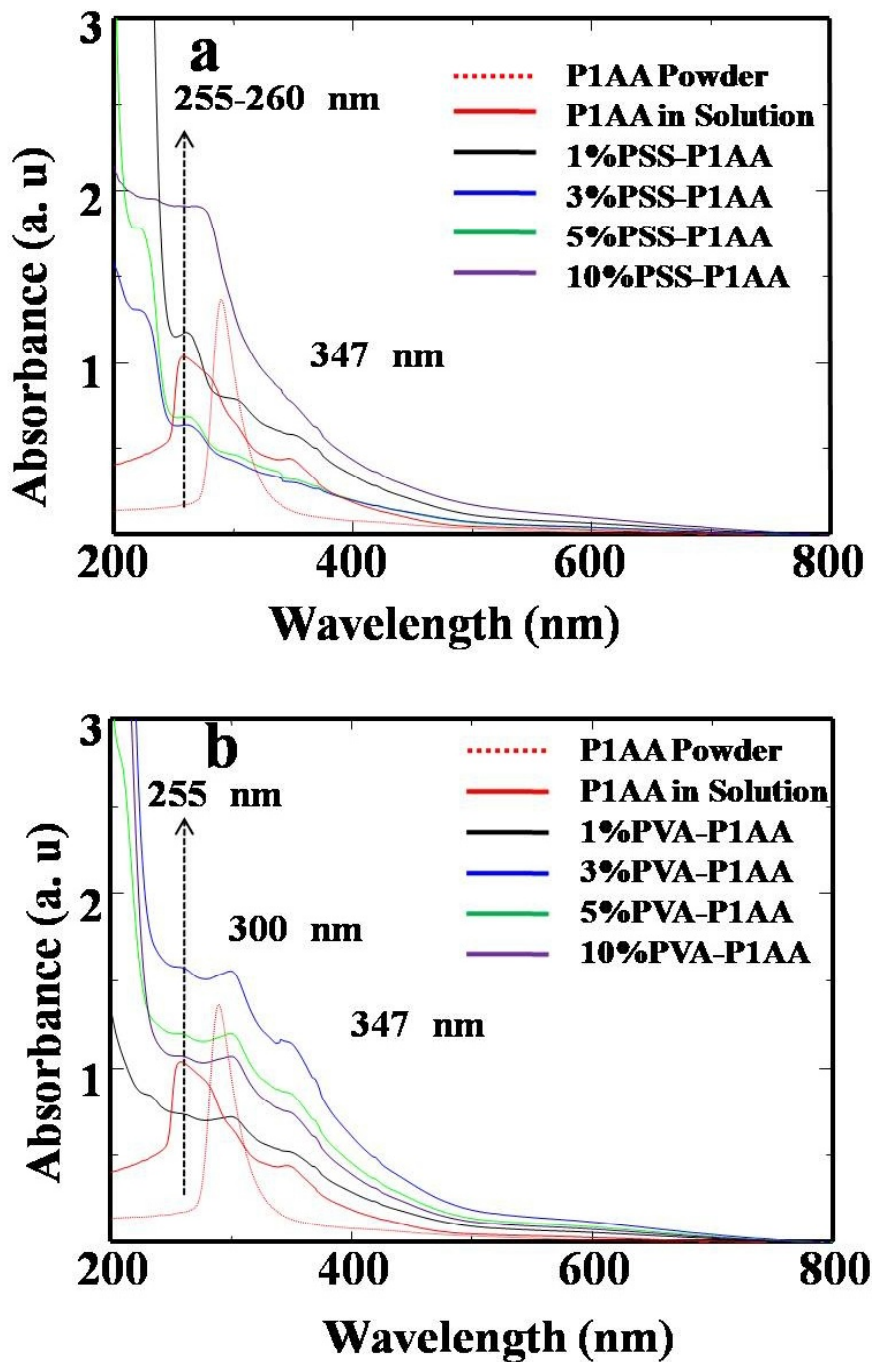
Figure 5.8 UV-vis spectra of PSS/P1AA composite films (a) and PVA/P1AA

composite films with different composition ratio. Powdery P1AA (red dotted line) and

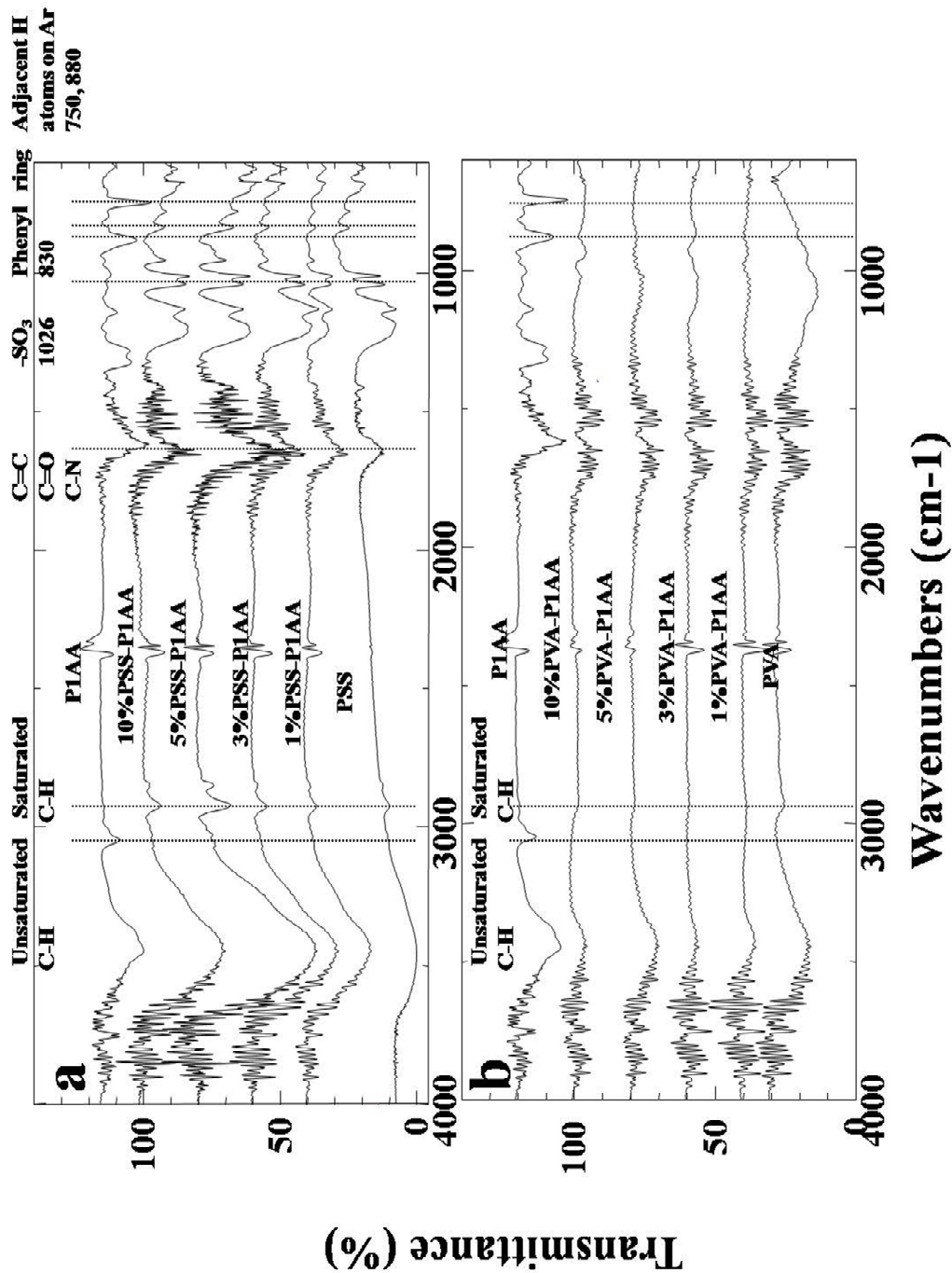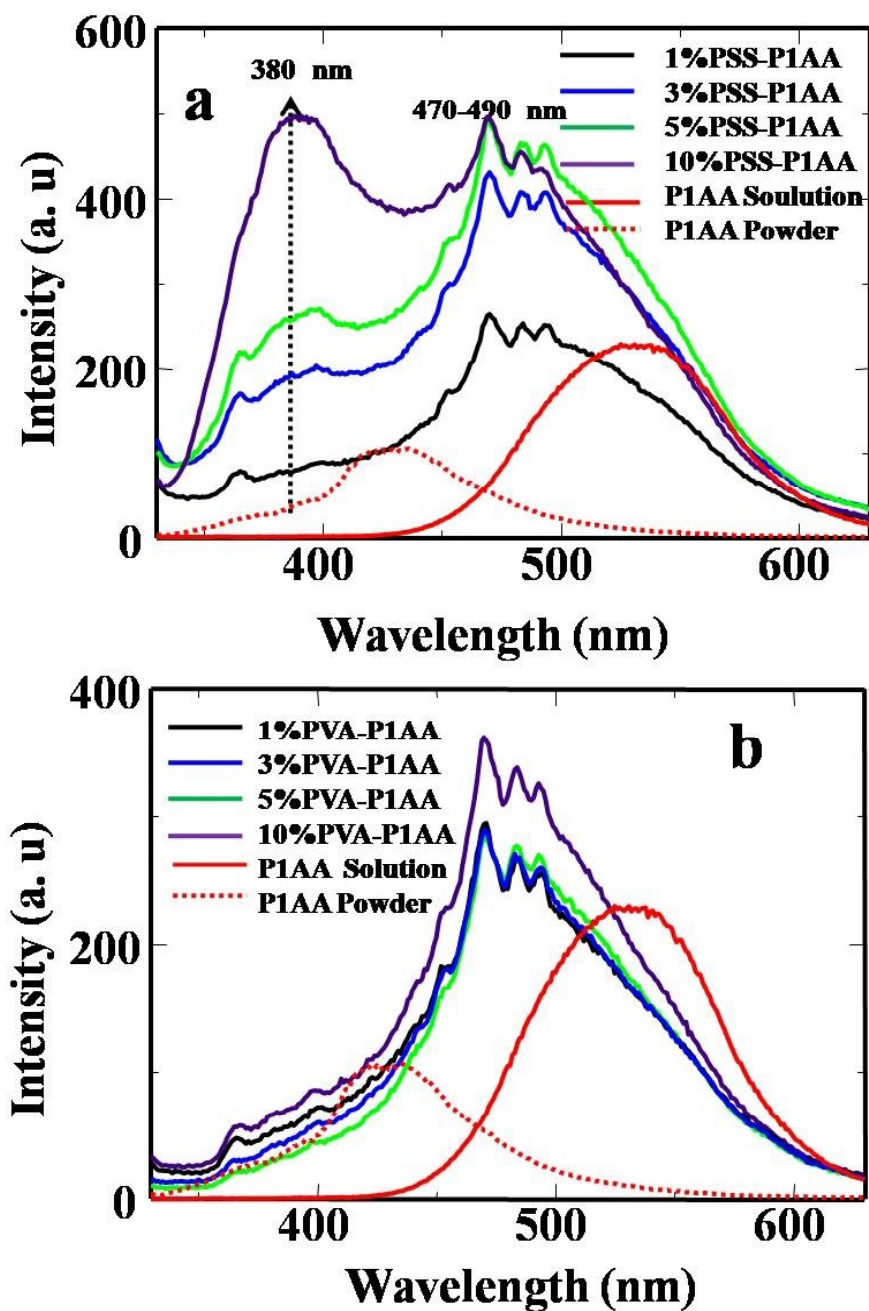P1AA solution (red soild line) was shown as a comparison.

**Figure 5.9** IR spectra of each composite film comparison with neat P1AA, PSS and PVA.

Figure 5.10 Fluorescence spectra of PSS/P1AA composite films (a) and PVA/P1AA

composite films. The exited wavelength was at 320 nm. Powdery P1AA (red dotted line)

and P1AA solution (red solid line) were shown as a comparison.

π–π* transition of anthracene moiety, which shifted to longer wavelength from 255 to 260 nm. In case of PVA, no shift was observed. This was like caused by the electrostatic interaction between aminoanthracene conjugated backbone and the sulfo group [1]. It was obviously noted that the peak at 300 and 340 nm originated from the n-π* transition adjacent anthracene moieties were enhanced for both composited films. It was consider that in the composite films, the agglomeration of conjugated chain in P1AA (intermolecular π-π stacking) was weaken by wrapping with PVA or PSS. Meanwhile, the FT-IR spectra for each composite film were measured (Figure 5.9). In Figure 5.9b, because of the well mechanical performance of hydrated PVA composite films, most characteristic peaks could not observe very clearly. In Figure 5.9a, the characteristic peaks of the sulfonic group stretching at about 1134 and 1026 cm^{-1} were observed [1]. The characteristic peaks of the P1AA were seen except the disappeared adjacent H atoms on the anthracene aromatic ring assigned at 750 and 880 cm^{-1} [6]. It was reasonable to attribute to the wrapping of P1AA with PVA or PSS molecular. Figure 5.10 shows the fluorescence spectra of PSS/P1AA composite films (a) and PVA/P1AA composite films exited at 320 nm with different composition ratio. Here, both of these composite films had incontinuous emission peaks at round 470-490 nm. It was quite different in the abserve and present of PSS with P1AA. The P1AA solution

showed a maximum peak at 527 nm assigned to the formation of anthracene dimer or excimer emission [32]. By contrast the P1AA in solution (red solid line), the powdery P1AA showed a broad emission peak at 430 nm. It was known that anthracene molecular owns three sharply emission peaks at 385, 405, 430 nm, respectively [32]. The solid P1AA emitted monomer-like emission spectra in the film. In DMSO solution, the π-conjugated anthracene main chains were stretch and removable and solvated in DMSO. Therefore, they were easily stacked together freely to form the unstable dimer or excimer [34].

Then, the film properties of the composites with PSS were shown. Figure 5.11 shows surface morphology of the composite films. It could observe that both PSS and P1AA composite films formed an irregularity blocky structure on the surfaces. For the neat PSS film, it was considered that the existence of sodium salt might make the irregularly surface morphology rough. With the addition of PSS in the composite films, the surface morphology became more roughly, probably due to the PSS warping with the P1AA conjugated chains by the electrostatic interaction. The thickness of the PSS/P1AA composite films could be calculated from the cross-sectional images, rising from 12 to 23 μm for 1wt%PSS/P1AA and 10wt%PSS/P1AA composite films. It also could observe that the blocky particulate structure in cross-sectional might be attributed
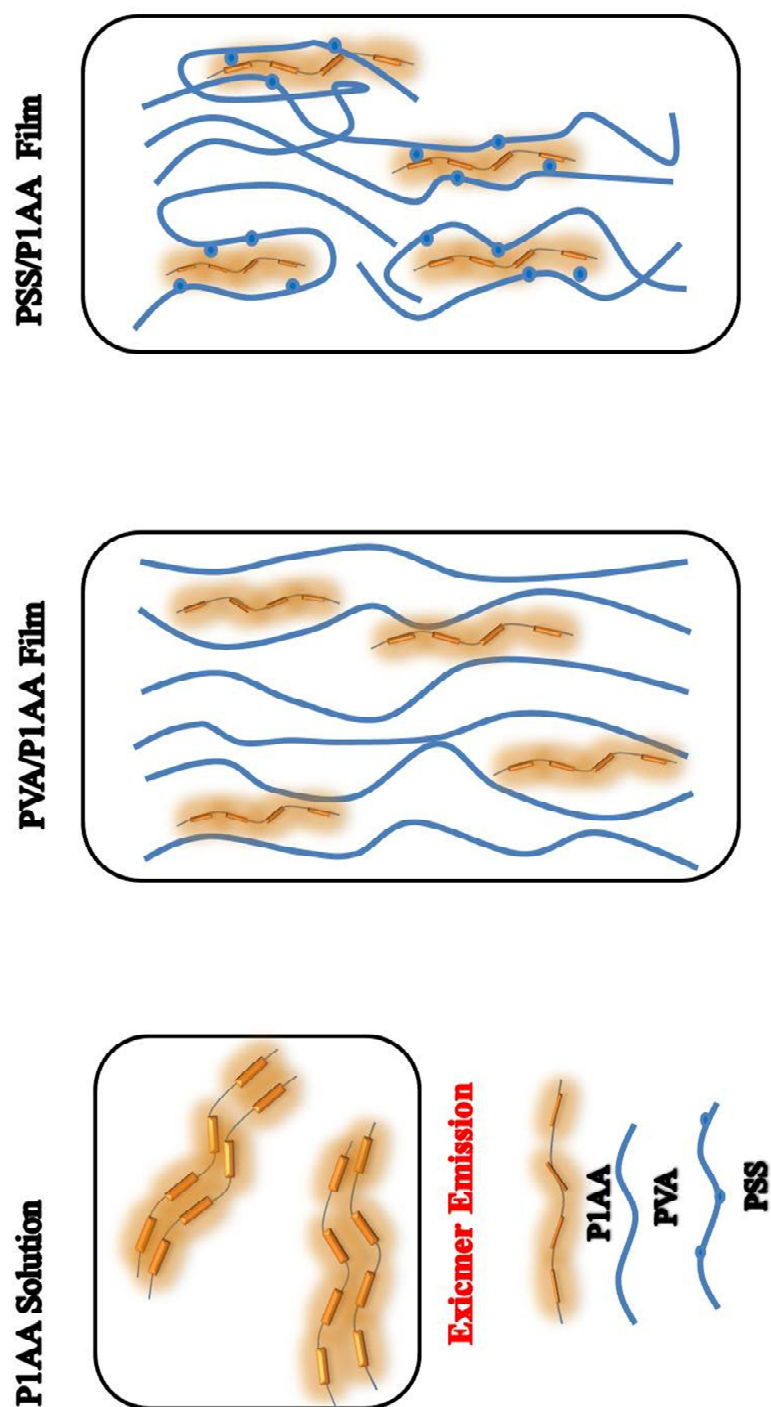
Scheme 5.3 Illumination of the relationship between emission spectra and the film

forming process.
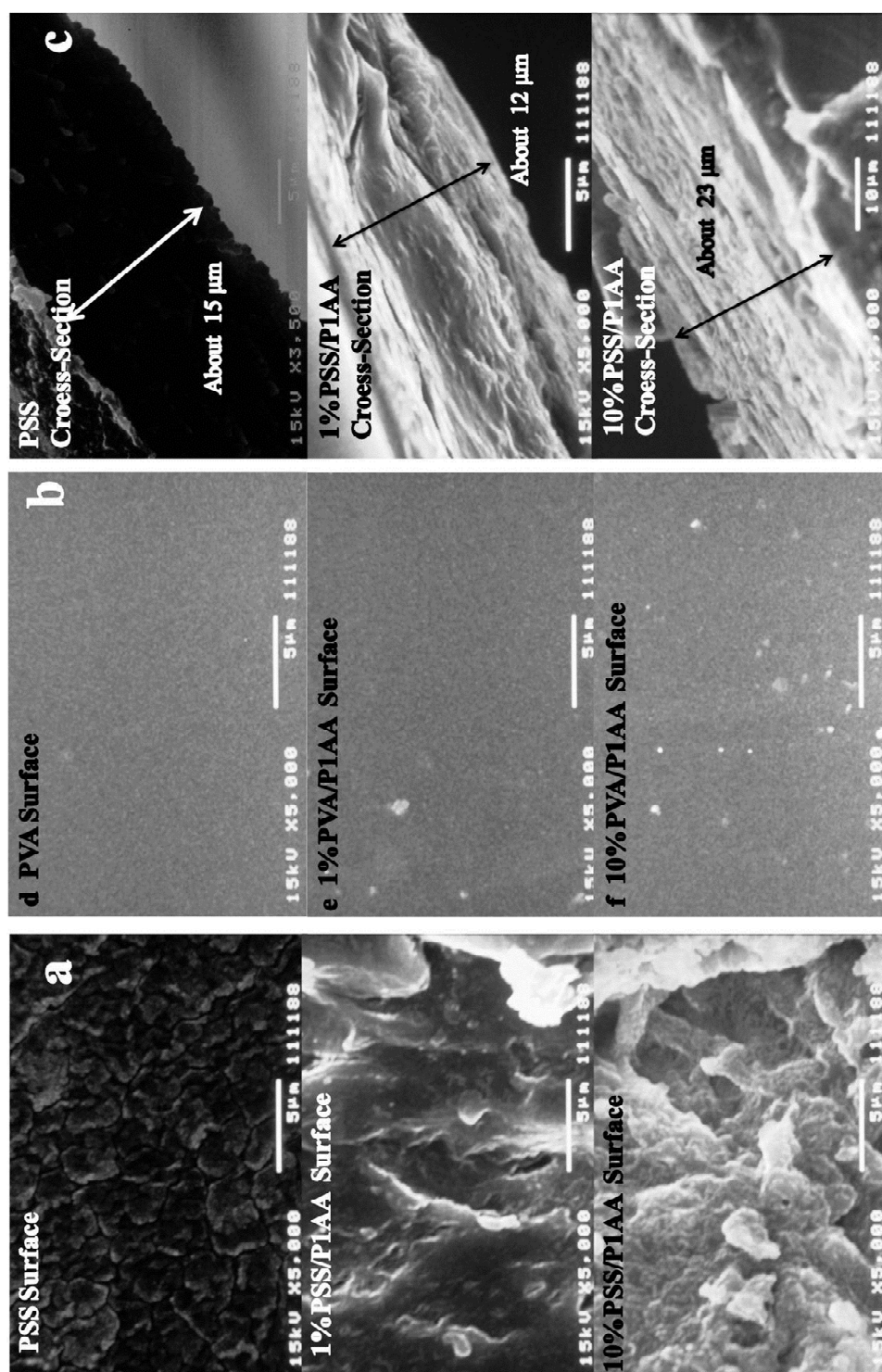
Figure 5.11 Surface (a), cross-sectional (c) SEM images of PSS and PSS/P1AA

composite films and surface images of PVA and PVA/ composite films (b).

to the interaction between the PSS and P1AA molecular chain in the film formation

process. In Figure 5.11c, the PVA composite films expressed flat morphology and

showed almost similarly surface morphology compared with the PVA films. In this case,

it was considered that the P1AA was uniformly distributed in the composite films.

Figure 5.12 shows the 3D-AFM images for each composites films. The topo AFM

images directly suggest that the PSS/P1AA films showed the presence of particulate

surfaces, exhibiting a rougher surface than PVA/P1AA composite films. The roughness

of the PSS composte film increased with the addition of the PSS contents, probably duo

to the enhanced interaction bwtween PSS and P1AA [44-45]. Figure 5.13 summarizes

the obtained AFM parameters of such composited films, including the surface R_{rms} and

the average surface area of the nano–particulates. For the PSS composite film, the value

of the R_{rms} was greatly increased from 0.58 for PSS film to 11.2 nm for 10 wt% in the

PSS/P1AA composite. Similarly, the average surface area was also increased from 214

to 55300 nm^2, when the PSS was high at 10 wt% content. The PVA composite films had

no changes when the PVA contents increased. This comparison proved that the

interaction between PSS and P1AA promoted the PSS warping with the P1AA

conjugated chains and agglomeration in the composite film. These support the
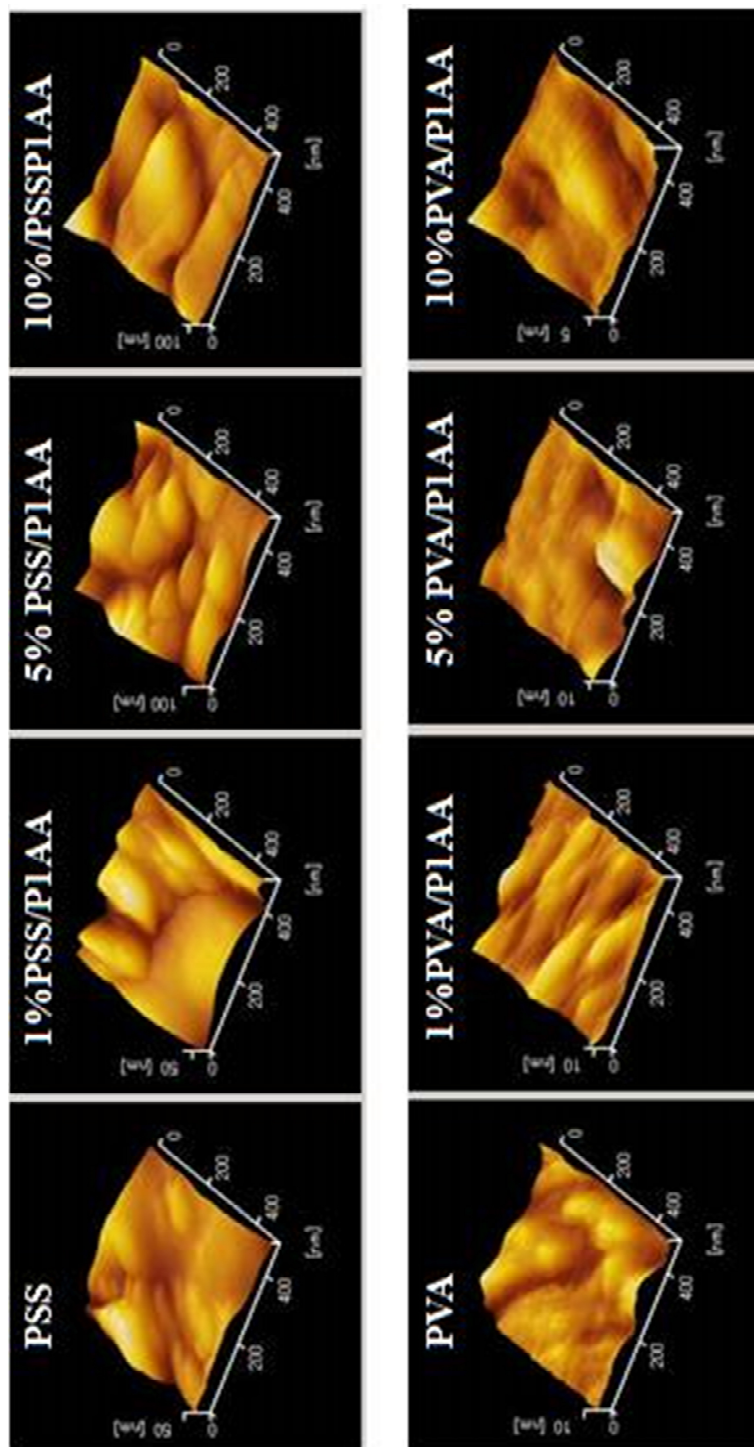
illustrated structure in Scheme 5.3.

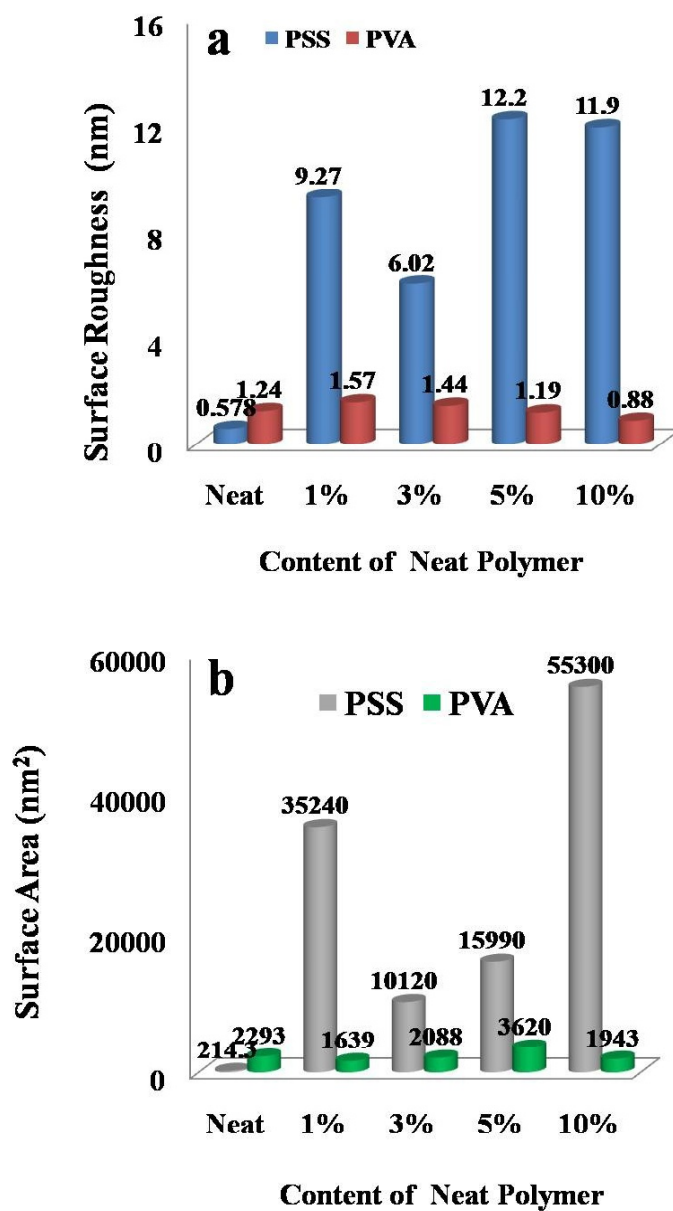**Figure 5.12** Topo AFM images of each composite films.

Figure 5.13 AFM parameters of R*rm* (a) and surface area (b) for each composite films

5.4 Conclusions

In this chapter, new conjugated polymer having anthryl group were prepared, regarding chemical structure and optical properties of soluble π–conjugate polyaminoanthracenes. H NMR and FT–IR studies revealed that the possible chemical structure was confirmed in the presence of functional moieties on the conjugated backbone of PAAs. Results suggested that the P1AA might show high possibility to form stable anthracene excimer relative to that of P9AA, due to the inter chain interactions of the anthracene moiety being easily possible for the P1AA. The solvent effect of fluorescence emission on fluorophore in different solvents was evaluated. The results concluded that conjugated PAAs excited with the π–π^* transition, the excitation state could be much stable and existed for a longer time in solvent with a higher polarity. The fluorescent composite films consisting of P1AA and PVA or PSS could be prepared by the electrostatic interaction between the P1AA and SO^{3-} group of PSS. This was greatly affected on the surface morphology and the optical properties for P1AA/PSS composite films by the wrapping of P1AA with PVA or PSS molecular.

5.5 References

[1]. Pietsch, M.; Bashouti, M. Y.; Christiansen, S. The role of hole transport in hybrid inorganic/organic silicon/ poly (3,4-ethylenedioxy-thiophene): poly (styrenesulfonate) heterojunction solar cells. *J. Phys. Chem. C* **2013**, *117*, 9049.

[2]. Zou, W.; Yan, Y.; Fang, J.; Yang, Y.; Liang, J.; Deng, K.; Yao, J.; Wei, Z. Biomimetic superhelical conducting microfibers with homochirality for enantioselective sensing. *J. Am. Chem. Soc*. **2014**, *136*, 578.

[3]. Tao, Y.; Ma, B.; Segalman, R. A. Self-assembly of rod-coil block copolymers and their application in electroluminescent devices. *Macromolecules* **2008**, *41*, 7152.

[4]. Shinde, S. D.; Jayakannan, M. Probing the molecular interactions at the conducting polyaniline nanomaterial surface via a pyrene fluorophore. *J. Phys. Chem. C* **2010**, *114*, 15491.

[5]. Raigaonkara, B. V.; Vijayana, L. P.; Chawlab, S.; Dubeya, R. N.; Qureshia, M. S. Structural and spectral investigations of anthracene doped polyaniline. *Synth. Met*. **2011**, *161*, 348.

[6]. Moon, D. K.; Osakada, K.; Maruyama, T.; Kubota, K.; Yamamoto, T. Synthesis of poly (1-aminonaphthalene) and poly (1-aminoanthracene) by chemical oxidative polymerization and characterization of the polymers. *Macromolecules* **1993**, *26*, 6992.

[7]. Kim, Y. H.; Kwon, S. K. Novel blue-light-emitting polymers based on a diphenylanthracene moiety. *J. Appl. Polym. Sci*. **2006**, *100*, 2151.

[8]. Lyu, Y. Y.; Kwak, J.; Kwon, O.; Lee, S. H.; Kim, D.; Lee, C.; Char, K. Silicon-cored anthracene derivatives as host materials for highly efficient blue organic light-emitting devices. *Adv. Mater*. **2008**, *20*, 2720.

[9]. Vellis, P. D.; Mikroyannidis, J. A.; Bagnis, D.; Valentini, L.; Kenny, J. M. New anthracene-containing phenylene- or thienylene-vinylene copolymers: Synthesis, characterization, photophysics, and photovoltaics. *J. Appl. Polym. Sci*. **2009**, *113*, 1173.

[10]. Fraind, A. M.; Tovar, J. D. Comparative survey of conducting polymers containing benzene, naphthalene, and anthracene cores: Interplay of localized aromaticity and polymer electronic structures. *J. Phys. Chem. B* **2010**, *114*, 3104.

[11]. Troiani, E. P.; Faria, R. C. The influence of the cathodic pretreatment on the electrochemical detection of dopamine by poly (1-aminoanthracene) modified electrode. *Electroanalysis*. **2010**, *22*, 2284.

[12]. Chen, R.; Ling, J.; Hogen–Esch, T. E. Synthesis and spectroscopic studies of macrocyclic polystyrene containing two fluorene units and single 9,10-anthracenylidene group. *Macromolecules* **2009**, *42*, 6015.

[13]. Yamaguchi, I.; Higashi, H.; Sato, M. Synthesis and chemical properties of

photoluminescent self-doped polyanilines. *J. Mater. Sci.* **2009**, *44*, 6408.

[14]. Ikedu, S.; Nishimura, Y.; Arai, T. Kinetics of hydrogen bonding between anthracene urea derivatives and anions in the excited state. *J. Phys. Chem. A* **2011**, *115*, 8227.

[15]. Mori, H.; Tando, I.; Tanaka, H. Synthesis and optoelectronic properties of alternating copolymers containing anthracene unit in the main chain by radical ring-opening polymerization. *Macromolecules* **2010**, *43*, 7011.

[16]. Tanemura, K.; Suzuki.; Horaguchi, T. Synthesis of sulfonated polynaphthalene, polyanthracene, and polypyrene as strong solid acids via oxidative coupling polymerization. *J. Appl. Polym. Sci.* **2013**, *113*, 1173.

[17]. Chou, T. C.; Wu, R. T.; Liao, K. C.; Wang, C. H. N-1- and N-2-anthryl succinimide derivatives: C-N bond rotational behaviors and fluorescence energy transfer. *J. Org. Chem.* **2011**, *76*, 6813.

[18]. Sato, S.; Nakamura, T.; Nitobe, S.; Kiba, T.; Hosokawa, K.; Kasajima, T.; Otsuka, I.; Akimoto, S.; Kakuchi, T. Structure and excitation relaxation dynamics of dimethylanthracene dimer in a γ-cyclodextrin nanocavity in aqueous solution. *J. Phys. Chem. B* **2006**, *110*, 21444.

[19]. Huang, M. R.; Huang, S. J.; Li, X. G. Facile synthesis of

polysulfoaminoanthraquinone nanosorbents for rapid removal and ultrasensitive fluorescent detection of heavy metal ions. *J. Phys. Chem. C* **2011**, *115*, 5301.

[20]. Kaur, K.; Kumar, S. 1-Aminoanthracene-9,10-dione based chromogenic molecular sensors: effect of nature and number of nitrogen atoms on metal ion sensing behavior. *Tetrahedron*. **2010**, *66*, 6990.

[21]. Druzhinin, S. I.; Galievsky, V. A.; Yoshihara, T.; Zachariasse, K. A. Intramolecular charge transfer and dielectric solvent relaxation in n-propyl cyanide. N-phenylpyrrole and 4-dimethylamino-4-cyanostilbene. *J. Phys. Chem. A* **2006**, *110,* 12760.

[22]. Yang, B.; Li, G.; Zhang, X.; Shu, X.; Wang, A.; Zhu, X.; Zhu, J. Hg^{2+} detection by aniline-based conjugated copolymers with high selectivity. *Polymer*. **2011**, *52*, 2537.

[23]. H. J. Yen, G. S. Liou. Novel thermally stable triarylamine-containing aromatic polyamides bearing anthrylamine chromophores for highlyefficient green-light-emitting materials. *J. Polym. Sci. A: Polym. Chem*. **2008**, *46*, 7354.

[24]. S. Ikedu, Y. Nishimura, T. Arai. Kinetics of hydrogen bonding between anthracene urea derivatives and anions in the excited state. *J. Phys. Chem. A* **2011**, *115*, 8227.

[25]. Prokes, J.; Trchova, M.; Hlavata, D.; Stejskal, J. Conductivity ageing in

temperature-cycled polyaniline. *J. Polym. Degrad. Stab*. **2002**, *78*, 393.

[26]. Nicolau, Y. F.; Beadle, P. M.; Banka, E. Spectrophotometric investigation of CSA-protonated polyaniline solutions and films. *Synth. Met*. **1997**, *84*, 585.

[27]. Zhang. J, Shan. D, Mu. S. L. Chemical synthesis and electric properties of the conducting copolymer of aniline and o-aminophenol. *J. Polym. Sci. A: Polym. Chem*. **2007**, *45*, 5573.

[28]. Mu, S. L.; Yang, Y. F. Spectral characteristics of polyaniline nanostructures synthesized by using cyclic voltammetry at different scan rates. *J. Phys. Chem. C* **2008**, *112*, 11558.

[29]. Gill, M. T.; Chapman, S. E.; DeArmit, C. L.; Aines, F. L.; Dadswell, C. M.; Stamper, J. G.; Lawless, G. A.; Billingham, N. G.; Ames, S. P. A study of the kinetics of polymerization of aniline using proton NMR spectroscopy. *Synth. Met*. **1998**, *93*, 227.

[30]. Huang, J. X.; Kaner. R. B. The intrinsic nanofibrillar morphology of polyaniline *Chem. Comm*. **2006**, 367.

[31]. Yu, B.; Jiang, X. S.; Yin, J. Multiresponsive square hybrid nanosheets of POSS-Ended hyperbranched poly (ether amine) (hPEA). *Macromolecules* **2012**, *45*, 7135.

[32]. Shirashi, Y.; Miyamoto, R.; Hirai, T. Temperature-driven on/off fluorescent indicator of pH window: an anthracene-conjugated thermoresponsive polymer. *Tetrahedron. Lett*. **2007**, *48*, 6660.

[33]. Hasewage, W.; Suzuki, A.; Matsumura, S.; Toshima, K. Molecular design, chemical synthesis, and evaluation of novel anthracene derivatives as a new family of protein photo cleavers. *Sci. Tech. Adv. Mater*. **2006**, 7, 169.

[34]. Subudhi, P. C.; Kanamaru, N.; Lim, E. C. Luminescence from a sandwich dimer of anthracene. *Chem. Phys. Lett.* **1975**, *32*, 503.

[35]. Miyamoto, K.; Iwanaga, T.; Toyota, S. Chemistry of anthracene–acetylene oligomers XVI. Influence of conformation of 9,10-anthrylene rotors on structures and self-association properties of macrocyclic arylene-alkynylene oligomers. *Chem. lett.* **2010**, *3*, 288.

[36]. Van Hal, P. A.; Beckers, E. H. A.; Peeters, E.; Apperloo, J. J.; Janssen R. A. J. Photoinduced intermolecular electron transfer between oligo(p-phenylene vinylene)s and N-methylfulleropyrrolidine in a polar solvent. *Chem. Phys. Lett.* **2000**, *328*, 403

[37]. Apperloo, J. J.; Janssen, R. A. J. Improved expression of charge-carrier mobility in disordered semiconducting polymers considering dependence on temperature, electric field and charge-carrier density. *Synth. Met.* **1999**, *101*, 373.

[38]. Surwadea, S. P.; Agnihotraa, S. R.; Duaa, V.; Kolla, H. S.; Zhang, X.; Manoharb, S. K. A fluorescent molecular switch driven by the input sequence of metal cations: An azamacrocyclic ligand containing bipolar anthracene fragments. *Synth. Met*. **2009**, *159*, 2153.

[39]. Nishimura, G.; Maehara, H.; Shiraishi, Y.; Hirai, T. *Chem. Eur. J.* **2008**, *14*, 259.

[40]. Egbe, D. A. M.; Tiirk, S.; Rathgeber, S.; Kiiuhnlenz, F.; Jadhav, R.; Wild, A.; Birckner, E.; Adam, G.; Pivrikas, A.; Cimrova, V.; Knor, G.; Sariciftci, N. S.; Hoppe, H. *Macromolecules* **2010**, *43*, 1261.

[41]. Morishima, Y.; Kobayshi, T.; Nozakura, S. Preferential excimer emission from amphiphilic alternating copolymer of 2-vinylanphthalene and maleic acid in aqueous solution. *Macromolecules* **1987**, *20*, 807.

[42]. Jang, J.; Cho, J. Fabrication of water-dispersible polyaniline-poly (4-styrenesulfonate) nanoparticles for inkjet-printed chemical-sensor applications. *Adv. Mater*. **2007**, *19*, 1772.

[43]. Naidu, B. V. K.; Sairam, M.; Raju, K. V. S. N.; Aminabhavi, T. M. Pervaporation separation of water + isopropanol mixtures using novel nanocomposite membranes of poly(vinyl alcohol) and polyaniline. *J. Membr. Sci*. **2005**, *260*, 142.

[44]. Schrote, K.; Frey, M. W. Effect of irradiation on poly (3,

4–ethylenedioxythiophene): poly(styrenesulfonate) nanofiber conductivity. *Polymer*.

2013, *54*, 737.

[45]. Simoes, F. R.; Marchesi, L. F. Q. P.; Pocrifka, L. A.; Pereira, E. C. Investigation

of electrochemical degradation process in polyaniline/polystyrene sulfonated

self–assembly films by impedance spectroscopy. *J. Phys. Chem B* **2011**, *115*, 11092.

Chapter 6

Conjugated Polyaminoanthracenes for Sensitive Fluorometric Detection of Heavy Metal Irons

ABSTRACT: Conjugated polymers constructed by anthracene structure in main chain were synthesized through facile chemical oxidative polymerization. Metal ion responsive properties of PAAs were investigated by UV-vis absorption spectra and Fluorescence spectra. The interaction of ions with the bonding site of PAAs were formed, according to maximum absorption peaks were shift slightly to longer wavelength with the addition of metal ions. Comparative investigations of adsorption behaviors revealed the Polyaminoanthracenes showed detection capacity towards several metal ions. Especially P1AA suggested that such fluorescence result of the anthracene moiety was applicable for the Pb^{2+} sensitivity by the quenching behavior. In combination with UV-vis results, this is potential ability to use as sensitive fluorometric for detection of Pb^{2+}.

6.1 Introduction

In recent years, electrical conductive polymers have been widely investigated due to their increasing numerous of applications. Among them, conductive polymers with anthracene-containing structure in backbone are considerable scientific and industrial interest and valuable for fabrication of organic light emitting diode materials or chemosensors, owing to their strong absorption and high quantum yield [1-4]. Until now most research concerning chemical synthesis of these polymers are confined within Pd-catalyzed coupling reaction or other complex polymerization methods under extreme reaction condition with limitation in preparation and application [5-6]. Only few report pay attention to the simple chemical or electrical method for anthracene-containing conductive polymers [7-9]. Meanwhile, fluorescent chemsensor for detection heavy metal ions has been attracting more and more attention due to their accuracy and simplicity [10-12]. It was reported a lot based on small molecules, including macrocyclic compound linking fluorohphore, inorganic hybrid fluorescent materials, etc [13-14]. However, various disadvantages such as specific detection limit or complex preparation, which greatly restricted their further application. It is attractive to develop polymer-based chemsensor to advance the knowledge of this subject. Compared with small molecules compounds, the research on polymer-based fluorescence chemsensors

for detection heavy metal ions is emerging as an area of current interest in the recent years [15-17]. Therein, conjugated polymers having polyfunctional groups, such as O, N or S atoms could show ability to coordinate and detect the different metal ions. Also, the repeated π-π conjugated unit along the backbone could enlarge the fluorescence signal to improve the sensitivity of the chemsensor [18]. Some effort has been done to synthesis of anthracene-containning structure polymers and to expand their application [19-20]. However, still little is known about such polymeric fluorescent chemsensor for detection heavy metal ions.

In the present study, we report facile chemical oxidative polymerization of 1-aminonathracene (1-AA) and 9-aminoanthracene (9-AA) by the presence of $FeCl_3$ catalyst (Scheme 6.1) and extend their application for effective fluorescent detection of heavy metal ions.
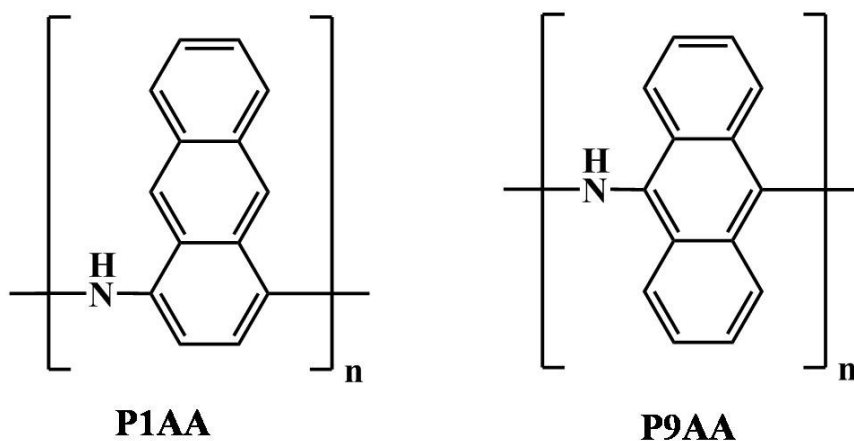
Scheme 6.1 Calculated structures of polyaminoanthracenes.

6.2 Experimental Section

6.2.1 Reagents

Poly (1-aminoanthracene) and poly (9-aminoanthracen) were synthesized according to the previously reported procedures as followed Chapter 5. Other chemicals were purchased and used as received.

6.2.2 Measurments

UV-vis spectra in solutions were recorded on a Jasco UV-570 spectrophotometer at room temperature. Photoluminescence property of polymers doped with various dopants was studied by using FP-5300PC spectrophotometer at room temperature.

6.2.3 Metal ion responsive titration

Each metal ion responsive experiment was carried out in a quartz cell with 4.0 ml PAAs DMSO solution with a fixed concentration (1.0×10^{-5} M). A variety of metal nitrate aqueous solutions in an original ion concentration range from 1.0×10^{-5} to 1.0×10^{-3} M were used for the titration. Titration experiments were performed by successive adding aliquots of 2 µl selected metal ion solutions into the polymers DMSO solution for one time. The totally addition volume for metal ion solutions was 10 µl for

each ion concentration. The volume of added metal ion solution was negligible.

Therefore, it could be calculated that the metal ion concentration in the quartz cell was 0,

0.02, 0.04, 0.06, 0.08, 0.1, 0.2, 0.4, 0.6, 0.8, 1.0) $\times 10^{-4}$ M for each adding time when the

original ion concentration range from 1.0×10^{-4} to 1.0×10^{-3} M, as shown in Scheme 6.2.
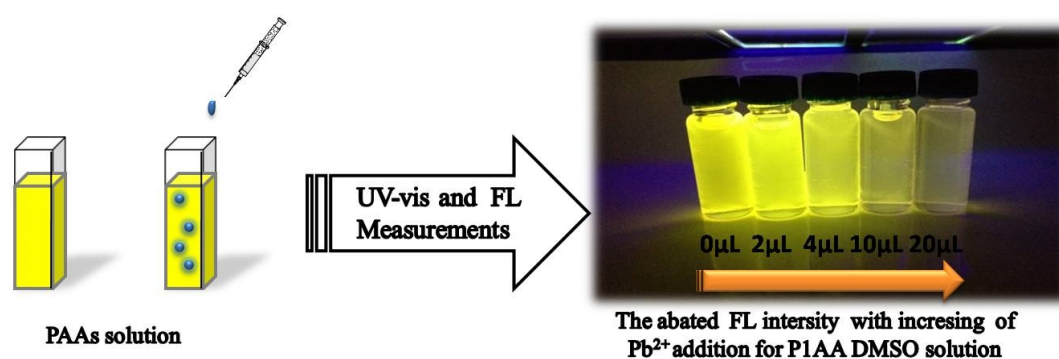
Scheme 6.2 Schematic diagram of Metal ion responsive titration

6.3 Results and Discussions

6.3.1 UV-vis spectra with addition of metal ions

Metal ion responsive of PAAs was investigated by UV-vis absorption spectra. Hereby,

the mole ratio between added polymers and metal ions was 10:1, when the maximum

concentration of ions was added. Figure 6.1 and 6.2 showed the UV-vis spectra of P1AA

and P9AA in the absence and presence of Pb^{2+} and Li^+ with increasing addition amount,

respectively. Obviously, with the increasing of addition of Pb^{2+}, the UV absorbance for

both of the PAAs was increased. In case of addition of Li^+, there was only an unobvious

reduction. In Figure 6.3, the change of the absorption spectra for PAAs ([Ar] $=1.0\times10^{-5}$

M) in the absence and presence of several metal ion in their aqueous solutions ([M]

$=1.0\times10^{-4}$ M) were presented. Both polymers exhibited a strong absorption band around

255 nm assigned to the π-π* transition of anthracene moiety and broad region of

absorption peak from 300 nm to 500 nm probably originated from the adjacent

anthracene moieties [21]. In details, by addition of Pb^{2+} ion into the polymer solution,

the absorption spectra showed a remarkable increase in intensity at 255 nm but a tiny

increase at 430 nm. On the contrary, with the increasing of addition concentration for

other metal ions, the absorbance intensity showed a tiny reduction at different level. The

maximum absorption reduction was observed in the case of Cd^{2+} for both polymers. It

could be observed that the position of maximum absorption peaks was shifted slightly

toward longer wavelength side, when the metal ion was added. This implied that the

heavy metal ions interacted by the coordination with PAAs. Because the presence of

large amount of –NH- and -N= groups on the polymer backbone could efficiently bond

metal ions through sharing lone electron to obtain metal ion coordination complex

[22-23]. It was noted that P1AA showed a better bonding ability for Pb^{2+} in the spectral

change and relatively bonding ability for Cd^{2+}, suggesting that the complex was formed

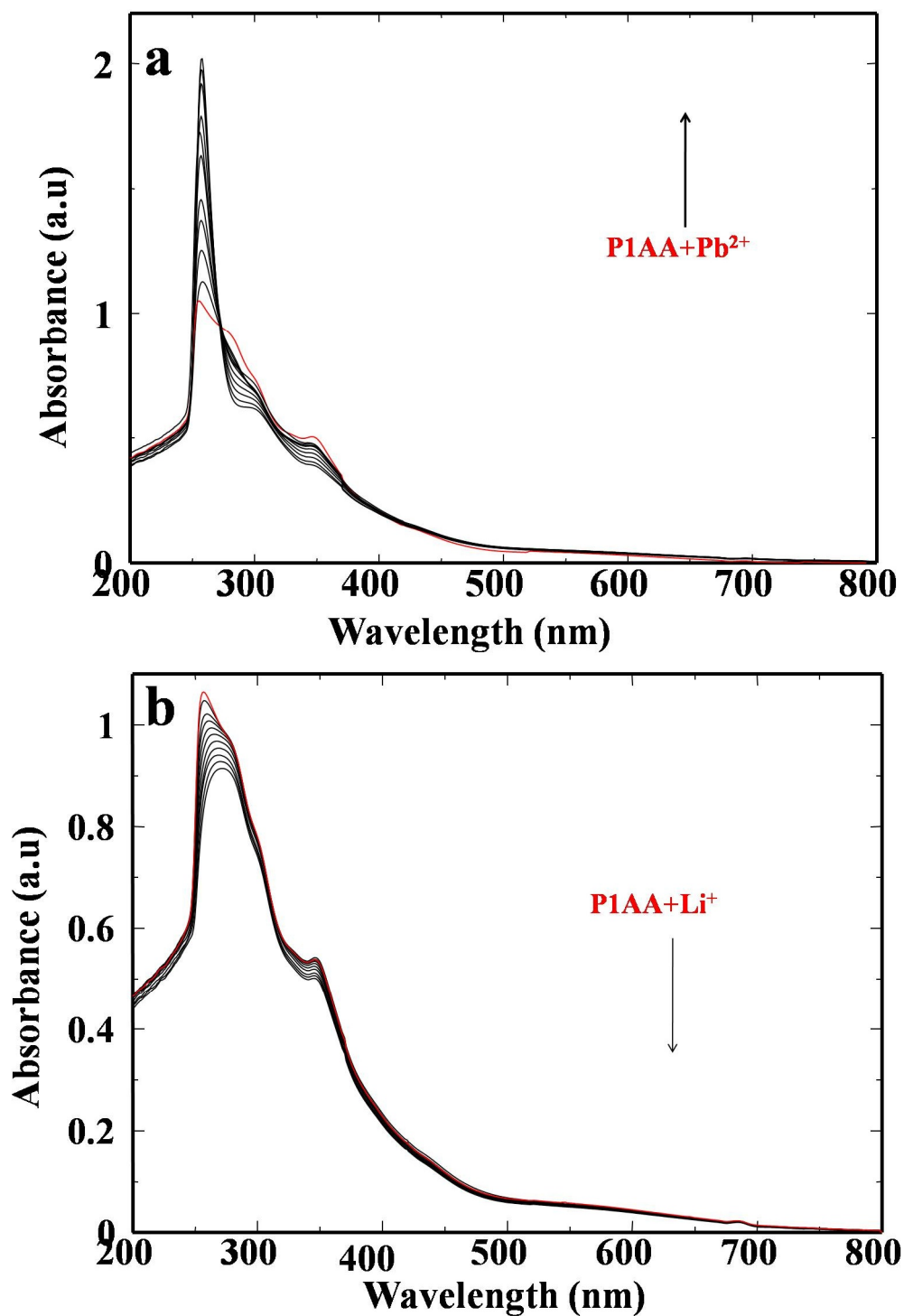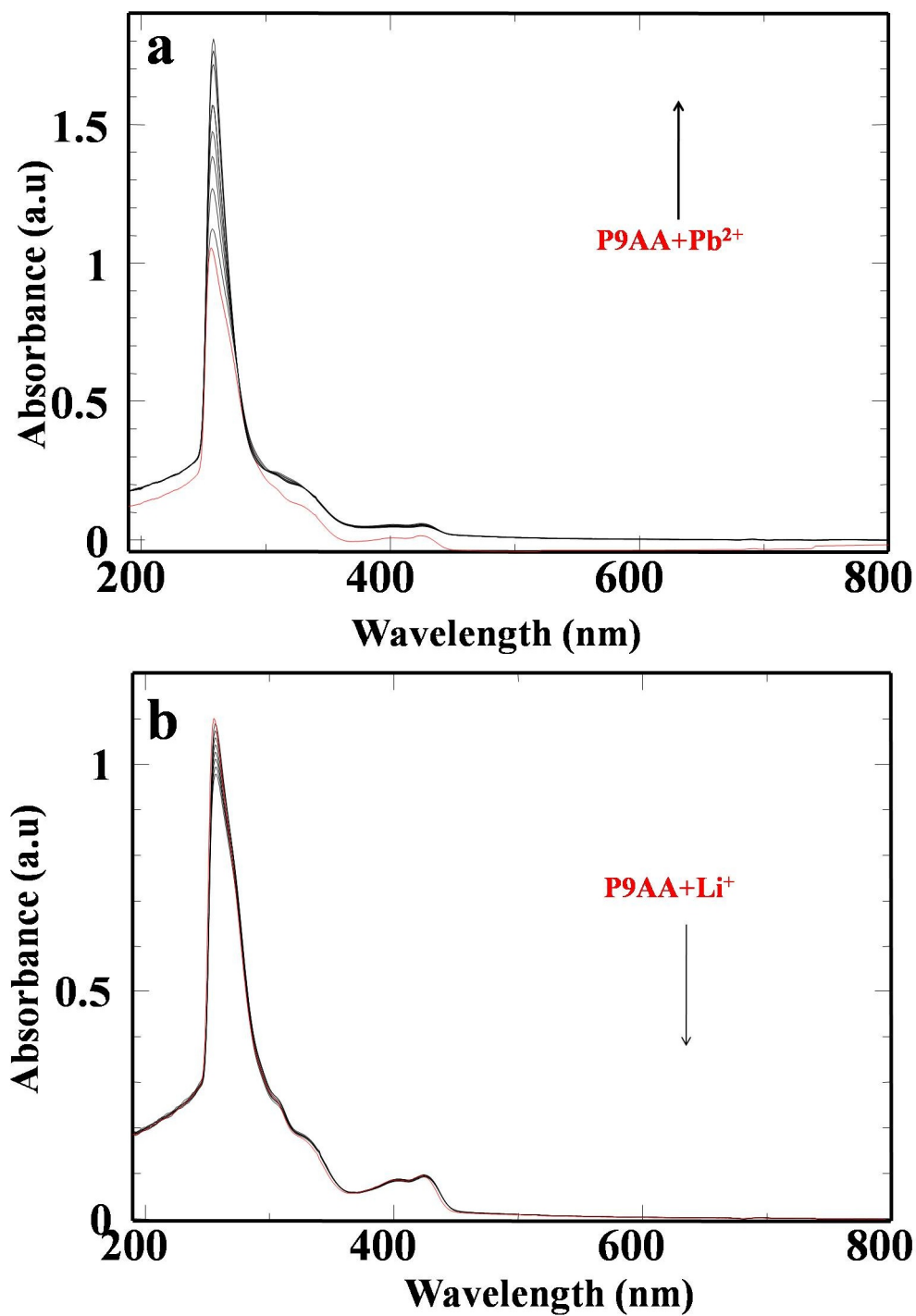**Figure 6.1** UV-vis spectra of P1AA at 1.0×10^{-5}M after the addition of Pb^{2+} and Li^{+}.

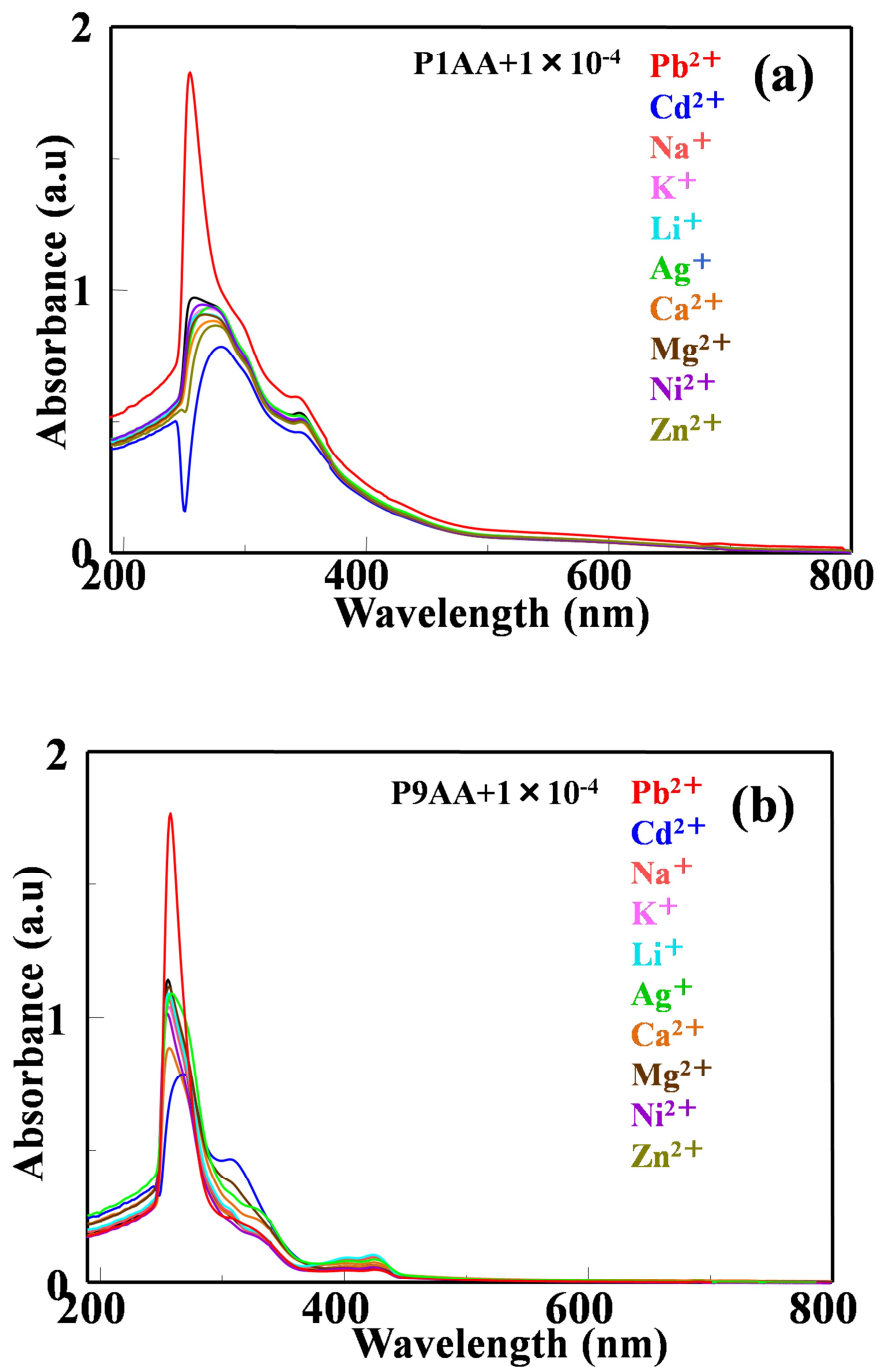$[Pb^{2+}$ and $Li^{+}]=$ (0, 0.02, 0.04, 0.06, 0.08, 0.1, 0.2, 0.4, 0.6, 0.8, 1.0) $\times 10^{-4}$ M.

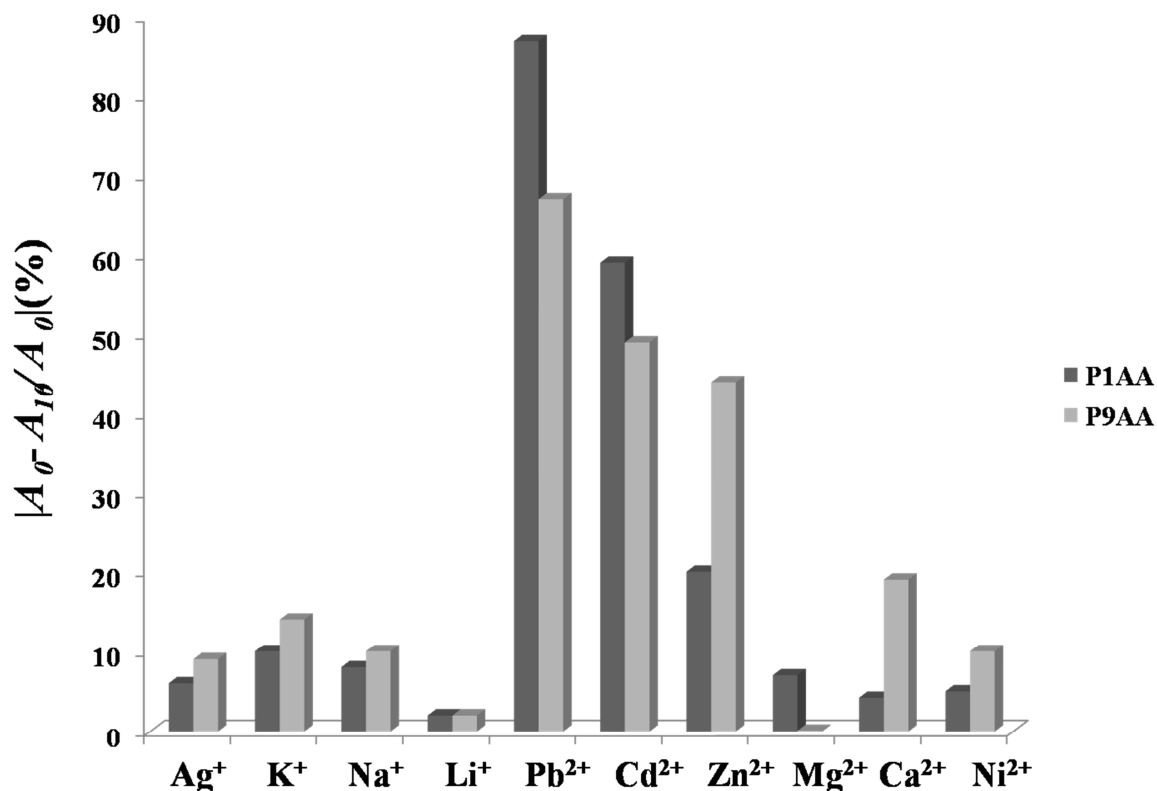**Figure 6.2** UV-vis spectra of P9AA at 1.0×10^{-5}M after the addition of Pb^{2+} and Li^{+}.

$[Pb^{2+}$ and $Li^{+}]= (0, 0.02, 0.04, 0.06, 0.08, 0.1, 0.2, 0.4, 0.6, 0.8, 1.0) \times 10^{-4}$ M.

Figure 6.3 UV-vis spectra of P1AA (a) and P9AA (b) ([Ar]=1.0×10^{-5} M) in the absence

and presence of metal ions ([M]=1.0×10^{-4} M) in DMSO solution.

**Figure 6.4** UV-vis absorbance ($|A_0 - A_{10}/A_0|$) of of Polyaminoanthracenes (1.0×10^{-5} M)

in the presence of various metal ions (1.0×10^{-4} M) in DMSO.

much easier than any other ions. For P9AA, it could perform that significant absorption

ability was shown toward Pb^{2+}, and relatively bonding ability for Cd^{2+} and Zn^{2+} (Figure

6.4).

6.3.2 Fluorescence spectra with addition of metal ions

Figure 6.5 and Figure 6.6 shows fluorescence spectra of P1AA and P9AA with addition of Pb^{2+} and Li^+ ions from 0.02 to 1.0×10^{-4} M concentration. P1AA presented an inconspicuous tailing peak at around 445 nm and a broad peak from 450 to 650 nm with a maximum at 530 nm with typical yellow-green emission. In contrast, broad tailing peaks were observed around 430, 450 nm and another broad peak was visible at 520nm corresponding to green-yellow emission for P9AA. These are attributed from the anthracene moieties existed in backbone [24-25]. The anthracene molecule was well-known to form the relatively stable excimer or exciplex [26]. Therein, the strong peaks appeared at 530 nm could probably be caused by the formation of excimer of anthracene moieties. The P1AA might show high possibility to form stable anthracene excimer relative to that of P9AA, because it was reported that anthracene as a typical polynuclear aromatic molecular had well planarity [27]. Therefore, if the rigidity π-conjugated anthracene plane was rotated by the stereo-hindrance effect, the rotational behaviors of anthracene moieties in backbone could be a greatly influenced on the formation of dimer especially in the case of P1AA. It could imply that the P9AA showed a better planarity to form the relatively unstable face to face excimer between polymer segments [28] such chemical structure of PAAs indicated that the eximer
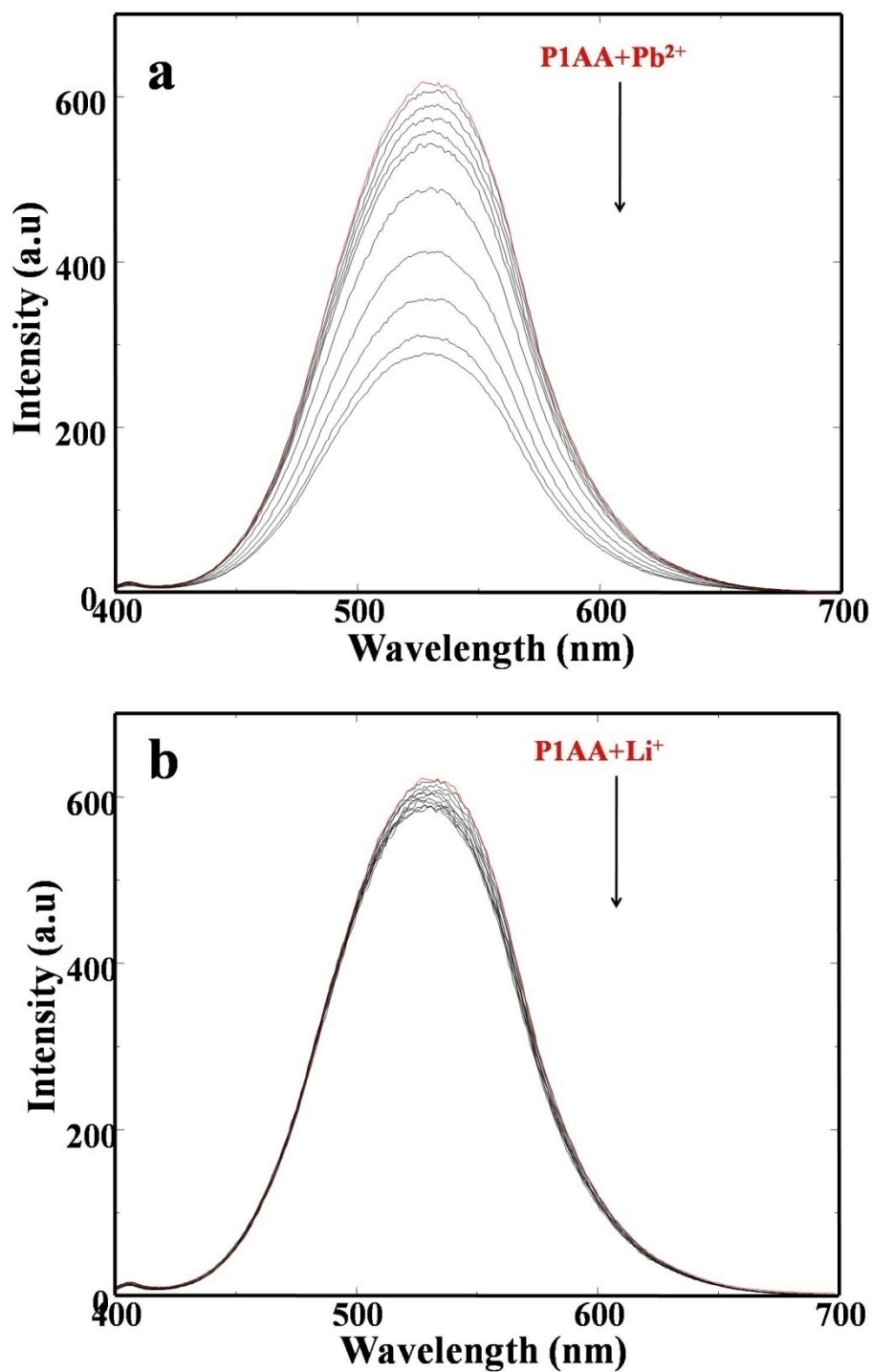
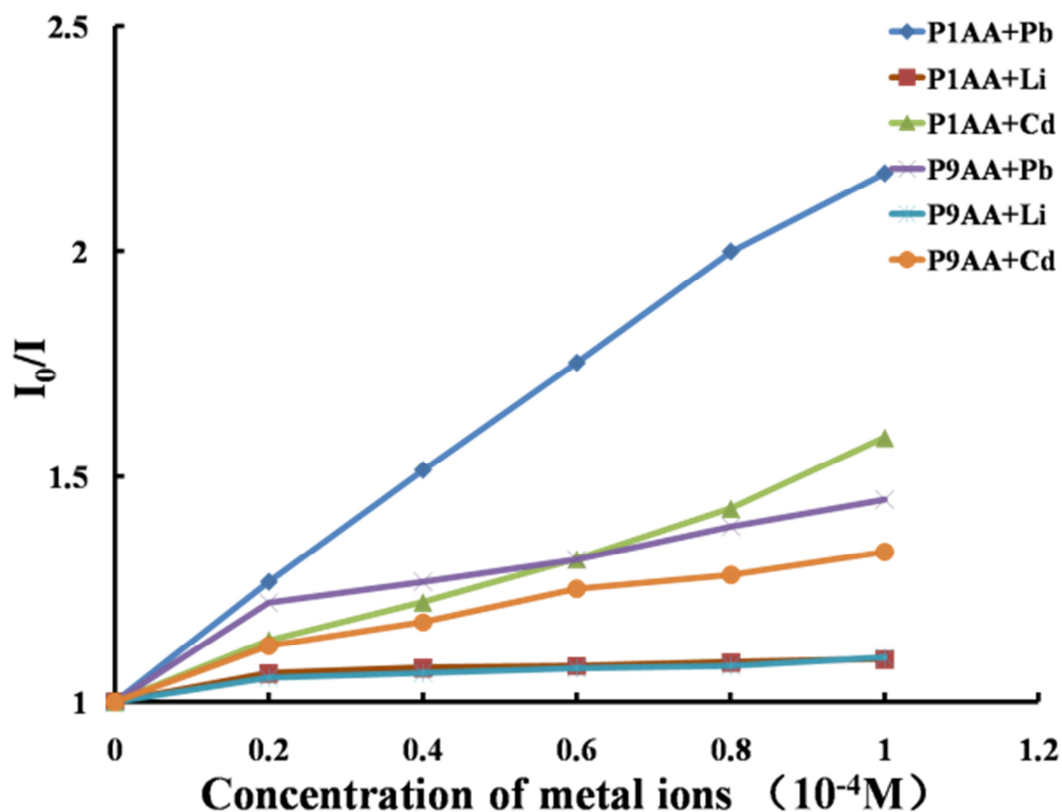**Figure 6.5** Fluorescence spectra of P1AA at [Ar] =1.0×10^{-5} M upon addition of Pb^{2+} (a)

and Li^+ (b). [Pb^{2+} and Li^+] = (0, 0.02, 0.04, 0.06, 0.08, 0.1, 0.2, 0.4, 0.6, 0.8, 1.0) $\times 10^{-4}$

M.
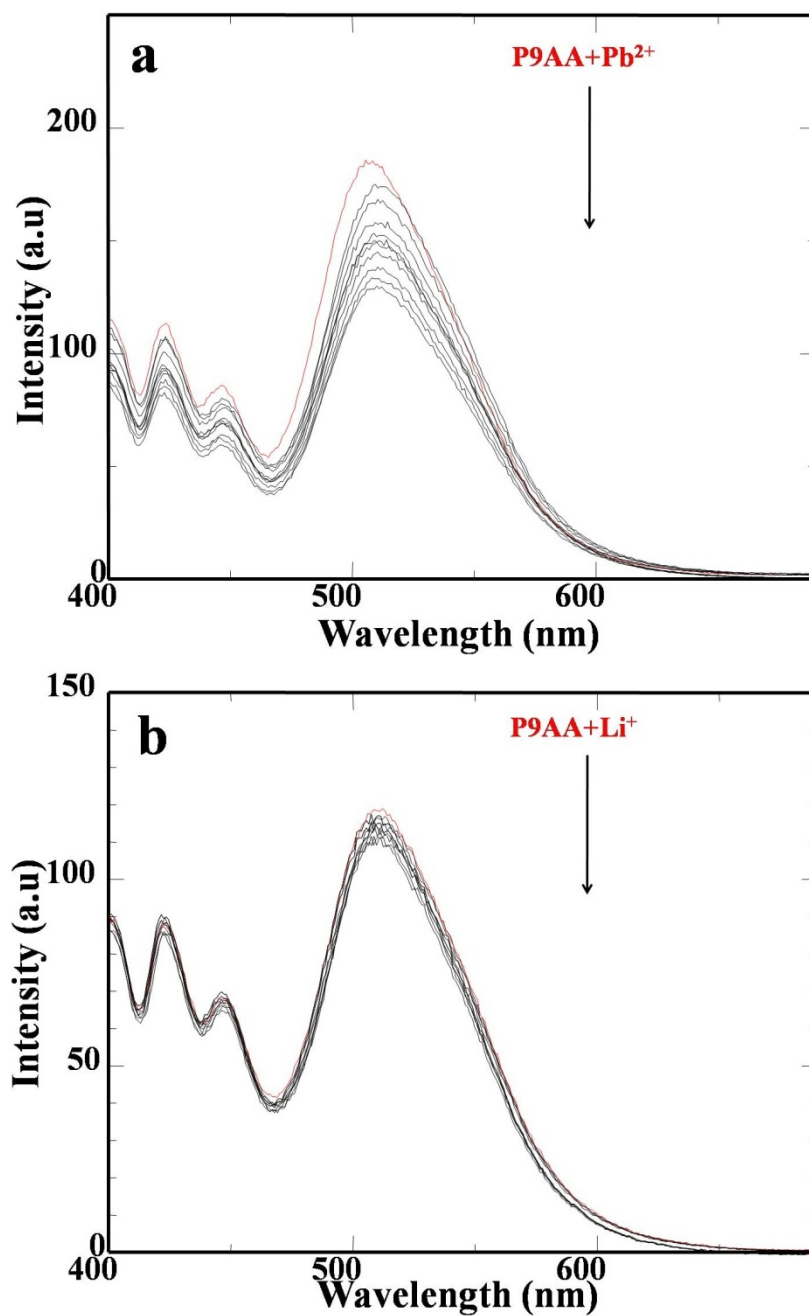
Figure 6.6 Fluorescence spectra of P9AA at [Ar] $=1.0\times10^{-5}$ M upon addition of Pb^{2+} (a)

and Li^+ (b). [Pb^{2+} and Li^+] $= (0, 0.02, 0.04, 0.06, 0.08, 0.1, 0.2, 0.4, 0.6, 0.8, 1.0) \times 10^{-4}$

M.

Figure 6.7 Stern–Volmer plots associated with the PAAs in the several metal ions

concentration range around [M]= 1.0×10^{-4} M. I_0 and I are taken as the fluorescence

intensity at the maximum emission wavelength. ([Ar] = 1.0×10^{-5} M, Excitation

wavelength: 360 nm).

formation might affect the coordination sites with metal ions for the quenching

efficiency. There was no significant difference in the peak position between the

polymers obtained in the presence and absence of metal ions. However, the fluorescence

intensity was changed greatly upon addition of Pb^{2+} aqueous solution in the case of P1AA, meaning that the coordination sites of N atoms in the P1AA showed better location to the metal ions.

Figure 6.7 presented Stern–Volmer plots associated with the various metal ions titration of PAAs with the heavy metal ion in the range around $0-1.0\times10^{-4}$ M. The variation of the fluorescence emission intensity with different concentration of Pb^{2+} ions was observed a nearly linear response on the relationship. The results followed the typical Stern-Volmer equation. The good linear relation between I_0/I and Pb^{2+} concentration led quenching constant (K_{sv}) as high as 1.19×10^4 M^{-1} for P1AA and 0.40×10^4 M^{-1} for P9AA, to 0.08×10^4 M^{-1} for P1AA and 0.08×10^4 M^{-1} for P9AA in the case of Li^+ ion. The higher K_{sv} could directly indicate the higher sensitivity in the trace level [22-23]. Beyond Pb^{2+} and Li^+, the fluorescence response properties of polymers toward other metal ions also examined in Figure 6.8. The valves of K_{sv} showed a considerable reduction degree by addition of Cd^{2+} and a tiny reduction at different levels by the addition of Li^+, Ag^+, Zn^{2+}, Na^{2+}, Ca^{2+}, Ni^+, K^+, Mg^{2+}, respectively. These results indicated that these polymers were much more sensitive toward Pb^{2+} than other metal ions. By combinations with the UV-vis absorbance spectra, the polymers could be expected to use as a Pb^{2+} fluorescence sensor with considerably selectivity. The

sensitivity toward Pb^{2+} could be attributed to several factors, such as the radius, coordination numbers, or the positive charge of metal ions. The stronger binding ability of anthracene unit and the coordinated formation of Pb-N binding could be considered by sharing lone pairs of electrons to form metal ion complexes [29]. It could be estimated that the P1AA showed a better ability to coordinate and detect the different heavy metal ions than P9AA. It was probably because the torsion structure of P1AA due to the steric hindrance was beneficial to the formation of coordination between polymer backbone and metal ions as mentioned above (Scheme 6.3). For efficient excimer quenching by Pb^{2+} in P1AA, it might be performed that Pb^{2+} seemed to be coordinated with ligand portions of the anthracene nitrogen with P1AA and be taken into the P1AA conjugated backbone. The comparison of P1AA and P9AA indicated importance of polymer-structure on the efficient quenching.
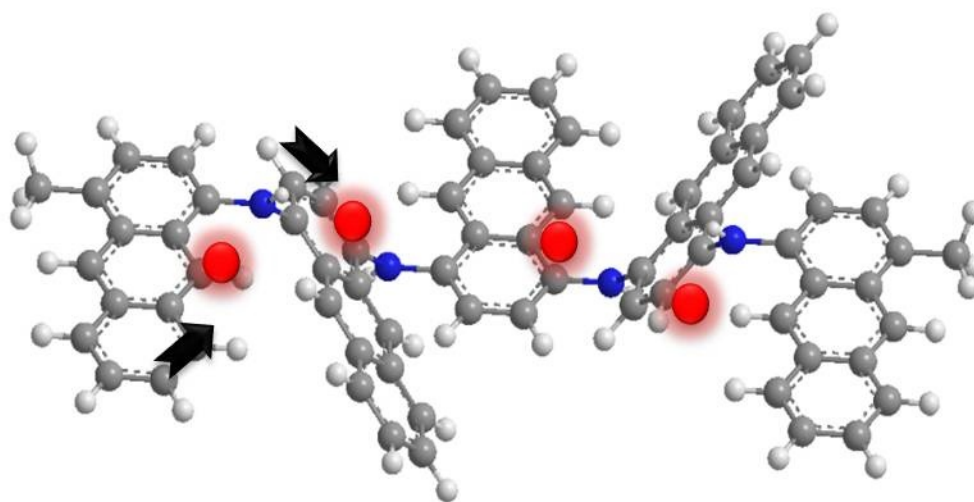
P1AA
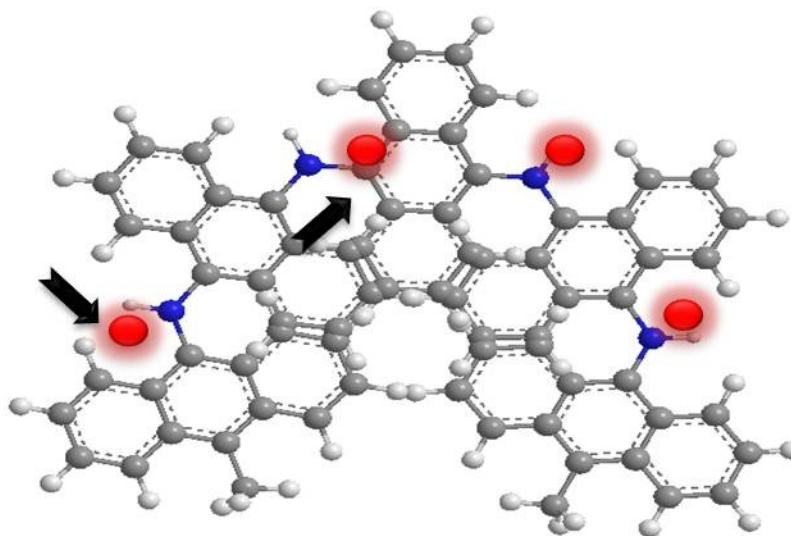
P9AA

Scheme 6.3 Calculated structure and proposed coordination model of PAAs.
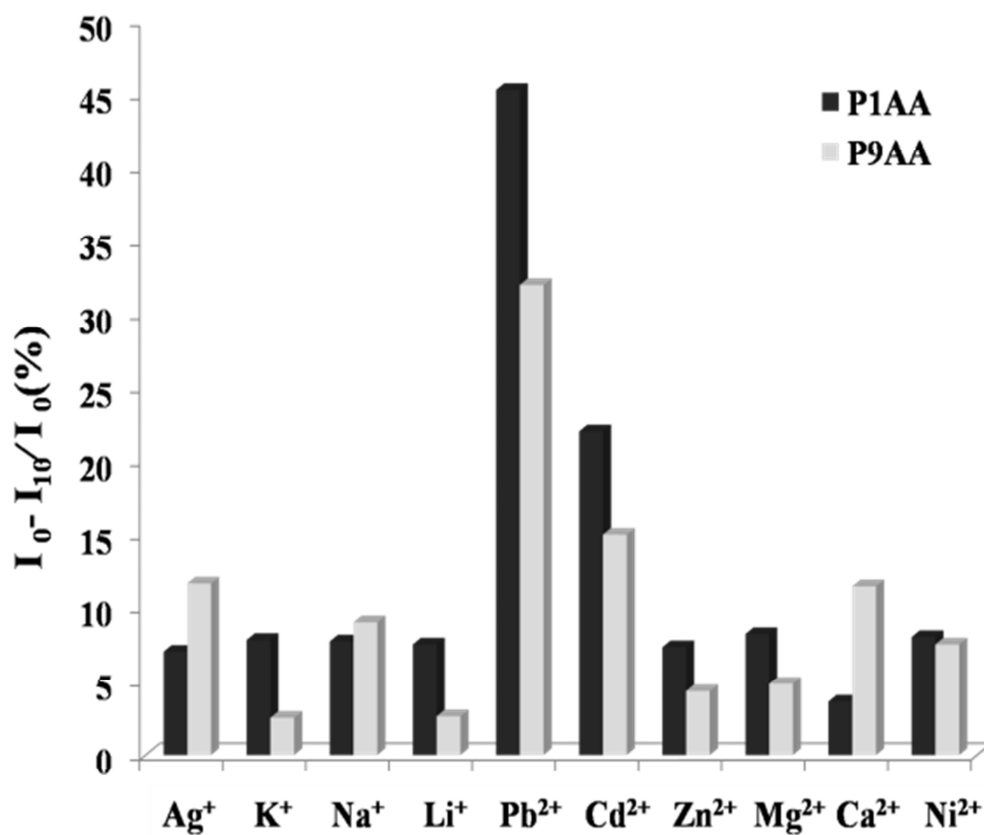
Figure 6.8 Fluorescence quenching efficiencies (I_0-I)/I_0 of Polyaminoanthracene ([Ar] = 1.0×10^{-5} M) in the presence of various metal ions (1.0×10^{-4} M for each metal ion in 4 ml polymer solution).

6.4 Conclusions

In conclusion, soluble anthracene-based polymers were synthesized through a sample oxidation polymerization and their fluorescent properties toward a variety of metal ions were studied intensively. The interaction of ions with the bonding site of PAAs were formed, according to maximum absorption peaks were shift slightly to longer wavelength with the addition of metal ions. Comparative investigations of adsorption behaviors revealed the PAAs showed detection capacity towards several metal ions. Especially P1AA suggested that such fluorescence result of the anthracene moiety was applicable for the Pb^{2+} sensitivity by the quenching behavior. In combination with UV-vis results, this is potential ability to use as sensitive fluorometric for detection of Pb^{2+}.

6.5 References

[1]. Li, X. G.; Li, M. H.; Huang, M. R.; Moloney, M. G. Synthesis and multifunctionality of self-stabilized poly(aminoanthraquinone) nanofibrils. *J. Phys. Chem. C* **2011***, 115*, 9486.

[2]. Rabindranath, A. R.; Zhu, Y.; Zhang, K.; Tieke, B. Purple red and luminescent polyiminoarylenes containing the 1,4-diketo-3,6-diphenylpyrrolo[3,4-c]pyrrole (DPP) chromophore. *Polymer*. **2009**, *50*, 1637.

[3]. Yen, H. J.; Liou, G. S. Novel thermally stable triarylamine-containing aromatic polyamides bearing anthrylamine chromophores for highly efficient green-light-emitting materials. *J. Polym. Sci. A: Polym. Chem*. **2008**, *46*, 7354.

[4]. Kondo, M.; Miyake, J.; Tada, K.; Kawatsuki, N. Tuning photoluminescent wavelength of water-soluble oligothiophene/polymer complex film by proton bonding. *Chem. Lett*. **2011**, *40*, 264.

[5]. Chen, R.; Ling, J.; Hogen-Esch, T. E. Synthesis and spectroscopic studies of macrocyclic polystyrene. Containing two fluorene units and single 9, 10-anthracenylidene group. *Macromolecules* **2009**, *42*, 6015.

[6]. Fraind, A.; Tovar, J. D.   Comparative survey of conducting polymers containing benzene, naphthalene, and anthracene cores: Interplay of localized aromaticity and polymer electronic structures. *J. Phys. Chem. B* **2010**, *114*, 3104.

[7]. Paul, A. W.; Kenneth, A. E.; Anne, B. P.; Hall, H. K. New polyaromatic quinone imines from anthraquinone. *Macromolecules* **1993**, *26*, 5820.

[8]. Fariaa , G. C.; Bulhoes, L. O. S. Synthesis and electrochemical response of poly (1-aminoanthracene) films. *Electrochimica Acta*. **1999**, *10*,1597.

[9]. Doo, K. M.; Kohtaro, O.; Tsukasa, M.; Kenji, K.; Takakazu, Y. Synthesis of poly (1-aminonaphthalene) and poly (1-aminoanthracene) by chemical oxidative polymerization and characterization of the polymers. *Macromolecules* **1993**. *26*, 6992.

[10]. Nakatsuji, Y.; Nakamura, M.; Oka, T.; Muraoka, M. Selective fluorometric sensing of calcium cation by c-pivot lariat monoaza-crown ether with two pyrene moieties. *Chem. Lett*. **2011**, *40*, 1226.

[11]. Kim, H. J.; Lee, M. H.; Mutihac, L.; Vicens, J.; Kim, J. S. Host-guest sensing by calixarenes on the surfaces. *Chem. Soc. Rev.* **2012**, *41*, 1173.

[12]. Miles, B. N.; Ivanov, A. P.; Wilson, K. A.; Doğan, F.; Japrung, D.; Edel, J. B. Single molecule sensing with solid-state nanopores: novel materials, methods, and applications. *Chem. Soc. Rev.* **2013**, *42*, 15.

[13]. Nolan, E. M.; Lippard, S. J. Tools and tactics for the optical detection of mercuric ion. *Chem Rev*. **2008**, *108*, 344.

[14]. Jiao, L.; Meng, T.; Chen, Y.; Zhang, M.; Wang, X.; Hao, E. Triazolyl-linked 8-hydroxyquinoline dimer as a selective turn-on fluorosensor for Cd^{2+}. *Chem. Lett*. **2010**, *39*, 803.

[15]. Tang, Y.; He, F.; Yu, M.; Feng, F.; An, L.; Sun, H. A reversible and highly selective fluorescent sensor for Mercury (II) using poly (thiophene)s that contain thymine moieties. *Macromol. Rapid. Commun.* **2006**, *27*, 389.

[16]. Liu, X.; Tang, Y.; Wang, L.; Zhang, J.; Song, S.; Fan, C. Optical detection of Mercury (II) in aqueous solutions by using conjugated polymers and label-free oligonucleotides. *Adv. Mater*. **2007**, *19*, 1471.

[17]. He, S.; Buelt, A. A.; Hanley, J. M.; Morgan, B. P.; Tennyson, A. G. Sterically encumbered bipyridyl-derivatized conjugated polymers and metallopolymers incorporating phenylenevinylene, phenyleneethynylene, and fluorenylene segments. *Macromolecules* **2012**, *45*, 6344.

[18]. Bredas, J. L.; Street, G. B. Polarons, bipolarons, and solitons in conducting polymers. *Chem. Res*. **1985**, *18*, 309.

[19]. Yu, B.; Jiang, X. S.; Yin, J. Multiresponsive square hybrid nanosheets of POSS-ended hyperbranched poly (ether amine) (hPEA). *Macromolecules* **2012**, *45*, 7135.

[20]. Shirashi, Y.; Miyamoto, R.; Hirai, T. Temperature-driven on/off fluorescent indicator of pH window: an anthracene-conjugated thermoresponsive polymer. *Tetrahedron Lett*. **2007**, 48, 6660.

[21]. Mori, H.; Tando, I.; Tanaka, H. Synthesis and optoelectronic properties of alternating copolymers containing anthracene unit in the main chain by radical ring-opening polymerization. *Macromolecules*. **2010**, *43*, 7011.

[22]. Huang, M. R.; Huang, S. J.; Li, X. G. Facile synthesis of polysulfoaminoanthraquinone nanosorbents for rapid removal and ultrasensitive fluorescent detection of heavy metal ions. *J. Phys. Chem. C* **2011**, *115*, 5301.

[23]. Yang, B.; Li, G.; Zhang, X.; Xin, S.; Shu, X.; Wang, A.; Zhu, X.; Zhu, J. Hg^{2+} detection by aniline-based conjugated copolymers with high selectivity. *Polymer*. **2011**, *52*, 2537.

[24]. Jou, J. H.; Chiu, S.; Wang, R. Y.; Hu, H. C.;C. Wang, C. P.; Lin, H. W. Efficient, color-stable fluorescent white organic light-emitting diodes with an effective exciton-confining device architecture. *Org. Electron*. **2006**, *7*, 8.

[25]. Hasewage, M.; Suzuki, A.; Matsumura, S.; Toshima, K. Molecular design, chemical synthesis, and evaluation of novel anthracene derivatives as a new family of protein photocleavers. *Sci. Tech. Adv. Mater*. **2006**, *7*, 169.

[26]. Subudhi, P. C.; Kanamaru, N.; Lim, E. C. Luminescence from a sandwich dimer of anthracene. *Chem. Phys. Lett.* **1975**, *32*, 503.

[27]. Miyamoto, K.; Iwanaga, T.; Toyota, S. Influence of conformation of 9,10-anthrylene rotors on structures and self-association properties of macrocyclic arylene–alkynylene oligomers. *Chem. Lett*. **2010**, *3*, 288

[28]. Chou, T. C.; Wu, R. T.; Liao, K. C.; Wang, C. H. N-1- and N-2-anthryl succinimide derivatives: C-N bond rotational behaviors and fluorescence energy transfer. *J. Org. Chem.* **2011**, *76*, 6813.

[29]. Zou, Y.; Wan, M.; Sang, G.; Ye, M.; Li Y. An alternative copolymer of carbazole and thieno[3,4b]-pyrazine: synthesis and mercury detection. *Adv. Funct. Mater.* **2008**, *18*, 2724.

Chapter 7

Summary

In this thesis, two series of new approaches including novel substitutive conductive PPy copolymer composited films were applied for charge storage materials and fluorescent polyaminoanthracenes were applied for metal sensing materials. This thesis are discussed and expected to contribute to the understanding of these new kinds of functional films for their potential applications.

Chapter 1 summarized a brief introduction to related topics to electrically conductive polymers. The synthetic method, basic property, main application fields of heterocyclic aromatic conductive polymers were summarized in this chapter.

Chapter 2 revealed the facile syntheses of P(Py-*co*-FFr) film by chemical copolymerization of pyrrole(Py) and Furfural(FFr). Results demonstrated that conjugate chemical bonds obtained from methine group found in the copolymer film, implying a better thermo and electrochemical stability. Meanwhile, the formation of density and smooth surface was considered to contribute to performance of metal-like luster. The broad spectrum reflection of the incident light was also benefit to the metal-like luster. The obtained films are expected as a new conductive polymeric material to show the potential advantage for industrial application.

Chapter 3 focused the similarly method for the fabrication of composite films consisting of poly (pyrrole–*co*–formylpyrrole) copolymers P(Py-*co*-FPy) and MWCNTs through chemical polymerization. The composite films exhibited better film–forming ability and improved conductivity than pure PPy and P(Py-*co*-FPy), probably due to highly conjugated backbone of the P(Py-*co*-FPy) interacted with the MWCNTs. Results of CV suggested that the P(Py-*co*-FPy)/MWCNTs composites showed better capacitance with 184 F/g, when the scan rate was 10mV/s. The electrochemical behavior of the composite films could be improved as the MWCNTs amount was increased in the film.

Chapter 4 described the investigation on a novel capacitance films prepared by poly (pyrrole–*co*–formylpyrrole) prepared on poly (4–styrenesulfonate acid) (PSS) with electrostatic self–assembly layer–by–layer process. Benefit of the doping effect of the sulfonic group, the layer cycles gave rise to increased electrical conductivity 2 layers to 10 layers. The electrostatic interaction between the P(Py–*co*–FPy) and the PSS layer was confirmed from UV–visible spectra and enhanced by the number of layers and PSS concentration. Electrochemical results showed that the electrochemical capacitance of those multilayer films is influenced by the increase of the number of layers and the PSS concentration, suggesting that the multilayer film morphology affects the

electrochemical behavior.

In Chapter 5, π-conjugated poly (9–aminoanthracene) and poly (1–aminoanthracene) were synthesized through a facile chemical oxidative polymerization. Results suggested that the P1AA might show high possibility to form stable anthracene excimer relative to that of P9AA. The solvent effect of fluorescence emission on fluorophore concluded that the excitation state of conjugated PAAs could be much stable and existed for a longer time in solvent with a higher polarity. The fluorescent composite films consisting of P1AA and PVA/PSS were prepared. Results suggested that the electrostatic interaction between the P1AA and sulfo group was greatly effect on the surface morphology and the optical properties for P1AA/PSS composite films.

Chapter 6 revealed the fluorescent properties toward several kinds of metal ions for the obtained polyaminoanthracenes (PAAs) intensively. Comparative investigations revealed that both of the P1AA and P9AA showed detection capacity towards several heavy metal ions. Especially results of P1AA suggested that fluorescence of the anthracene moiety was applicable for sensitivity and selectivity toward heavy metal ions in the quenching behavior. In combination with UV data, this is potential ability to use as sensitive fluorometric for detection of Pb^{2+}.

−250−

In addition, as studying of such novel conductive polymers and their functional films for significantly electro/optical properties, I hope that this study could contribute to extend the understanding of such new kind of conductive materials and attractive for their future applications in industry.

List of Publication

(1). <u>Kun Wang</u>, Yang Cao, Motohiro Tagaya, Takaomi Kobayashi.

Electrochemical capacitance of poly(pyrrole–*co*–formylpyrrole)/sulfonated polystyrene layer–by–layer assembled multilayer films, *Journal of Materials Science*, **2014**, *49*, 5746–5756.

(2). <u>Kun Wang</u>, Yusuke Hoshina, Yang Cao, Motohiro Tagaya, and Takaomi Kobayashi.

Novel metal–like luster conductive film made of pyrrole and furfural in straightforward chemical copolymerization, *Industrial & Engineering Chemistry Research*, **2013**, *52*, 2762–2771.

(3). <u>Kun Wang</u>, Motohiro Tagaya, Shi–jun Zheng, Takaomi Kobayashi.

Facile syntheses of conjugated polyaminoanthracenes by chemical oxidation polymerization for sensitive fluorometric detection of heavy metal ions, *Chemistry letters*, **2013**, *42*, 427–429.

Other Related Papers

(1). Prasit Pattananuwat, <u>Kun Wang</u>, Motohiro Tagaya, Takaomi Kobayashi.

Cyclic voltammetric deposition of poly(pyrrole-*co*-2-formyl pyrrole)/multiwall carbon nanotube composite for highly specific capacitive electrodes, *Chemistry letters*, **2014**, *43*, 1155−1157.

(2). Kun Zhao, Jin–tao Wang, Cheng–zi Wang, Kai Li, Shi–jun Zheng, <u>Kun Wang</u> and Takaomi Kobayashi.

Linearly polarized white fluoresence from shish–kebab type liquid crystalline Poly(p–phenylenevlene)s, *Chinese Journal of Polymer Science*, **2012**, *2*, 1−7.

Presentations in International/National Conference and Symposium

(1). **The 2nd International GIGAKU Conference, Nagaoka, Japan.** (June, 2013)

<u>Kun Wang</u>, Motohiro Tagaya, Shi–jun Zheng,Takaomi Kobayashi. **Conjugated polyaminoanthracenes prepared by chemical oxidation polymerization**.

(2). **The 2nd Joint Symposium CU–NUT, Bangkok, Thailand.** (October, 2012)

<u>Kun Wang</u>, Yusuke Hoshina, Yang Cao, Takaomi Kobayashi. **Novel metal–like luster conductive film made of pyrrole–furfural by straightforward chemical copolymerization**.

(3). **International Symposium on Global Multidisciplinary Engineering 2011, Nagaoka, Japan.** (January, 2011)

<u>Wang Kun</u>, Shi–jun Zheng ,Takaomi Kobayashi. **New method to prepare single polymer with linearly polarized white fluorescence**.